The impact of triboelectrification on desert dust flow dynamics

Vasiliki Daskalopoulou

Department of Physics

University of Crete

Supervisor: Vassilis Amiridis

National Observatory of Athens

Submitted in Partial Fulfillment of the Requirements

for the Degree of

Doctor of Philosophy

October 2023

"Hope clouds observation."

Frank Herbert, Dune

To *my parents*, Dimitris & Eleni,

and *my brother* Stathis for their unconditional love.

This research is co-financed by Greece and the European Union (European Social Fund- ESF) through the Operational Programme **«Human Resources Development, Education and Lifelong Learning»** in the context of the project "**Strengthening Human Resources Research Potential via Doctorate Research – 2nd Cycle**" (MIS-5000432), implemented by the **State Scholarships Foundation** (IKY).

Ευρωπαϊκή Ένωση
European Social Fund

Operational Programme
Human Resources Development, Education and Lifelong Learning
Co-financed by Greece and the European Union

ΕΣΠΑ 2014-2020
ανάπτυξη - εργασία - αλληλεγγύη

The dissertation of V. Daskalopoulou was reviewed and approved by the following committee:

Vassilis Amiridis
Research Director - National Observatory of Athens
Dissertation Advisor, Chair of Committee

Konstantinos Tassis
Professor of Astrophysics - University of Crete
Researcher - Inst. of Astrophysics, FORTH

Vassilis Charmandaris
Professor of Astrophysics - University of Crete
Director of Inst. of Astrophysics - FORTH

Declaration

I hereby declare that except where specific reference is made to the work of others, the contents of this dissertation are original and have not been submitted in whole or in part for consideration for any other degree or qualification in this, or any other university. This dissertation is my own work and contains nothing which is the outcome of work done in collaboration with others, except as specified in the text and Acknowledgements.

Vasiliki Daskalopoulou

October 2023

Acknowledgements

I would like to express foremost my deepest gratitude to my advisor Dr. Vassilis Amiridis, who believed in me during the years of my graduate program, gave me the opportunity to start my PhD in the National Observatory of Athens and become part of an ever-growing team of researchers and, later, colleagues. His restless yearning for new ideas and striving excellence pushed me to my limits, and beyond, for performing my best all these years. This work would not have been accomplished without his guidance, support and constant encouragement towards scientific autonomy.

This dissertation would not have been made possible, though, without the invaluable support from my other two academic supervisors from the University of Crete, Prof. Kostas Tassis and Prof. Vassilis Charmandaris, whom I deeply thank for their invaluable contributions and scholarly insights that have greatly enhanced the depth and breadth of this thesis. Their collective wisdom and collaborative spirit have been a source of inspiration and motivation.

Since all the research undertaken was within the National Observatory of Athens and its infrastructure, I would like to express special appreciation to the entire ReACT team for fostering an intellectually stimulating environment that facilitated the progression of this research over the years, but I feel especially obliged to my fellow researcher, Dr. Sotirios Mallios, whom I consider my scientific mentor. His expertise in the field was instrumental in shaping the trajectory of my work.

During these six years, I could not omit the immense help I have received from Prof. Joseph Ulanowski and Prof. William Martin, who later became my co-supervisors. I am deeply thankful for entrusting me with their instrumentation and providing invaluable insights during the course of this research. Their generosity and willingness to share their expertise, regardless of the circumstances, have been integral to the success of this academic endeavor.

I would like to express my gratitude to all my colleagues and fellow researchers who provided valuable input and constructive discussions throughout the entire journey.

Last but not least, to my loving family and friends (including my pet cat, Nebbie, that stayed by my side on countless sleepless nights) for their unwavering belief in me, Per Aspera Ad Astra !

Abstract

The Global Electric Circuit (GEC) represents the electric current pathway in the Earth's atmosphere. The electric current that flows upwards from thunderstorms and electrified clouds into the Ionosphere, spreads out over the globe along magnetic field lines to the opposite hemisphere, and returns to the surface of the Earth. Atmospheric electric parameters, such as the vertical Electric Field (E_z) and induced air-to-Earth current (I_c) through the GEC, greatly depend on ambient weather conditions and convective meteorological systems due to the re-distribution of charged or uncharged aerosols and terrestrial radioactive particles in the atmospheric circulation. Under fair weather conditions, the electrical circulation is dominated by the potential difference between the global capacitor, which in turn generates the fair weather electric field, and consequently the fair weather electric current.

Amongst aerosols affecting the atmospheric electrical content, Mineral Dust represents one of the most significant contributors, due to its abundant mass, various shapes and sizes which result in varying electrical properties of the dust particles. During dust storms, dust devils and subsequent advection of elevated dust layers, the electrical parameters can vary greatly from the values under fair weather conditions. The exact mechanisms that would explain and sufficiently describe the long-range electrification of dust are not clear yet, and are a subject of investigation. Major processes that are considered responsible for the electrification of dust particles include ion attachment and contact electrification, i.e. triboelectrification. Such processes are claimed to have large impact on desert dust transport and its influence in climate and ecosystems through the retention of larger dust particles in the atmosphere, as well as to particle vertical orientation with impact on radiative transfer. Ground-based electric field measurements can be indicative of the electrical behaviour of elevated dust layers and act as a proxy for the detection of charged particles within the layers. To gain a more comprehensive understanding of the electrical characteristics of airborne dust, synergistic model implementations and vertical profiling measurements within the layers are of outmost importance.

Initially, we introduce the development of a novel 1D numerical model that parametrizes both of the above charging processes in the presence of a large scale electric field, under stagnant

atmospheric conditions where wind contribution is neglected. The model is able to self-consistently calculate the modification of atmospheric ion densities and the subsequent alteration of the large scale electric field, when dust particles are present and atmospheric ions attach to them, and is further updated to account for the particle charging due to the efficient collisions between particles of various sizes. Furthermore, we demonstrate the feasibility of particle orientation under the influence of electric and gravitational fields through analytical calculations of the mean orientation angle of both charged/uncharged dust particles and comment on the pre-requisites on electric field strengths for the orientation to occur on particles of various sizes.

Then, in order to test the charging model hypothesis and, simultaneously, provide observational evidence of dust electrification, novel measurement techniques and instrumentation are developed, targeting signs of dust electrification from the ground and accurate profiles of the vertical electric field strength and the charge density within the layer. We demonstrate a novel methodology through ground-based observations, only, that indicates that electric field variations during Saharan dust advection can be a sign of charged dust occurrences. Synergistic observations of the vertical atmospheric electric field and lidar-derived quantities for the optical characterization of the layer, are employed. Both parameters were monitored for the first time in tandem, and in order to identify the influence of the elevated dust layers on the ground electric field, we extract a Localized Reference Electric Field from the timeseries that reflects the local fair weather activity. Then, we compare it with the reconstructed daily average behaviour of the electric field and the Saharan dust layers' evolution. To quantitatively approach our results, we examine the dependency of E_Z against theoretical assumptions for the distribution of separated charges within the electrified dust layer through a physical approximation that constitutes a more realistic description of the in-layer distribution of charges, as to what was previously assumed.

Being aware of the inherent challenges and instrumental ambiguities of atmospheric electricity measurements, we introduce the implementation of two low-cost and disposable atmospheric electricity sensors that measure the electric field strength and the space charge density, respectively, while they have launching capabilities on balloon-borne meteorological platforms. The sensors were designed, assembled and characterized in-house, their performance was assessed on-field over preparatory campaigns and eventually utilized in a major ESA Cal/Val experiment, where consistent dust observations were performed. Data by both sensors are assessed with respect

to the prevailing meteorological conditions and processed for different altitude domains, while showing a good overall agreement.

Finally, we target the elusive dust particle preferential orientation, which could be detected from the resulting dichroic extinction of the forward-scattered light as it transmits through dust layers in the atmosphere. We revisit an existing methodology by targeting dichroic extinction of transmitted sunlight by utilize an experimental direct-Sun polarimeter, SolPol, which is capable of continuous monitoring of the elevated layers. SolPol records the state of polarization of the direct sunlight, represented by the complete Stokes vector, at a default wavelength of 550 nm with a detection limit of 10^{-7}. We, firstly, fully characterize the instrument and delineate its measurement technique, produce a comprehensible and user-friendly instrument manual, and then provide unique observations of increasing trends of linear polarization for sunlight propagation through these dust layers, under various loads and solar zenith angles. Concluding, we attempt to interpret the measurements as a first indication of either vertical or horizontal dust particle orientation. The observed electric fields, nonetheless, are not adequate to orient larger particles totally vertically and retain them aloft, which presumably hints to other mechanisms leading to such a behavior.

As a closure to this effort, we comment that when all these scientific disciplines (models - implementations - observations) are combined, the presence of electrified dust in lofted layers away from the source is undisputable, meaning that the electrical properties of the particles impact their transport dynamics and future work will represent the modulation of particle electrification in a more realistic way.

Table of Contents

List of Figures

List of Tables

Nomenclature

AC	Alternating Current
ADC	Analog-to-Digital
ADDA	Amsterdam Discrete Dipole Approximation
AERONET	AErosol RObotic NETwork
AOD	Aerosol Optical Depth
ASCII	American Standard Code for Information Interchange
ASKOS	Experimental campaign over Cape Verde
BB	Barbados
Cal/Val	Calibration & Validation
CCD	Charge-Coupled Device
CCN	Cloud Condensation Nuclei
CIMEL	Sunphotometer manufacturing company
CMT	Carlsberg Meridian Telescope
CP	Circular Polarization
CV	Cape Verde or Cabo Verde
DC	Direct Current
DFM-09	Specific radiosonde type by GRAW (discontinued)
DH	Digital Holography
DOCP	Degree of Circular Polarization
DOLP	Degree of Linear Polarization
D-TECT	"Does Dust TriboElectrification affect our ClimaTe ?"
E-field	Electric Field
EQ3-SynScan	Equatorial Astronomical Mount type
EQmod	Equatorial mount module for direct PC connection
ERC	European Research Council
ESA	European Space Agency
EVDC	ESA Validation Data Center
EVPA	Electric Vector Polarization Angle

FENNEC	Experimental campaign over Cape Verde
FFT	Fast Fourier Transform
FM	Fieldmill Electrometer
FOV	Field-of-View
FW	Fair Weather
GEC	Global Electric Circuit
GRAW	Radiosonde manufacturing company
IN	Ice Nuclei
LP	Linear Polarization
LREF	Localized Reference Electric Field
MBL	Marine Boundary Layer
MiniMill	Miniature Fieldmill
MR	Mauritania
NASA	National Aeronautics and Space Administration
ND	Neutral Density (refers to filters)
NNE	North-North-East
NOA	National Observatory of Athens
OPC	Optical Particle Counter
PANGEA	PANhellenic GEophysical observatory of Antikythera
PBL	Planetary Boundary Layer
PEM	Photoelastic Modulator
PG	Potential Gradient
PI	Principal Investigator
PLDR	Particle Linear Depolarization Ratio
PSD	Particle Size Distribution
RI	Research Infrastructure
RS41	Specific radiosonde type by Vaisala
SAL	Saharan Air Layer
SALTRACE	Experimental campaign over Barbados
SEM	Scanning Electron Microscopy
SEP	Solar Energetic Particles
SolPol	Solar Polarimeter
SSA	Single Scattering Albedo
SZA	Solar Zenith Angle

TEM	Transmission Electron Microscopy
UART	Universal Asynchronous Receiver/Transmitter
UH	University of Hertfordshire
UT	Universal Time
UTC	Coordinated Universal Time
VLDR	Volume Linear Depolarization Ratio
WALL-E	Polarization lidar for Particle Orientation
WRF	Weather Research and Forecasting model
XDATA	eXternal DATA transmission protocol

R_c	Columnar resistance [Ω m^2]
$n^{\pm}$	Fair weather ion-densities [m^{-3}]
z_C	Layer central altitude [m]
$\boldsymbol{E_z}$	Vertical electric field strength [V m^{-1}]
$\boldsymbol{J_z}$	Conduction current [pA]
$\boldsymbol{M_{PEM}}$	PEM Mueller matrix (as retardation plate)
$\boldsymbol{M_{Pol.,a°}}$	Linear polarizer Mueller matrix for rotation angles $a°$
δ_v	Volume Linear Depolarization Ratio [%]
d	Layer depth [m]
DOLP, DOCP, LP, CP	Light polarization [ppm]
I, Q, U, V	Stokes parameters
l	Scaling height [m]
PG	Potential gradient [V m^{-1}]
R	Layer radius [km]
V	Electric potential [V]
β	Particle backscatter coefficient [Mm^{-1} sr^{-1}]
δ_{p}	Particle Linear Depolarization Ratio [%]
H	Ionospheric height [m]
λ	Wavelength [nm]
$\boldsymbol{\chi}$	Electric Vector Polarization angle [°]
$Q(t)$	Temporal dependence of induced charge on MiniMill plates
q	Ionization rate [pairs m^{-3} s^{-1}]
θ	Orientation angle [°]
ρ	Charge density [C m^{-3}]
σ	Atmospheric conductivity [S m^{-1}]

Chapter 1

Introduction

"Deep in the human unconscious is a pervasive need for a logical universe that makes sense. But the real universe is always one step beyond logic" - Frank Herbert

In the expansive realm of Atmospheric Sciences, this doctoral thesis is seeking to unravel the intricate relationships between atmospheric processes, desert dust, and electric fields. The research spans multiple dimensions, offering profound insights into aerosol dynamics that have global-scale climatic implications. The overarching goal is to fill existing gaps in our understanding on the role of electrification mechanisms to mineral desert dust transport and removal processes, through systematic observations of the key parameters driving the phenomena. Advanced remote sensing methods are employed, along with observational techniques targeting directly in the environment of transported dust layers through synergies between state-of-the-art instrumentation, in order to adopt a comprehensive approach of the scientific question at hand. Mineral dust plays an important role in the Earth's atmospheric system, as an undivided whole, by being one of the most abundant constituents and, therefore, creates a strong reciprocity with the atmospheric electrical content. Atmospheric electricity is, suitably, a field of study that can provide insight into the electrical properties and processes of the Earth's atmosphere, and their contribution to the transport of dust plumes. The presence of electric fields, charges, and currents in the atmosphere has been recognized for centuries, but it is only in the last few decades that significant progress has been made to link the influence of aerosols in shaping the dynamics of atmospheric electricity, and vice versa.

The research undergone here aims to contribute to the advancement of knowledge in the field by investigating several key areas. Through a combination of field observations, modelling of particle electrical properties and dynamics, and data processing, the thesis seeks to physically interpret the processes that lead to the charging of elevated dust. This dynamic exploration is crucial not only

for comprehending the impact of dust on local environments, but also for elucidating its planetary-scale broader consequences. The charged nature of these particles becomes a focal point, revealing how electrostatic interactions influence their behavior in the atmosphere through novel numerical models that parametrize the charging process. A pivotal shift in the research progress introduces a diverse array of new observational techniques. Ground-based measurements of the electric field strength and vertical profiling of atmospheric electrical properties emerge as key methodologies. These techniques serve as powerful tools, providing unique perspectives into the detection of the electrification state of dust particles. The aforementioned observation requirements involve a number of technical challenges. Obtaining accurate measurements of atmospheric electricity aloft and interpreting them can be quite complex, mainly because the electrical environment is affected by the presence of the measurement platform itself. The emphasis here is on the innovative nature of the observational approaches, highlighting the need for diverse methods to capture the nuanced behavior of charged particles in diverse atmospheric contexts.

The dissertation then delves into the elusive phenomenon of dust particle orientation. The alignment of dust particles in the atmosphere is attributed to their intrinsically elongated shape and is primarily influenced by the interplay of various forces, including aerodynamic, gravitational, and electrostatic forces. These forces act on the particles as they move through the air, leading to their alignment in specific orientations. Aerodynamic forces, arising from the particle's interaction with air currents, can cause alignment based on particle shape. Gravitational forces tend to align particles with respect to the gravitational field. Additionally, electrostatic forces, influenced by the electric field in the atmosphere, can play a significant role in orienting charged dust particles. Leveraging the capabilities of a novel solar polarimetry instrument, meticulously characterized throughout the research, the study uncovers unprecedented insights into particle orientation by using direct sun measurements and highlights the effect this process can have on Earth’s radiative budget. The respective sections serve as a testament to the advancements made in observational capabilities, pushing the boundaries of what we can understand about the behavior of dust particles within the Earth’s atmosphere.

Elevating the research paradigm further, the thesis introduces state-of-the-art sensors for vertical profiling studies. The meticulous deployment of these sensors during various experimental campaigns results in the creation of an unparalleled dataset, emphasizing the novelty of the approach and the invaluable resource it provides for advancing our understanding of dust dynamics.

The comprehensive dataset becomes a cornerstone, offering a wealth of information that enriches our understanding of the vertical distribution of atmospheric electrical properties and extends beyond desert dust studies. The legacy of this research is underscored, with all data, algorithms, manuals, and designs made accessible in public repositories. This commitment to transparency and openness ensures that the broader scientific community can build upon this foundational work.

At this point, we highlight the multidisciplinary nature of the undertaken research. The atmospheric electricity community is poised to benefit from the datasets, by expanding knowledge on diverse phenomena that affect the global electric circuit., while the broader atmospheric community's knowledge is advanced to the relatively under-represented particle charging mechanisms. Simultaneously, the first indications of particle orientation in the Earth's atmosphere shift the focus to the multitude of implications and applications such an observation has on radiative processes, particle scattering processes and the desert dust transport itself. All this benchmark study has the potential to be applied in future planetary studies and in particular to Martian dust processes, where dust electrification is prominently well-documented over the recent years and the high-level impact of this application can have to understanding in general such systems. Incorporating knowledge about dust electrification into atmospheric models for Mars can lead to more accurate simulations. This, in turn, aids in predicting atmospheric phenomena, such as dust storms, which have global-scale lasting consequences to the Martian climate and forthcoming planetary exploration missions.

1.1. The Global Electric Circuit

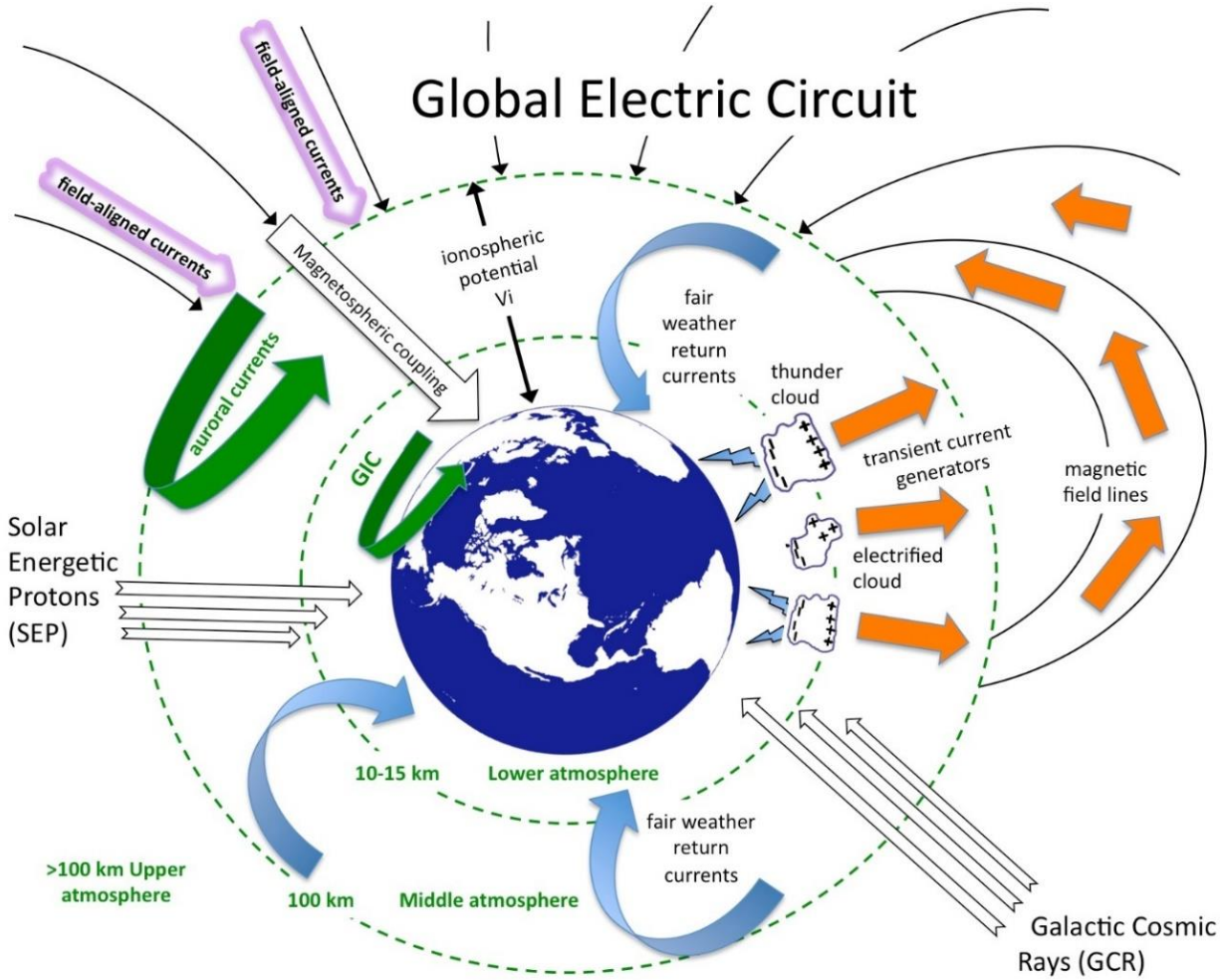

Figure 1.1: The Global Electric Circuit artistic representation, Source: Prof. Jeffrey Forbes, University of Colorado Boulder.

The Global Electric Circuit (GEC) represents the electric current pathway in the Earth's conductive atmosphere, seen in the schematic representation of Figure 1.1. The electric current that flows upwards from thunderstorms and electrified clouds into the Ionosphere, spreads out over the globe along magnetic field lines to the opposite hemisphere, and returns to the surface of the Earth as the fair weather air-to-Earth current (Bering et al., 1998). The GEC is established by the conducting atmosphere sandwiched between the conductive Earth and the conductive Mesosphere/Ionosphere (Williams, 2009). Atmospheric electric parameters, such as the vertical Electric Field (E_z) and

induced air-to-Earth current (I_c) through the GEC, greatly depend on ambient weather conditions and convective meteorological systems (Kourtidis et al., 2020) due to the re-distribution of charged or uncharged aerosols and terrestrial radioactive particles in the Earth's atmosphere (Harrison and Ingram, 2005; Wright, 1933). The GEC is significant not just as a product of global thunderstorm activity, but also as a highly responsive indicator of global land surface temperature and moisture levels associated with climate change, as indicated by Bering et al. in 1998. Furthermore, it has the potential to contribute to climate change itself by means of electrical influences on cloud microphysics. These influences can stem from both external and internal drivers (Tinsley and Zhou, 2006; Zhou and Tinsley, 2007).

As mentioned, the Earth's atmosphere is a conducting medium, attributed to the presence of ions, which are created by three main mechanisms (Tinsley and Zhou, 2006 and references therein): 1. *natural radioactivity* originating in the ground, including direct α, β, and γ radiation from the surface layers and dust aerosol, and also radiation from radioactive gases (principally ^{222}Rn but also ^{220}Rn) and daughter products, 2. *cosmic rays* (CRs) of galactic and solar origin and 3. *relativistic electrons* of a few MeV, precipitated from the radiation belts and peaking at sub-auroral latitudes, and the *Solar Energetic Particle* (SEP) events (mainly protons) in the polar and subpolar regions (Mishev, 2013). These ions attach to dust particles through the processes of ionic diffusion and Coulomb interaction and the polarization due to the presence of an external electric field (Gunn, 1954; Klett, 1971), leading to their subsequent charging (see Section 1.3.1) (Mallios et al., 2021a, 2022; Zhou and Tinsley, 2007).

1.1.1. Fair Weather Electrical conditions

A fundamental challenge in Atmospheric Electricity research has revolved around measuring the intensity and fluctuations (vertically resolved and near the surface) of the Earth's electric field, a parameter directly proportional to the ionospheric potential. The vertical E-field is the most common surface property measured to date, with more than 150 years of data in global scale. It is often intertwined with the Potential Gradient (PG) measurements ($\vec{\nabla}V = PG$), which represents the difference in potential between two vertically separated points (see Section 3.5.2) for the proper representation and sign convention used), with the lower boundary being typically the ground surface (Chalmers, 1967; Harrison, 2013; Harrison and Nicoll, 2018; Markson, 2007; Rycroft et al.,

2008). Recorded variability of methods over observatories around the globe, such as the Kelvin droplet method to the more commercial fieldmills, provide consistent measurements of the unperturbed E-field strength, but their data exhibit significant dissimilarities due to local factors that influence the fair weather E-field and the air-Earth conduction current. Such perturbation drivers are: i. aerosol concentrations produced by manmade activities that affect the atmospheric conductivity, ii. the electrode effect that creates a positive charge a few meters from the ocean's surface, iii. electrified ice crystals or other charge accumulation layers, iv. space charge produced by combustion and industry, v. changes caused by the lower conductivity of cloud boundaries, vi. electrified clouds, vii. modifications to the electric field strength due to the selected installation location of the sensors, viii. atmospheric conductivity changes caused by relative humidity variations (Chalmers, 1967; Markson, 2007). In order to compare ground-based PG measurements from different sites, these need to be, firstly, standardized under conditions of no distorting effects and, then, create a benchmark for the selection of the daily measurements that best represent the local fair weather conditions (see Section 4.3).

During fair weather conditions, which are defined according to international standards as those with cloudiness less than 0.2, wind speed less than 5 m s^{-1} and the absence of fog or precipitation (Chalmers, 1967; Harrison and Nicoll, 2018), the atmospheric electrical circulation is dominated by the potential difference between the global capacitor planes (about 250 kV, e.g., Rycroft et al., 2008), which in turn generates the fair weather electric field, and consequently the fair weather electric current in the presence of the conducting atmosphere. An average current density of 2 pA m^{-2} and a downward looking (by convention positive, e.g., Rakov and Uman, 2003, pp.8) electric field equal to a typical value of about 130 V m^{-1} are expected, respectively (Rycroft et al., 2008). The daily variation of the global thunderstorm activity modulates the fair weather E-field strength and the resulting diurnal variation is represented by the Carnegie curve (Figure 1.2), named after the survey vessel of the Carnegie Institution and its original measurement campaigns in the early 20th century (Harrison, 2013 and references therein). Ideally, under strict fair weather conditions, complete lack of aerosol particles in the atmospheric circulation is expected, since it guarantees that the only mechanism of atmospheric ions loss is the ion-ion recombination. As the concentration of aerosols increases, additional loss can be due to ions attaching to the particles, which leads to a perturbation of the ion density from fair weather values. In actual conditions, aerosols always exist, but under fair weather conditions their concentrations are small enough to not significantly affect

the ionic content of the atmosphere. Therefore, for the modelling purposes of fair weather conditions, aerosol concentrations can be neglected. However, the presence of aerosols in the atmosphere and consequently dust particles, affects atmospheric conductivity (Harrison, 2003; Siingh et al., 2007; Tinsley and Zhou, 2006; Zhou and Tinsley, 2007) and, thus, the near surface electric field strength (see Section 4.4).

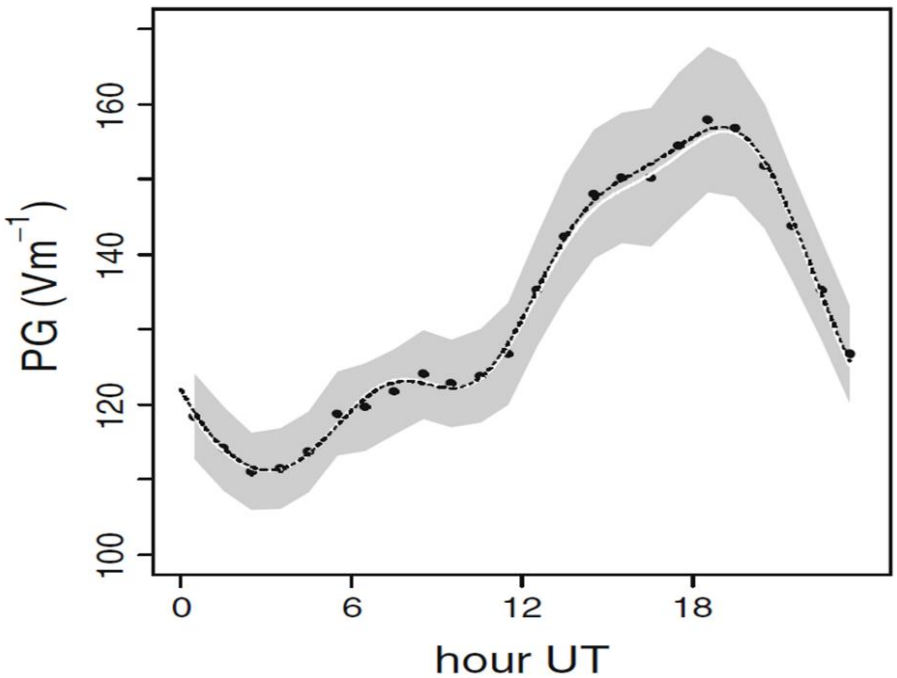

Figure 1.2: The Carnegie curve **(**solid white line) obtained from the original vessel data processing, the modern harmonic analysis (dotted black line) and the annual mean values of hourly PG in V m$^{-1.}$ Adapted from *Harrison et al. (2013).*

In terms of the most reliable measurement of the fair weather atmospheric electric potential, vertical profiling techniques through balloon-borne soundings are considered the best option, which was pointed by Markson et al. (1999 and 2007), so as to avoid local effects and inherent instrument biases. The research undergone in this thesis is heavily based to such measurement techniques and the implementation of novel sensors for the quantification of the atmospheric electrical parameters. A comprehensive approach of the columnar electrical properties is presented in Mallios et al. (2021a). They calculated the crucial parameters of fair weather electrical conditions along the altitude (Figure 1.3), by taking into account the variability of the ionization rates with the

geomagnetic latitude (two simplifications were introduced that neglected the effect of the ground natural radioactivity and involve a generic temporal ionization rate profile). Motivated by the major transport routes of one of the most abundant aerosols in the atmospheric circulation, desert dust, three locations were selected for the quantification of ionization rates, Mauritania (MR), Cape Verde (CV) and Barbados (BB). We observe that quantities, as the E-field strength, are expected to exponentially decrease with the altitude while other increase, but generally present minimal relative differences from location to location. This points that the ionization rate dependence, solely, on the geomagnetic latitude does not create significant variations of the initial fair weather electrical conditions along the transatlantic transport of the dust particles. This behavior will serve as reference for accurate electrification modelling schemes and serve as a comparison for perturbations caused by the presence of electrically active dust particles.

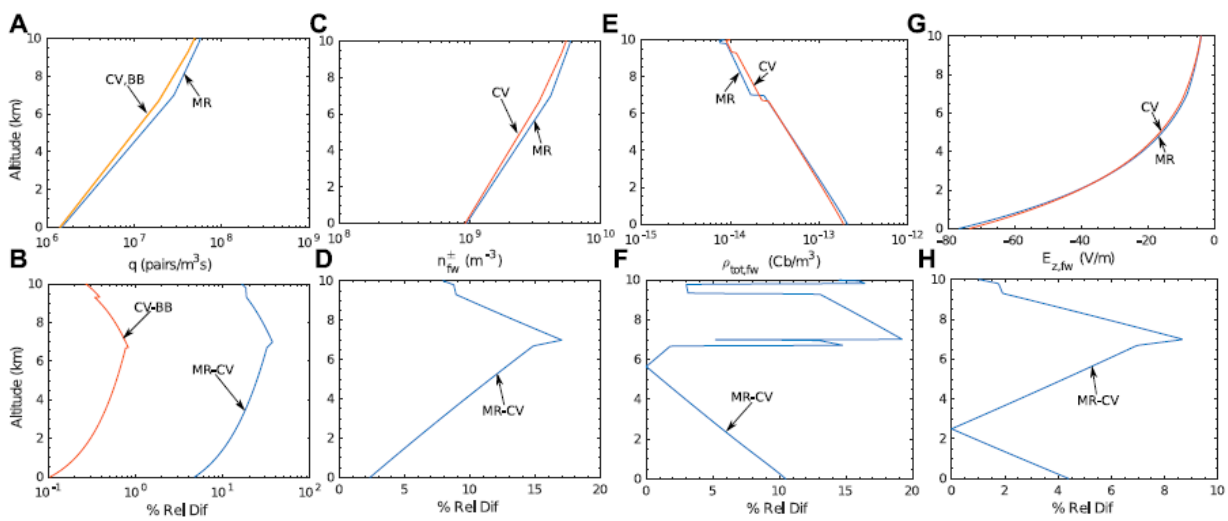

Figure 1.3: Initial fair weather conditions along the altitude as calculated by Mallios et al. (2021a) for Mauritania (M), Cape Verde (CV) and Barbados (B), with: (**A**) ionization rates, (**B**) Relative difference between ionization rates, (**C**) fair weather ion densities, (**D**) relative difference between fair weather ion densities, (**E**) fair weather total charge densities, (**F**) relative difference between fair weather total charge densities, (**G**) fair weather electric field magnitudes, (**H**) relative difference between fair weather electric field magnitudes. Source: *Mallios et al. (2021a).*

1.2. Desert Dust transport in the Earth's Atmosphere

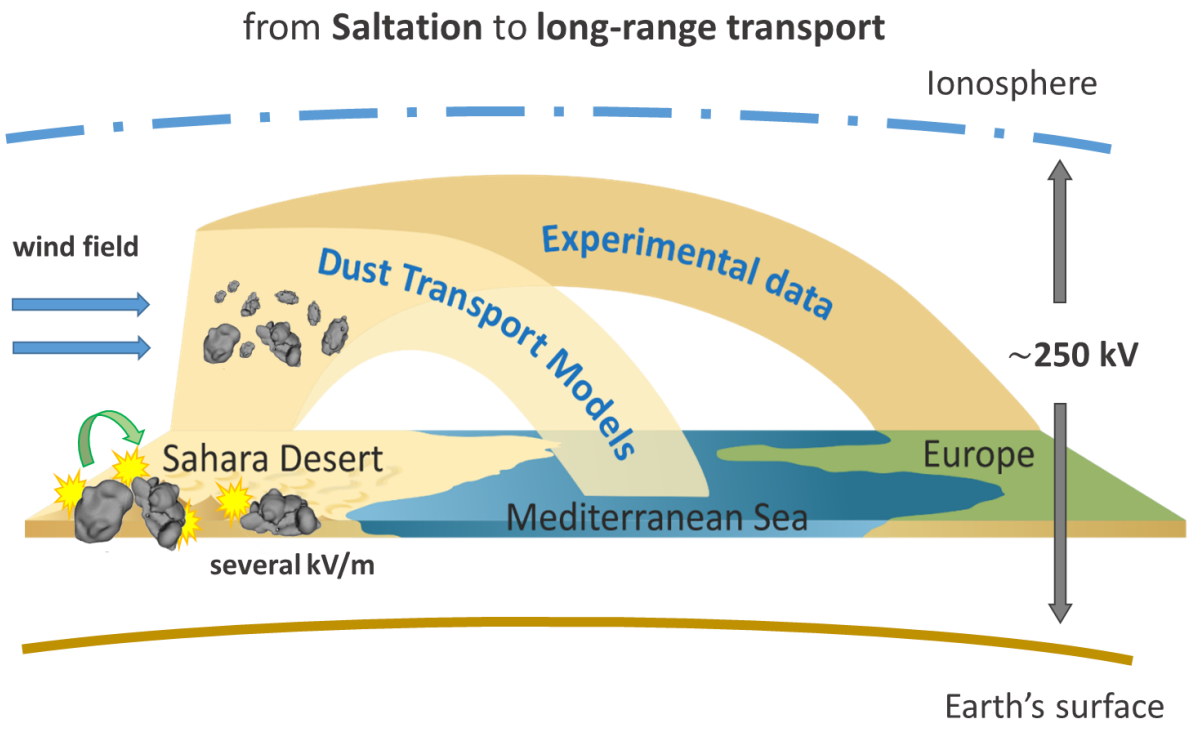

Figure 1.4: Representation of desert dust transport from saltation to lifting and travelling over large distances within the electrically active Earth's Atmosphere. Source: Image adaptation from the *ERC D-TECT* project (https://d-tect.space.noa.gr/), by the *author*.

Mineral dust plays an important role in the Earth's atmospheric system as an undivided whole. It originates, primarily, from arid and semi-arid regions (Cakmur et al., 2006), volcanic eruptions, ephemeral water bodies, and anthropogenic activities, constituting a significant and complex component which dynamically evolves within the Earth's atmosphere (Chen et al., 2018; Ginoux et al., 2001). It constitutes one of the most abundant atmospheric aerosols in terms of dry mass and optical depth (Tegen et al., 1997), thus, plays a significant role to the radiative forcing of the global climate (Miller and Tegen 1998, Miller et al. 2014) being the dominant source of aerosol forcing downwind of major dust sources, such as the Sahara Desert (Li et al. 1996; Chaibouet al. 2020). Airborne dust particles have an impact on the Earth's radiation budget, as well, via interactions with clouds, ecosystems, and radiation (Li et al., 2004), as dust particles absorb shortwave and long-

wave radiation, potentially causing a net atmospheric warming (Kok et al., 2017). This creates a significant uncertainty in understanding past and projecting future climate effects (Kok et al., 2023).

Dust originates primarily from the major deserts, concentrated in arid regions located at low latitudes within a belt spanning from 25° to 35° latitude, in both the Northern and Southern hemispheres. This geographical alignment coincides with the subtropical anticyclonic descending motion of dry air through the Hadley cell circulation. As the dry air descends, it effectively suppresses the ascent of evaporated water vapor, preventing adiabatic cooling and inhibiting convective processes. Consequently, cloud formation becomes exceedingly rare, and precipitation is virtually absent in these regions. The Sahara Desert is the largest and most active low altitude source of wind-blown sediments in the planet, lying under the subtropical ridge over Northern Africa (e.g., Kok et al., 2021 and references therein). The geographical terrain exerts a notable influence on the surface wind patterns, which, in turn, constitute the predominant driving force governing the generation and long-range transport of dust (Figure 1.4) and determine the specific locations of dust source regions.

The basic mechanisms capable to lift dust and aggregate grains from the ground surface are separated in three distinct processes, as discussed by Shao et al. (2011b), i. the direct aerodynamic entrainment of dust particles, ii. saltation bombardment and iii. the disintegration of aggregates (disaggregation) (Figure 1.5). Saltation and disaggregation are the most dominant mechanisms that result in the large concentrations injected in the atmosphere from the dust sources. Saltation is defined as the repeated bouncing motion of large and heavy sand particles (62.5 μm to 2000 μm in diameter) across the surface during an erosion event, which can dislodge additional smaller particles as the larger particles impact the ground, creating a cascading effect that shapes a substantial portion of the Earth's surface by creating sand dunes and spectacular ripples. Wind-blown dust significantly affects the surface structure of many planetary systems subjected to aeolian processes, such as Mars, and from their time evolution information on the system climate can be actively inferred (Kok et al., 2012). In addition, particles that are violently transported over the surface during saltation, dust storms and dust devils get charged through contact electrification, a common process expected in fluidized beds of industrial granular materials, strongly correlated to the acquired charge-to-mass ratio of the particles (Kamra, 1972; Kok and Renno, 2008, 2009; Williams et al., 2009; Zhang et al., 2013; Zhang and Zheng, 2018) (see Section 3.1.2).

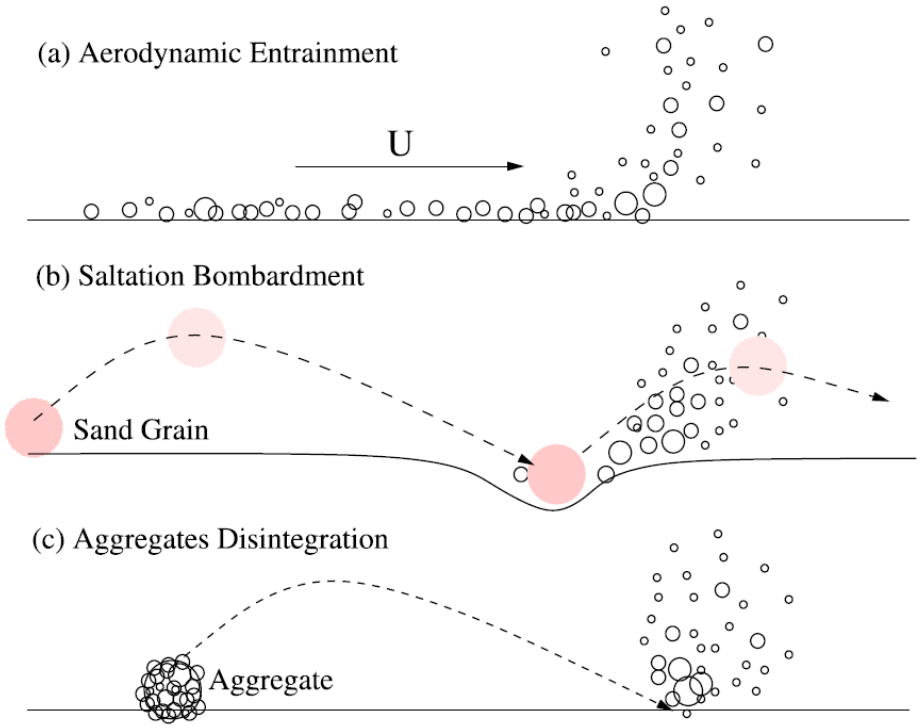

Figure 1.5: The three mechanisms of dust emission. Source: *Shao et al. (2011b)*.

Following ejection, dust particles are transported over vast distances by prevailing turbulent fluctuations, enter short-term or long-term suspension and deposit both locally and globally (Kok et al., 2012). Their journey, the dust cycle, involves intricate processes influenced by atmospheric dynamics, meteorological conditions and seasonal changes of the global wind patterns (a detailed overview can be found in Shao et al., 2011a). Dust interacts with liquid or ice clouds, acting effectively as Cloud Condensation Nuclei (CCN) and Ice Nuclei (IN) depending on the particle size, age and chemical composition and, thus, modifying cloud optical properties and lifetimes (e.g., DeMott et al., 2003; Marinou et al., 2019; Solomos et al., 2011). Since, the airborne dust particles can modify cloud microphysical properties, such as the droplet size and water phase, they subsequently affect the precipitation processes (Creamean et al., 2013). Moreover, the lifetime of the dust particles affects the deposition fluxes over land and ocean, as these have been observed to transport in distances far from the source (van der Does et al., 2018, Figure 1.4). Therefore, the aeolian transport of dust is crucial, also, for the sustainability of marine and terrestrial ecosystems through the deposition of mineral inputs and nutrients (e.g., Jickells et al., 2005). Van der Does et al. (2018) discussed four potential different mechanisms that could facilitate long-range transport

of large-to-giant dust particles. These mechanisms include: 1. *strong winds* causing fast horizontal transport, 2. *turbulence* that keeps particles in suspension for longer durations (Garcia-Carreras et al., 2015), 3. *electrical forces* that can potentially balance the gravitational force (Nicoll et al., 2011a; Renard et al., 2018; Toth III et al., 2019), and 4. the presence of t*hunderstorms* or *tropical cyclones* that can create *strong uplifts*. Atmospheric Electricity can provide insights on the electrical processes and their contribution to the transport of dust plumes.

1.2.1. Particle Size Distribution (PSD)

One of the causes of the large uncertainty in the climatic impact of dust, is that the size distribution of emitted dust aerosols is poorly understood. The dust Particle Size Distribution (PSD) changes rapidly after emission due to the preferential gravitational settling of the larger particles. The settling process of dust particles is still an open question and the physical mechanisms that influence it are under investigation. Dust particle sizes are typically categorized into three distinct modes, in fine, coarse and giant mode, without specific size boundaries being rigidly defined (Knippertz and Stuut, 2014). Airborne particles have been observed with sizes up to 300 μm, while particles with even larger diameters were collected in deposition buoys over the Atlantic ocean, revealing a first ever indication of the giant mode long-range transport (van der Does et al., 2018). These samples were mostly well-rounded quartz particles up to 450 μm in polar diameter, with what appeared to be high aspect ratios, i.e., the diameter of the particle longest dimension to the diameter of the particle shortest dimension as defined in most of the relevant literature (Figure 1.6).

Generally, observations of dust PSDs gathered from experimental campaigns reveal a longer lifetime of coarse particles than the one estimated by dust transport models (Figure 1.4), which consistently overestimate the large particle removal (Adebiyi and Kok, 2020; Drakaki et al., 2022; Mallios et al., 2020). The vast majority of mineral dust sizes transported from arid continental areas to distant regions vary from tenths of nanometres to hundreds of microns (Mahowald et al., 2014), while there is a discrepancy between results obtained by Earth System Models or transport models and observations.

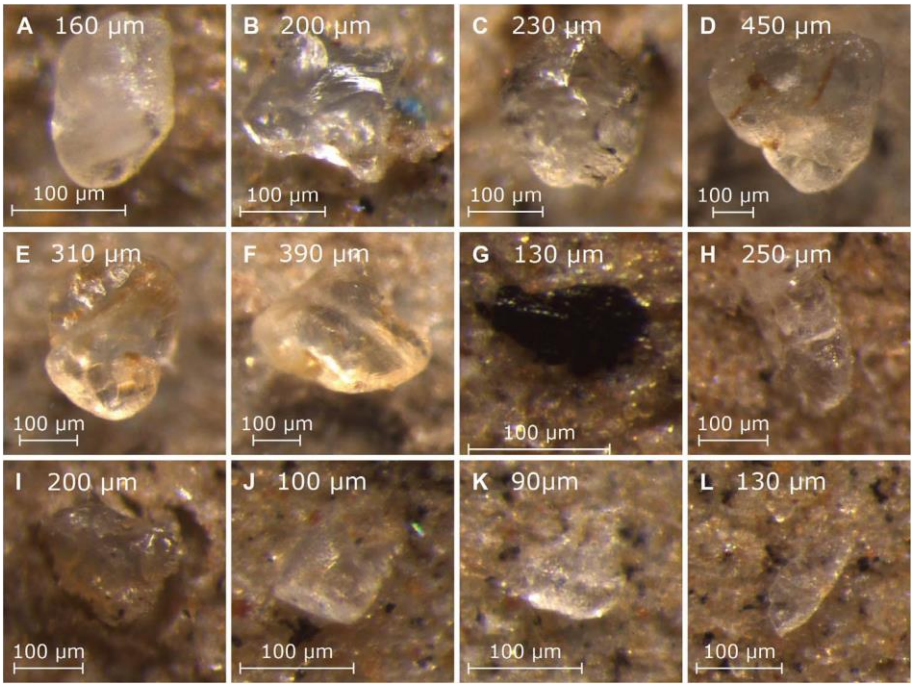

Figure 1.6: Mineral dust particles within the giant range of diameters, collected by the dedicated moored dust-collecting buoys in the tropical Atlantic Ocean. Source: *van der Does et al., 2018*.

Furthermore, dust model inter-comparison by Huneeus, et al. (2011) found that, the model estimates of deposition vary over a large range, yet mainly underestimating the observations. Adebiyi and Kok (2020) showed that the mass of coarse dust (with a diameter larger than 5 µm) in the atmosphere is about four times greater than the simulated in current climate models, resulting in greater total dust mass load. This suggests that other processes counterbalance particle loss during transport and signifies the importance of proper modelling of the mineral dust deposition. Denjean et al. (2016) showed that the effective diameter of the Saharan dust coarse mode does not vary with dust age over the Mediterranean for transport times between 1.5 and 7 days.

This conclusion has been drawn by consolidating high-quality aircraft measurements of dust PSDs performed during recent years in the framework of few large-scale experimental campaigns (e.g., Formenti et al., 2011; Ryder et al., 2013, 2018a; Weinzierl et al., 2017). Weinzierl, et al. (2017) presented results of aircraft and ground-based measurements during the SALTRACE campaign in the tropical Atlantic in 2013/2014. Particles with sizes in the range of 10–30 µm were detected over Barbados, during a Langrangian flight sequence from Cape Verde, far beyond the Stokes gravitational settling expectations. Most of these campaigns employ multi-sensory techniques in

order to quantify the optical particle diameters via optical sizing instruments, such as the optical particle counters (OPCs) (e.g., Kezoudi et al., 2021; Renard et al., 2016; Smith et al., 2019), or the projected area-equivalent diameters from particle samplers and spectrometers (e.g., Baumgardner et al., 2001), for varying particle size ranges according to the individual instrument capabilities.

Another, very important campaign that retrieved valuable information on PSDs, close to the emission source, was the FENNEC 2011 aircraft experiment over Mauritania and Mali, performed by Ryder et al. (2013). The mean size distribution between altitudes of 1–6 km at STP measured, is frequently used as the dust particle size distribution concerning multitude of studies from the coarse mode deposition schemes in forecasting models, such as the Weather Research and Forecasting model (WRF) (e.g., Drakaki et al., 2022) to the effective parametrization of the dust particle electrical properties (Mallios et al., 2021a, 2022). Figure 1.7 presents: a. the mean number distribution and b. the mean volume distribution as derived from all the overflights of FENNEC and by synthesizing the measurements from all the on-board samplers and optical counters, compared to those from other aircraft campaigns. Similar conclusions were also validated by the Van der Does et al. (2018) samplers. Moreover, Goudie and Middleton (2001) reported that particles larger than 62.5 μm are commonly carried from Sahara to the British Isles.

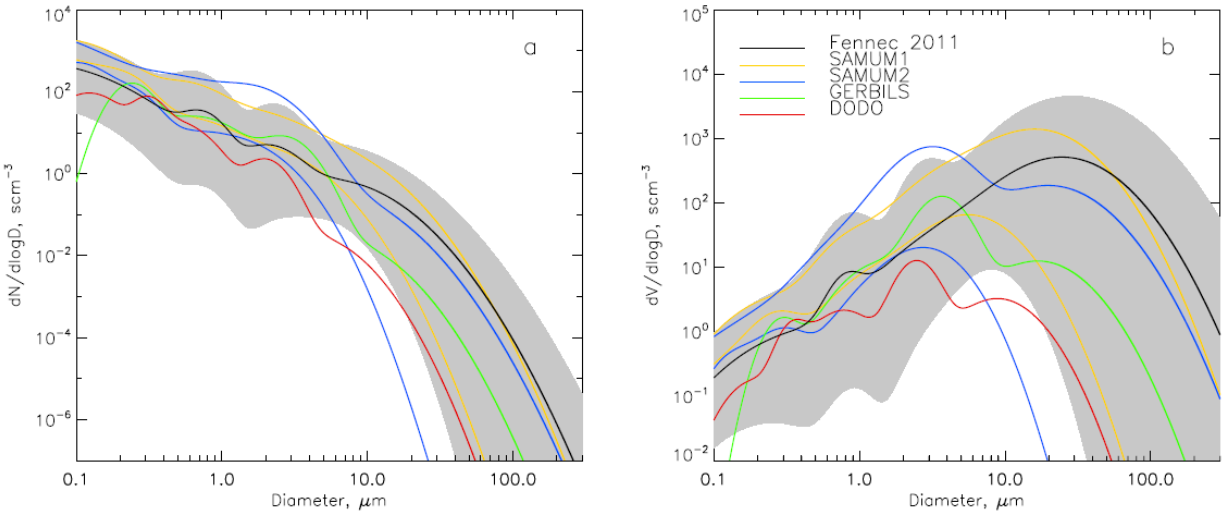

Figure 1.7: Mean Fennec 2011 size distribution compared to those from other recent aircraft campaigns, for (a) number distribution and (b) volume distribution. Fennec size distribution is shown in black, with grey shading representing the minimum and maximum throughout the campaign. Source: adapted from *Ryder et al. (2013).*

Particle charging, especially that of dust particles, is another intrinsic parameter that is size-dependent. Wind tunnel experiments coupled with numerical modelling that simulated the generated electrification of sand particles, showed that the sign of the measured electric charge is mainly dependent on the diameter of the particles (Zheng et al., 2003). However, accurately measuring and modeling the charge acquired by dust particles suspended and settling into the Earth's atmosphere poses a distinct challenge. Mallios et al. (2021a and 2022) pointed the importance of using realistic PSDs in order to achieve self-consistent results in the electrification schemes employed. Crucial parameters of the input PSD are pointed as: a. *the size bin apportionment*, as the PSD discretization along with the size of each bin, have to ensure that the initial size distribution is properly introduced to the model without significant loss of information and non-convergence of the model final results (Figure 1.8), and b. *the spatial distribution of the number density*, as the divergence from the mean distributions, which for instance could denote a case of densely packed dust particles within a transported layer, can lead to different electrical properties overall (Mallios et al., 2021a).

1.2.2. Dust Particle Shape

One of the microphysical properties proposed in literature as a potential cause of the longer lifetimes of transported dust, is the particle aspherical shape. The shape of desert dust particles significantly influences their transport dynamics. Dust particles from arid regions, such as deserts, can have various shapes, including irregular, angular, and elongated ones and are often aggregates of mixed mineralogical composition. Based on the variability of the source soils, the lifted dust composition may also vary considerably. Though, common mineral components have been reported from samples of every major desert source including quartz, phyllosilicates, such as kaolinite, and inter-stratified clay minerals in general. Furthermore, particles can have from a more prominent and smooth crystalline structure in the center of the grain to a more irregular multifaceted and rough shape (Figure 1.9, Nousiainen and Kandler, 2015 and references therein). These shapes play a crucial role in determining how dust particles are lifted, transported, and deposited in different region, while their variations can significantly alter the particle single scattering properties (e.g., Gasteiger et al., 2011; Formenti et al., 2011; Mehri et al., 2018; Nousiainen and Kandler, 2015).

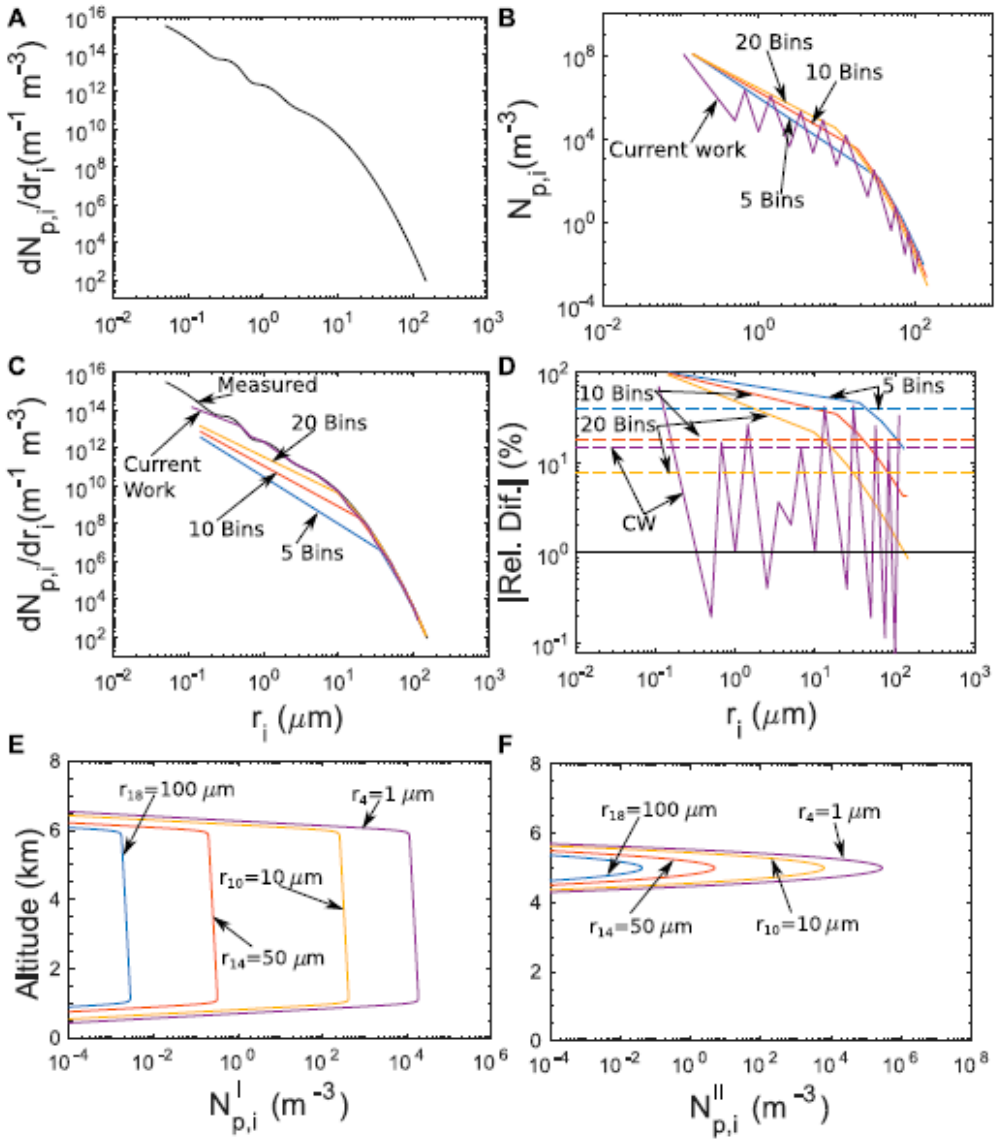

Figure 1.8: Binning method for the particle number distribution of FENNEC (**A**) with the optimal sizing being that of 19 bins (CW) of varying lengths (**B**), the reconstructed mean size distribution (**C**) and the relative difference from the measured one (**D**) showing the minimal loss of information with the binning and two different (**E**)-(**F**) spatial distribution used to simulate dust layers. Source: *Mallios et al. (2021a)*.

The most popular method, in the atmospheric community, of directly measuring the particle shape is electron microscopy, including Scanning Electron Microscopy (SEM) (Jokinen et al., 2018) and Transmission Electron Microscopy (TEM) (e.g., Kandler et al., 2011), being a powerful technique for visualizing and characterizing the morphology and orientation of individual dust particles. These methods are bound to 2D imaging restrictions and cannot provide truly three-

dimensional morphologies, moreover they are considered invasive to the innate particle conditions mainly due to the sample collecting methods employed. Perhaps, the most suitable technique available for similar studies is optical light scattering due to its contact-free and immediate nature, since the scattering pattern of a particle is sensitive to the particle morphological characteristics.

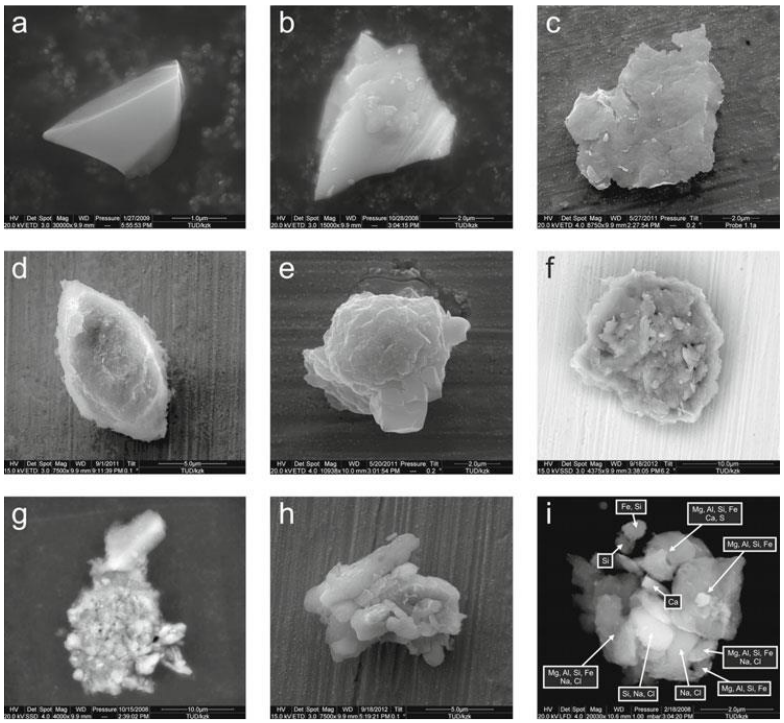

Figure 1.9: Electron microscopy images of particle structure types found in mineral dust from two samples of the same airmass over Morocco and one in Praia, Cape Verde from transported Saharan dust. The presence of certain elements marked in the last image was determined by X-ray fluorescence. Source: *Nousiainen and Kandler, 2005.*

Unfortunately, the inference from scattering is not unique to a single particle properties (inverse problem), especially in the case of coarse mode dust particles where inhomogeneities in composition and complex crystalline structures perplex the particle shape and, thus, the produced scattering matrices (Bohren, 1983; Van de Hulst, 1958; Mischenko et al., 2002a). Light scattering numerical methods used for simulating the interaction of electromagnetic waves with particles of arbitrary shape and composition, such as the Amsterdam Discrete Dipole Approximation (ADDA) (Yurkin and Hoekstra, 2007, 2011), have been extensively used with models of realistic dust particle shapes (Figure 1.10, Gasteiger et al., 2011) in order to accurately represent dust, with limitations to the used size parameter ($\chi = 2\pi r_{eq}/\lambda$, where r_{eq} is the radius of the particle and for non-spherical

particles, the radius of an equivalent-volume sphere is used). In recent years, the emerging approach of Digital Holography (DH) directly records the diffraction interference pattern of incident and scattered light with a camera without any lens or objective and, provides aerosol characterization capabilities with minimum interference to the particle environment (Berg and Videen, 2011; David et al., 2018). This technique also presents a potential of solving the dust coarse mode misrepresentation within a flowing aerosol stream (Berg et al., 2017). Moreover, efforts have been made towards the implementation of airborne DH systems that can provide images of free-suspended dust particles and reduce the uncertainty in the quantitative characterization of aerosol particles and their loading in the atmosphere (Kemppinen et al., 2020).

Typically, the shape of the dust particles affects the following processes:

1. *Lift-off and Emission*: The aerodynamic properties of the dust particles depend on their shape which is reflected in the definition of the particle Reynolds number, *Re* and the experimental and/or numerical expression of the particle drag coefficients (Bagheri and Bonadonna, 2016; Connolly et al., 2020; Dioguardi et al., 2018; Mallios et al., 2020), which is a measure of the effectiveness of a streamline aerodynamic body shape in reducing the air resistance to the forward motion. Irregular and angular particles tend to have higher drag coefficients compared to smoother, spherical particles. As a result, irregular particles may require stronger winds to initialize the saltation. Due to the influence of the particle irregularities, the irregular particle drag coefficient calculations are difficult. Therefore, particle shape can influence the threshold wind speed required for their emission from the surface.

2. *Transport Distance*: Particle shape affects the efficiency of transport over long distances. Spheroidal, more streamlined particles are more easily carried by upper-level winds, allowing them to travel longer distances before settling (Drakaki et al., 2022; Ginoux, 2003; Huang et al., 2020; Mallios et al., 2020). Yang et al. (2013) provided the first observational evidence from the CALIOP lidar depolarization measurements of shape-induced gravitational sorting of Saharan dust during their transatlantic voyage. This happens because aspherical particles fall more slowly that their spherical counterparts, for a given volume and particle mass. Mallios et al. 2020 recently tested the aforementioned observations and found that spheroidal particles fall indeed slower than spherical

particles of the same size, but the particle preferential orientation due to elongated shape affects the gravitational sorting as well.

3. *Vertical Distribution*: The shape of dust particles can impact their vertical distribution in the atmosphere. Elongated particles align themselves with wind patterns, updrafts and electric fields (Mallios et al., 2021b; Ulanowski et al., 2007) in the atmosphere leading to a more organized vertical distribution. This alignment can influence the way dust particles scatter sunlight (Bailey et al., 2008; Daskalopoulou et al., 2023a) and contribute to radiative processes (Ito et al., 2021).

4. *Radiative Processes*: Dust particles interact with sunlight and influence radiative processes in the atmosphere (Adebiyi et al., 2023). Particle shape affects the scattering and absorption of solar radiation, which can impact regional and global climate. For example, irregular particles might scatter sunlight in different directions compared to spherical particles, leading to altered radiative effects (Saito et al., 2021; Saito and Yang, 2021).

5. *Cloud Nucleation*: Dust particles can serve as cloud condensation nuclei (CCN) or ice nuclei (IN), affecting cloud properties and precipitation (DeMott et al., 2003). Shape can influence the efficiency with which dust particles act as CCN/IN as the variable curvature and surface roughness of more irregular particles compared to spherical ones offers sites for water vapor condensation. It can also affect particle interaction leading to larger agglomerates that can act as more efficient CCNs. Thereby, dust particle shape impacts cloud formation and characteristics (Marinou et al., 2017 and references therein).

6. *Deposition Patterns*: The settling and deposition of dust particles are influenced by their shape. Irregular particles may have a more complex settling pattern, leading to varying deposition rates in different regions (e.g., Drakaki et al., 2022). This can have implications for soil fertility and general ecosystem health (Jickells et al., 2005).

7. *Particle Electrical Properties*: Settling dust particles are subject to gravitational, aerodynamic and electrical torques. The latter are exerted as the particles move within the external electric field which redistributes the acquired charge on the particles surface, thus creating a dipole moment (Fuchs et al., 1964). Charge distribution in the particle's surface is shape dependent as sharp edges on facets and areas of high curvature typically concentrate charges more and lead to non-uniform electric fields around the particle (see Sections 1.3.1, 1.3.2). Moreover, dust grains with realistic shapes can exhibit anisotropic dielectric behavior which is not quantifiable, up till now, for these particles as it would require computationally intense polarizability models that need to take into

account the internal structure and composition of the particles with respect to complex input shape models. Lastly, particles form large agglomerates through coagulation that is affected by the particle shape and leads to changes in the particle surface area and subsequent acquisition of charges through contact electrification.

8. *Health Impacts*: Inhalation of desert dust particles below 5 μm can have health effects on humans. The irregular/fractured with angular surfaces shape of the emitted particles can influence the respiratory impact of dust exposure, as it is more likely to become trapped in the respiratory system, potentially due to increased surface radicals (Leinardi et al., 2020; Wieland et al., 2022).

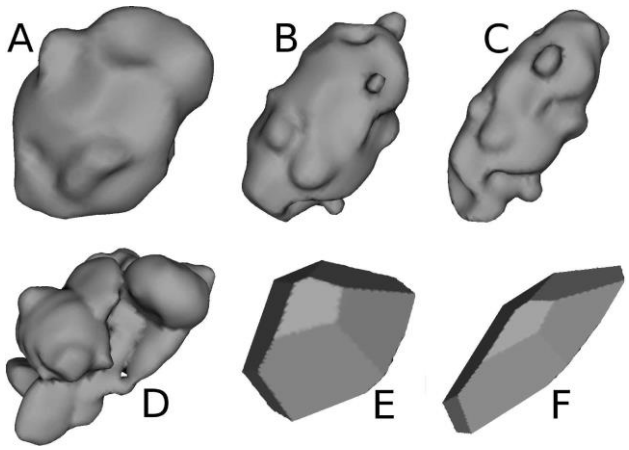

Figure 1.10: Irregularly shaped particles for model calculations. Source: *Gasteiger et al., 2011*.

From the in-situ experiments that PSDs originate from, it becomes apparent that each instrument has its own measurement discrepancies, and particle shape should be accounted for in the various size representations. Since dust transport models, on the other hand, use a different type of the particle diameter than the in-situ instrumentation, a unification would simplify the approaches.A recent study that compiled measurements of dust shapes worldwide concluded that a mean particle aspect ratio of 1.5 is a good approximation for dust particles (Huang et al., 2020). Because irregularly shaped dust has substantially different optical, geometric, and aerodynamic properties from spherical dust (e.g., Kemppinen et al., 2015; Lindqvist et al., 2014). Huang et al. (2021) pointed that diameter conversions that assume a spherical shape are problematic and unifying representations that take into account the particle asphericity can lead to observational constraints of the measured PSDs. Additionally, the particle shape induces particle orientation which can also

influence the dust particle transport time (Huang et al., 2020; Mallios et al., 2020; Mallios et al., 2021b). Specifically, Mallios et al. (2020, 2021a) showed that simulating dust particles as prolate spheroids, they can remain much longer in the atmosphere than their spherical counterparts, and that the particle vertical orientation can increase the residual time in the atmosphere significantly, compared to the horizontal one (see Section 2.2).

1.3. Charged Dust Particles Falling in the Earth's Atmosphere

Amongst the aerosols affecting the atmospheric electrical content (Whitby and Liu, 1966), mineral dust represents one of the most significant contributors, along with volcanic ash (Harrison et al., 2010), due to its mineralogical composition that results in different electrical properties of the dust particles (Kamra, 1972) and its abundance in terms of dry mass (Tegen et al., 1997). During dust storms, dust devils and subsequent advection of elevated dust layers the electrical parameters can vary greatly from the values reported under fair weather conditions (Harrison et al., 2016; Renno and Kok, 2008; Zheng, 2013) which points to particles becoming differentially charged by the turbulent movement within the atmospheric column. Major processes that are considered responsible for the electrification of dust particles include: i. *ion attachment* (Mallios et al., 2021a; Tinsley and Zhou, 2006) and ii. particle-to-surface or particle-to-particle collisions, i.e. *triboelectrification* (Kamra, 1972; Lacks and Shinbrot, 2019; Mallios et al., 2022; Waitukaitis et al., 2014). Figure 1.11 shows a schematic representation of these two mechanisms for an elongated particle moving vertically in the Earth's gravitational and electric fields, approximated by a spheroidal shape for visualization purposes. Such electrification processes are claimed to have large impact on desert dust transport and its influence in climate and ecosystems through the aforementioned retention of larger dust particles in the atmosphere (van der Does et al., 2018; Ryder et al., 2018b), as well as to the particle vertical orientation with impact on radiative transfer (Bailey et al., 2008; Mallios et al., 2021b; Ulanowski et al., 2007). For example, the electrical forces exerted on the charged (or uncharged) particles were hypothesized to reduce the settling velocity of the coarse mode, but would require forces capable of reproducing an 80% reduction in order for observations to match with transport models outputs (Eden and Vonnegut, 1973).

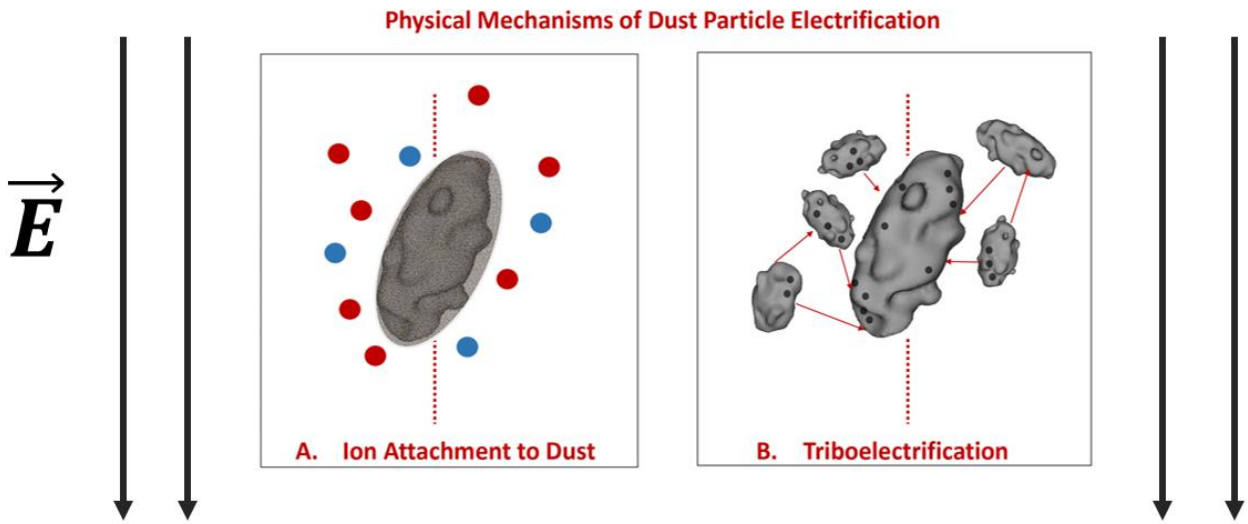

Figure 1.11: Schematic representation of the two major physical mechanisms of dust particle charging, A. ion attachment and B. triboelectrification as the particles settle within the large scale atmospheric electric field. For visualization purposes, a realistic elongated dust shape is assumed, from the Gasteiger et al., 2011, which can be approximated by a prolate spheroid of specific aspect ratio.

The field of Atmospheric Electricity research can provide valuable insight on the electrical processes and their contribution to desert dust transport. Charged dust layers have been reportedly observed to reach in large distances from the emission source and affect the local electric field strength, both vertically and near the ground surface (see Section 3.1) (Harrison et al., 2018; Katz et al., 2018; Nicoll, 2012; Nicoll et al., 2011b, 2018; Silva et al., 2016; Yair et al., 2016; Yaniv et al., 2017). The exact mechanisms that would explain and sufficiently describe the retainment of dust electrification, though, during horizontal transport are not clear yet, and remain under investigation as they require long-term measurements at grain scale and ambient atmospheric conditions for the validation of numerical models. Parameters such as particle hygroscopicity, humidity and horizontal shear winds that push particles to regions of varying atmospheric conductivity could play a crucial role in the charge retention. Previous studies in granular insulator materials and fluidized beds have shown a tendency of smaller particles to become negatively charged and larger particles to be positively charged, when accounting for the particle-to-particle collisions charging mechanism (Duff and Lacks, 2008; Forward et al., 2009a; Lacks and Levandovsky, 2007). The same polarity has been observed in field studies of dust storms, dust devils and volcanic plumes (Ette, 1971; Farrell, 2004; Harrison et al., 2016; Houghton et al., 2013; Kok and Renno, 2009; Nicoll et al., 2019; Renno and Kok, 2008), and most laboratory experiments

on triboelectric charging in granular systems simulating the dust dynamics both within the Earth's atmosphere and in a diverse planetary environment such as that of Mars (Forward et al., 2009b; Harper et al., 2022; Toth III et al., 2019).

It has been generally argued that, as dust settles during transport, the larger and mainly positively charged particles separate from the smaller negatively charged particles due to the gravitational sedimentation, which sorts the dust particles by size and induces charge separation. This process develops vertical electric fields within the dust layer that is added to the already enhanced fair weather electric field due to the depletion of atmospheric conductivity imposed by the presence of the dust layer. Depending on its strength, the total electric field within the dust layer can: (a) *counteract the gravitational settling of large particles* and (b) *cause a preferential orientation of the non-spherical particles along the vertical direction* (Fuks, 1958, p. 277; Ulanowski et al., 2007), affecting the particle aerodynamics. In the following sections, we describe the two basic mechanisms that act simultaneously and lead to dust particle charging, ion attachment and triboelectrification, along with the limitations under which each mechanism contributes the most via state-of-the art electrification models.

1.3.1. Ion Attachment to Dust Particles

The Earth's atmosphere is a conducting medium attributed to the constant presence of ions created by ionization due to galactic cosmic ray radiation. Aerosols, in general, tend to scavenge these atmospheric ions due to: i. electrostatic interactions with the electric field (conduction and polarization) and ii. due to ion thermal diffusion (Klett, 1971). The presence of aerosols within the atmospheric column results in a reduction of the atmospheric ion density, and consequently of the atmospheric electrical conductivity. This process, among other parameters, depends on the particle size and the ion concentration. If there is a collection of particles of the same size, then the ion attachment process depends also on the concentration of the particles. These charging effects on elevated particles may, consequently, affect the particle coagulation rates and further modify the particle size distributions. Concerning the first process, conduction occurs when the particles dynamically exist in a total electric field that is considered a superposition of the external large scale electric field, the induced dipole electric field and the field due to charges on the particles (Gunn, 1954; Klett, 1971; Long and Yao, 2010). This large scale electric field is created by the

potential difference between the lower part of the ionosphere and the Earth's surface (Rycroft et al., 2008), and is modified by the ion density reduction caused by the ion attachment process, which leads to the electrical conductivity reduction and the atmospheric columnar resistance enhancement (Baumgaertner et al., 2014; Zhou and Tinsley, 2007). Past literature on quantification of ion attachment rates to aerosols is divided in three distinct categories with respect to the comparison between particle size and the ionic mean free path, as such we have: a. the *continuum theories* that treat particles larger than the ionic mean free path, charged through ionic diffusion to the particles' surface (Fjeld et al., 1983; Fjeld and McFarland, 1989), b. the *free molecular - effusive - theories* that employ kinetic theory for particles much smaller than the ionic mean free path and c. the *transition regime theories*, based heavily on the limiting sphere method developed by Fuchs (1963) for the stationary charge distribution on aerosols within the bipolar ionic atmosphere (Yair and Levin, 1989). In this case, the diffusion approximation is obtained by neglecting the effect of the external electric field on the particle and on the ion transport, while retaining the effect of the particle charge, while the field approximation is obtained by neglecting diffusion, and calculating the charging rate from the transport of ions along the electric field lines to the surface of the particle (Fjeld and McFarland, 1989).

Several theoretical expressions that combine the mechanisms or that numerically solve the field-diffusion problem have been proposed in the past (e.g., Fjeld et al., 1983; Fjeld and McFarland, 1989; Klett, 1971; Lawless, 1996). However, these expressions cannot be easily expanded to other cases such as moving particles, or different shapes, because they contain parts of approximate solutions that restrict the generalization. On the other hand, simple superpositions, such as those of proposed by Chiu (Chiu, 1978), although not rigorous, offer the flexibility of generalization, because each individual charging mechanism has been studied extensively on a broad spectrum of applications. Unfortunately, these expressions cannot be easily expanded to other cases such as moving particles, or different shapes, because they contain parts of approximate solutions that restrict further generalization.

To enable flexibility in the generalization, Mallios et al., (2021b) model proposed a new superposition in the diffusion-field theory that resulted in a novel version of the continuity equation for positive and negative small ion densities, that is easily expandable to moving spherical dust particles. The new ion-attachment model is discussed in Chapter 2.

1.3.2. Collisional Charging of Dust Particles

In a multitude of phenomena, the aggravations of a system comprising of granular particles with different dielectric properties causes the particles to develop electrostatic charges through collisions. This tribocharging, or otherwise known as triboelectrification, occurs due to electron exchange between particles of different materials during their rubbing process. Interestingly, this is observed also in violent natural events with increased particle concentrations of the same type of particles such as sand storms, dust devils and volcanic emissions as mentioned previously. Dust particles can be charged via collisions and, there are two mechanisms that act during the process and depend on the particle electrical behavior. When particles are considered insulators of electricity, the triboelectric effect causes electron exchange between them (e.g., Eden & Vonnegut, 1973; Ette, 1971;), that results in large particles being predominantly positively charged and small particles negatively (e.g., Forward et al., 2009; Kok & Lacks, 2009; Kok & Renno, 2006; Lacks et al., 2008; Lacks & Levandovsky, 2007; Merrison et al., 2012; Renno, 2004; Xie et al., 2013). If the particles are considered good conductors of electricity and are polarized by an external large scale electric field, then there is charge transfer between colliding and rebounding particles, commonly referred to as inductive charging mechanism (Davis, 1964; Kamra and Vonnegut, 1971; Sartor, 1967). This mechanism results also in positive large particles and negative small particles (Latham & Mason, 1962). Alternate explanations of charge transfer between similar particles include a composition variation with particle size, particle-size-dependent adsorption of contaminants and a particle size-dependent roughness or shape that affects the inter-particle contact (Zhao et al., 2003).

In the case of particle-to-particle contact electrification the collision efficiency of the particles depends on their size, because it regulates the minimum distance that they must have for a collision to take place (for spheres it is two times their radii). For realistic shapes such as prolate spheroids, this distance depends on their orientation. For vertically oriented spheroids this distance can be two times the minor semi-axis length, while for horizontally oriented spheroids it is two times their major semi-axis length. Quantification of the collision efficiency for such a simple shape is very complex, let alone for irregular shapes, due to the fact that particle orientation changes with time and collisions, but also because the forces acting upon the body cannot be quantified for the majority of geometric shapes. Up to the point of the conclusion of this dissertation there is no relevant literature stating otherwise.

1.4. Dust Particle Orientation

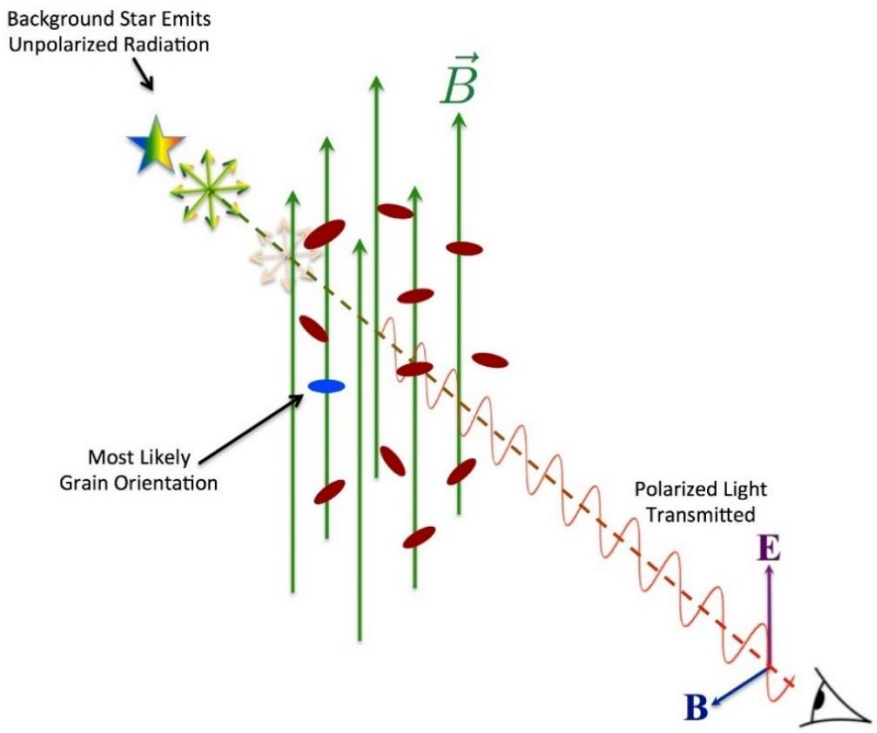

Figure 1.12: Elongated aligned grains intercepting light from a background star. The unpolarized starlight acquires specific polarization. Source: *B. G. Andersson* http://bgandersson.net/grain-alignment.

Since mineral dust grains are asymmetric and tend to be elongated, they are expected to preferentially align with streamlines in viscous flows and/or to dynamic field lines by the applied torques. Dust grain alignment has been a proposed theory for nearly six decades and is well-documented for the case of interstellar and interplanetary grains (Dolginov, 1972 and references theirein). There are various co-existing proposed mechanisms leading to such an effect within supersonic corpuscular or anisotropic radiative fluxes, with one of the most prominent ones being the alignment due to the Galactic magnetic field. In this case, orientation is probed by distinct interstellar light polarization features. Preferentially oriented elongated grains, scatter light polarised along their long axis. Therefore, the extinction of the light polarization components is different (i.e., dichroic extinction) and the transmitted starlight becomes polarized. The dichroic extinction of transmitted starlight through oriented dust is the primary observational technique of the phenomenon (Figure 1.12). Dichroism measurements provide information on the magnetic field

orientation, which is the dominant alignment mechanism for these sub-micron particles (Andersson et al., 2015; Dasgupta Ajou K., 1983; Kolokolova and Nagdimunov, 2014; Lazarian, 2007; Siebenmorgen, 2014; Skalidis and Tassis, 2020). The rapid development of instrumentation has greatly expanded the scope of observations, which now include advanced polarimetry and spectropolarimetry from the far ultraviolet to the far infrared (e.g., Ramaprakash et al., 2019).

As an analogue for the much larger atmospheric dust particles, the geomagnetic field is considered a weak alignment mechanism for particles moving in the Earth's atmosphere, since multiple processes such as the bombardment of gas particles, the imposed aerodynamic and electrical torques (Mallios et al., 2021b; Ulanowski et al., 2007 and references therein), but also turbulence (Klett, 1995) compete (or counter-balance) for the most dominant atmospheric particle alignment mechanism. Ulanowski et al. (2007) calculated the mean orientation angle $\langle\theta\rangle$ of uncharged prolate ellipsoidal dust particles, falling under gravity and subjected to a vertical electric field. They assumed existence of thermal equilibrium between the dust particles and their environment. They showed that in the case of dust particles with an aspect ratio $\varepsilon = 1.5$ an electric field of strength equal to 2 kV m^{-1} is sufficient to partially align ($\langle\theta\rangle \leq 10°$) particles of sizes between 10 – 25 μm with the vertical electric field lines. Mallios, Drakaki, and Amiridis (2020) showed that simulating dust particles as prolate spheroids, they can remain much longer in the atmosphere than their spherical counterparts, and that the particle vertical orientation can increase the residual time in the atmosphere significantly, compared to the horizontal one. A focus point of the dissertation is the investigation of dust particle alignment due to competing aerodynamic and electrical torques and whether atmospheric electricity alone can produce total vertical/horizontal orientation of particles within the atmospheric column. To tackle this, we approach the processes both from a modelling dynamics perspective and validate the theory through novel vertical electrical profiling observations within transported dust layers (see Chapter 5 and Section 3.3 for new developments).

The observational detection of atmospheric dust orientation is under-documented in recent literature due to the inherent challenge in interpreting similar optical features. Incoming solar radiation is considered unpolarized before it enters the Earth's atmosphere. Throughout its propagation its polarization changes, through the absorption and scattering interactions with various atmospheric components including aerosol particles, water droplets, ice crystals and molecules. The transmitted (direct) sunlight is always unpolarised, except when it propagates through atmospheric layers via multiple particle interactions and when it encounters oriented aerosols in the atmosphere.

Interpreting linear polarization measurements in the direct direction (i.e., measurements taken when the observer looks directly towards the Sun) can be challenging due to the overwhelming intensity of sunlight and secondary sources of linear polarization in the observational line-of-sight. Based on a similar optical approach as interstellar dust, though, atmospheric dust may provide distinct linear polarization (LP) signatures, as vertically oriented particles can lead to dichroic extinction of the transmitted sunlight. This was indicated for starlight observations during nighttime (see Section 3.2.1), which included predominantly horizontally polarized light during a Saharan dust episode in La Palma (Bailey et al., 2008; Ulanowski et al., 2007). Also in the same study, modelling of the forward scattering matrix through T-matrix calculations was employed and showed that excess polarization for spheroidal particles of a specific composition and orientation is to be expected for particle sizes larger than 3 μm. The prolate shape is hypothesized by the authors, in an effort to explain the observed polarization excess with respect to the background sky.

Motivated by the observational importance of preferential orientation for the particle dynamics, a significant part of the thesis is dedicated to the use of a novel instrument, SolPol (solar polarimeter) that is meticulously characterized and then employed in order to detect linear polarization signatures attributed to dust orientation within the dust layers (see Section 3.4 for the instrument design and principles of operation and Chapter 6 for the experimental results).

1.5. Thesis Outline

The dissertation begins with a thorough theoretical introduction of the main Atmospheric Electricity crucial processes and quantities that interact with the moving mineral dust particles within the atmospheric circulation. Then, it heavily gravitates towards the basic dust particle attributes influencing the flow dynamics such as the particle size and particle shape, and delineate the effect these microphysical properties have on the electrification of these particles. The above is a targeted review and places the dissertation in a broader context of the required parameters in order to approach the impact of particle charging to their transport dynamics. As a continuation, the major particle charging mechanisms are introduced and, then, bridged to the phenomenon of dust particle orientation, as a hypothesized driver for the preferential alignment of particles in the Earth's

atmosphere is the electrostatic nature of mineral dust. Concluding the specific chapter, the previous research work that motivated the investigation of orientation is presented.

Chapter 2 extends to the modelling of the exact electrical properties of the dust particles, acquired as the particles settle within the Earth's atmosphere. by considering the two distinct charging mechanisms of spherical dust particles, ion attachment and contact electrification or triboelectrification. The 1D-model based on the work of Mallios et al. (2022) that self-consistently calculates the ion attachment mechanism is discussed and expanded for the case of triboelectrification. We, then, comment on the model outputs according to various particle sizes, focusing on which mechanism is dominant at either size range. Moreover, the study further investigates the feasibility of particle preferential orientation, in terms of particle dynamics that are altered due to the particle's electrical characteristics and conclude on the required electric fields that should be capable to orient particles vertically.

The major objectives of the dissertation revolve around monitoring of the effect of the particle concentration to the near-ground electric field, to provide information on height-resolved dust electrical properties, and also target particle orientation on ambient conditions, along with co-located measurements of the particle charge density and electric field strength. For this reason, in Chapter 3 we re-visit the existing observational techniques of dust particle electrification and orientation, while highlighting the importance of complementing measurements that can resolve the criteria for a complete dust layer characterization. We, then, introduce novel instrumentation that was implemented and/or characterized throughout the doctoral research for: i. accurate vertical profiling measurements and ii. detection of particle orientation within the dust layers. Then, we describe the applicability of these new measurement techniques to field conditions in remote observational stations and experimental campaigns.

Chapter 4 is the observational extension of the previous chapter as it presents longterm dust electrification measurements based on ground-based method. We focus on monitoring perturbations of the electric field near the ground caused by the transported dust layers, with special emphasis on slow field perturbations with duration larger than 6 hours, and we attempt to classify and comment on the electrical activity of the dust layers. Four selected cases of Saharan dust plumes are examined, with data from a fieldmill electrometer, as well as through the particle backscatter properties by the sophisticated Polly^{XT} lidar system. Following, we, describe thoroughly a novel post-processing technique to extract a reference electric field for comparison purposes from our

timeseries, that reflects the local fair weather activity. Then, to quantitatively approach our results, we examine the dependency of the field by constructing a scheme representing the theoretical assumptions for the distribution of separated charges within the electrified dust layer.

Chapter 5 encompasses all the observational efforts to achieve accurate and consistent vertical profiling measurements of the electrical properties within elevated dust layers. We present numerous launches of specifically designed electrosondes, i.e. atmospheric electricity sensors on balloon-borne radiosondes, launches in two observational campaigns from which infer similar results on the accumulation of charges within the transported layers away from their source. We, also, cross-compare the electric field retrievals from our two sensors in alternate new approach so as to ensure quality assured data.

The core content of dissertation's concludes with a thorough study of the dust particle orientation phenomenon in Chapter 6 which encompasses all the effort behind consistent measurements of linear polarization under clear and dusty sky conditions with a novel instrument, the SolPol. The characterization of our measurements and the attempt to physically interpret the complex observations in terms of indications for particle orientation is presented, for our total acquired dataset on a selected two-year operation of the instrument and compare between days affected by elevated dust layers and days without dust loads. We discuss the dependence of the derived orientation trends to crucial parameters such as the Sun's position and the aerosol optical depth, so as to verify that the observed excess in linear polarization is attributed to preferentially oriented dust particles within the examined layers. Lastly, we provide information on the particle orientation angles according to our indicators. Detailed calculations for the methodologies and technical descriptions presented in the chapter can be found in the form of an Appendix.

Finally, we provide our conclusive remarks on this effort.

Chapter 2

Modelling Dust Particle Electrification & Orientation[1]

In this chapter, we will discuss the physical continuation of the previous logic that extends to modelling the exact electrical properties of the dust particles, acquired as the particles settle within the Earth's atmosphere. There are two distinct charging mechanisms of spherical dust particles, ion attachment (Mallios et al., 2021b) and contact electrification or triboelectrification. We assume spherical particles as there are no analytical expressions of the required charge transfer equations for irregular particle shapes and the dust particles are assumed to be good conductors of electricity. The latter approximation is valid regardless of the particle mineralogical composition and dielectric properties, since latent humidity gets adsorbed in the particle surface, thus creating a thin conduction film encapsulating the particle.

The mechanisms are studied in parallel through the extensive work of Mallios et al. (2022 and 2021a), as they are the major electrification processes that affect the particle charge, the atmospheric conductivity and the large scale electric field. A novel 1D numerical model has been developed that parametrizes the charging processes in the presence of a large scale electric field, under stagnant atmospheric conditions where wind contribution is neglected. The model is able to analytically

[1] **This chapter is based on my contribution in:**

Mallios, S. A., **Daskalopoulou, V**., & Amiridis, V. (2022). *Modeling of the electrical interaction between desert dust particles and the Earth's atmosphere*. Journal of Aerosol Science, 165(June), 106044. https://doi.org/10.1016/j.jaerosci.2022.106044.

Mallios, S. A., Papangelis, G., Hloupis, G., Papaioannou, A., **Daskalopoulou, V.**, & Amiridis, V. (2021). *Modeling of Spherical Dust Particle Charging due to Ion Attachment*. Frontiers in Earth Science, 9(August), 1–22. https://doi.org/10.3389/feart.2021.709890.

Mallios, S. A., **Daskalopoulou, V.** and Amiridis, V.: *Orientation of non spherical prolate dust particles moving vertically in the Earth's atmosphere*, J. Aerosol Sci., 151(January), 105657, doi: https://doi.org/10.1016/j.jaerosci.2020.105657 , 2021b.

represent the phenomena by integrating a measured size distribution of spherical dust particles, in the 1D model that incorporates the calculation of new attachment rates of non-stationary spherical particles and is able to self-consistently calculate the modification of atmospheric ion densities and the subsequent alteration of the large scale electric field. Moreover, the model is further updated to account for the particle charging due to the efficient collisions between particles of sizes ranging from fine (less than 1 μm in radius) to giant mode (larger than 50 μm in radius) particles.

2.1. Electrification Model Formalism

The ion attachment is characterized by three processes that act simultaneously. The diffusion of ions on the particle's surface. The electrical attraction of ions due to the particle's electric field. The polarization of the particles in the presence of an external large scale electric field (the charge on the particle's surface is redistributed according to the external electric field, creating regions of positive and negative charge and these regions attract ions of opposite polarity). Even in the case of spherical particles there is no analytical solution when these 3 processes act simultaneously and it is assumed that each process acts independently and their effects are then linearly superposed. The diffusion mechanism depends on the particles self-capacitance which is shape dependent. The particle's electric field distribution is also shape dependent. Finally, the polarization of the particle and the charge density distribution on its surface is shape dependent.

In the case of particle-particle contact electrification the collision efficiency of the particles depends on their size, because it regulates the minimum distance that they must have for a collision to take place (for spheres is two times their radii). In the case of prolate spheroids, this distance depends on their orientation. Vertically oriented spheroids this distance is two times the minor semi-axis length, while for horizontally oriented spheroids it is two times their major semi-axis length. The quantification of the collision efficiency of such a simple shape is already complex, since the orientation varies in time and with collisions, and because the forces acting upon the body cannot be quantified for the majority of the geometrical shapes.

Due to the lack of rigorous mathematical expression for the quantification of the particle collision process, the mechanical and electrostatic effects are modeled independently, based on works in the past literature, and then are combined by a simple superposition principle. Additionally,

the electrostatic effects are studied in the presence of weak external electric fields (less than 1 kV m-1). Moreover, for the same reasons a simple superposition principle has been applied for the quantification of the mechanisms resulting in the ion attachment process. All these assumptions lead to an approximation of the actual phenomenon, but this method can lead to physically reasonable results, highlighting the impact of several processes to the eventual charging of the dust particles.

Mallios et al. (2021c) developed an 1D numerical model to parameterize the charging process of dust particles due to the ion attachment mechanism in the presence of a large-scale electric field. The model was able to self-consistently calculate the modification of atmospheric ion densities in the presence of the dust particles, and the consequent alteration of the atmospheric electrical conductivity and the large-scale electric field. Using observed dust size distributions, they found that the particles can acquire electrical charge in the range of 1-1000 elementary charges depending on their size and number density. The particles become mainly negatively charged, but under specific conditions giant mode particles (larger than 50 μm radius) can be positive. However, their approach showed that the resultant electrical force is not enough to significantly influence their gravitational settling, as the ratio between the electrical force magnitude and the gravity magnitude does not exceed the value of 0.01. This indicates that the process of ion attachment alone is not sufficient to create strong electrical effects for the modification of particle dynamics. Therefore, other processes, such as the triboelectric effect and wind speed, must be included in the model to fully represent the impact of electricity on particle dynamics.

By binning integration of a realistic particle size distribution in the model, the acquired electrical charge on the dust particles is calculated in the range of 0.5 to 2000 elementary charges (Figure 2.1). The particles become on average negatively charged, but under specific conditions giant mode particles can be locally and temporarily positive, congruently to previously reported laboratory experiments. Moreover, the electrical force that is applied on the particles by each mechanism individually and through the superposition of both, is extracted and compared to the gravitational force acting on each particle. However, the 1D results indicate that the electrical force is not enough to significantly influence the gravitational settling of the charged particles, as it is more than one order of magnitude less than gravity. This designates that although the electrical processes alone are accounted for, significant meteorological processes such as updrafts, wind shears, or horizontal winds need to be included in the model to accurately represent the modulation of particle

electrification and so as to represent the impact of electricity on particle dynamics in a more realistic way.

The particle shape assumed is again spherical, as all the processes involved in ionic attachment are shape-dependent and since there are no analytical mathematical forms for the quantification of each for arbitrary shapes, apart from spheroidal shapes (prolate/oblate), the use of spheres is an adequate approximation. In the aforementioned study, dust particles of observed size distributions from the Fennec 2011 aircraft in-situ experiment were utilized (Ryder et al., 2013) and were found to be able to acquire an electrical charge in the range between 1 to 1000 elementary charges, with respect to their size and number densities.

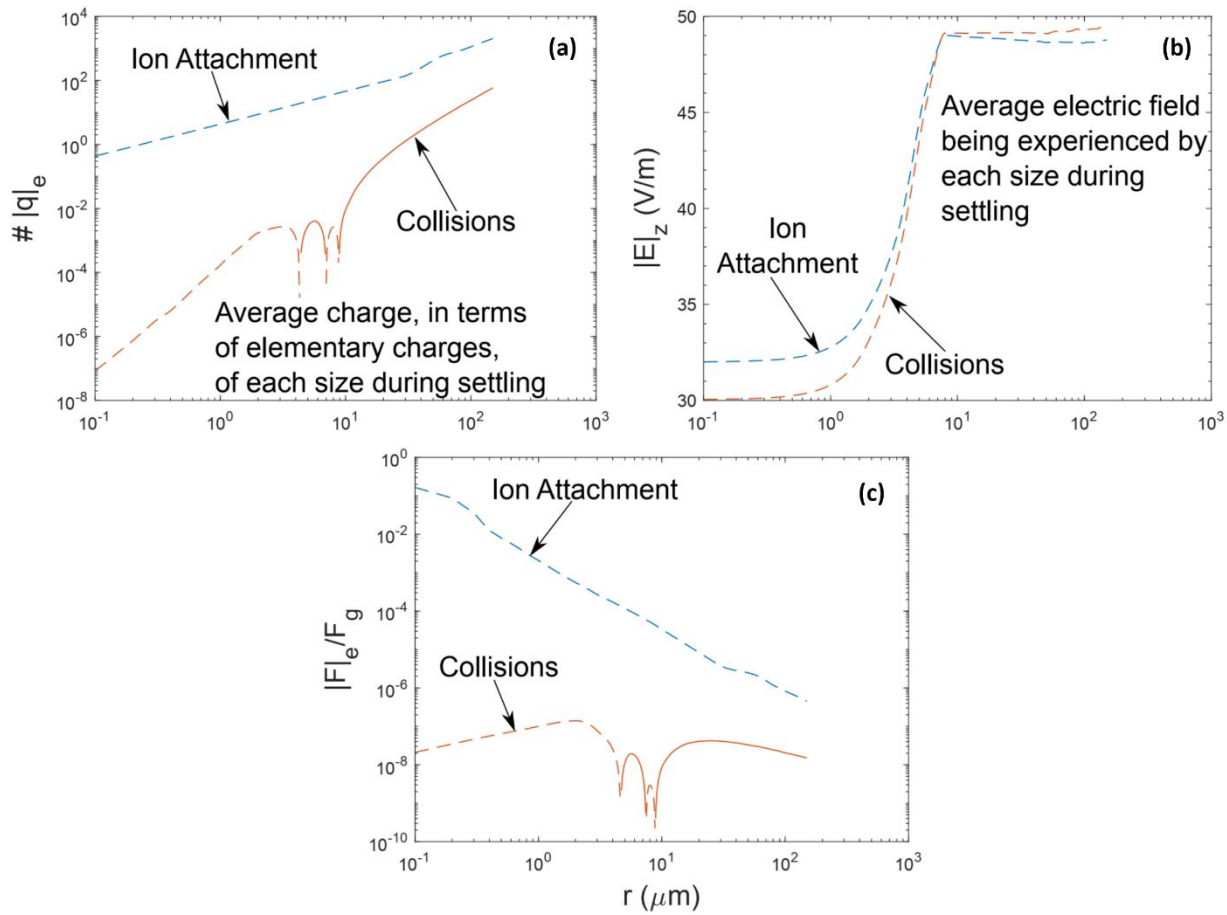

Figure 2.1: Time dynamics of spatio-temporally averaged electrical properties of dust particles, with the particle radius, under the assumption that each charging mechanism acts individually, and assuming specific number densities $N_{0,i}$ for each size bin. Net charge in terms of elementary charges (**a**), electric field magnitude "sensed" by a particle (**b**) and ratio between the electrical force magnitude and the gravity acted upon a particle (**c**). Source: Adapted from *Mallios et al. (2022)*.

Moreover, Mallios et al. (2021b) postulated that particles become mainly negatively charged, but giant mode particles with radii larger than 50 μm, can under specific conditions be positively charged by ion attachment alone. Similar conclusions were derived by Yair and Levin (1989) that studied polydisperse spherical conducting aerosols with radii up to 0.5 μm and found that for small aerosol concentrations, particles were charged mostly negatively. When aerosol concentrations were increased, this led to differential charging and resulted in opposite charging of the small (mostly negative) and the large (mostly positive) particles. This effect was enhanced for size distributions which had a significant component of larger particles (Figure 2.1). Although, their results showed dependency only on the particle concentration, Mallios et al. (2021b) work showed dependency on the particle concentrations with respect to the atmospheric ion concentrations. The latter distinction is attributed to the difference in assumed regimes as the particle sizes integrated, as opposed to the Yair and Levin study, are larger than the ionic mean free path and therefore the ionic diffusion is expected to largely influence the attachment process.

In the close vicinity of the emission sources and a few meters above the ground, the contact electrification becomes dominant because the concentrations of the particles are very large. Therefore, the small particles are expected to acquire negative charge and large particles are positively charged, which is consistent with the findings of various experiments in labs. As the particles are lifted and start moving away from the source, particle-to-particle contact become less frequent because of dilution and particle number reduction during transit. Then, the ion attachment becomes the main regulator of the particles' charge, and since the negative ions have larger electrical mobility than the positive ions, they attach more effectively leading to negative charge to all particles. Additionally, the ion attachment leads to a reduction of the large charge values that might have been acquired in the emission source to some steady state values which are in the order of 1000 elementary charges, on average, for particles with radius 100 μm, up to 0.5 elementary charges, on average, for particles with 0.1 μm radius. This large different between the sizes stems mainly from the large difference of their concentrations and the particle competition mechanism that come to play (the more the particles the less ions attach to each one of them).

2.2. Orientation of Prolate Spheroidal Particles

In order to provide the theoretical feasibility of orientation, a potential mechanism that is capable of aligning the lofted dust particles, is the large scale atmospheric electric field that acts on charged dust particles through coupled electrical and aerodynamic torque interactions (Mallios et al. 2021, Ulanowski et al. 2007). For charged dust particles, the polarity of particle charge and the direction of the electric field influence particle motion and, therefore, the aerodynamic torque. Depending on its strength, the total electric field within the dust layer can: (a) counteract the gravitational settling of large particles and (b) cause a preferential orientation of the non-spherical particles along the vertical direction. Mallios et al. (2021b) stipulated that aerodynamic torque, caused by the misalignment between the center of pressure and center of gravity on a spheroid dust particle, tends to rotate it horizontally, while the electrical torque, caused by the misalignment of the electrical dipole moment and the electric field direction due to the asymmetry between the spheroid axes, tends to rotate the particle vertically (Figure 2.2). As the particle aspect ratio, ε, increases the required electric field strength, E_{lim}, for the electrical torque to dominate increases. Particles of sizes less than 1 μm are always randomly oriented due to the Brownian motion being dominant, while particles in the range of 1-100 μm can become vertically oriented for sufficiently large electric field strengths. Particles larger than 100 μm are mainly horizontally oriented, because the atmospheric electric field can never reach the required electric strength (Mallios et al., 2021b).

Mallios et al. (2020,2021a) provided new expressions for the drag coefficient of prolate spheroids that are valid beyond the Stokes' regime (specifically for Re≤100) and that take into account the orientation and the aspect ratio of the particle. They showed that in the case the aspect ratio ranges between 1.4 and 2.4, prolate spheroids fall faster than their spherical counterparts of the same volume. This is attributed to the projected area of the prolate spheroids, which depends strongly on the particle orientation (although on average it is larger for ellipsoids than spheres (Vickers, 1996), the projected area of ellipsoids becomes smaller than the projected area of spheres of the same volume as the particle becomes vertically oriented), and the aerodynamic properties due to the impact of the prolate spheroid shape factors on their drag coefficients. They also showed that when comparing prolate spheroids with spherical particles of the same maximum dimension the conclusions are different. In the case of particles with aspect ratio equal to 1.4, the settling velocity of prolate spheroids is on average 6% (in the case of horizontal orientation) up to 23% (in

the case of vertical orientation) less than their spherical counterparts (of the same maximum dimension). As the aspect ratio increases to 2.4, the difference becomes 20% (for horizontal orientation) and 52% (for vertical orientation).

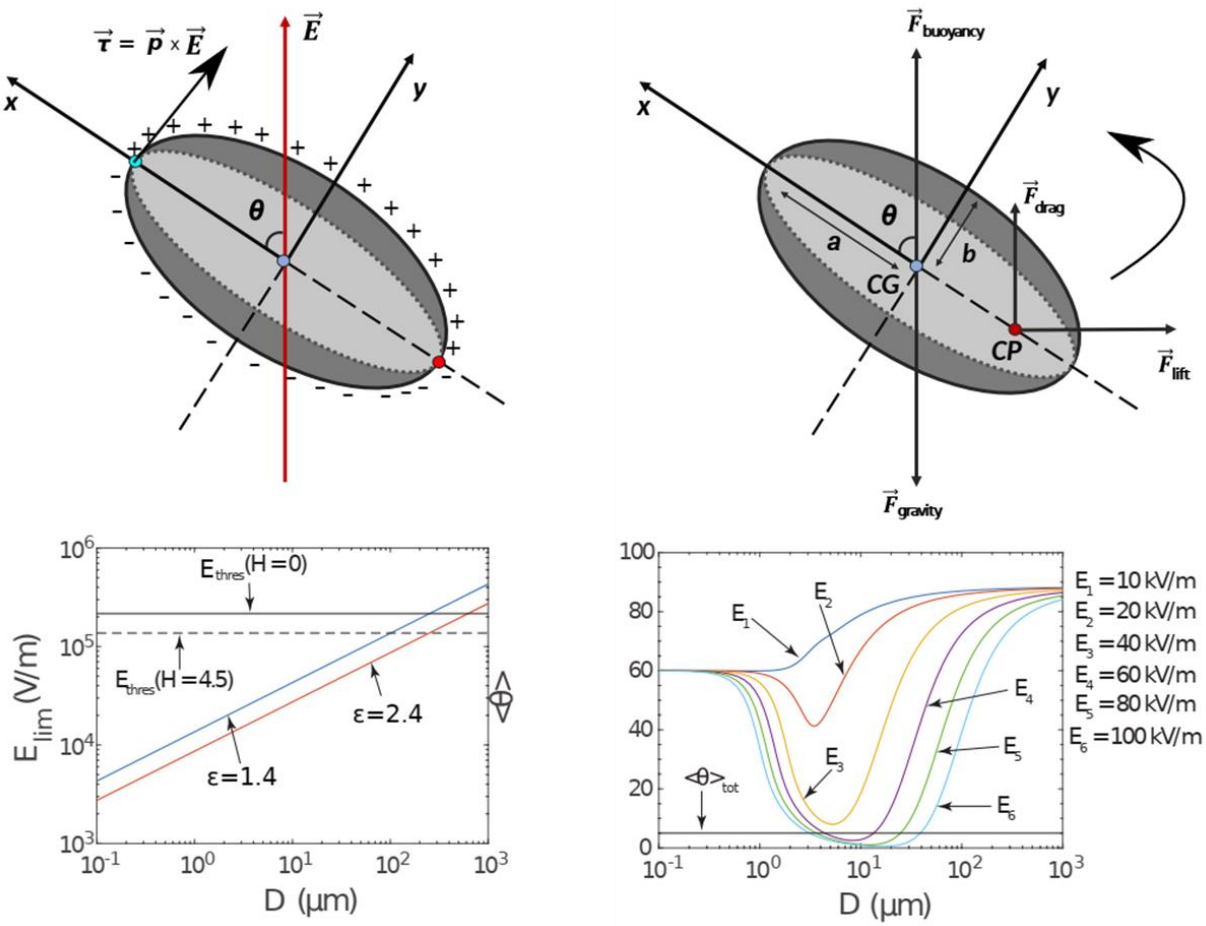

Figure 2.2: **Top panel:** Illustration of a prolate spheroidal particle settling in the Earth's atmosphere with the electrical torque (left) and aerodynamic torque (right) exerted to the particle. **Bottom panel:** The limiting electric field strength over which the electrical torque dominates over the aerodynamic torque (left) and the mean orientation angle as a function of the particle diameter for various electric field strengths. Adapted from *Mallios et al. (2021b).*

Mallios et al. (2021b) derived semi-analytical expressions for the mean orientation angle of prolate spheroids moving vertically in the Earth's atmosphere in the presence of electrical and gravitational forces. They found that the random orientation assumption is, in principle, valid only for particles with size (two times the particle major semi-axis) less than 2 μm. As the size increases, the gravity or the electrical force tend to create sufficient torque to rotate the particle horizontally

or vertically with respect to the ground, respectively (depending on the particle net electrical charge and the large scale atmospheric electric field). The vertical orientation becomes possible for particles with sizes in the range of 2-30 μm, in the presence of external large scale electric fields of strength in the order of 10^4 V/m (two orders of magnitude greater than the fair weather electric field values). Depending on the particle size, the particle net charge value and polarity and the direction of the electric field, the required electric field strength for vertical orientation can be reduced in the order of 10^3 V m^{-1}. On top of that, in the case that the electrical force counterbalances the gravitational force, and the drag force becomes equal to zero, the required electrical field for vertical orientation reduces further to 10^2 V m^{-1}, which is in the same order of magnitude with the fair weather value, and the particle size range for vertical orientation increases up to sizes of 1 mm.

In principle, vertical orientation becomes possible in the presence of external large scale electric fields of strength in the order of 10^4 V m^{-1}, which is wo orders of magnitude greater than the fair weather electric field values. But, depending on the particle size, the particle net charge value and polarity and the direction of the electric field, the required electric field strength for vertical orientation can be in the order of 10^3 V m^{-1} (Mallios et al., 2021b).

Chapter 3

Development of Measurement Techniques & Instrumentation for Dust particle Electrification & Orientation [2]

Resolving the scientific question of the impact of triboelectrification, and dust electrification in general, on dust removal processes requires systematic observations of the key parameters driving the phenomenon, along with the application of electrostatic and dust transport theories. An ideal observational strategy is to focus on lofted dust layers, both from the ground and in vertical distributions with the altitude. The objective is to monitor the effect of the particle concentration to the near-ground electric field, provide information on height-resolved dust electrical properties, and also target particle orientation on ambient conditions, along with co-located measurements of the particle charge density and electric field strength. For this reason, we re-visit the existing observational techniques of dust particle electrification and orientation, while highlighting the importance of complementing measurements that can resolve the criteria for a complete dust layer characterization. We, then, introduce novel instrumentation that was implemented and/or

[2] **This chapter is based on my contribution in:**

Daskalopoulou, V., Mallios, S. A., Ulanowski, Z., Hloupis, G., Gialitaki, A., Tsikoudi, I., Tassis, K. and Amiridis, V.: *The electrical activity of Saharan dust as perceived from surface electric field observations,* Atmos. Chem. Phys., 21(2), 927–949, doi:10.5194/acp-21-927-2021, 2021a.

Daskalopoulou, V., Hloupis, G., Mallios, S. A., Makrakis, I., Skoubris, E., Kezoudi, M., Ulanowski, Z. and Amiridis, V.: *Vertical profiling of the electrical properties of charged desert dust during the pre-ASKOS campaign*., COMECAP, 1–6 [online] Available from: https://nora.nerc.ac.uk/id/eprint/531299/, 2021b and **related implementations**.

Daskalopoulou, V., Raptis, P. I., Tsekeri, A., Amiridis, V., Kazadzis, S., Ulanowski, Z., Charmandaris, V., Tassis, K., and Martin, W.: *Linear polarization signatures of atmospheric dust with the SolPol direct-sun polarimeter,* Atmos. Meas. Tech., 16(19), 4529–4550, doi:10.5194/amt-16-4529-2023, 2023a.

characterized throughout the doctoral research for: i. *accurate* ***vertical profiling measurements*** and ii. ***detection of particle orientation*** within the dust layers.

3.1. Existing Observational Techniques of Dust Electrification

It is well documented that over deserts the emission process of dust particles can generate large atmospheric electric fields (Esposito et al., 2016; Renno and Kok, 2008; Zheng, 2013) that affect their flow dynamics (Kok and Renno, 2006). Charged dust occurrences are recorded via ground-based methods also in destinations further away from the source (Harrison et al., 2018; Katz et al., 2018; Silva et al., 2016; Yair et al., 2016; Yaniv et al., 2017), while balloon-borne observations (Kamra, 1972; Nicoll et al., 2011a) indicate that space charge is indeed persistent within lofted dust layers during their transport to long distances.

3.1.1. Detection of Dust Electrification from Surface Electric Field Observations

Ground-based electric field measurements can be indicative of the electrical behaviour of elevated dust layers. These measurements can provide useful information if they are combined with other retrievals on aerosol profiling (e.g. lidar, ceilometer) (Nicoll et al., 2020). However, features of E-field timeseries, such as the enhancement of the near-ground electric field during dust outbreaks, are still unexplained in broad literature (Yaniv et al., 2016, 2017). Observations of enhanced or even reversed E-field at the height of the ground-based sensor, e.g. an electrostatic fieldmeter, are attributed by Ette (1971) and Freier (1960) to charge separation within electrically active dust. According to several laboratory studies (Duff and Lacks, 2008; Forward et al., 2009b; Inculet et al., 2006; Waitukaitis et al., 2014), charge transfer processes lead to smaller particles being negatively charged while larger particles tend to be positively charged, therefore charge separation within lofted dust layers is also possible due to the expected size selective gravitational settling that could stratify the fine and coarse mode particles (Ulanowski et al., 2007).

An observed reduction of the E-field in a mountainous area is attributed to the superposition of two dust layers in different heights with respect to the ground-based sensor (Katz et al., 2018). Moreover, layers that exhibit large particle densities lead to more particles competing for the same

amount of ions (ion-particle competition, e.g. Gunn, 1954; Reiter, 1992), hence they act as a passive element within the atmospheric circulation and can reduce the near-ground electric field. A similar reduction of the electric field can be expected whenever, for any reason, the charge separation does not occur. As an example, one can think meteorological conditions that force the particles to move randomly, cancelling their vertical movement and, therefore, the charge separation. Nonetheless, systematic profiling measurements are needed so as to fully characterize the electrical properties of the dust particles aloft, with respect to the locally occurring meteorological conditions.

3.1.2. Electrification of Saltating Dust Particles

Saltation is the principal physical process for dispersing mineral aerosols, dust and sand grains from the Earth's surface into the atmosphere and is a generator of particle charging by intermittent contact with the surface. Studies of atmospheric electric field measurements during violent dust storms (haboobs) which originate from the major deserts, have reported E-field strengths that could reach up to ~ 3 kV m^{-1}, generally an order of magnitude larger than the fair weather electric field, from co-located radar and electric fieldmill measurements (Williams et al., 2009). The field perturbations recorded were just above the saltation layer which indicated that not only monopolar negative charging of the saltation layer due to proximity with the ground (Zheng et al., 2003) was present but, also, bipolar volume charging of the elevated dust above the measurement instrument due to charge separation (see Section 4.4). Zheng et al. (2013) authored a concise review over the electrification of wind-blown sand introducing field campaign apparatuses for electrification studies near the surface and concluded that for experimental techniques, it is imperative to develop an integrated non-contact measurement system which can not only perform a real-time and synchronous measurement of electric charges, and the direction and intensity of 3D E-fields, but also provide simultaneous information pertaining to the wind velocity, temperature, humidity, particle size distribution.

Another impactful study on dust emission by Esposito et al. (2016) has shown for the first time that depending on the relative humidity conditions, E-fields contribute to increase up to a factor of ten the number of particles emitted into the atmosphere, pointing that electrical forces and humidity are critical quantities in the dust emission process. They, moreover, found that emission causes particles to be electrically charged and produces strong atmospheric electric fields of up to 20 kV

m^{-1} at a height of 2 m, with generally downward looking fields observed suggesting a dependence of charging to the lifting particle composition.

Toth et al. (2020) made an attempt to extrapolate their in-house experiment logic to the long-range transport of dust. It is concluded that even the fair weather electric could maintain large dust particles aloft, assuming extreme values of charge densities found in lab conditions. Which therefore renders the results ambiguous. The research conducted here aims to clarify the assumptions and provide consistent measurements of dust electrification aloft.

3.1.3. Detection of Charged Dust Particles within Elevated Layers

By examining the electrical properties of dust particles at different altitudes, along with the prevailing meteorological conditions, we can gain insights into the processes that influence dust dispersion, such as atmospheric dynamics, wind patterns, and electrostatic forces. Small aircraft flights with specifically designed and geometrically distributed fieldmills on an on-board network, have been used extensively for cloud and thunderstorm studies, where the produced electric fields are significantly stronger and close to the discharge limit (Buguet et al., 2021; Mach, D. M., Koshak, W. J., 2007; Mach et al., 2009). The method, nonetheless, is somewhat invasive and in the case of dust layers where the layer boundaries can be more loosely determined, such an airborne platform would disturb the dust flow dynamics causing increased parasitic fields in the flight altitude.

A measurement platform with significantly less overhead in terms of design, preparation, calibration and logistics, is the meteorological balloon sounding used widely for the profiling of atmospheric meteorological parameters when the payload relies on commercial meteorological radiosondes, such as the RS41s from Vaisala and the DFM-09s GRAW. Measurement strategies that could combine these parameters with the quantification of E-field strength/direction, charge densities and ion mobilities are sparse (Nicoll et al., 2011b). Instruments that are otherwise used in the ground or on-board heavier platforms need to be miniaturized in terms of electronics but retain the required measurement accuracy. Often, they need to be low-cost during overall assembly procedures because the radiosondes are statistically non-retrievable (Aplin et al., 2017; Harrison and Marlton, 2020; Nicoll, 2013). Nicoll et al. (2011b) conducted two balloon launches from the Cape Verde islands in order to intercept major dust transport layers. The soundings carried a specifically designed electrometer (Nicoll, 2013; based to the earlier: Nicoll and Harrison, 2009)

and an aerosol particle counter along a Vaisala digital radiosonde that provided the meteorological data with a 1 Hz frequency transmission rate. This experiment established that individual dust particles aloft are charged despite the slow charge relaxation expected in the atmospheric conductivity, with charge densities reaching up to 25 pC m^{-3} within the elevated layers (Figure 3.1), when the fair weather charge densities are of the order of 10^{-14} - 10^{-13} C for similar altitudes (Figure 1.3). While balloon-borne soundings offer significant advantages, it's important to note that they are just one component of a comprehensive approach to studying atmospheric electricity. Ground-based measurements, satellite observations, and other techniques contribute to a holistic understanding of the Earth's electric field.

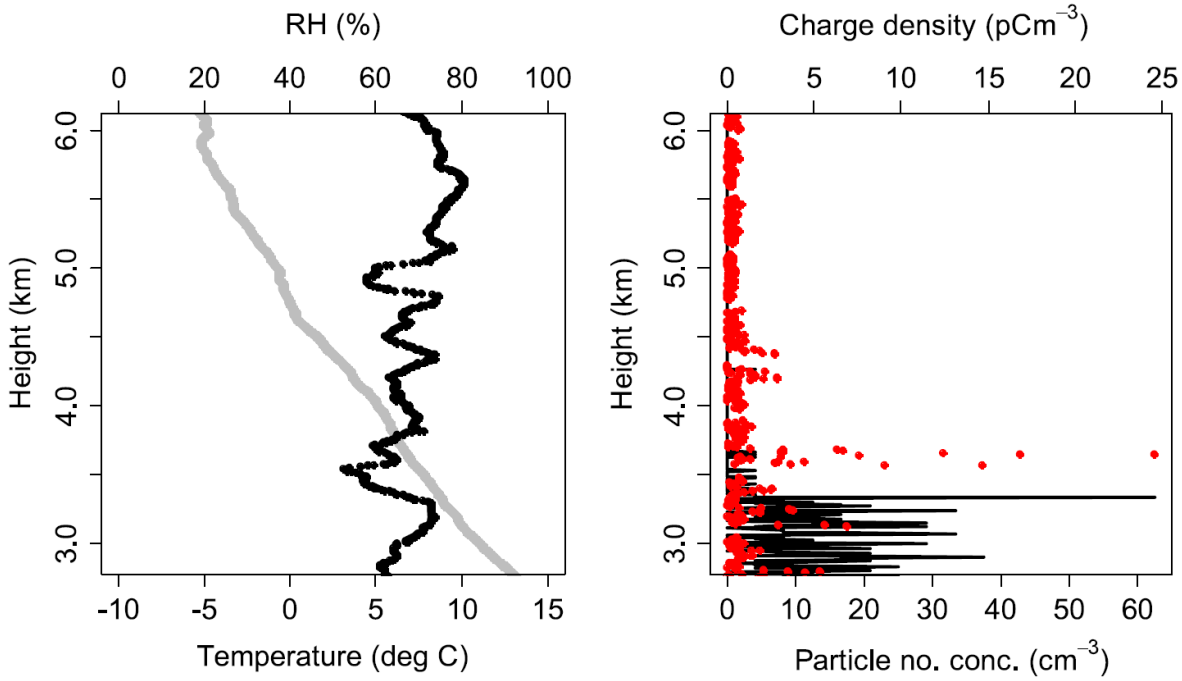

Figure 3.1: Vertical profile of (a) temperature (grey) and relative humidity, RH (black), (b) total aerosol particle number concentration (black lines) and magnitude of charge density (red points) measured on sounding. Source: adapted from Nicoll et al. (2011b).

On the other hand, laboratory efforts from Harper et al., (2022) employing an interesting apparatus of acoustic levitation (no contact) tried to quantify a single particle charge and found that it decreases with time as negative ions attach to it. Moreover, the particle seems to retain its charge even as long as one week under conditions of controlled humidity. Although this is a promising experimental work, it does not yet represent phenomena that make the quantification of travelling

dust particles charges a challenge, such as particle competition in an ionic environment of multiple particles which is the case of transported layers. Since, as particle number density increases then on average less ions will attach to a single particle and therefore the acquired ionic charge will decrease. Furthermore, the initial control parameters of the experiment do not reflect realistic values, such as the huge initial charge assumed where there is no observational evidence that a charge that large exists even above the emission sources.

3.2. Existing Observational Techniques of Dust Particle Orientation

Observations of the alignment of atmospheric dust have somewhat been elusive for the past years, in contrast to the other atmospheric constituents such as ice crystals and in-cloud particles that exhibit clearer trends with an impact on skylight observations where they produce intense halos (e.g., Moilanen and Gritsevich, 2022), on cloud radar observations and radar simulations (e.g., Hendry and Antar, 1982), but also on polarization lidars (Geier and Arienti, 2014; Hayman et al., 2014; Neely et al., 2018). Some of the commonly used observational techniques for studying particle orientation can be summed in the following general categories and potentially be used for the observation of anisotropic dust particles:

1. *Polarized Light Scattering*: Polarized light scattering is a fundamental technique used to study the orientation of dust particles. When light interacts with anisotropic particles, such as non-spherical dust particles and particles that contain homochiral organics (i.e., organic molecules that exhibit optical activity mainly circular birefringence), the scattered light becomes polarized. It has been well documented that many dust particles contain materials with significant dielectric contrast, for example iron oxides or inhomogeneities in structure, such as internal pores, that can noticeably affect the light scattered by the particles (Kemppinen et al., 2015). Observing the polarization state of scattered light probes the information about the orientation, size and shape of the dust particles. The principles behind the detection of scattered light polarization are employed both in the retrieval of cosmic/interstellar dust properties that are aligned in the interstellar magnetic field lines (e.g., Dolginov, 1972; Cox et al., 2011; Andersson et al., 2015; Yang and Li, 2020 and references therein) and those of the much larger in size atmospheric dust (Geier and Arienti, 2014; Tsekeri et al., 2021). The ability to make observations in a rapid way and without contact, makes optical light scattering

the best method for studying aerosol particles in their native environment. Since the particle's scattering pattern depends on its morphology, composition, and orientation, proper interpretation of a measured pattern can be useful for its characterization.

2. *Total Sky Polarimetry*: Sky polarimetry involves measuring the polarization patterns of the sky. The unpolarized light from the Sun scatters in the atmosphere, and the scattered light becomes polarized due to multiple interactions with the molecular atmosphere and the oceanic surface, showing certain distribution patterns that contain information on the degree of linear polarization. A factor that can contribute to skylight polarization is the preferred orientation of atmospheric particles, including dust, which can produce specific patterns to a sub-part of total skylight, the forward scattered light. By analyzing these background polarization patterns, researchers can gain insights into the alignment of dust particles in the atmosphere through cross-comparing with multiple scattering computational models (Guan et al., 2018; Li et al., 2023; Pan et al., 2023).

3. *Polarimetric Remote Sensing*: Polarimetric remote sensing techniques, such as ground-based and satellite-based polarimetric instruments, can be used to measure the polarization state of light backscattered from aerosols and dust in the atmosphere (Cairns et al., 2003, 2009; Dubovik et al., 2019). These measurements provide information on the dust particle microphysics such as the size distribution, shape and orientation of the dust particles in different atmospheric layers.

3.1. *Lidar Polarimetry*: A sub-category of the above general technique are the widely used Lidars (Light Detection and Ranging). Lidars are powerful remote sensing instruments that emit polarized light and detect the backscattered light to probe the atmospheric properties. Oriented particles can exhibit different polarization properties than randomly oriented particles (Mischenko et al., 2002b; Mishchenko et al., 1997). Lidar polarimetry involves analyzing the polarization characteristics of the backscattered laser light to deduce the full scattering matrix of the probing aerosols and subsequently deduce their orientation properties (Geier and Arienti, 2014; Hayman et al., 2012, 2014; Tsekeri et al., 2021) (see Section 3.2.2).

3.2. *Polarimetric Sun/Star Photometry*: Polarimetric star photometry is used to measure the polarization of sunlight or any other known polarization from stars as light gets directly scattered by the atmosphere (Bailey et al., 2008, 2020; Daskalopoulou et al., 2021a, 2023b; Hough et al., 2006; Kemp et al., 1987; Kemp and Barbour, 1981; Mallios et al., 2021b; Stenflo, 2005). This technique provides information about the alignment of aerosols and dust particles in the atmospheric column (see Section 3.2.1).

6. *Polarimetric Imaging*: Polarimetric imaging instruments capture the polarization state of light from a scene. In the context of studying dust particle orientation, polarimetric imaging can help reveal the distribution and alignment of dust particles in various atmospheric conditions (Kemppinen et al., 2020).

7. *Electron Microscopy*: Electron microscopy, including scanning electron microscopy (SEM) (Jokinen et al., 2018) and transmission electron microscopy (TEM) (e.g., Kandler et al., 2011), is a powerful technique used in laboratory settings to directly visualize and characterize the morphology and orientation of individual dust particles.

8. *In-Situ Particle Sampling*: A popular but invasive technique employs in situ sampling instrumentation, such as impactors, particle traps and/or particle counters, on board small aircrafts (Formenti et al., 2011; Ryder et al., 2013, 2015, 2018b; Weinzierl et al., 2017) and on unmanned vehicles to collect dust particle (e.g., Kezoudi et al., 2021) samples under dedicated measurement periods. Subsequently, they analyze the particle optical properties and indirectly deduce their orientation or by directly collecting the dust particles and analyzing the samples using microscopy and supplementary techniques. Both of the above techniques can be considered invasive as the dust layer is aerodynamically disturbed during the overflights, resulting in measurement biases to the particle orientation.

Combining observational platforms (e.g., Knobelspiesse et al., 2020) and the observational techniques with advanced numerical modeling and data analysis (Drakaki et al., 2022; Huang et al., 2021; Mallios et al., 2020) allows researchers to gain comprehensive insights into dust particle orientation and its impact on atmospheric transport and radiative processes. Such studies are vital for understanding climate, air quality, and environmental changes driven by atmospheric aerosols.

3.2.1. Alignment Detection through Starlight Polarimetry

The major breakthrough study that heavily influenced the investigation of dust particle orientation in this dissertation, is summed in the observations reported by Bailey et al. (2008) and the earlier work by Ulanowski et al. (2007) that aimed at a plausible physical explanation of the phenomenon for the same measurement period. Bailey and his colleagues, motivated by the use of astronomical polarimetry as a means of probing the presence of exoplanets, and provided that such observations require high accuracy/sensitivity systems (of the order of 10^{-6} in polarization terms), strived to

establish whether atmospheric effects can be comparable to their measurements and impact their system's performance. For that purpose, they built and tested a high-sensitivity passive polarimeter, the PlanetPol (Hough et al., 2006), that could be mounted on intermediate astronomical telescopes of known internal polarization and which employed photoelastic modulators, avalanche photodiodes and achieved a photon-noise–limited sensitivity of at least 1 in 10^6 in fractional polarization (Bailey et al., 2008). Up until that point, it was generally believed that the Earth's atmosphere did not affect the polarization of light traveling through it and as then detected by ground-based telescopes for astronomical investigations. Therefore, Bailey et al. targeted linear polarization measurements with PlanetPol over a mountainous observatory in La Palma, Canary Islands, which is frequently affected by severe dust events from the Sahara, with the prospect of monitoring polarization in diverse ambient conditions.

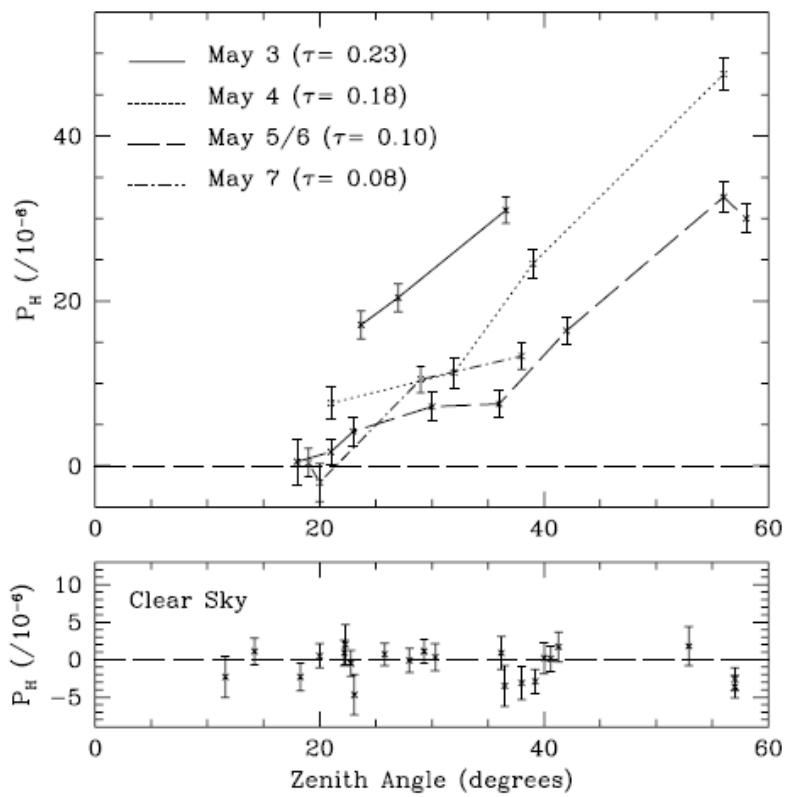

Figure 3.2: Clear sky (lower panel) and dust affected (upper panel) excess linear polarization as a function of zenith distance. The dust optical depth (τ) measured by the Carlsberg Meridian Telescope (CMT) is indicated for each night. The data for May 5 and 6 have been combined as the two nights have almost the same dust optical depth (Bailey et al., 2008).

The observations were performed during nighttime and focused on starlight originating from four stars with peak spectral responses between 590 nm to 1000 nm and with known little polarization (Hough et al., 2006). Polarization values were obtained between the period of April 27 2005 to May 8 2005, under clear conditions when the mean polarization was calculated and under dust events of various loads, when they observed a significant deviation from the polarization trends recorded in the clear cases. They recorded an excess linear polarization predominantly in the horizontal direction of the order of 10^{-5} which intensified with increasing zenith angle (Figure 3.2). By contract, the clear day values were of the order of a few ppms (parts per million, 10^{-6}) with no observed correlation to the zenith distance. Moreover, the polarization changed from night to night, roughly in proportion to the change in the aerosol optical depth (Figure 3.2). Therefore, Bailey et al. attributed this characteristic linear polarization increase in dichroic extinction of the forward scattered starlight from preferentially vertically oriented dust particles in the atmosphere.

This statement was, to our knowledge, the first indication of atmospheric dust orientation and thus sparked the need for further research investigation (see Section 3.4 and Chapter 5).

3.2.2. Alignment Detection through Active Polarimetry

The aforementioned measurement technique of dust particle orientation via starlight detection refers to column-integrated values that are not capable of determining the vertical distribution of the phenomenon throughout the dust layer only by means of a Stokes polarimeter, since information for the complete backscatter phase matrix needs to be retrieved. Active remote sensing instruments, such as specifically designed lidars, are capable of providing vertically resolved information in a few km within the atmospheric column (Hayman et al., 2012, 2014), as conventional lidars in most cases assume randomly oriented particles which can affect their depolarization ratio measurements Such a case was presented by Hayman et al. (2014) when they first recorded signs of oriented rain droplets and later the same year, Geier and Arienti (2014), proposed their theoretical design on a four-channel polarization lidar system with particular focus on detection of preferentially oriented aerosol particles and potential expandability to atmospheric dust particles. Lidars have also been previously utilized to demonstrate whether ice crystals in cirrus clouds exhibit signatures of alignment (e.g., Kokhanenko et al., 2020 and references therein).

It has been demonstrated that although linearly polarized backscattered light from lidar measurements is adequate to discern ice crystal orientation, detection of the same phenomenon for dust particles with the use of only linearly polarized light is not feasible due to the signature being orders of magnitude less than in the case of ice crystals (Geier and Arienti, 2014). A different approach employed by the newly developed WALL-E lidar system (Tsekeri et al., 2021) aims for direct measurements of dust orientation, without having to retrieve the individual off-diagonal elements of the backscatter phase matrix that completely describes the particle orientation state. It also aims at increasing the information content of the measurements for dust microphysical properties by using a dual laser - dual telescope set up that emits/collects interleaving linearly polarized light at a 45 degrees plane along with elliptically polarized light (Tsekeri et al., 2021). The first observations of WALL-E on rain particle orientation over the city of Athens are quite promising and the instrument provided a lengthy dataset of continuous near real-time profiles of particle orientation flags in the Saharan Air Layer (SAL) within the framework of the ASKOS experiment (see Section 3.5.4). Future intercomparison between the passive and active polarimetric techniques for particle orientation will enable a new era of synergistic measurements dedicated to the phenomenon.

3.3. New Developments for Dust Vertical Profiling

Balloon-borne soundings are often considered the most reliable and minimally invasive method for probing the atmospheric electric potential for several reasons:

- *Vertical Profiling*: Balloon soundings allow for vertical profiling measurements of the electrical properties of dust particles, which are essential for several reasons as they can contribute greatly to the understanding of dust transport and dispersion. By ascending through different atmospheric layers, the measurements can capture variations in the electric field with altitude. This is crucial for understanding how the electric potential changes with height.
- *Direct Measurement*: Instruments attached to the airborne platforms directly measure the atmospheric electric properties. This direct measurement provides accurate and real-time data without relying on indirect proxies.

- *High Altitude Reach*: Meteorological balloons can reach low stratospheric heights with ease, depending on the payload weight, and providing access to regions of the atmosphere that are not easily accessible by ground-based instruments. This allows researchers to study the electric potential in the upper atmosphere.
- *Uninterrupted Vertical Profile*: Unlike ground-based measurements that are limited to specific locations, balloon soundings provide an uninterrupted vertical profile. This is particularly beneficial for studying the electric potential across a wide range of altitudes.
- *Minimized Ground Effects*: Ground-based measurements can be influenced by local factors such as buildings, terrain, and other structures that may interfere with the accuracy of measurements. Balloon soundings minimize these ground effects, providing a clearer picture of the atmospheric electric potential.
- *Mobility and Flexibility*: Balloons offer mobility and flexibility in terms of deployment. They can be launched from various locations and are not constrained to fixed measurement sites. This mobility allows researchers to target specific regions of interest.
- *Reduced Interference*: The specific measurement methods are less susceptible to interference from ground-based electrical equipment and anthropogenic sources, leading to cleaner data.
- Temporary Instrumentation: Instruments attached to balloons can be designed for temporary deployment and are often lightweight and disposable. This allows for cost-effective measurements without the need for permanent infrastructure.
- *Study of Localized Phenomena*: Soundings enable the study of localized atmospheric phenomena, such as electric field variations associated with specific weather events or geographical features.

As mentioned previously, they have been used as means of probing the electrical properties within elevated layers (Nicoll et al., 2011b) and with the appropriate instrumentation payload they can prove invaluable with unprecedent datasets. The author has developed two novel (designs) lightweight, low-cost and disposable atmospheric electricity sensors within the timeframe of the dissertation, a. *a miniature fieldmill electrometer*, the so-called MiniMill, employed to measure the vertical electric filed strength and b. a *space charge sensor,* to measure the space charge density. The instruments were designed, assembled and characterized in-house at NOA within the framework of the D-TECT ERC project and extensively calibrated at PANGEA, while several launches with prototypes were performed for the quality control of the data. Eventually, we

produced multitudes of sensors (x 30 of each) so as to be launched in pairs, tethered to meteorological radiosondes that served as the data transfer proxy to the respective ground-station. The overarching goal was to target transient dust loads with high dust concentrations where we could test the theories of particle electrification and aim at detecting strongly generated fields within the layers for a potential to simultaneously observe dust orientation within the stratified layers. ASKOS Cal/Val experimental campaign offered the perfect opportunity for consecutive soundings at ambient conditions as often as possible, described in detail in Section 3.5.4 and Chapter 5, but most importantly offered the multi-instrumental approach needed to fully characterize such layers.

Overall, the primary measured quantities are:

- Electric field strength (V m^{-1}) at an XYZ axis co-ordinates bases (direct measurement from the MiniMill)
- Total Electric field strength (V m^{-1}) (indirect measurement from the Space charge sensor)
- Space Charge density (C m^{-3}) (direct measurement from the Space charge sensor)

The ancillary quantities are:

- Rotational angles Roll, Pitch, Yaw (°) (direct measurement from the MiniMill)
- Pressure (kPa), Temperature (°C), Relative Humidity (%), Wind Speed (m/s), Wind direction (°), Altitude (m) (direct measurement from a GRAW DFM-09 radiosonde)

In the following sections, we describe the atmospheric electricity sensors' capabilities and the rationale behind their implementation. We also provide the technical specifications, in short mention of the Appendix section A.2 and we advise the reader to follow the GitHub repository created for the needs of the sensor's documentation. All designs, schematics, source code and procedures implemented during this effort are open and publicly available to the https://github.com/NOA-ReACT/electricity-sensors, under CC-BY-SA (CC) and GPL3 licenses. The raw data from the ASKOS launches can be found in the ESA Validation Data Center (EVDC) repository: https://evdc.esa.int/publications/askos-campaign-dataset/.

3.3.1. MiniMill Electrometer

The lightweight miniature fieldmill electrometer (MiniMill) design is quite robust, easy to reproduce and assemble, lightweight (~300 gr max assembled weight) and constructed from widely accessible materials, e.g., aluminium laser cut parts, or copper plated PCBs. It is influenced by the similar designs of larger fieldmill electrometers as the commercial JCI fieldmill used in our ground-based studies (Chubb, 2014), the ones described and characterized by Cui et al. (2017) for the quantification of electric fields under high-voltage power lines and the portable field meter of Harrison et al. (2020). Most of the above designs (except the one from Harrison et al. (20202)) lack the required accuracy in low E-fields of the order of fair weather values as they are targeting towards measuring larger E-fields that originate from thunderstorm activity, in the case of atmospheric studies. Therefore, a sensitivity of a few mV per v m^{-1} is required for applications involving dust generated fields.

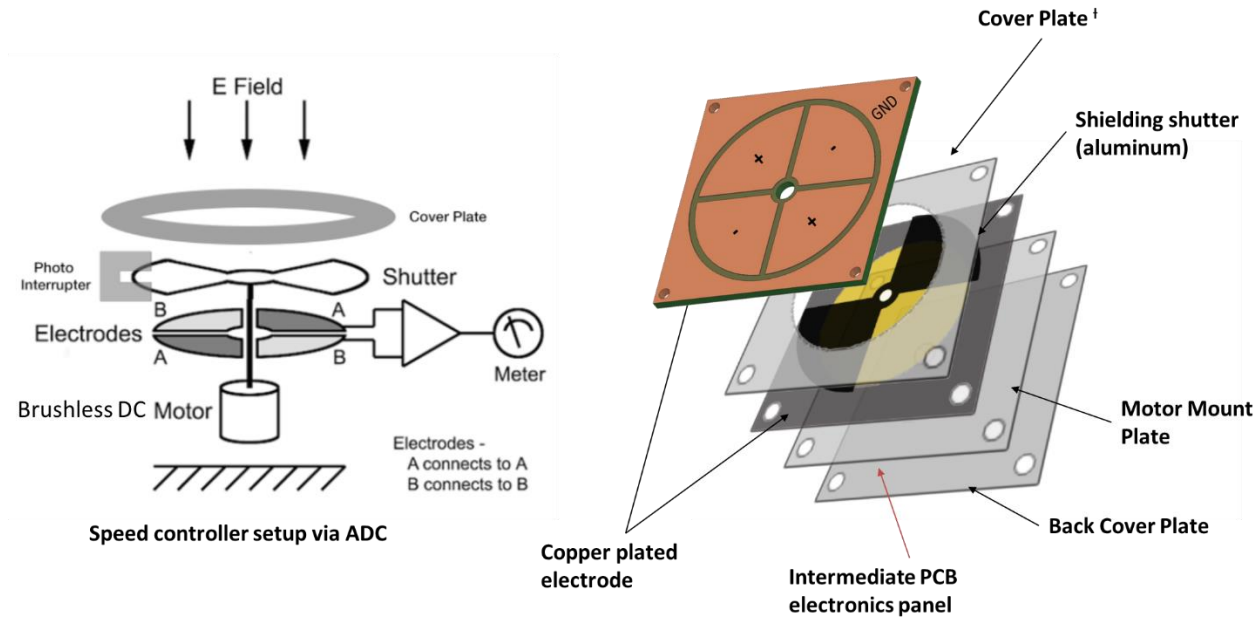

Figure 3.3: The MiniMill basic elements of operation (left) and layered design (right). Schematics by the *author*.

The essential components of a single MiniMill are shown in Figure 3.3 and are a sensing electrode plate with two mutually grounded electrodes, which are covered and uncovered by an earthed rotating shutter (through the motor), an electrometer to measure the induced charges on the

electrode, and an optical switch (photo-interrupter) to synchronize the electrometer with the shutter's position to allow phase-locked signal detection. The sensing electrode plate is copper plated for better conductivity, while the pair of sensing electrodes are divided in circle quarters reflecting the optimal vane quantity for the specific induced currents. The mill covering vanes are designed so as to cover/uncover the exact electrode area below them and are earthed through the brushless motor. An innovation of the specific design is the use of such a low-rpm DC motor that enables the required discharging rate for low ambient E-fields and minimizes the electromagnetic interference to the actual measurement. The DC motor speed is initially adjusted and kept constant (2400 cycles or 40 Hz on average) by a speed controller setup via connection to an ADC microcontroller.

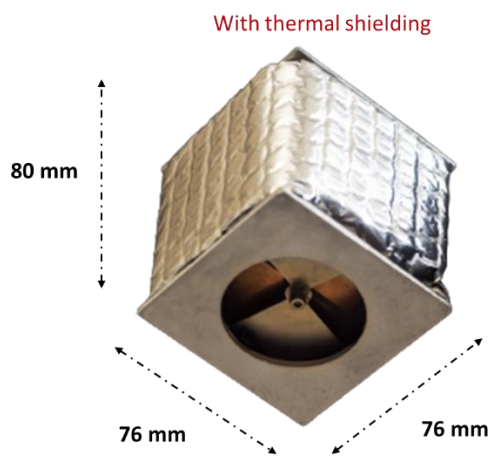

Figure 3.4: Left: The latest MiniMill model with thermal shielding and the aluminum plate cover which was eventually not utilized. Right: The production of multiple MiniMills for launching purposes.

A 3-axis accelerometer returns the angular position of the sensor with respect to the initial relaxation position. The instrument resolution is at ± 2.4 kV with a sensitivity of 1 ADC count, ± 2.3 mV per V m^{-1}, response time of 1s and can withstand temperature variations between -50 °C to 40 °C (Figure 3.4) translating to a maximum altitude operation, this corresponds to ~13 km msl. The sensor power consumption requirements are below 160 mA and can be powered by a single 9V batter, which seems to be fading in capacitance after the ~12 km and potentially lowering the motor speed.

In terms of operation principal, the two electrode layers (electrode plate vs screening shutter) are essentially a parallel plate capacitor that gets periodically charged and discharged by the external E-filed. When static, the input impedance of the meter allows charges to move from one electrode to the other until the voltage between them is zero, discharging it and cancelling out the ambient field. As the rotor rotates, it induces charges onto and off the plates, and the measured output is the current created by that movement. This depends entirely on the external vertical E-field and the rotor speed, so we can use it to calculate the field the sensor is in.

For an effective sensing area S that has a temporal dependence, we get:

$$Q(t) = \sum_{S} q = \varepsilon_0 E S(t) \tag{3.1}$$

where S depends on the circular sector angle, Q is the change in charge on one electrode and E is the constant electric field strength applied. The induced current, thus, is:

$$i(t) = \varepsilon_0 E \frac{dS(t)}{dt} \tag{3.2}$$

Since this is a differential measurement, the measured voltage in the ADC is twice the amplified output voltage from each electrode. The choice of input resistance determines the time constant of the system, which, for the current generated to be independent of the shutter rotation rate, should be much longer than the interval for which the electrode is shielded during the rotation (Harrison et al., 2020). In order to prepare the sensors for launch, a set of calibration procedures where implemented consisting of a hard vibration test, a temperature resilience test, the MiniMill's response compared to the commercial JCI 131 fieldmill response, zero field response in a Faraday cage (on all sensors), the basic parallel plates calibration for calibration curve determination (on all sensors) and a test radiosonde flight to assess the sensor's performance and connectivity to the meteorological radiosonde. Technical information for these procedures is beyond the scope of this dissertation and is otherwise documented in the GitHub public repository.

3.3.2. Space Charge Sensor

A miniaturized self-calibrating electrometer, referred to as Space charge sensor, is implemented based on the designs and previous calibration work of the lightweight balloon-carried charge sensor

discussed Nicoll et al. (2009, 2013). The sensor is used for direct atmospheric charge density measurements and electric field measurements, also used on-board the meteorological radiosonde launches and low-cost and disposable after each launch (Figure 3.5). Based on a brass spherical electrode collector protruding from the formation, it is capable to collect charged particles as it ascends through the atmosphere. The electrode dimensions are crucial for the determination of the effective sensing area. The space charge density measurement is directly related to the voltage output as (connection through the Gauss' law):

$$\rho = \frac{\varepsilon_0}{d_{eff}} \frac{1}{w} \frac{dV_{out}}{dt} \tag{3.3}$$

where ρ is the space charge density, w is the radiosonde ascend rate and V_{out} is the sensor output voltage. In our sensor, the used sphere is 15 mm of diameter, 1.5 mm in thickness (hollow) and the estimated (through parallel plates calibration) effective sensing diameter, d_{eff}, is 25.4 mm a factor of 1.7 larger than the physical diameter, coinciding with what Nicoll et al. (2009) pointed. The instrument can detect charges in the range of a few fC m^{-3} to the order of nC m^{-3}, with a sensitivity to the output voltage of ± 2.3 mV and an accuracy of ~ 10 mV.

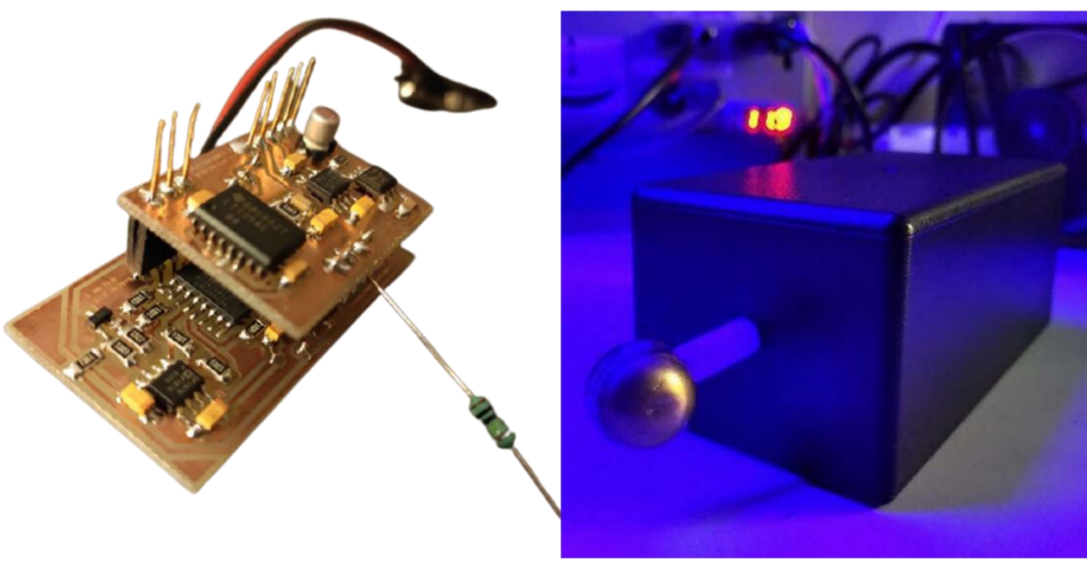

Figure 3.5: The space charge sensor design with (right) and without (left) the protective casing.

A total measurement period lasts for five minutes, followed by 10 s of +2.5 pA calibration current that discharges the electrode and another 10 s of -2.5 pA. The relationship between the current flowing to the electrode, i and the recorded output voltage V_{out}, is derived from the known calibration currents. For each 5 min measurement period, a linear fit is made between the mean output voltage during the two calibration periods (mean of at least 10 points), against the known calibration currents of +2.5 pA and−2.5 pA. This yields an expression of the form for the output current of: $i = aV_{out} + b$, where we estimate $a \approx 6.83\text{E} - 12$ and $b \approx -1.43543\text{E} - 11$. Data transmission is done solely from the meteorological radiosonde and the sensor firmware is designed to buffer data received from the MiniMill, when tethered, and then connect to the radiosonde through the external data (XDATA) protocol.

3.3.3. Integration to Meteorological Radiosondes

The quickest way, in the limited timeframe that we had available, to transmit the sensor data to the ground was when the sensors' output is attached the transmission protocol of the radiosonde. The GRAW DFM-09 radiosonde has a 4 pin header which can be used to transmit data to the ground using the XDATA protocol. The header has a UART port we hook up to your microcontroller. The baud rate is 9600bps 8 data bits, no parity, one stop bit (8N1). The MiniMill sensor firmware we have implemented transmits the sensor data whether through a UART serial connection or through daisy chaining to the second space charge sensor. The sampling rate is set at 9500 samples per second when on individual connection and at 1 sample (average) per second when coupled to the radiosonde. The XDATA protocol describes packages sent over UART (9600 bps, 8N1) in ASCII. Each package consists of a mandatory package header (xdata=), a sensor ID, a daisy-chain counter and finally, your data. Everything except the header must be encoded in hexadecimal. The sensor ID must be equal to 0x01, which GRAW recognizes as an Ozone sensor. For bytes 8-9, we have found references online that they are supposed to be a daisy chain counter, for sensors that support forwarding XDATA packages of other sensors.

3.4. Detection of Dust Orientation with a Ground-based Polarimeter: The SolPol solar polarimeter

We have extensively discussed the novel models and synergistic measurement techniques for desert dust electrification in the previous sections and addressed the necessity for consistent vertical profiling measurements that give crucial electric parameters within the dust layers. But can we address another parameter of aerosol dynamics, orientation, and potentially corelate this orientation with the prevailing electrical conditions? A first step would be to carefully monitor elevated dust layers for orientation signatures. Considering the recent gap in literature concerning the somewhat elusive detection of particle orientation and the impact of such oriented dust to direct sun polarimetric measurements, along with being motivated by previous observations of starlight dichroic extinction due to oriented dust (Bailey et al., 2008; Ulanowski et al., 2007), we employ a novel direct sun solar polarimeter (SolPol) and investigate the orientation signatures of dust particles within the atmospheric column for two consecutive years of instrument operation. The capabilities of direct sun polarimetric measurements are discussed in Kemp et al. (1987) and Kemp and Barbour (1981), setting the detection threshold as low as sensitivities of the order of 10^{-7}, for perturbations to the polarization of forward scattered light.

SolPol is a passive ground-based polarimeter that has been developed at the University of Hertfordshire. It was initially implemented as a laboratory experimental configuration in order to acquire both linear and circular polarization signatures of scattered light from biological materials and cyanobacteria, to demonstrate the detection capabilities of potential life presence on exoplanetary atmospheres (Martin et al., 2010, 2016). It was, after that, kindly conferred to NOA-ReACT team for operation purposes that exceeded its indoor capabilities, as it was installed in the remote PANhellenic GEophysical observatory of Antikythera (PANGEA), under the framework of the D-TECT European Research Council project. As we aimed at monitoring potential orientation signatures on-demand in elevated dust layers, the instrument was housed in an astronomical dome for protection and was operational during seasonal periods of intense dust circulation over the station area. The instrument has a small compact design (the main body of the assembly is about 50 cm x 20 cm x 20 cm and easily fits in a medium sized metallic hardcase) and due to its ability to operate for consecutive hours with some degree of regular supervision, it was also operated in the

two experimental campaigns of ASKOS, the preparatory phase of November 2019 in Cyprus and main Phases A and B of June/September 2022 in Cape Verde (see Sections 3.5.4).

In Sect. 3.4.1 and 3.4.2, we present a comprehensive description of the instrument design, the side components that comprise the configuration and delineate the basic principles of operation focusing on measuring the Stokes parameters of the transmitted light. In Sect. 3.4.3, we describe the process of acquiring quality-assured data with SolPol and the followed methodology for each measurement sequence regardless of the ambient conditions.

3.4.1. SolPol Design

The design of the SolPol instrument is quite robust and follows that of its astronomical counterpart and predecessor, PlanetPol (Bailey et al., 2008; Hough et al., 2006). Figure 3.6 illustrates the polarimeter individual parts, spanning from the head to the instrument support and data acquisition peripherals. A more detailed representation can be found in the SolPol manual document under the thesis Appendix a. The instrument's principal operation is heavily based on a Hinds Instruments Photo Elastic Modulator (PEM) head (Figure 3.6), as most astronomical spectropolarimeters, due to the PEM high sensitivity to polarization fraction of the order of 10^{-6} (Hough et al., 2006; Kemp and Barbour, 1981; Povel, 1995). The PEM is comprised of a birefringent crystal that is mechanically strained at a principal resonant frequency (ω) of 47 kHz and induces a sinusoidal phase (modulation) retardation of $0.382 \cdot \lambda$ to the input signal, where λ is the incoming light wavelength. By exploiting the fundamental vibration along the PEM crystal optical axis, different polarization states are refracted in different directions, enabling the full Stokes parameters quantification with a single rotation of the PEM by 45° (e.g. Kemp and Barbour, 1981).

The polarimeter has a default limiting field-of-view (FOV) aperture of 5.5 mm diameter with a possibility of employing different iris sizes. The default aperture exactly encompasses the solar disk with an apparent angular diameter of 0.5 degrees, provided that sun-tracking is stable throughout the measurement. This is ensured in our case before every observational sequence. As seen in the electronics schematic (Figure 3.7), there are no optical elements before the PEM, which is directly followed by a rotatable linear polarizer with its passing axis aligned to the PEM long axis per manufacturing. Both the polarizer and PEM head can be rotated as a whole, through a Pyxis

commercial rotator, and their position is controlled from a LabView virtual instrument program, which also controls the recording of data from the detector.

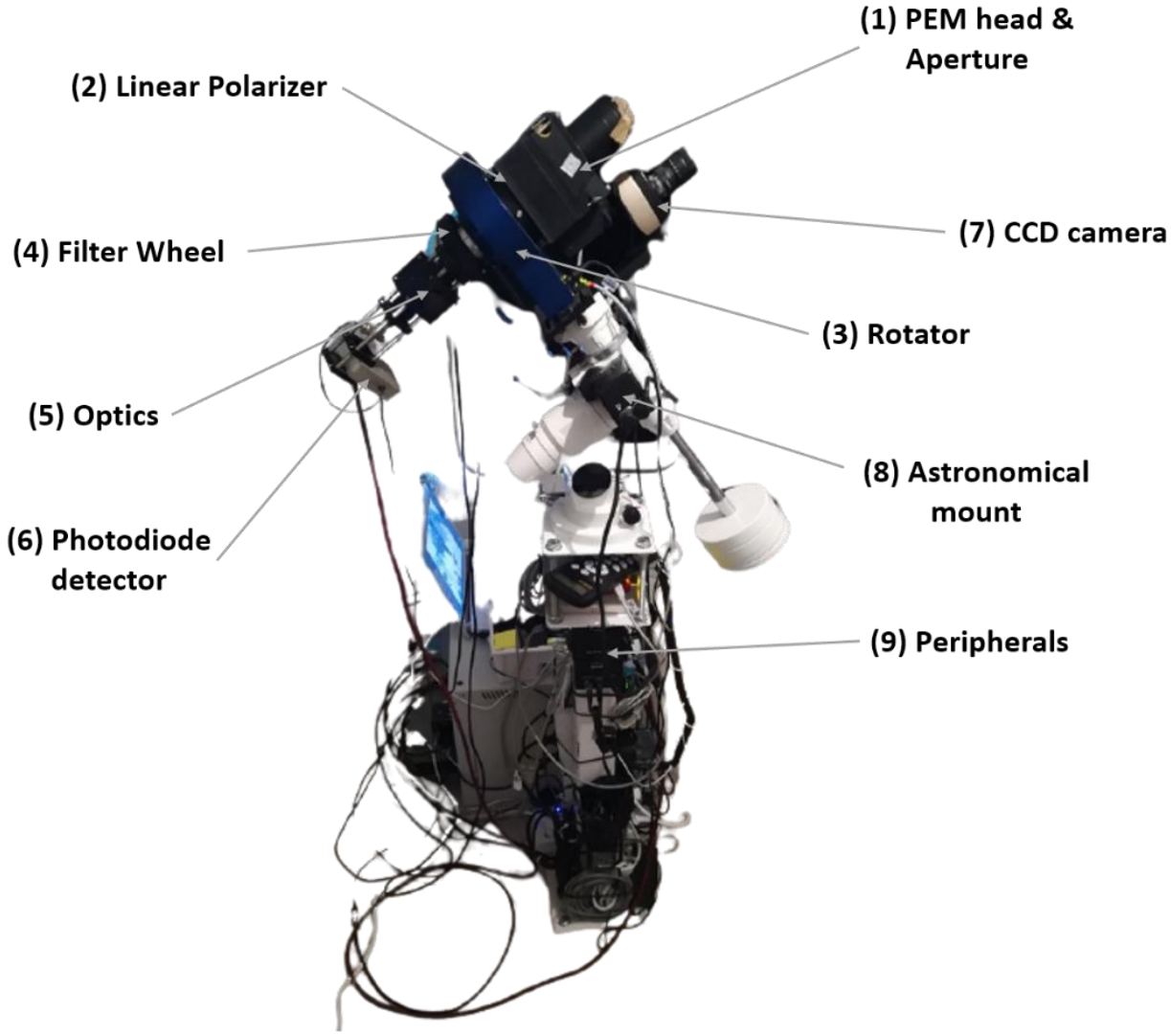

Figure 3.6: The SolPol direct sun solar polarimeter comprising of: (**1**) the Photoelastic Modulator Head (PEM) with the appropriate aperture, (**2**) the Linear Polarizer, (**3**) the assembly Pyxis Rotator, (**4**) the rotating Filter Wheel with the 550 nm centred narrowband filter, (**5**) the system Optics consisting of a Galilean telescope, (**6**) the 1-cm silicon Photodiode Detector. The instrument is mounted on (**8**), which is an EQ3 SynScan Astronomical mount and completed by (**9**) the essential Peripherals for the assembly operation, rotation and signal modulation, complemented by a CCD camera (**7)** for optical sun targeting. SolPol is operated in a 3-m astronomical dome installed at the PANGEA observatory in Antikythera, Greece.

Neutral density (ND) filters are employed next, on the filter wheel (Figure 3.6), containing six RGB broad band ND filters with measured transmission curves and three 40 nm narrow band interference filters at 400, 550, and 700 nm centre wavelengths. The polarimeter capabilities are tuned at 550 nm monochromatic operation for the present study. The ND filter wheel is followed by a simple Galilean telescope configuration, labelled as "Optics" in Figure 3.6, which collects and focuses the signal levels at the 1-cm silicon photodiode detector. The detector uses a transimpedance amplifier to generate the signal voltage. A 12-bit Analog-to-Digital converter (ADC) records the diode output signal and an SR830 Lock-in amplifier (labelled as "Peripherals") records the first (1ω) and second harmonic (2ω) AC de-modulation signals that are the outcome of the operation of the PEM. Lastly, SolPol continuously tracks the sun through a lightweight EQ3 SynScan astronomical mount. An external CCD camera, also on the mount, assists with the visual alignment of the instrument. By way of clarification, we will refer to components (1) - (7) as the "assembly" for the remainder of this paper in order to better describe the required SolPol movement for the acquisition of the complete Stokes vector $[I\ Q\ U\ V]^T$ (e.g., Hansen and Travis, 1974).

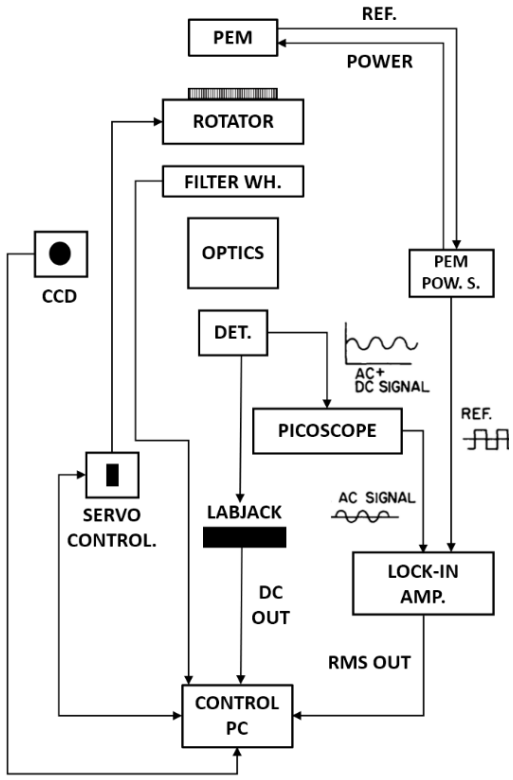

Figure 3.7: SolPol electronics and data acquisition diagram.

SolPol is a non-imaging polarimeter, hence its calibration technique varies from most known imaging polarimeters (Povel, 1995). In principle, the linear polariser and the PEM are carefully mechanically aligned by careful nulling of the signal, with respect to the polarizer rotation positions, from an arbitrarily polarised source. This sets the signal-to-noise ratio for the minimum detectable polarisation. Current instrument configuration has the capabilities of detecting a minimum of the order of 10^{-7}. If the field-of-view with respect to the solar disk was asymmetrical, offset, (i.e., the alignment is not optimum) then the measured polarisations are expected to increase since the measurements will also include polarized diffuse sunlight. This makes stable closed loop Sun tracking a pre-requite for the minimization of measurement errors.

3.4.2. Principles of Operation

SolPol measures the polarization fractions of linear polarization (expressed by the Q and U Stokes parameters) and circular polarization (V Stokes parameter) from the whole solar disk and the entirety of the atmospheric column, depending on its limiting field-of-view aperture and the choice of mounting telescope. The measurements of the degree of linear and circular polarization (i.e., $DOLP = \sqrt{Q^2 + U^2}/I$ and $DOCP = V/I$, respectively, e.g., general expression from Hansen and Travis 1974) have an absolute accuracy of 1 % and precision of 1 part per million (ppm, 10^{-6}) in polarization terms. The first observing sequence is performed with the assembly at the rest position (zero degrees) and the rotating of the linear polarizer in steps of 90 degrees. The corresponding relative positions of the PEM and linear polarizer for the assembly rotation is shown in Figure 3.8. For a complete polarizer rotation (360 degrees) we acquire measurements for four minutes. The specific sequence provides measurements of three of the four Stokes parameters. This is followed by the second observing sequence, performed after the rotation of the entire assembly, about the PEM crystal optical axis, over 45 degrees. This observing sequence provides measurements of the fourth Stokes parameter (V), and measurements for the removal of the biases and residual polarizations due to high frequency strain of the PEM for another four minutes.

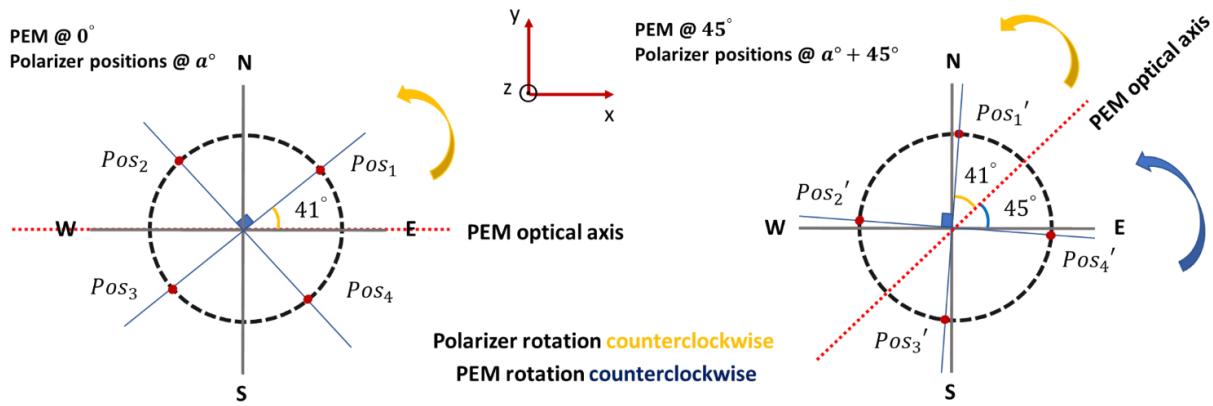

Figure 3.8: SolPol assembly positioning as seen from the incoming sunlight reference frame. Left arrangement: The initial sequence begins with the PEM and linear polarizer at the rest position of 0°, then the polarizer rotates by 90° starting from 41° (Pos_1), to 131° (Pos_2), 221° (Pos_3) and 311° (Pos_4) counter-clockwise. A complete polarizer rotation with the PEM at 0° provides measurements of the U Stokes parameter. Right arrangement: assembly rotation by 45° and subsequent similar rotation of the polarizer by 90° intervals from Pos_1' to Pos_4'. This configuration provides measurements of the Q Stokes parameter.

Therefore, each full measurement cycle has a duration of eight minutes in total and is comprised of two distinct sets: i. solar irradiance measurements on four positions of the linear polarizer at 41°, 131°, 221° and 311° with the assembly being at 0°, this configuration provides measurements of the *I*, *U* and *V* Stokes parameters and ii. measurements for the same relative positions of the linear polarizer, but the whole assembly is being rotated by 45° which provides measurements of the *I*, *Q* and *V* Stokes parameters (Figure 3.8). Measuring *I* and *V* twice provides information for the removal of biases and residual polarization in the measurements.

The Stokes vector of light that reaches the PM can be expressed using the Mueller formulation (e.g., Van de Hulst, 1957), considering as reference coordinate system the one of the incoming sunlight, as in Equation (3.4):

$$\begin{cases} \boldsymbol{I}'_{\alpha^o} = \boldsymbol{M}_{\boldsymbol{Pol.,a^\circ}} \boldsymbol{M}_{\boldsymbol{PEM}} \boldsymbol{I} \\ \boldsymbol{I}'_{\boldsymbol{rot,\alpha^o}} = \boldsymbol{M}_{\boldsymbol{Pol.,a^\circ}} \boldsymbol{M}_{\boldsymbol{PEM}} \boldsymbol{I}_{\boldsymbol{rot}} \end{cases}, \tag{3.4}$$

where $\boldsymbol{I} = [I\ Q\ U\ V]^T$ is the Stokes vector of the input light polarization state, $\boldsymbol{I}'_{\alpha^o}$ is the output polarization state with the assembly at zero degrees,

$$\boldsymbol{M_{Pol.,a^\circ}} = \frac{1}{2}\begin{bmatrix} 1 & \cos 2a & \sin 2a & 0 \\ \cos 2a & \cos^2 2a & \sin 2a \cos 2a & 0 \\ \sin 2a & \sin 2a \cos 2a & \sin^2 2a & 0 \\ 0 & 0 & 0 & 0 \end{bmatrix}, \tag{3.5}$$

is the Mueller matrix of the linear polarizer at each position angle α° ∈ (41°, 131°, 221°, 311°) and

$$\boldsymbol{M_{PEM}} = \begin{bmatrix} 1 & 0 & 0 & 0 \\ 0 & 1 & 0 & 0 \\ 0 & 0 & \cos\delta & \sin\delta \\ 0 & 0 & -\sin\delta & \cos\delta \end{bmatrix}, \tag{3.6}$$

is the Mueller matrix of the PEM that induces an input sinusoidal retardation of $\delta(t) = A\sin\omega t$, for A: the peak modulation amplitude and ω: the modulation frequency. When the whole assembly is rotated by 45°, the reference coordinate system is rotated by the same angle, hence $\boldsymbol{I'_{rot,\alpha^o}}$ is the Stokes vector of the output light for this rotational scheme. The incoming sunlight at each α° position, appears to be rotated by an angle of -45° and is calculated through the rotation matrix $\boldsymbol{R_{-45^\circ}}$ as $\boldsymbol{I_{rot}} = [I\ U - Q\ V]^T$ (as in Freudenthaler, 2016, S.5.1.7; Martin et al., 2010; Supplementary material/SolPol manual, Eq. 8). We utilize a Bessel functions expansion of the retardation δ and derive the measurements of the Stokes parameters of the incoming sunlight, at detector level, as a function of the linear polarizer angles and the assembly rotation (Table 3.1). The J_n(A) are the n-order Bessel functions and, for the specific PEM, the modulation amplitude is fixed at $A = 2.4048$ so that $J_0(A) = 0$, which makes the Q- and U-dependent DC terms equal to zero. Third order and above harmonic frequency terms are considered negligible, O (n > 2) → 0. We, then, sum over the four linear polarizer orientations per each assembly position, in order to eliminate the $\cos 2a$ dependent terms on the I derivation shown in Table 3.1, while the marginal $\sin 2a$ residuals on the other Stokes parameters are also accounted for in the data processing chain.

As discussed in Bailey et al. (2008) and Ulanowski et al. (2007), in case of aligned particles in the atmosphere, DOLP is expected to increase over larger solar zenith angles (SZA) since the direct sunlight travels through a larger airmass, and the effect of the dichroic extinction increases. With the increase of the SZA, the particle alignment angle changes with respect to the direction of observation, which is expected to influence the dichroic extinction and the measured linear polarization.

Table 3.1: Measurements of the Stokes parameters, from DC and AC measurements as a function of the modulation frequency, linear polarizer position angle and assembly rotation.

n	I'	Assembly without rotation	Assembly rotated at 45°
0	DC	$\frac{1}{2}(I + Q\cos 2a + UJ_0(A)\sin 2a)$	$\frac{1}{2}(I - QJ_0(A)\sin 2a + U\cos 2a)$
1	1ωt	$VJ_1(A)\ \sin\omega t\ \sin 2a$	$VJ_1(A)\ \sin\omega t\ \sin 2a$
2	2ωt	$UJ_2(A)\cos 2\omega t\ \sin 2a$	$-QJ_2(A)\cos 2\omega t \sin 2a$

3.4.3. Data acquisition and Data Processing

A detailed description of the technical characteristics of the instrument is provided in the form of an instrument manual and test measurements documentation in the thesis Appendix. Core information about the instrument operation and the data processing algorithm can also be found in the following publicly available GitHub repository: https://github.com/NOA-ReACT/SolPol (under CC-BY-SA (CC) and GPL3 licenses). Data availability is also open to the public in the following Zenodo repository, provided that all related data products abide also to the CC-BY-SA (CC) rights and are cited accordingly[3].

The raw data acquisition comprises a set of five similar measurements over each polarizer angular position per PEM rotation (total duration of 8 min), with each measurement associated with auxiliary information such as the polarizer specific angle, the PEM position, measurement time in UTC, the voltage outputs in the ADC and the two channels of the lock-in amplifier. In order to optimize data handling, we perform an initial data reduction to each measurement sequence by selecting the fifth measurement set for the same linear polarizer positions. The DC signal amplitude returned from the PM detector is simultaneously recorded by the ADC in volts (Figure 3.7) and gives the magnitude of the total irradiance I (3.7) as seen in Table 3.1. By turning the linear polarizer at specific positions, we acquire the amplitude and phase of the rms (root-mean-square) AC

[3] **Cite as:** Daskalopoulou, Vasiliki, Raptis, Panagiotis I., Tsekeri, Alexandra, Amiridis, Vassilis, Kazadzis, Stelios, Ulanowski, Zbigniew, Charmandaris, Vassilis, Tassis, Konstantinos, & Martin, William. (2022). D-TECT: SolPol measurements [Data set]. Zenodo. https://doi.org/10.5281/zenodo.7233498

modulated signals as outputs of the lock-in amplifier respective channels, and each is directly proportional to the magnitude of Q and U for even ωt (3.8 & (3.9) and to the magnitude of V for odd ωt (3.10). However, the two signals are processed through separate electronic channels on the amplifier, inducing a different proportionality factor for linear and circular polarization that depends on the modulation frequency and which is considered in data processing. Therefore, the recorded voltages from which we derive the Stokes parameters, are:

$$v_{DC} = I/2 \tag{3.7}$$

$$v_{2\omega,0^\circ} = UJ_2(A)/\sqrt{2} \tag{3.8}$$

$$v_{2\omega,45^\circ} = -QJ_2(A)/\sqrt{2} \tag{3.9}$$

$$v_{1\omega} = VJ_1(A)/\sqrt{2} \tag{3.10}$$

where $J_1(A)$ = 0.5192 and $J_2(A)$ = 0.4317 are the first and second order Bessel functions for A = 2.4048.

For further data smoothing, we impose the Chauvenet criterion, exactly as described in Section 4.3, on each daily dataset with a 120-min duration since it is the maximum consecutive measurement duration of SolPol, and detect outliers to the Stokes parameters due to instrument misalignment and persisting perturbations to the measurements caused by passing low clouds.

3.4.4. Dark measurements bias correction

For the majority of the cases, bias readings (e.g., PM detector temperature-dependent offsets) provided by dark signal measurements, are interspersed between all sequences for the quantification of biases on the measured DC signal. Detailed dark tests carried out with SolPol can be found in the Dark Tests section under the Appendix a.ib of the thesis. Bias readings are not treated as regular polarization measurements but instead the dark flux is solely exploited as an absolute value. The mean dark DC flux, $I_{mean,dark}$, is one order of magnitude lower than the total intensity measurements I for the cases that it maximizes, while there are cases that it becomes less than two orders of magnitude. The days that lack such measurements are treated instead with the mean dark flux of all the days during which dark measurements were acquired. In order to acquire representative background conditions over the station, we selected a “clean day” with small non-

depolarizing aerosol concentrations and layer homogeneity, no clouds and a relatively smooth near-surface wind profile. During relatively calm sea surface conditions, specular reflection phenomena intensify and could potentially contaminate the direct-sun measurements with linearly polarized reflected light of the same magnitude as the expected dichroic extinction from the dust particles. We do not observe such a behavior with SolPol, although the observational site is in close proximity to the wavy sea surface (about 1.5 km in optical path towards the eastern direction). This can be explained as the established viewing geometry, which is confined by low elevation and rapidly increasing SZA, does not enclose Brewster angle reflections within the instrument field-of-view.

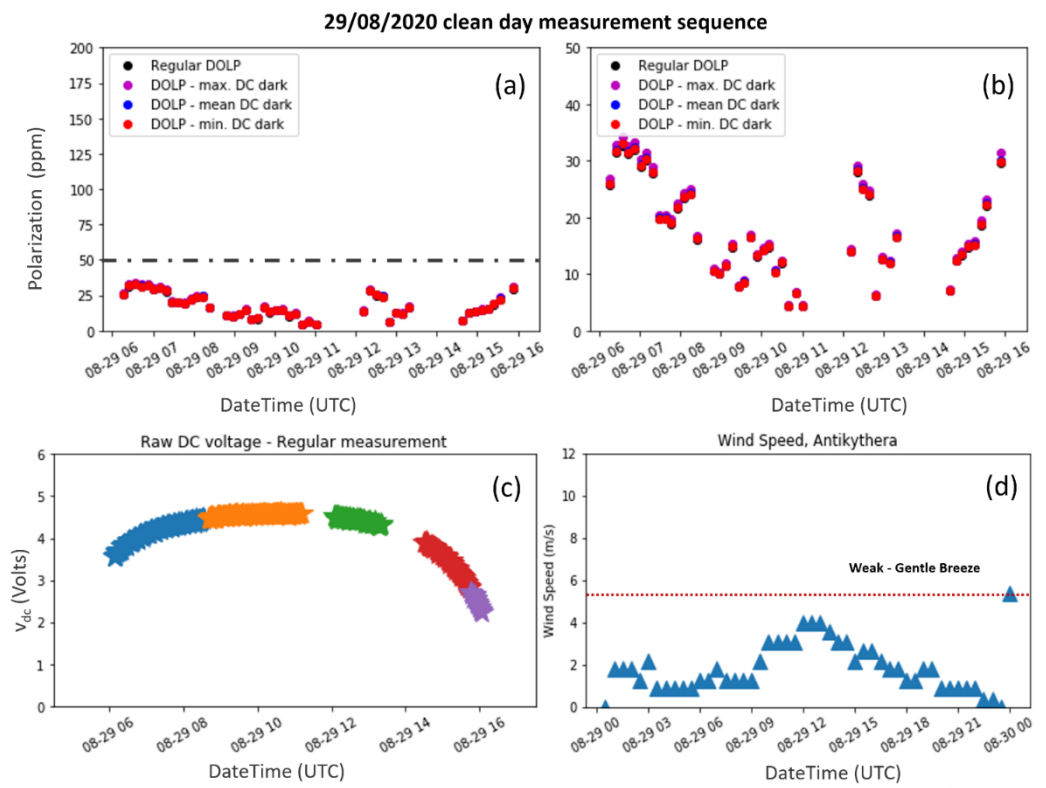

Figure 3.9: SolPol measurement on August 29th 2020, spanning from 06:00 to 16:00 UTC at the PANGEA observatory, Antikythera. The day is labelled as "clean day" due to the very low aerosol content; zero percent cloud-cover and the acquired measurements consist a "background reference measurement" for the instrument. In panels: (**a**) the Degree of Linear Polarization (DOLP) plotted in parts per million (ppm) for four different test cases: calculated without subtracting the dark DC voltage for the specific day (black dots), by subtracting the maximum value (purple dots), average (blue dots) and minimum (red dots) values of the dark DC voltage output. The dash-dotted grey line signifies the instrument noise level at 50 ppm, (**b**) a zoomed representation of (a), (**c**) the total incoming sunlight intensity, v_{dc} in Volts as recorded by the lock-in amplifier. Different colours signify the corresponding measurement subsets within the day and (**d**) the recorded wind speed in m s^{-1} for 30-minute averages on the specific day. During the SolPol measurements generally low-winds were blowing over the station.

In Figure 3.9, we examine the change in the DOLP calculations, for a specific case study, to the subtraction from I of one of the three following parameters: i. the minimum recorded dark intensity for the specific day, $I_{min,dark}$, ii. The average dark intensity, $I_{mean,dark}$ and iii. The maximum value of the recorded dark intensity, $I_{max,dark}$, as a way to constraint the sensitivity of DOLP to the dark current variability. Figure 3.9a, shows the four values derived for DOLP and their variability within the day, considering different values for the dark intensity. The measurement spans from 06:00 to 17:00 UTC and DOLP is plotted in ppm reaching maximum values of ~ 35 ppm for every case, as seen in the zoomed representation of the measurement (Figure 3.9b). The relative difference between the methods is below 0.1 %, which is considered negligible, and subsequently we keep the subtraction of $I_{mean,dark}$ for the remainder of our processing chain. The polarimeter line-of-sight is unobscured during the observing sequence, as depicted to the typical and unperturbed behaviour of the measured irradiance (Figure 3.9c). Different colours signify the corresponding measurement subsets within the day and the recorded wind speeds for 30-minute averages do not exceed 4 m s^{-1} (Figure 3.9d).

We apply the same bias correction methodology under a dust-affected case on September 2nd 2020. Figure 3.10 and Table 3.2 showcase the similarities with the clean day case and the measured dark DC fluxes. The specific day is affected by a persistent dust outbreak above the station, has zero percent cloud-cover and consists a typical dust-driven measurement for the instrument. In Figure 3.10a, the DOLP is plotted in parts per million in polarization for four test cases: calculated without subtracting the dark DC voltage for the specific day (black dots), by subtracting the maximum value (purple dots), average (blue dots) and minimum (red dots) values of the dark DC voltage output. Again, the different methods greatly converge, which is expected as the voltage outputs from the dark measurement tests (see Appendix a.ib) are between one to two orders of magnitude below the regular DC voltage.

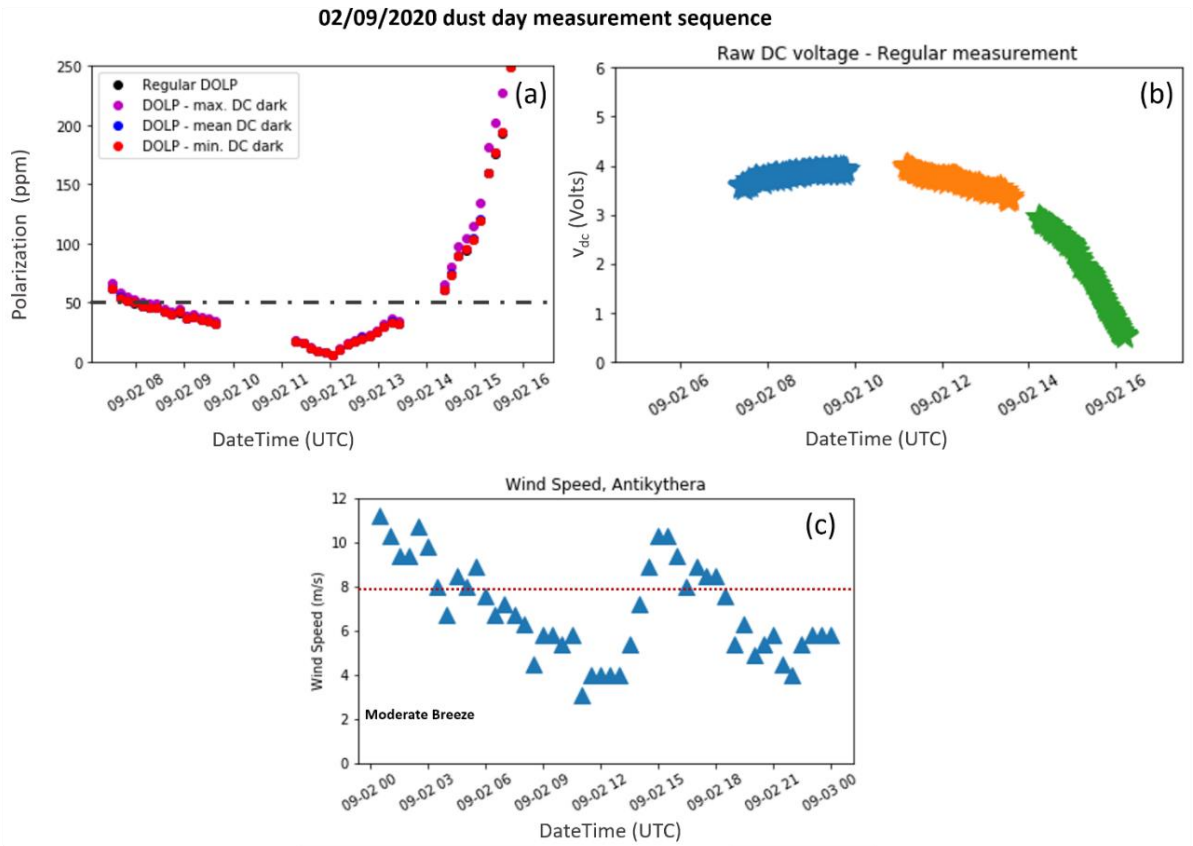

Figure 3.10: SolPol daily measurement on September 2nd 2020, spanning from 07:00 to 16:00 UTC at the PANGEA observatory, Antikythera. The specific day is affected by a persistent dust outbreak above the station, has zero percent cloud-cover and consists a typical dust-driven measurement for the instrument. In panels: (**a**) the DOLP is plotted in parts per million in polarization for four test cases: calculated without subtracting the dark DC voltage for the specific day (black dots), by subtracting the maximum value (purple dots), average (blue dots) and minimum (red dots) values of the dark DC voltage output. The dash-dotted grey line signifies the instrument noise level at 50 ppm, (**b**) the total incoming sunlight intensity, v_{dc} in Volts as recorded by the lock-in amplifier. Different colours signify the corresponding measurement subsets within the day, (**c**) the recorded wind speed in m s^{-1} for 30-minute averages for the specific day. During the SolPol measurement moderate winds were blowing over the station.

Table 3.2: Measured minimum/maximum dark DC signal intensity and the calculated average value for the selected days of bias correction demonstration.

Dark DC (Volts)	29/08/2020 (C)	02/09/2020 (D)
$I_{min,dark}$	0.03095	0.00408
$I_{mean,dark}$	0.04778	0.01148
$I_{max,dark}$	0.16665	0.24016

3.5. Field Applications of the Techniques

In the following sections, we provide an overview of the basic observational station - PANGEA where the atmospheric electricity instrumentation and SolPol were setup for the longterm monitoring of desert dust, along with the major observational campaigns that the author co-organized and participated in, which were pivotal for the quantification of the dust layers' electrical properties.

3.5.1. Systematic Observations at PANGEA

The establishment of a novel and emblematic flagship research infrastructure that traverses all three Institutes of the National Observatory of Athens (NOA) is the PANhellenic GEophysical observatory of Antikythera (PANGEA), in the remote island of Antikythera. The island covers an area of just 20.43 km^2 and is devoid of heavy human activity which makes it an ideal background observatory for the Eastern Mediterranean. The station location is carefully selected, as the island is placed at a "crossroad" of different aerosol air masses (Lelieveld et al., 2002), with NNE winds being prominent between August and February, while in spring and early summer the western airflows largely favor dust transport from the Sahara desert. The prevailing meteorological conditions are representative of the broader region with warm and dry days in the summer, while colder and wetter days are typical during the winter. It was recently, decided by NOA to provide continuous monitoring of essential climate variables, as well as the geophysical activity, and to stream real-time information to the scientific community, focusing in particular on the:

- provision of continuous certified monitoring data and expertise on issues related to climate change, atmospheric pollution and chemical composition as well as seismic activity.
- improvement of climate projections at the regional scale, for effective mitigation and adaptation.
- scientific contribution towards the increase of the share of renewable resources in the national energy program.

Early stages of PANGEA back in 2018; photo credits: *the author*

PANGEA was critically acclaimed and eventually funded by the European Investment Bank so as to address a number of societal objectives related to challenges, such as the climate change and its impact on severe weather and natural disasters in Greece and the Eastern Mediterranean, but also monitor seismic activity, especially of the southeast Mediterranean, which is poorly monitored to date but essential due to the intense tectonic activity. Essential monitoring data are already provided since 2019 to European and global research networks, like ACTRIS, and strive to expand to WMO-Global Atmospheric Watch once the complete instrumental suite is installed and operated in the station. NOA-ReACT (Remote sensing of Aerosols, Clouds and Trace gases) research entity will provide its expertise in aerosol remote sensing, specifically as it concerns the installation, calibration and continuous operation of advanced atmospheric remote sensing instrumentation. NOA-ReACT operates the NASA-AERONET Atmospheric Remote Sensing Station of Athens

since 2008, while on April 2015 ReACT developed the sophisticated Polly^{XT} lidar system in collaboration with TROPOS (Engelmann et al., 2016; Baars et al., 2016). After participating in several experiments (e.g., ACTRIS campaigns in Athens and Cyprus), NOA-ReACT installed the Polly^{XT} system at Finokalia, Crete, and operated the station for one year in 24/7 mode. In 2019, the team established the PANGEA Aerosol Remote Sensing National Facility at the island of Antikythera, the initial inspiration behind the observatory, including the Polly^{XT}, the NASA-AERONET CIMEL Sunphotometer, the SolPol Polarimeter (see Section 3.4.1), the Ultraviolet Multi-filter Radiometer and a JCI 131 Fieldmill electrometer (see Section 3.5.2), while three additional polarimetric lidars developed (ERC lidar WALL-E, ESA lidar EVE, ESA A-lidar) will also operate in PANGEA, along with the acquisition of a fully-operational actinometric station, wind and cloud radars and an upper-atmosphere balloon sounding system for the facility need. As part of NOA-ReACT and core member of the initiative, I have organized and participated to several maintenance trips to the station from its early stages, installed and operated SolPol and its housing astronomical dome, installed, operated and maintained the fieldmill for 24/7 operation and, also, installed and supervised the operation of a commercial Davis weather station.

The observatory will contribute specifically and substantially to the development of Antikythera as “the island of science” in the Eastern Mediterranean region.

3.5.2. JCI 131 Fieldmill Electrometer

In order to continuously monitor the near-ground vertical electric field, we exploit the capabilities of a ground-based commercial JCI 131 Fieldmill (FM) electrometer (Chubb, 2014; Chubb, 2015). Fieldmills are robust instruments, mostly used for lightning warning and radioactive detection applications providing, though, sufficient sensitivity for the detection of weaker electric field strengths and changes to the field polarity. Most of the literature studies referenced use commercial fieldmills with the same principle of operation, for the ground E-field measurements. The fieldmill consists of multiple sensing electrodes arranged in a circular pattern, which are typically made of metal or any conductive material evenly spaced apart. Each sensing electrode forms a capacitor with a common reference electrode located at the center of the array and measurements of the electric field at its sensing aperture provide a direct analogue to the ambient atmospheric electric field. The electric field strength at each sensing electrode's position affects the capacitance of the

corresponding capacitor and induces a charge transfer between the sensing and reference electrodes. The sensor employs an earthed rotor with fixed rotational speed to periodically modulate the DC electric field by alternately exposing and covering the electrodes to the external electric field, sampled as voltage outputs by the instrument's circuitry.

Figure 3.11: JCI 131 Fieldmill installation at the remote island of Antikythera. The instrument is powered by solar cells and two 12V batteries, while data transmission directly to the station of PANGEA is coupled with an antenna transceiver.

There are various FM designs and configurations suited for different measurement requirements simply by varying the sensing plate area, the number of electrodes, rotor sensing speed and/-or the installation height (e.g., Cui et al., 2018) and typically such an instrument is calibrated by applying a constant homogeneous E-field through a parallel capacitors calibration configuration. FMs have also being miniaturized by retaining the same principles of operation in order to be employed on aircraft monitoring platforms of in-situ cloud electrification (Mach, D. M., Koshak, W. J., 2007;

Mach et al., 2009) or to be lightweight enough for balloon-borne launches. We have newly designed a miniature fieldmill electrometer for vertical profiling studies on board meteorological radiosondes and have launched several instruments during experimental campaigns, described in detail in Section 3.5.4. For the JCI 131, the sensor is usually mounted on a 3 m aluminium mast, the exact configuration used for both station setups, and as distant as possible from physical obstacles, buildings and any metallic objects that could create distortions to the electric field. The signal output range was set to the most sensitive scale of 2.0 kV (full scale) with a sensitivity of the order of 1 V m^{-1} for 1 Hz measurement frequency and the data were acquired from a 24-bit local data-logger. Due to its portability and robustness, the fieldmill was subsequently used in two scientific campaigns, part of the ESA-ASKOS experiment, for measuring 24/7 the near-ground electric field during various meteorological conditions, dust loads and as a reference instrument during atmospheric electricity radiosonde launches (see Chapter 5).

The instrument output voltage in Volts is proportional to the ambient E-field as:

$$E_{field}\,[\mathrm{V/m}] = FM_{output}\,[\mathrm{V}] \cdot \mathrm{d}\,[\mathrm{m}] \cdot \text{ range } [\mathrm{V/m \text{ per } V}] \,/\, h\,[\mathrm{m}]$$
$$= FM_{output}\,[\mathrm{V}] \cdot 102 \cdot (1\mathrm{e}\text{-}6) \cdot (1\mathrm{e}4) \,/\, 2.7$$

where d is the sensing head effective diameter, we are operating it at the 200 kV/m per 2 V max output sensitivity range and at a clear instrument height from electrode to ground of: h = 2.7 m (JCI131 Electrostatic Fieldmeter instrument manual, pg. 7). To this point, we should note that, fieldmills pose the inherent problem of detecting parasitic fields with transient behavior due to the colliding charged particles to the instrument rotating vanes and which could eventually impact their accuracy. We attempt to dissipate that by post-processing and targeting detached elevated dust layers with little -to-no ground concentrations.

Most literature documents when referring to ground based atmospheric electricity measurements, define the potential gradient (PG, $\vec{\nabla}V = PG$) as the dominant measured quantity with various conventions regarding its sign. The vector electric field is defined as $\vec{E} = -\vec{\nabla}V - \frac{\partial \vec{A}}{\partial t}$, where $\vec{E}$ is the electric field vector, V is the scalar potential, and $\vec{A}$ is the magnetic vector potential. In the special case that the electric field is irrotational ($\vec{\nabla} \times \vec{E} = 0$) which happens when the electric and magnetic fields are decoupled, we can write that $\vec{E} = -\vec{\nabla}V = -PG$, and PG is pointing in the

opposite direction. Positive and negative directions can be chosen at will and regarding the application. Moreover, the PG is by definition a 3D vector as $PG = \frac{\partial V}{\partial x}\hat{x} + \frac{\partial V}{\partial y}\hat{y} + \frac{\partial V}{\partial z}\hat{z}$, under the special case where the horizontal variability of the electric field is symmetric and much less than the vertical direction, then it has only the vertical component as $PG = \frac{\partial V}{\partial z}$. In the presence of particle concentrations such as water droplets within clouds and dust particles within dust layers, there will be strong radial components of the E-field especially at the boundary of the collections, as a consequence of the current continuity (Baumgaertner et al., 2014). Therefore, the 1D simplification might be misleading in the PG terminology especially when the instrument is affected by edge effects from the transient layers.

3.5.2.1. Fieldmill Installation at Finokalia and PANGEA

The first atmospheric monitoring station is situated in the remote location of Finokalia (35.338° N, 25.670° E) on the north eastern coast of Crete, which the main station of the PANACEA Research Infrastructure (RI), with the nearest large urban center being the city of Heraklion located 70 km to the west. The station is located at the top of a hill (252 m asl) facing the sea within a sector of 270° to 90° and the climatic characteristics are typical of the eastern Mediterranean basin exhibiting two distinctive seasons, the dry season (April to September) characterized by increased levels of pollution and biomass burning and the wet season (October to April). Significant Saharan dust transport occurs when S/SW winds are prevalent during the intermediate season of March till June and may lead to ground concentrations exceeding 1 mg m^{-3} (Solomos et al., 2018). Since there is no significant human activity occurring at a distance shorter than 15 km within the above sector, it makes it an appropriate location for monitoring dust layers advected directly from the Sahara. The fieldmill operated in Crete from April 2017 until May 2018, for a total of 382 days, but was placed on the edge of a hilly elevation which added a topography factor, not quantified in the specific research due to the lack of typical flat ground measurements in the area.

The instrument was then re-located to PANGEA (Figure 3.11) in Antikythera (35.861° N, 23.310° E, 193 m asl) where it remained operational until March 2022, for a total of 847 days. The island covers an area of just 20.43 km^2, 38 km south-east of the larger island of Kythera and is devoid of human activity as its inhabitants are at most twenty people during early fall to mid-summer. The station location is ideal as the island is placed at a crossroad of air masses (Lelieveld

et al., 2002), with NNE winds being prominent between August and February, while in spring and early summer western airflows that favor dust transport are observed. Moreover, the prevailing meteorological conditions on the island are again representative of the eastern Mediterranean with warm and dry days in summer in contrast to winter, when the days are colder and wetter days are typical. At PANGEA, the installation location was carefully selected to avoid orography, obstacles and power grid lines in the instrument's proximity. FM was completely autonomous since it was powered by solar cells and two 12V batteries, while data transmission directly to the station was coupled with an antenna transceiver.

3.5.3. SolPol Installation at PANGEA

SolPol has been primarily installed at the PANGEA observatory since September 2018. Weather limitations and increased salinity due to the coastal site effect, led to housing the SolPol in a specifically built motorized 3M astronomical dome (Scope Dome) that offered protection from various extreme weather conditions, could be autonomous and operate in sync with the instrument tracking. For that purpose, we built a custom steel base where we mounted an EQ3 SynScan tracker and then plug SolPol for on-demand direct sun observations. During the overall period of operation in PANGEA, we conducted multiple test measurements with the new instrument setup to configure the best possible sequence and achieve accurate polarization measurements. We, also, determined the atmospheric conditions under which SolPol's detection limits were strained and characterized the individual steps for the instrument's basic principle of operation.

The datasets presented for the specific study were acquired from May 2020 to June 2021, under various atmospheric conditions and aerosol loads, specifically targeting days with dust outbreaks but also days that are representative of the local background conditions. Even a small cloud coverage can highly influence the transmitted light polarization state on optical wavelengths due to multiple scattering from cloud droplets or due to dichroic extinction from aligned ice crystals, in the case of cirrus clouds, that can lead to polarization effects in the forward direction (Baran, 2004; Bohren, 1987; Emde et al., 2004; Ulanowski et al., 2006). Accordingly, the affected SolPol measurements are screened and in cases of prolonged transient clouds over the station the instrument was shut down. All the measurements are always direct sun.

3.5.4. The ASKOS Cal/Val experiment

The European Space Agency (ESA) and the National Aeronautics and Space Administration (NASA) organized the Joint Aeolus Tropical Atlantic Campaign (JATAC) in the tropical islands of Cabo Verde from July to September 2021, with the main aim being to provide quality-assured reference measurements to validate the ongoing products of the ESA Aeolus satellite mission and the preparation of the forthcoming EarthCARE mission (Marinou et al., 2023). ASKOS is the ground-based component of JATAC that was held in Mindelo on the island of Sao Vicente in Cabo Verde, where high quality ground-based wind, aerosol and cloud observations were collected using advanced instrumentation aiming to provide reference values for the Aeolus calibration and validation (Cal/Val) efforts (https://askos.space.noa.gr/).

3.5.4.1. Mission and Objectives

The ASKOS campaign was implemented in two official phases, the first phase was during the July and September 2021 operations of the JATAC campaign, while the second phase a year later in June and September 2022. A preparative phase was implemented in the Cyprus Institute in Nicosia, Cyprus, during November 2019 (pre-ASKOS). The main focus of ASKOS was to perform ground-based observations with instruments dedicated to characterize aerosols and clouds, including aerosol lidars, ceilometers, photometers, microwave radiometers, cloud radars, and electrometers. The experimental suite was also complemented by UAV in-situ observations and dedicated meteorological radiosonde observations. In addition, aerosol modelling support for forecasting during the campaign and the analysis of the data acquired in the frame of the campaign was an essential part of the implementations.

The objectives of the experiment can be summarized in the:

1. acquisition of aerosol and cloud data from active and passive ground-based systems, including correlative observations with Aeolus overpasses and airborne observations.
2. analysis of preliminary data quality during the campaign.

3. processing and scientifical analysis of the observations with respect to the Aeolus mission Validation requirements.
4. preparation and provision of the data for the in-depth analysis in the frame of the Aeolus Data, Innovation, and Science Cluster.
5. evaluation of the Aeolus L2A aerosol and cloud product performance for dust/marine aerosols.
6. estimation of the uncertainty in the Aeolus backscatter caused by the undetected cross-polar signal return from non-spherical particles.
7. estimation of the impact of particle orientation in Aeolus products for mineral particles and ice crystals.
8. determination of the size specific aerosol optical properties: scattering, backscattering, absorption, SSA, extinction.
9. provision of an unprecedented amount of quality assured datasets for evaluating more Aeolus applications (e.g., improvements in desert dust modeling, sea salt emission estimations and radiative forcing of dust/marine aerosols).
10. study of the ice nucleation due to dust particles and validate the existing parameterizations.
11. evaluation of the Aeolus wind measurements with those by aircraft and radiosonde.
12. study of the impact of Aeolus winds on the analysis and forecast of tropical wave disturbances and their associated rainfall and dust fields.

3.5.4.2. Site of Operations

The site of operations during ASKOS was the Ocean Science Center of Mindelo (OSCM) on the island of Sao Vicente in Cabo Verde (Figure 3.12). OSCM has been operating in Mindelo since 2017, providing a multifunctional basis for long-term ocean observation and field research in the tropical Northeast Atlantic region. The islands of Cabo Verde are located in an ideal position in the Tropics for studying circulation patterns, atmospheric dynamics, as well as impacts on precipitation and desert dust. The generally high dust loads in this region are a prerequisite to provide good quality backscatter signals for the lidar. During boreal summer, the midlevel African easterly jet (AEJ) is located near Cabo Verde and allows for the formation of synoptic-scale African easterly waves (AEWs) through baroclinic-barotropic instability. AEW disturbances typically reach their

maximum intensity close to the coast of West Africa. The Cabo Verde environment is ideal for aerosol studies and desert dust specifically. Situated downwind of the Sahara Desert, Cabo Verde receives a large influx of dust, particularly in summer during the peak of the dust season. Mindelo is located at the north part of Sao Vicente Island. The surrounding topography includes a series of mountains in Sao Vicente not exceeding the 600 m east and south of Mindelo, while higher mountains (~ 1400 m) are present at the neighbouring island of Santo Antao at about 25 km north of Mindelo. Thus, possible channelling, downslope accelerations and wind gusts near the surface could be expected especially for north winds.

Figure 3.12: **Top panel:** the OSCM facilities in Mindelo, Cabo Verde. **Bottom panel:** re-installation of JCI 131 fieldmill electrometer (left), the SolPol (middle) and the GRAW ground-station antenna at the rooftop of OSCM close to the rest of the remote sensing suite of ASKOS.

At the rooftop of OSCM, an aerosol and cloud remote sensing facility of the Aerosol, Clouds, and Trace Gases Research Infrastructure (ACTRIS) was set up in June 2021. The instrumentation included a multiwavelength Raman-polarization lidar (Polly^{XT}), an AERONET sun-photometer, a Scanning Doppler wind lidar (HALO), a microwave radiometer and a cloud radar belonging to ESA fiducial reference network (FRM4Radar). Next to these aerosol, cloud, and wind remote sensing facilities, ESA's novel ground reference lidar system eVe, a combined linear/circular polarization lidar system with Raman capabilities, was deployed which can mimic the observations of the space-borne lidar ALADIN onboard Aeolus. An actinometric platform and a net radiation instrument have been installed on the site as well, providing in-situ broadband total, direct and diffuse solar radiation and incoming - outgoing radiation measurements respectively. In June 2022 more instruments were set up focusing on desert dust dynamics: the polarization lidar WALL-E, providing measurements of particle orientation, was used to monitor the possibility of dust orientation in the atmosphere, along with the SolPol solar polarimeter, which also provided dust particle orientation measurements. The latter was operated for only three days in total during the ASKOS period due to overcast conditions and general instrument malfunctions. GRAW meteorological radiosondes equipment (antenna, ground station, balloon fillings) were also installed at the OSCM premises and were used for a total of 23 launches with DFM-09 meteorological radiosondes on dedicated periods for the PBL characterization. To complement the above measurements, vertical profiling of the dust layer electrical activity was conducted with tethered atmospheric electricity sensors on board the meteorological radiosondes (nominally called Electrosondes), total of 28 launches, during the June/September 2022 ASKOS phases. The prototype sensors were designed and assembled in NOA and measured the electric field strength and space charge density within the layer, respectively. In parallel, the ground-based JCI 131 fieldmill was also re-located to the rooftop of OSCM, so as to minimize human and electrical interference to the instrument. The fieldmill was operational during the aforementioned period 24/7 providing the near surface electric field strength and used as a reference instrument during the Electrosonde launches.

Chapter 4

Longterm Dust Electrification measurements based on Ground-based methods[4]

In this chapter, we focus on monitoring perturbations of the E-field near the ground caused by the transported dust layers, with special emphasis on slow E-field perturbations (with duration larger than 6 hours to exclude phenomena with small timescales or local effects of random origin), and we attempt to classify and comment on the electrical activity of the dust layers. As electrically active, we define the layers that exhibit charge separation and behave as electrostatic generators in the GEC, similarly to electrified shower clouds and thunderstorms (e.g. Mallios and Pasko, 2012). Conversely, electrically neutral are assumed to be the layers with no charge separation which, therefore, act as passive elements in the GEC, similarly to the non-electrified shower clouds (e.g. Baumgaertner et al., 2014). Four selected cases of Saharan dust plumes are examined, as captured over Finokalia, Crete and PANGEA, Antikythera atmospheric observatories by the same ground-based electrometer, as well as through the particle backscatter properties by the sophisticated Polly^{XT} lidar system. The field mill timeseries are processed to extract the diurnal variations of the GEC and to remove fast field perturbations due to peak lightning activity.

In order to identify the influence of the elevated dust layers on the ground E_z, we extract a Localized Reference Electric Field (LREF) from the timeseries that reflects the local fair weather

[4] **This chapter is based on my contribution in:**

Daskalopoulou, V., Mallios, S. A., Ulanowski, Z., Hloupis, G., Gialitaki, A., Tsikoudi, I., Tassis, K. and Amiridis, V.: *The electrical activity of Saharan dust as perceived from surface electric field observations,* Atmos. Chem. Phys., 21(2), 927–949, doi:10.5194/acp-21-927-2021, 2021a.

activity. Then, we compare it with the reconstructed daily average behaviour of the electric field and the Saharan dust layers' evolution, as depicted by the lidar. The observed enhancement of the vertical electric field (up to ~ 100 V m^{-1}), for detached pure dust layers, suggests the presence of in-layer electric charges. Although higher dust loads are expected to result in such a field enhancement, episodic cases that reduce the electric field are also observed (up to ~ 60 V m^{-1}). To quantitatively approach our results, we examine the dependency of E_z against theoretical assumptions for the distribution of separated charges within the electrified dust layer. Electrically neutral dust is approximated by atmospheric conductivity reduction, while charge separation areas within electrically active dust layers are approximated as finite extent cylinders. This physical approximation constitutes a more realistic description of the distribution of charges, as opposed to infinite extent geometries, and allows for analytical solutions of the electric field strength, so that the observed variations during the monitored dust outbreaks can be explained.

4.1. Data acquisition and Methodology

By firstly processing the Finokalia dataset, we extract the daily diurnal variation of the PG (for this case the downward looking electric field is considered negative, thus the PG positive), we calculate the mean PG and simultaneously compare with the Carnegie curve data acquired via the geophysical survey vessel of the Carnegie Institution of Washington provided in the Harrison et al. (2013) publication (Figure 4.1). The Finokalia curve exhibits a similar behavior to the global variation of the electric field, with low fields present in the first morning hours (in UT time) and the field peaks at around 1300 UT, while there is a lack of the night enhancement as compared to the Carnegie curve with a small double-peak present between 1900 to 2300 UT. The specific behavior could be due to the increasing human activity, prolonged vehicle emissions and frequent anthropogenic dust emissions from construction works from the nearby city of Heraklion, that decrease the atmospheric conductivity and therefore the electric field strength. We have also marked in a red circle the increasing E-field trend that is attributed to the documented sunrise effect that seems to not be masked by electrode layer effects (charge separation due to vertical downward movement of positive charges) in the lower stratosphere and potentially co-exist with temperature

and humidity variations at the specific time-period within the day (Muir, 1977; Raina and Makhdomi, 1980).

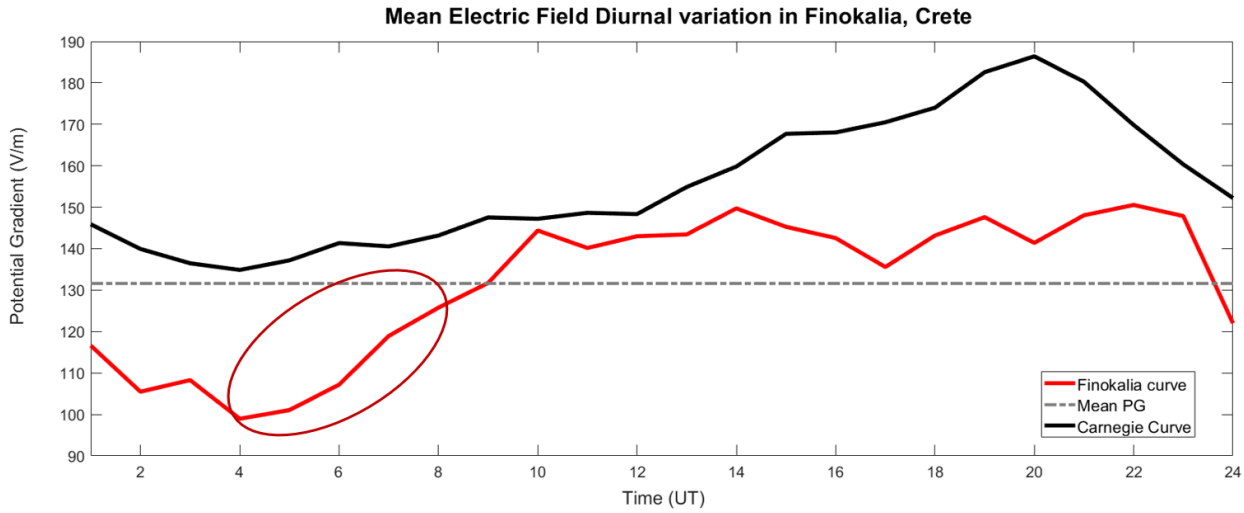

Figure 4.1: Timeseries of the Potential Gradient (PG) recorded from the station of Finokalia for a total duration of one year (red solid line), overplotted with the Carnegie curve (black solid line) and the mean PG value (gray dash dotted line). Red circle denotes the sunrise effect enhancement.

We have also attempted to create a preliminary flag that would recognize fair weather days, primarily from the Finokalia dataset and would later be expanded to the Antikythera timeseries, through the use of AOD measurements from the co-located CIMEL sunphotometer (see Section 4.2.2). The criteria for the simplistic flag consisted of: i. PG measurements constrained by AOD values lower than 0.1 at 550 nm, which indicates a low aerosol content in the atmosphere and that at least ten such measurements would exist from AERONET per day and ii. the PG values should not exceed a nominal value of 350 V m^{-1} (twice the mean PG) in order to eliminate perturbations due to strong winds, convective clouds and thermally driven sea breeze circulations that could enhance the fair weather electric field (Nicoll et al., 2020). From the described process a total of 43 fair weather days were identified. Figure 4.2 shows the change on the Finokalia timeseries diurnal variation when filtering for various AOD values from very low aerosol content (AOD 0.05 at 550 nm) to the distinction of medium loads where dust particles become present in the atmospheric column (AOD 0.1) to very large loads which are somewhat sparse over the station of Finokalia (AOD 0.5 to 1). It becomes apparent that the PG curve becomes slightly pushed towards smaller values with the increasing optical depth as particle concentrations increase within the atmospheric

column and the columnar resistance increases. But in order to have a more statistically and physically representative extraction procedure for our fair weather days, we will investigate a new reference field derived only from signal processing methods irrespective of the station /- instrument installation properties (see Section 4.3).

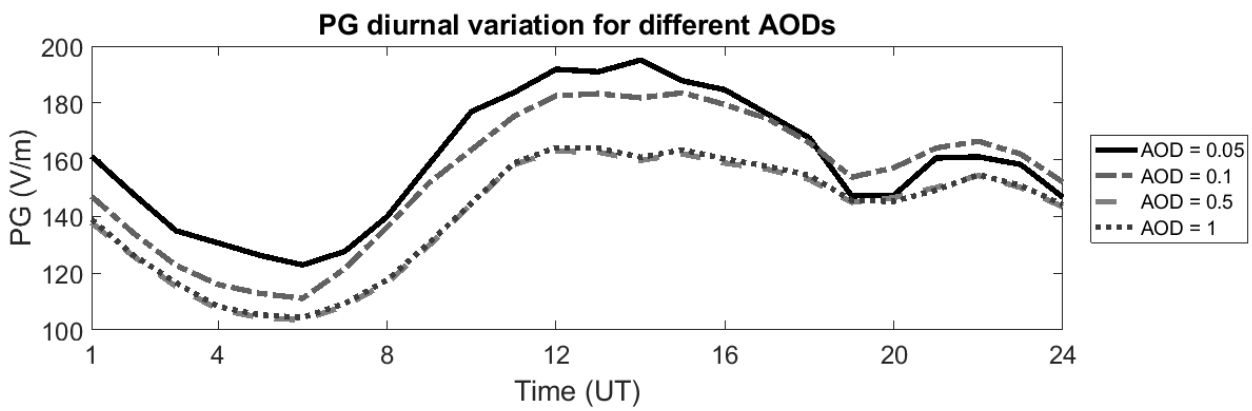

Figure 4.2: PG diurnal variation curves according to different AOD values for the days under measurement.

In order to interpret the field mill measurements, it is essential to compare the data with a reference field representative of the local fair weather conditions. For the scope of this thesis, we examine the entire Finokalia dataset and the Antikythera timeseries that span from June 2018 to June 2019 (243 days), for E-fields on instrument mast height and specifically target prominent transport of dust particles over the two observational sites. We analyse a total of four Saharan dust outbreaks, on the 25th of July 2017 and March 16th 2018 in Finokalia, October 20th 2018 and June 23rd 2019 in Antikythera, which were selected due to the presence of elevated detached dust layers in the co-located lidar profiles.

4.2. Aerosol monitoring and Characterization

4.2.1. Lidar measurements

For the comprehensive characterization of dust particle optical properties, we exploit the profiling capabilities of the Polly^{XT} Raman polarization lidar (Engelmann et al., 2016) of the National

Observatory of Athens (NOA), as part of the European Aerosol Research Lidar Network (EARLINET). This multi-wavelength system is equipped with three elastic channels at 355, 532 and 1064 nm, two vibrational Raman channels at 387 and 607 nm, two channels for the detection of the cross-polarized backscattered signal at 355 and 532 nm, and one water vapour channel at 407 nm. The system employs two detectors, a near-field and a far-field telescope provide reliable aerosol optical property profiles from close to the ground to the upper troposphere. The basic lidar quantities used for the monitoring and characterization of dust loads in our study, are the total attenuated backscatter coefficient (Mm^{-1} sr^{-1}) at 532 nm (calibrated range-corrected signal) to account for particle concentrations and the Volume Linear Depolarization Ratio (VLDR, δ_v) at 532 nm. VLDR (%) is the ratio of the cross–polarized to the co-polarized backscattered signal (Freudenthaler et al., 2009), where cross- and co- are defined with respect to the plane of polarization of the emitted laser pulses. It encloses the influence of both atmospheric particles and molecules, with high δ_v values being indicative of irregular particles (i.e., atmospheric dust). However, for a comprehensive aerosol characterization, the particle backscatter coefficient (β) and Particle Linear Depolarization Ratio (PLDR, δ_p) are needed. PLDR (%) is derived from VLDR by correcting for molecular depolarization with atmospheric parameters extracted from radiosonde measurements (i.e., atmospheric pressure and temperature). In the selected case studies, we also present the δ_p and β profiles, as derived in the timeframe when each dust episode was fully developed (averaged between 18:00 and 21:00 UTC for all dust cases). Typical δ_p values for Saharan dust are in the range of 25 % to 35 % at 532 nm, while large β values are representative of substantial particle concentrations (Haarig et al., 2017; Veselovskii et al., 2016, 2020).

4.2.2. Ancillary aerosol and trajectory information

The Aerosol Optical Depth (AOD) was monitored by a CIMEL sunphotometer, part of the Aerosol Robotic Network (AERONET - https://aeronet.gsfc.nasa.gov/), which was co-located with the lidar on both stations. For the cases examined here, the AOD varied from 0.221 to 0.366 at 500 nm. To characterize the air masses in regard to their origin we use the NOAA HYSPLIT back trajectory model, driven by GDAS meteorological data (https://www.ready.noaa.gov/HYSPLIT.php). The arrival heights for dust over the observational sites were selected in HYSPLIT according to the prevailing layering depicted by our lidar measurements (Figure 4.3).

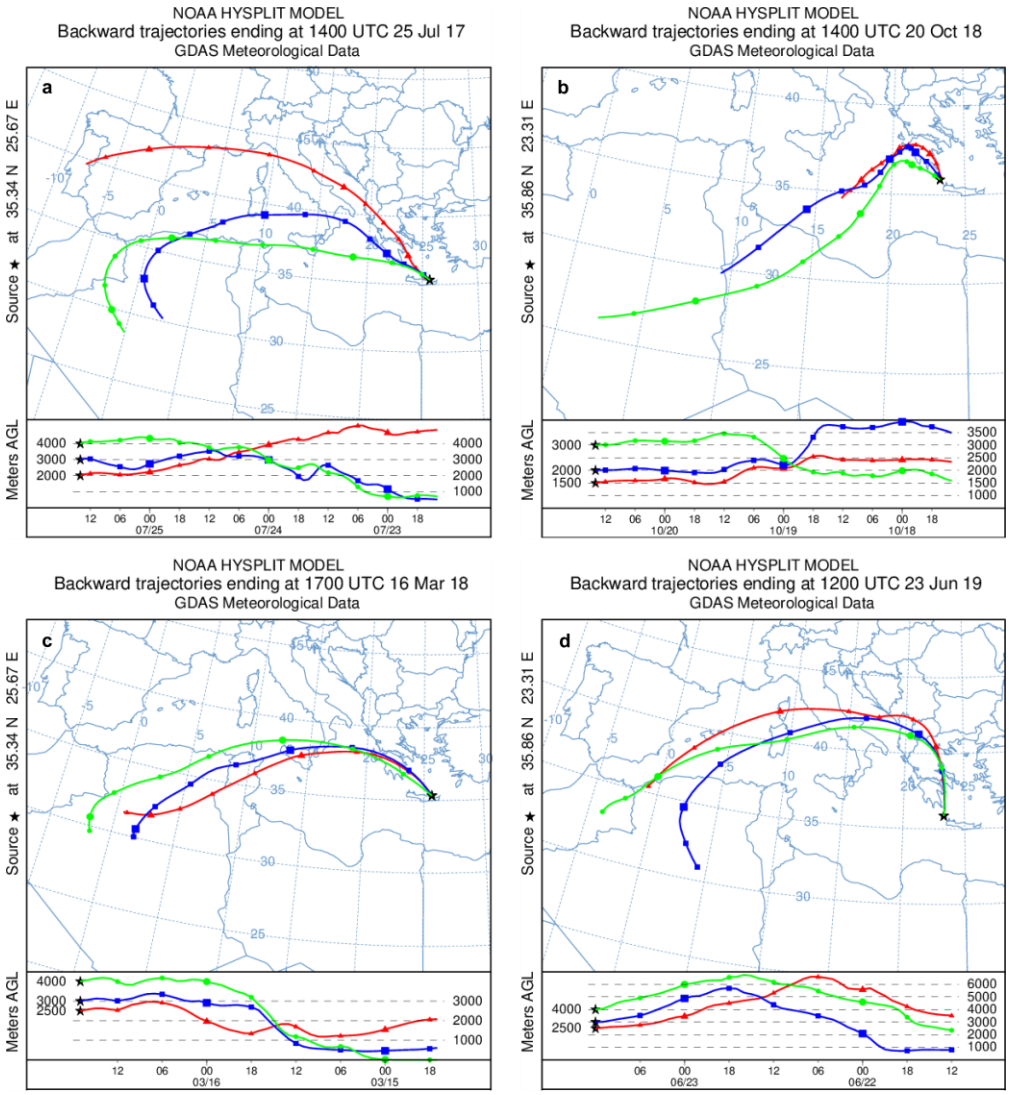

Figure 4.3: NOAA HYSPLIT backward-trajectory model with GDAS assimilated data input for (**a**) 25 July 2017 with 72 h backward propagation of air masses towards Finokalia, (**b**) 20 October 2018 with 72 h backward propagation of air masses towards Antikythera, (**c**) 16 March 2018 with 48 h backward propagation of air masses towards Finokalia and (**d**) 23 June 2019 with 48 h backward propagation of air masses towards Antikythera (https://www.ready.noaa.gov/HYSPLIT.php, 3 July 2020). Please note that some dates in the figure are given in the format of month day.

4.3. Localized Reference Electric Field (LREF)

The classification of the vertical electric field behaviour under dust influenced conditions, as that of an enhanced, reduced or reversed E-field, necessitates comparison with the local long-term fair weather electric field (Daskalopoulou et al., 2021b). In order to represent solely the diurnal GEC influence at each observational site, away from electric generators perturbing the near ground E-field (e.g., Zhou and Tinsley, 2007), we construct a Localized Reference Electric Field (LREF) by exploiting only the timeseries inherent attributes and the measuring quantity itself, through the processing chain described below (Figure 4.4). Various authors have presented different methodologies for determining fair weather conditions (e.g., Anisimov et al., 2014). For the specific study, the selected constraints of fair weather are based on the classification of fair weather days as the less electrically disturbed days, also assumed by the Carnegie Institute researchers (Harrison, 2013). Although, local effects on the E-field at each site can be of random nature (wind gusts, lightning strikes, radon emission and turbulent flows due to orography), the selection of fair weather data can be based on noise reduction by subtracting values which are clearly dominated by local influences and not directly addressing the meteorological criteria of fair weather (Harrison and Nicoll, 2018).

As such, the FM data are pre-processed by applying the appropriate scaling factor for the 3 m mounting mast of the electrometer (Chubb, 2015) and then days with no missing values due to either instrument malfunction, power outages or pc communication failures, are selected (Filter no. 1). Under local fair weather conditions, the E-field, as measured here, is positive therefore imposing the second filtering step with a non-negativity constraint (Filter no. 2). When representing the E-field diurnal variation by the Carnegie Curve, which is used consistently as a reference against locally measured atmospheric electricity parameters, the hourly variations of the field that shape the curve correspond to the 24, 12, 8, and 6-hour durations, as deduced from previous consistent observations of the Carnegie vessel (Harrison, 2013). In the specific study, we attempt to derive the local harmonic fit in the form of the LREF, based on the Carnegie curve morphology, and assuming that this trend should be followed by the reference field as well.

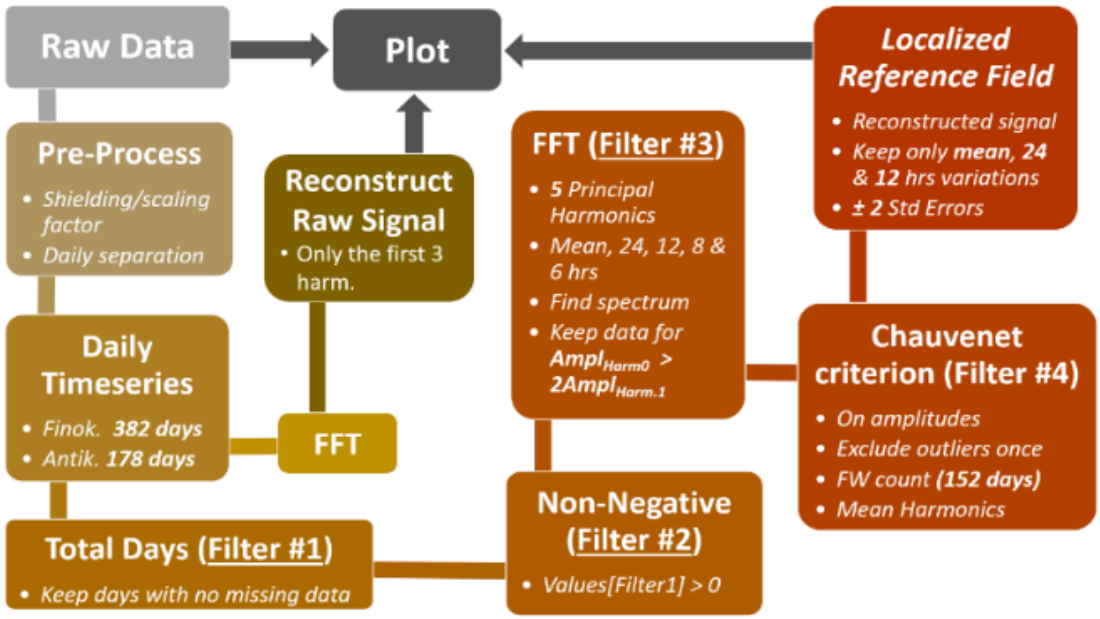

Figure 4.4: Signal processing chain for: (i) the derivation of the Localized Reference Electric Field (LREF) that represents the local fair weather (FW) conditions following the proposed filtering process (filters no. 1 to no. 4, yellow to orange) of the field mill electric field data and (ii) the derivation of the daily mean electric field under dust-driven days from the same dataset (yellow to olive green). The LREF is compared to the mean electric field values in order to assess the electric field behavior. Ampl: amplitude; harm.: harmonic

Consequently, the averaged 1s data to 1-minute data (datalogger configuration) are shifted to the frequency domain through a Fast Fourier Transform (FFT) representation so as to evaluate the relative contributions of the first five principal harmonics to the diurnal cycle of the electric field (hourly variations including daily mean), which are depicted in the following signal equation for $S(t)$ (4.1). We note, that days with missing data are removed, because the uneven temporal distribution of the measurements modifies the time window for the FFT algorithm, and therefore, modifies the timeseries spectrum.

$$S(t) = A_0 + A_1 \cos(2\pi f_1 + \varphi_1) + A_2 \cos(2\pi f_2 + \varphi_2) + A_3 \cos(2\pi f_3 + \varphi_3) + A_4 \cos(2\pi f_4 + \varphi_4)\,, \tag{4.1}$$

where S is the electric field at time t in hrs (UTC), A_i for $i = 0,..4$ with A_0 representing the mean value (constant, zeroth harmonic) and A_1 to A_4 (first to fourth harmonic) represent the amplitudes of the 24, 12, 8, and 6-hour variations, $f_i = i\frac{t}{24}360°$ is the frequency of each harmonic, where $f_0 = 0$ and φ_i are the respective phases in degrees, with $\varphi_0 = 0$ (Harrison, 2013). Based on the form of

the Carnegie curve, and assuming that this trend should be followed by LREF, we find empirically that the ratio between the zeroth harmonic and the first harmonic is around two. Therefore, the E_z values for which the amplitude A_0 is larger than two times the amplitude A_1 are kept (Filter no. 3). The same filter is applied to the other harmonics as well (A_0 is larger than two times the A_i), making sure that no fast-transient contribution is kept.

Lastly, since the amplitude of each harmonic is expected to be constant for all days (as the amplitudes in the Carnegie curve do), we impose the Chauvenet criterion on each of the filtered five harmonics amplitude, so as to detect outliers. The criterion is imposed once with the use of the relation below:

$$N\, erfc\left(\frac{d^j}{\sqrt{2}s}\right) < \frac{1}{2}, \tag{4.2}$$

where:

$d^j = \left|A_i{}^j - \bar{A}_i\right|$, is the deviation for $i = 0,..4$ referring to the ith harmonic, $j = 0,..N$ the day number and N the total number of days, for:

$\bar{A}_i = \frac{1}{N}\sum_{j=1}^{N} A_i{}^j$, where A_{ij} is the ith harmonic amplitude per day and summated over j gives $\bar{A}_i$ as the mean amplitude of each harmonic.

Lastly, s is the unbiased sample variance and is defined as:

$$s^2 = \frac{\sum_{j=1}^{N}\left(A_i{}^j - \bar{A}_i\right)^2}{N-1},$$

within erfc(x) which is the complementary error function, defined as:

$$erfc(x) = 1 - erf(x) = 1 - \frac{2}{\sqrt{\pi}}\int_0^x e^{-t^2}dt.$$

In order to compare LREF with the daily variation of the electric field during the dust events, the acquired field mill measurements are also shifted to the frequency domain through an FFT. Again, the first five harmonics are retained and from the specific dataset, a smoothed slow varying field is reconstructed, otherwise referred to as reconstructed mean, from the set of mean amplitudes and phases of the first three harmonics. This filtered field retains the main characteristics of the local reference field, since fast transient events which are less than 6 hrs in duration are removed. Therefore, the LREF and reconstructed mean field signals can be compared since they have the

same spectral information. Moreover, to later compare the E-field timeseries with the optical properties of dust particles through lidar retrievals, the field mill data need to be averaged to the same timestep as the lidar products (for the lidar system used in this study an averaging to 5 mins is required).

4.3.1. Chauvenet criterion validity

In the previous section, we described the processing chain for the determination of the local fair weather days considering a complete potential gradient dataset. The novelty of the approach lies to the fact that only signal processing constraints are used, without incorporating criteria of local meteorological parameters that could redefine the initial conditions for the total fair weather days determination (Harrison and Nicoll, 2018). Nonetheless, threshold values concerning these factors are subjective, and may vary from study to study, which leads to differences in the extracted fair weather days. The specific study proposes a mathematically strict approach with the imposition of the Chauvenet criterion, which exploits only the ground fieldmill data and has a physical impact on the dataset. Under fair weather days, the mean electric field is approximately constant and the dust driven days (about 10 % of the days within a typical year for Eastern Mediterranean stations) will not influence significantly the reconstructed mean field value, but will be well beyond the standard deviation. The Chauvenet criterion excludes the days with such high variations as outliers and, therefore, the methodology for the reconstruction of the local reference field is less biased to variations occurring in dust driven days.

4.4. Influence of the Dust Layer to the Ground E-field

4.4.1. Cylindrical Model formalism

In the steady state of such an atmosphere, the divergence of the total current is zero $\vec{\nabla}\vec{J}_{tot} = 0$, as a direct consequence of the continuity equation and hence the conduction current remains constant with altitude. From Ohm's law, we can relate the conduction current, J_z, with the vertical component of the electric field, E_z (Figure 4.5a), as:

$$J_z = \sigma E_z \ , \tag{4.3}$$

where σ is the atmospheric conductivity and assume a smooth conductivity profile along the altitude z, as:

$$\sigma = \sigma_0 \ exp\left(\frac{z}{l}\right), \tag{4.4}$$

for σ_0 and l the constants that represent the near ground atmospheric conductivity and the atmospheric scale height, respectively. The given mathematical formalism of the atmospheric conductivity is adopted also by Ilin et al. (2020). The authors demonstrated that such a profile adequately describes the main aspects of the real conductivity distribution, and can be seen as a global mean conductivity profile.

We, then, express the conduction current at ground level, J_{z_0}, as a function of the columnar resistance R_c and the potential difference $\Delta V = V_{ion} - V_0$ (4.5), therefore:

$$J_{z_0} = \frac{\Delta V}{R_c} = \frac{V_{ion}}{R_c}, \tag{4.5}$$

where V_{ion} is the ionospheric potential at the altitude H, and V_0 is the potential at the Earth's surface which is considered a good conductor due to soil particles that are usually covered by a thin, conducting film of water (Kanagy and Mann, 1994), hence V_0 is set equal to zero.

The columnar resistance can be calculated from the conductivity profile of equation (4.4) (Rycroft et al., 2008), hence:

$$R_c = \int_0^H \frac{dz}{\sigma} = \frac{l}{\sigma_0}\left(1 - exp\left(-\frac{H}{l}\right)\right), \tag{4.6}$$

By combining equations (4.3), (4.5) and (4.6), the fair-weather electric field at ground level, E_{z_0}, is of the form (Gringel et al. 1986):

$$E_{z_0} = \frac{V_{ion}}{\sigma_0 R_c} = \frac{V_{ion}}{l\left(1-exp\left(-\frac{H}{l}\right)\right)}, \tag{4.7}$$

which depends solely on the scale height l and the ionospheric potential V_{ion}.

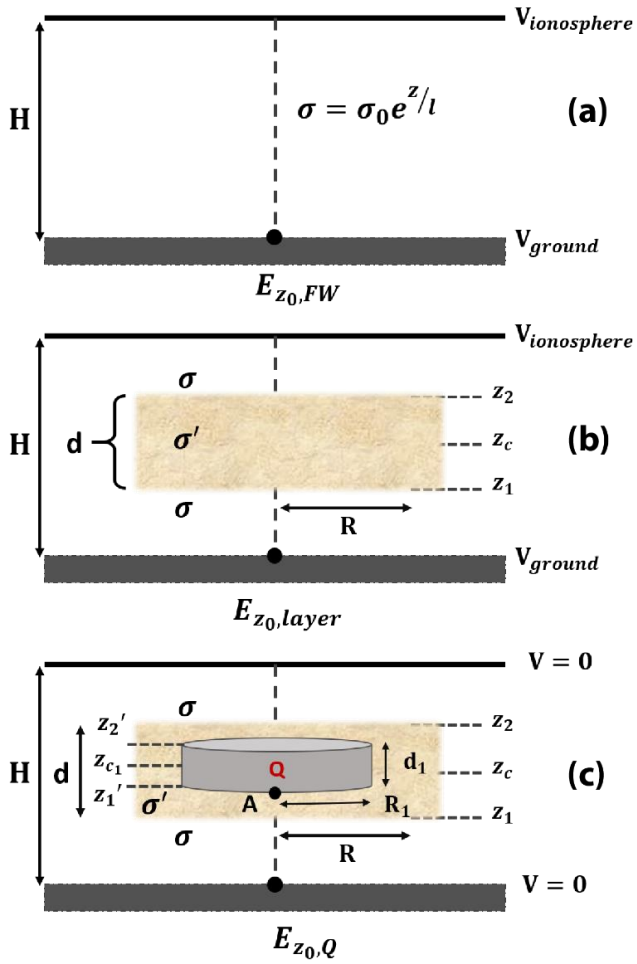

Figure 4.5: Schematic of the formalism for the calculation of the steady state near-ground electric field bounded between the ground potential (V_{ground}) and ionospheric potential ($V_{\text{ionosphere}}$) at height H, under: (**a**) fair weather conditions ($E_{z_{0,\text{FW}}}$) where atmospheric conductivity σ, follows an exponential distribution along the altitude z with respect to the scaling height l, (**b**) the presence of an electrically neutral dust layer ($E_{z_{0,\text{layer}}}$) with depth d and radius R, which modifies conductivity to σ' and (**c**) the hypothesis of a cylindrical charged monopole ($E_{z_{0,Q}}$) within the dust layer, with depth d_1, radius R_1 and total charge Q. The monopole case is a superposition of the electrically neutral dust layer with the charged cylinder within the bounded atmospheric potential.

The case of a steady state atmospheric desert dust layer that does not exhibit charge stratification is examined below. The layer acts as a passive electrical element (resistor), and reduces the fair weather atmospheric conductivity due to the ion attachment to dust particles, by a varying reduction factor n. Figure 4.5b, represents the above layer configuration, where the new conductivity profile within the layer along the altitude z, will be:

$$\sigma' = \frac{\sigma_0}{n} exp\left(\frac{z}{l}\right), \tag{4.8}$$

The electric field at ground due to the dust layer, $E_{z_0,layer}$, is given by:

$$E_{z_0,layer} = \frac{V_{ion}}{\sigma_0 R_c{}'}, \tag{4.9}$$

with the new columnar resistance, $R_c{}'$, being:

$$R_c{}' = \int_0^{z_1} \frac{dz}{\sigma} + \int_{z_1}^{z_1} \frac{dz}{\sigma'} + \int_{z_1}^{H} \frac{dz}{\sigma}, \qquad z \neq z_{1,2} \quad \Rightarrow$$

$$R_c{}' = \frac{l}{\sigma_0}\left[1 + (n-1)exp\left(-\frac{z_c - d/2}{l}\right)\left(1 - exp\left(-\frac{d}{l}\right)\right) - exp\left(-\frac{H}{l}\right)\right], \tag{4.10}$$

where $z_{1,2}$ are the layer bottom/top heights, z_c is the mean layer central height and $d = z_2 - z_1$ the mean layer depth. The dust layer horizontal extent R (radius), as depicted in Figure 4.5b, is assumed to be at least ten times larger than its vertical extent ($R \geq 10d$) for a thin layer approximation. And (4.9) gives through (4.10):

$$E_{z_0,layer} = \frac{V_{ion}}{l\left[1+(n-1)exp\left(-\frac{z_c-d/2}{l}\right)\left(1-exp\left(-\frac{d}{l}\right)\right)-exp\left(-\frac{H}{l}\right)\right]}, \tag{4.11}$$

Therefore, it is clear that $E_{z_0,layer}$ depends on the scale height parameter l, the reduction parameter n, the layer central height z_c and the layer depth d. A further investigation of the E-field dependence on the various parameters listed above can be found in Section 4.4.5.

On a next step, we parameterize an electrically active dust layer to calculate its impact on the surface E-field. Specifically, we construct a simplistic model for the atmospheric column (1D), based on the hypothesis that the charge accumulation areas within the dust layer can be approximated by charged cylinders of a total charge density $\pm\rho$ (Figure 4.5c). For the cylinder, we assume that its horizontal extent, as represented by the cylinder radius R_1 in Figure 4.5c, is at least ten times larger than the vertical extent (large cloud approximation), to ensure that the field lines are vertical with only weak radial dependence directly below the center of the layer (e.g., Riousset et al., 2007). The electric field of such an idealized finite extent charged layer is dependent on the distance from the layer. Departures from this behaviour occur near layer edges and distances comparable to the layer extent. Moreover, the hypothesis of the presence of image charges is also

applied due to the ground being a good conductor, ensuring that the calculated electric potentials are solutions to the Poisson equation.

The formulation for such an electrically active layer consists of a superposition of the electrically neutral dust layer case with the monopole charged cylinder case, constrained for zero ground and zero ionospheric potentials. The derivation of the ground electric field due to the presence of a total charge density of ρ is given below. We calculate the potential at point A (central lower point of the charged cylinder, Figure 4.5c), which is given as the sum of the potential from the total charge Q and the potential from its image charge, Q_{img}, where $Q_{img} = -Q$:

$$V_A = V_Q + V_{Q_{img}}. \tag{4.12}$$

The solution for the potential at the central axis of a solid charged cylinder with total charge density ρ_1, is given by (e.g., Griffiths '*Instructor's Solution Manual for Introduction to Electrodynamics*', 4th Edition, 2013):

$$V_Q = \frac{\rho_1}{4\varepsilon_0}\left\{d_1\sqrt{{R_1}^2 + {d_1}^2} + {R_1}^2 \ln\left[\frac{d_1 + \sqrt{{R_1}^2 + {d_1}^2}}{R_1}\right] - {d_1}^2\right\}, \qquad for\ R_1 \geq 10d_1 \tag{4.13}$$

$$V_{Q_{img}} = \frac{-\rho_1}{4\varepsilon_0}\left\{2z_{c_1}\sqrt{{R_1}^2 + \left(2z_{c_1}\right)^2} - \left(2z_{c_1} - d_1\right)\sqrt{{R_1}^2 + \left(2z_{c_1} - d_1\right)^2} + {R_1}^2 \ln\left[\frac{2z_{c_1} + \sqrt{{R_1}^2 + \left(2z_{c_1}\right)^2}}{\left(2z_{c_1} - d_1\right) + \sqrt{{R_1}^2 + \left(2z_{c_1} - d_1\right)^2}}\right] - 2d_1\left(2z_{c_1} - \frac{d_1}{2}\right)\right\}, \tag{4.14}$$

where ε_0 is the permittivity of vacuum, R_1 the charge region horizontal extent presented by the cylinder radius, $d_1 = {z_2}' - {z_1}'$ the cylinder depth (charge region vertical extent) and ρ_1 is the total charge density. Correspondingly, the potential at point A due to the image charge is calculated as:

for z_{c_1} the charged area central height. The new columnar resistance up to the height of point A, will be:

$$R_{c_1} = \int_0^{z_1} \frac{dz}{\sigma} + \int_{z_1}^{{z_1}'} \frac{dz}{\sigma'} \Rightarrow$$

$$R_{c_1} = \frac{l}{\sigma_0}\left[1 - exp\left(-\frac{z_c - d/2}{l}\right)\right] + \frac{nl}{\sigma_0}\left[exp\left(-\frac{z_c - d/2}{l}\right) - exp\left(-\frac{z_{c_1} - d_1/2}{l}\right)\right], \tag{4.15}$$

calculated from the ground to the dust layer bottom height z_1, and from there to the cylindrical charged area bottom height $z_1{}'$ (Figure 4.5c). Note that d is the layer depth while d_1 is the cylinder depth. And again, from Ohm's law and equation (4.15), we get the electric field at ground level for the case of a charged cylindrical monopole as:

$$E_{z_0,Q} = \frac{V_A}{l\left[1 - exp\left(-\frac{z_c - d/2}{l}\right)\right] + nl\left[exp\left(-\frac{z_c - d/2}{l}\right) - exp\left(-\frac{z_{c_1} - d_1/2}{l}\right)\right]}, \tag{4.16}$$

where V_A is given from equations (4.12) to (4.14), with $E_{z_0,Q}$ being dependent on the scale height l, the conductivity reduction factor n, the central layer height z_c and charged area central height z_{c_1}.

In the case of multiple stratified charged areas within the layer, the electric field at ground level is a superposition of the contribution to the field from each charge and its image (E_{z_0,Q_i}), along with the non-stratified dust layer's contribution attributed to the imposed conductivity reduction ($E_{z_0,\text{layer}}$), hence:

$$E_{z_0,multipole} = \sum E_{z_0,Q_i} + E_{z_0,layer} \Rightarrow$$
$$E_{z_0,dipole} = E_{z_0,\text{lower cylinder}} + E_{z_0,\text{upper cylinder}} + E_{z_0,layer}, \tag{4.17}$$

where, subsequently, if we assume a dipole charge configuration within the dust layer, the total contribution to the ground E-field ($E_{z_0,\text{dipole}}$) will be a superposition of the influence from the lower ($E_{z_0,\text{lower cylinder}}$) and upper ($E_{z_0,\text{upper cylinder}}$) charged areas, along with the electrically neutral dust layer's contribution ($E_{z_0,\text{layer}}$).

4.4.2. Electric Field below the Fair Weather Field

As a result of the mathematical formalism described above, we present the 1D model results and restrictions under which the various behaviours of the near-ground E-field strength can be exhibited in comparison to the calculated fair weather E-field. Following this formulation, the dust layer that exhibits charge separation is approximated with a dipole of oppositely charged cylinders. The

influence of small charge imbalances, less than 10 %, in the bipolar case, which could quantitatively explain the enhancement or reduction in the E-field is also investigated. If multiple charge accumulation regions are suspected within the dust layer (Zhang and Zhou, 2020), the problem can be still represented by the model output through a superposition of several cylindrical monopoles with different charge densities, polarities and separation distances.

In this section, we describe the possible cases under which lofted dust layers can reduce the near-ground E-field strength below the reference electric field values, and we investigate whether electrified dust layers can reproduce such a behaviour. $E_{z_0,\mathrm{layer}}$ dependency on the various atmospheric parameters, points to atmospheric conductivity as the dominant factor that affects the E-field (see Section 4.4.5). Therefore, we expect that if the dust layer is electrically neutral and acts as a passive element by reducing the atmospheric conductivity, it will greatly affect the field by forcing it below the local reference values.

Table 4.1: Dust layer central height and depth, as derived from the PLDR profiles.

Dust Outbreak	$\boldsymbol{z_{c_i}}$ $(\boldsymbol{km})$	$\boldsymbol{d_i}$ $(\boldsymbol{km})$
25/07/2017 (Fin.)	3	4
20/10/2018 (Ant.)	3	4
16/03/2018 (Fin.)	3.5	2.5
23/06/2019 (Ant.)	3.5	3

Since vertical profiling data within the dust layers were sparse during the objective setting of this thesis, we utilize earlier measurements of electric field variation with the altitude. These indicated a charge density of $\rho = \pm$ 25 pC m^{-3} within a transported Saharan dust layer away from the emission source (Nicoll et al., 2011a). From the specific value, the total charge Q is estimated for the different model cylinder extents. Gringel and Muhleisen (1978) measured a reduction of the electrical conductivity, compared to the fair weather values, by a factor of four within an elevated dust layer and we, therefore, adopt a reduction factor of $n = 4$ in the present study (see also Section 4.4.5). For E_{z_0}, $E_{z_0,layer}$ and $E_{z_0,Q}$ estimations, the scale height is fixed to a globally average value of $l = 6$ km (Kalinin et al., 2014; Stolzenburg and Marshall, 2008), the ionospheric potential is fixed at V_{ion} = 250 kV and the ionospheric height is at $H = 70$ km. The mean central height of the dust

layer and mean layer depth are both set equal to 3 km (z_c = d = 3 km), since this height represents the average value for the four dust cases according to the lidar PLDR profiles (Table 4.1).

4.4.2.1. Balanced/Imbalanced dipole field below Fair-weather field

We consider the case of two oppositely charged cylinders with similar geometries as in Figure 4.5c, assuming they are within a dust layer with a mean height of 3 km and a mean depth of 3 km. The lower cylinder central height z_{c_1} starts at 2.95 km and decreases, the upper cylinder central height z_{c_2} starts also at 2.95 km for zero separation distance (at this limit, it represents electrically neutral dust that lacks internal E-field generation due to the absence of charge separation) and increases within the dust layer boundaries (varying separation distance), while their depth is fixed at 100 m, in order to be of finite vertical extend but quite thin. The separation distance between the two cylinders is defined as the difference between their central heights and the ground E-field is a superposition of the electric field of the upper and lower cylinders. We assume the bottom cylinder to be positively charged with density $+\rho$ and the upper one to be negatively charged with $-\rho$ (Figure 4.6), in order to simulate gravitational settling conditions for larger and, most probably, positively charged dust particles (Forward et al., 2009b; Waitukaitis et al., 2014). From equations (4.12) to (4.17), the field is analytically calculated directly on the axis of the charged cylinders and plotted against the cylinder radius R for separation distances up to 800 m.

As seen in Figure 4.6, the resulting electric field values on ground level are consistently below the fair weather constant value. When the dipole separation distance increases, the vertical electric field at ground level increases. This happens due to the stronger influence of the lower charged cylindrical layer to the surface resistance. The fact that the upper charged cylinder moves to higher altitudes signifies that the resistance between the specific layer and the ground increases, therefore the conduction current at the ground decreases.

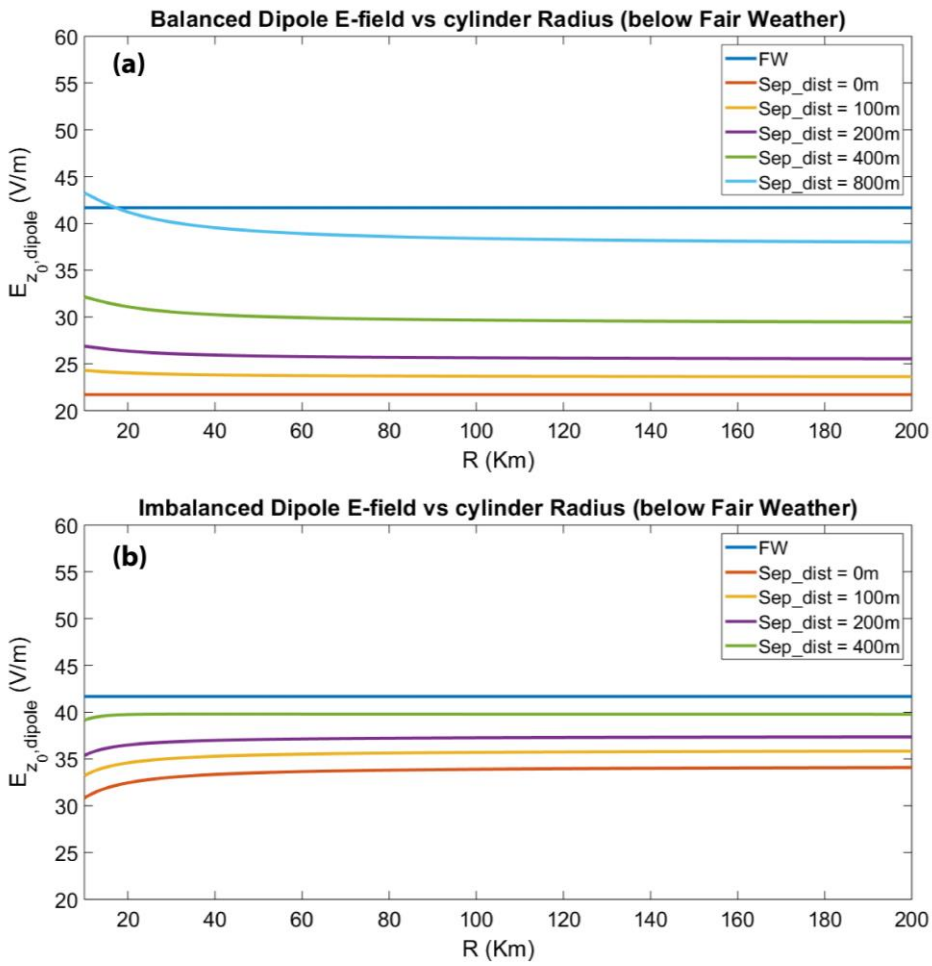

Figure 4.6: Vertical electric field strength at ground level ($E_{z_0,\text{dipole}}$) below the fair weather field (blue line), for a dipole of: (**a**) finite uniformly charged cylinders and (**b**) non-uniformly charged cylinders exhibiting a charge imbalance of 8 %, within an elevated dust layer as a function of the cylinder radius R. $E_{z_0,\text{dipole}}$ is calculated for separation distances (Sep_dist) of 0 (electrically neutral dust), 100, 200, 400 and 800 m (balanced dipole case only) between the charged layers.

The conduction current due to the upper charged layer, then, becomes weaker than the conduction current due to the lower charged layer, which moves towards the ground. Since the conductivity at the ground is undisturbed by the dust layer (Figure 4.5c) and equal to the fair weather value, the ground electric field due to the upper layer decreases as the layer moves up, while the field due to the lower layer increases as the layer approaches the ground, leading to an increasing value of the total electric field with the increasing separation distance. When the separation distance is kept relatively small, the enhancement effect in the E-field is not significant enough to overcome the fair weather values (Figure 4.6). For large radii, although the infinite plates configuration is

asymptotically approached ($E_{z_0,dipole} \longrightarrow 0$), there is a nearly-constant residual field for the finite cylindrical geometry of the charged regions. Since the charged cylinders are placed in a conducting medium above a perfect conductor, the electric field at the ground will not be zero even if the cylinders have infinite extent. Due to the conductivity distribution, there is an uneven contribution of the electric fields of each cylinder and, therefore, the E-field is expected to converge to this non-zero value (Figure 4.6).

If the dipole charge density is not uniformly distributed to both cylinders, resulting in a charge imbalance within the layer, the electric field will be more sensitive to separation distance changes (Figure 4.6b). Such imbalance could be the result of (a) dust charging at the source, prior to any charge separation that may occur (Ette, 1971; Kamra, 1972), (b) charging due to atmospheric current, or (c) charge loss through dry deposition in the Planetary Boundary Layer (PBL). In Figure 4.7, the ground electric field dependence on the separation distance and cylinder radius is depicted, for a charge density difference of $\Delta\rho = 2$ pC m^{-3} (8 %) between the two charged cylindrical areas, with the upper one being less charged. This leads to a larger increase of the E-field than in the balanced dipole case (Figure 4.6a), as the effect of the upper cylinder not only decreases as it moves to higher altitudes, but it is also reduced due to the reduction of the total charge density which influences proportionally the electric field. Note that even a small imbalance can highly increase the external field. Nevertheless, for relatively small separation distances the resulting field values fall again below the fair weather value.

4.4.3. Electric Field above the Fair Weather Field

We examine the physical arrangement within the dust layer that can provide an enhancement to the electric field above the fair weather values and subsequently above the LREF.

4.4.3.1. Balanced/Imbalanced dipole field above Fair-weather field

For the same charged region geometries as discussed previously, larger separation distances are imposed for the balanced dipole case (Figure 4.7a), but we strictly remain within the base dust layer mean dimensions. Figure 4.7 shows that as the separation distance between the oppositely charged layers increases, an enhancement of the E-field above the local reference values occurs. This

enhancement becomes more prominent as the layers grow further apart within the dust plume and the contribution from the lower layer is significantly larger than the upper layer. The above dependence of the ground E-field on the separation distance is not expected in the case of charged infinite plates, as discussed in Section 4.4.2.14.4.2.1. Again, for a charge imbalance of 8 % between the two cylinders and for larger separation distances, the E-field is significantly enhanced and exceeds the local fair weather values (Figure 4.7b). This increase becomes more prominent as the separation distance increases and the lower positive cylinder moves closer to the sensor location.

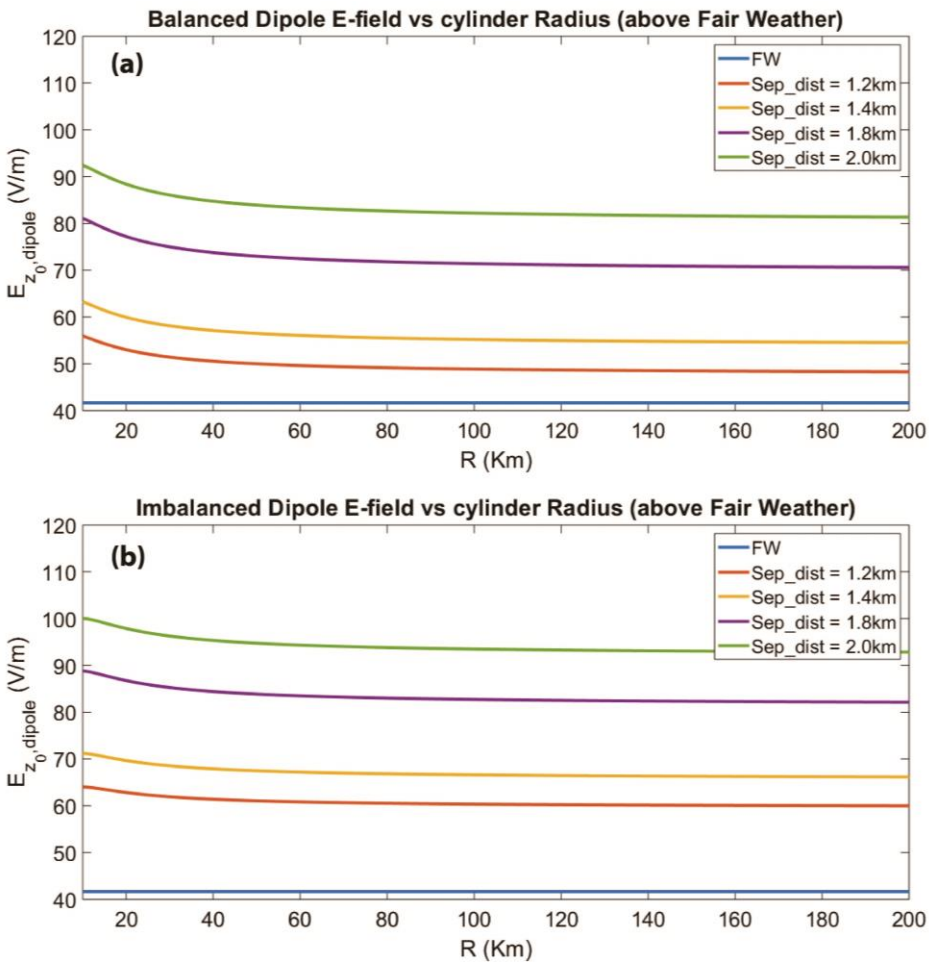

Figure 4.7: Vertical electric field strength at ground level ($E_{z_0,\mathrm{dipole}}$) above the fair weather field (blue line), for a dipole of: (**a**) finite uniformly charged cylinders and (**b**) non-uniformly charged cylinders exhibiting a charge imbalance of 8 %, within an elevated dust layer as a function of the cylinder radius R. $E_{z_0,\mathrm{dipole}}$ is calculated for separation distances (Sep_dist) of 1.2, 1.4, 1.8 and 2 km between the two charged layers.

The term large or small separation distance depends on the conductivity distribution and more specifically on the conductivity scale height, as can be seen in Equations (4.11) and (4.16).

4.4.4. How does a Reversed Electric Field Polarity affect the formalism?

If a reversed polarity E-field is observed (in our timeseries there were dust cases under which the field exhibited polarity reversal), with the opposite sign signifying that the field vector points upwards instead of downwards, then the investigated formalism is capable of explaining the reversal. As such, a similar cylindrical configuration could be assumed with the only difference being that the lower layer has to be negatively charged and the upper one, in the dipole case, to be positively charged. Under this condition, the conclusions derived from the model remain the same. Therefore, such an indication of reversal is explained only via reversed separated cylindrical charges and again points that lofted dust has to be electrified.

4.4.5. Dust Layer acting as a Passive Element

In Figure 4.8, the dependence of the near ground electric field strength, $E_{z_0,layer}$ (red line) of an electrically neutral dust layer on the conductivity reduction factor, the scale height, the layer central height and the layer depth, as given in (4.11), is plotted and compared to the fair weather electric field E_{z_0} at ground (blue line) which is given by (4.7). E_{z_0} depends only on the scale height and decreases as l increases, while it remains constant for the other varying parameters as expected from equation (4.7). The calculated fair weather field value of ~ 42 V m^{-1}, for the selected l, is comparable to the estimated value by Williams (2003) from Ohm's law, when dividing the globally integrated conduction current density by the mean atmospheric electrical conductivity at ground ($J_{z_0} \approx 2 \times 10^{-12}$ A m^{-2}, $\sigma_0 \approx 5 \times 10^{-14}$ S m^{-1}) and assuming an exponentially increasing conductivity profile above the Earth's surface (Haldoupis et al., 2017).

We note that this globally averaged value of E_{z_0} is much less from the typically measured which is around 100 V m^{-1} (e.g., Corney et al., 2003; Reddell et al., 2004). We believe that the average value is more suitable for global calculations, because it incorporates the variations of the conductivity distribution around the Earth. On the other hand, the typical value is tied to the location of the measurement, and it varies at different locations as the conductivity distribution changes. Consequently, $E_{z_0,layer}$ strongly depends on the conductivity reduction as depicted in the Figure 4.8 case (a) curve, where the field reduces with the increasing reduction factor more effectively

than with respect to the other three parameters, meaning that atmospheric conductivity reduction is the predominant factor that affects the E-field strength by largely lowering it. The E_{z_0} depends only on the varying scaling height as expected from Equation (4.7).

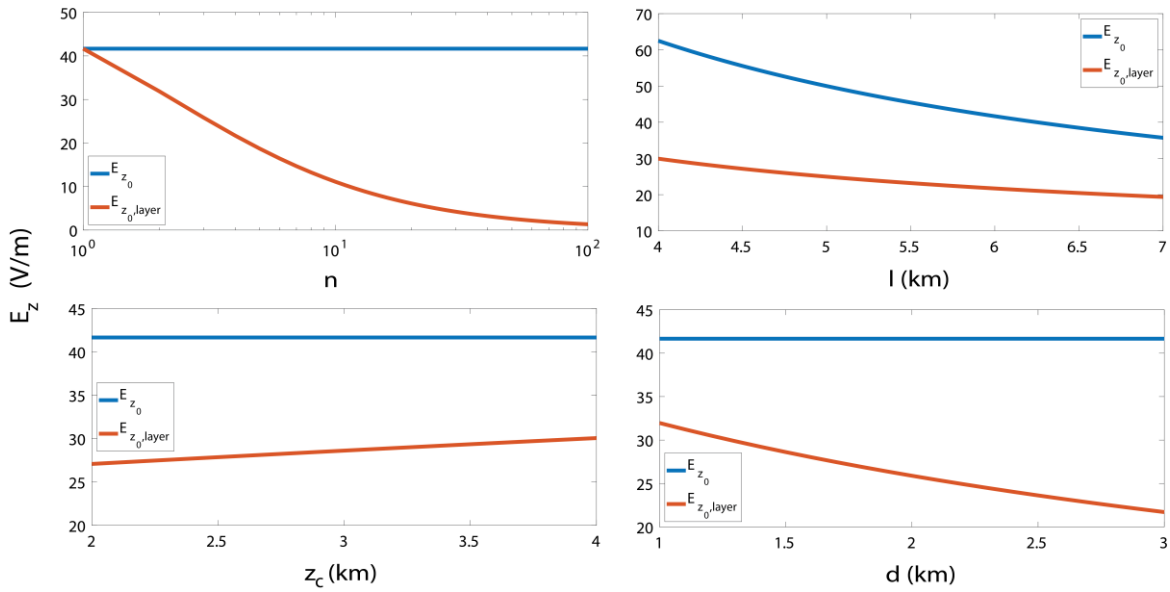

Figure 4.8: Dependence of the vertical electric field at ground level, under fair weather (E_{z_0}, blue line) and under the influence of an uncharged dust layer ($E_{z_0,\text{layer}}$, red line) on: (**a**) the reduction factor n, (**b**) the scaling height l, (**c**) the central layer height z_c and (**d**) the dust layer depth d, for $1/\sigma_0 = 3 \cdot 10^{13}$ Ω m, $V_{\text{ion}} = 250$ kV and $H = 70$ km.

4.5. Dust Layer Optical Properties

4.5.1. Characterization through the Polly^{XT} lidar

The July 2017 and March 2018 dust events in Finokalia are characterized by large concentrations of airborne dust particles from the middle of the day onwards, followed by dust settling towards the ground after 21:00 UTC, as indicated by the time-height plots of the total attenuated backscatter coefficient (Figure 4.9 and Figure 4.11) Larger particle concentrations are shown in red tones, with the β and δ_p (black lines) profiles superimposed to the respective attenuated backscatter coefficient (top panel) and δ_v (lower panel) quick-looks. For the first case study (Figure 4.9), beta values are between 3 to 4 (Mm^{-1} sr^{-1}) with a maximum value of 5 (Mm^{-1} sr^{-1}) inside the layer and denote large

particle concentrations. High δ_v values (> 10 %) are indicative of dust particles and δ_p values between ~ 25 % – 30 % in the afternoon are characteristic of pure dust. Settling of dust particles below 2 km, inside the Marine Boundary Layer (MABL) is revealed from the time-height evolution of the VLDR (see Figure 4.9, bottom panel). For the March 2018 case study (Figure 4.11), the elevated layer (small dust concentration was present near the surface) reached Finokalia at early noon. The layer was directly transported from Sahara and reached the station in less than 48 hours, as indicated by the backward trajectories analysis (Figure 4.3c). Examination of the β profile in Figure 4.11, shows values that reach up to 15 (Mm^{-1} sr^{-1}) at the top of the layer, indicating higher aerosol concentrations in this case. δ_v values close to 30 % are indicative of high dust particle concentration and δ_p values persistently of 30 % are characteristic of pure dust within the entirety of the layer (1 to 4 km), with dust downward mixing inside the MABL being less prominent.

The October 20th 2018 Antikythera layer (Figure 4.10), exhibits lower dust particle concentrations (β lower than 5 Mm^{-1} sr^{-1}) close to the ground up to 6 km in altitude, mostly mixed with marine aerosols below 2 km (Figure 4.3b and Figure 4.10). High δ_v values (> 20 %) are indicative of dust particle presence and δ_p between 25 % – 30 % in the afternoon is characteristic of pure dust. It is also observed that the near-ground dust concentration is very low, with the thin layer at 500 m being a mixture of dust particles and particles of marine origin with the VLDR around 15 %. The June 23rd 2019 dust outbreak consists primarily of high elevated dust concentrations, since δ_v values are greater than 15 % (Figure 4.12), after mid-day, with δ_p values reaching up to 30 % in the height range of 3 to 5 km, which are representative of pure dust (Figure 4.12). The dust plume was transported again directly from Sahara to Antikythera within 48 hours (Figure 4.3d) and very low concentrations of dust particles are also present within the MABL.

4.6. Local Mean Electric Field Behaviour

Considering the electrical properties of the layers detected in Finokalia (Figure 4.9 and Figure 4.10), the LREF and the reconstructed mean electric field are depicted, with the local diurnal variation resembling the Carnegie curve. The E_z values vary between a total minimum at ~ 05:00 UTC and the maximum at ~ 13:00 UTC with a mean value of ~ 173 V m^{-1}. An increase of the electric field is observed at about 22:00 UTC resulting in a double peak variations curve (Yaniv et al., 2016). The

reconstructed mean E-field is close to the expected fair weather value and the slight difference can be attributed to local meteorological factors, atmospheric boundary layer characteristics (Anisimov et al., 2017) and the station's coastal location. Complementarily, E_z diurnal variation in the station of Antikythera exhibits a minimum in early morning hours at ~ 23:00 UTC and a single maximum on early afternoon at ~ 19:00 UTC (Figure 4.11 and Figure 4.12), with a mean value of ~ 102 V m^{-1}. Since the timeseries in Antikythera are restricted to one year, the mean E-field value is statistically biased, therefore it is lower than the expected fair weather value.

4.7. Observed Electric Field compared to LREF

4.7.1. Cases of Electric Field Enhancement

In Figure 4.9 and Figure 4.10, we present the dust events that induced an enhanced electrical behaviour near the ground. The E-field strength measurements are averaged over 5 mins in order to be comparable with the lidar data. In the July 25th layer (Figure 4.9), dust advection is recorded since the first morning hours and areas of increased particle concentration can be spotted from early noon. The δ_p profile signifies that the layer consists primarily of dust which descends after ~ 16:00 UTC and falls entirely below 2 km at ~ 18:30 UTC, but the mean electric field (black line) remains above the reference field (red contoured line), showing an increase when particle density is maximized towards noon and a small drop when dust concentration within the MABL becomes significant. A similar electrical behaviour was observed during the dust event of October 2018 that reached the PANGEA observatory. Large lofted particle concentrations are attributed to dust according to the mean δ_p values that reach up to ~ 25 % – 27 % (Figure 4.10). For both cases, the mean E_z appears enhanced as compared to the LREF. According to the physical approximation of cylindrical charged areas (see Section 4.4.1), such an enhancement would be expected only when the lofted dust layer is electrically active and charge separation within the layer is prominent. From Figure 4.8b, it becomes apparent that the external E-field is more sensitive to charge imbalances, even small ones, than to separation distance variations, hence a charge imbalance within these layers could drive the E-field above the fair weather values, as observed in the above cases, for even smaller charge separation distances.

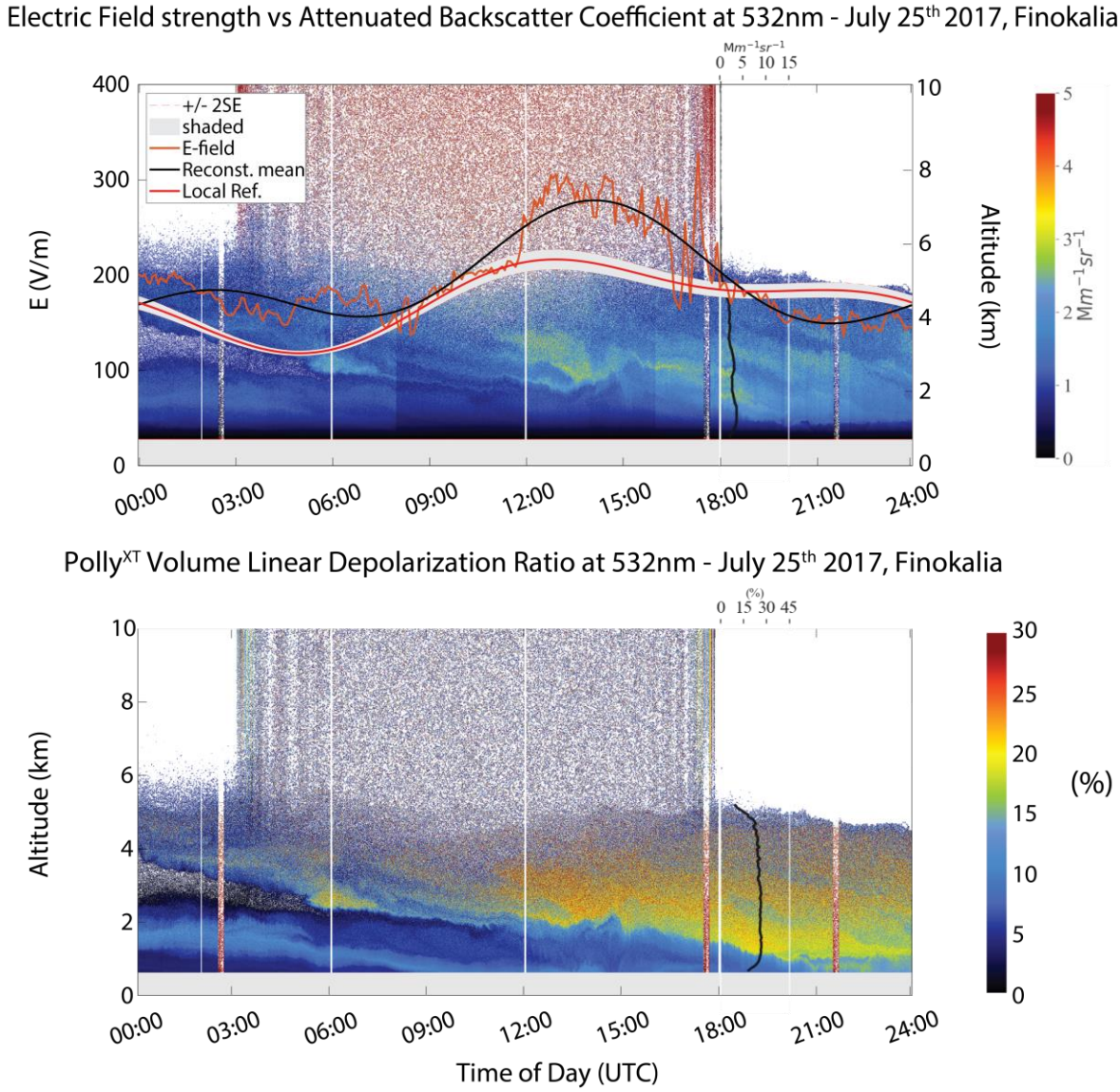

Figure 4.9: **<u>Top panel</u>:** Timeseries of the vertical electric field strength (orange), the extracted Localized Reference (ref.) Electric Field (red) and the reconstructed (reconstr.) mean electric field variation (black) from the field mill dataset, for the recorded 25 July 2017 dust layer at Finokalia. The E-field data are plotted with the time–height evolution of the attenuated backscatter coefficient (Mm^{-1} sr^{-1}) and the particle backscatter coefficient (β) profile (Mm^{-1} sr^{-1}, black vertical line) at 532 nm from the Polly^{XT} lidar, which was co-located with the field mill. Areas of increased particle concentration are denoted with reddish tones, while β values are derived by averaging between 18:00 and 21:00 UTC. **<u>Bottom panel</u>:** Volume Linear Depolarization Ratio (δ_v, %) at 532 nm for the same dust layer as obtained from the Polly^{XT} lidar and the Particle Linear Depolarization Ratio (δ_p, %) profile (black vertical line) again averaged between 18:00 and 21:00 UTC. Large δ_v values are depicted with reddish tones.

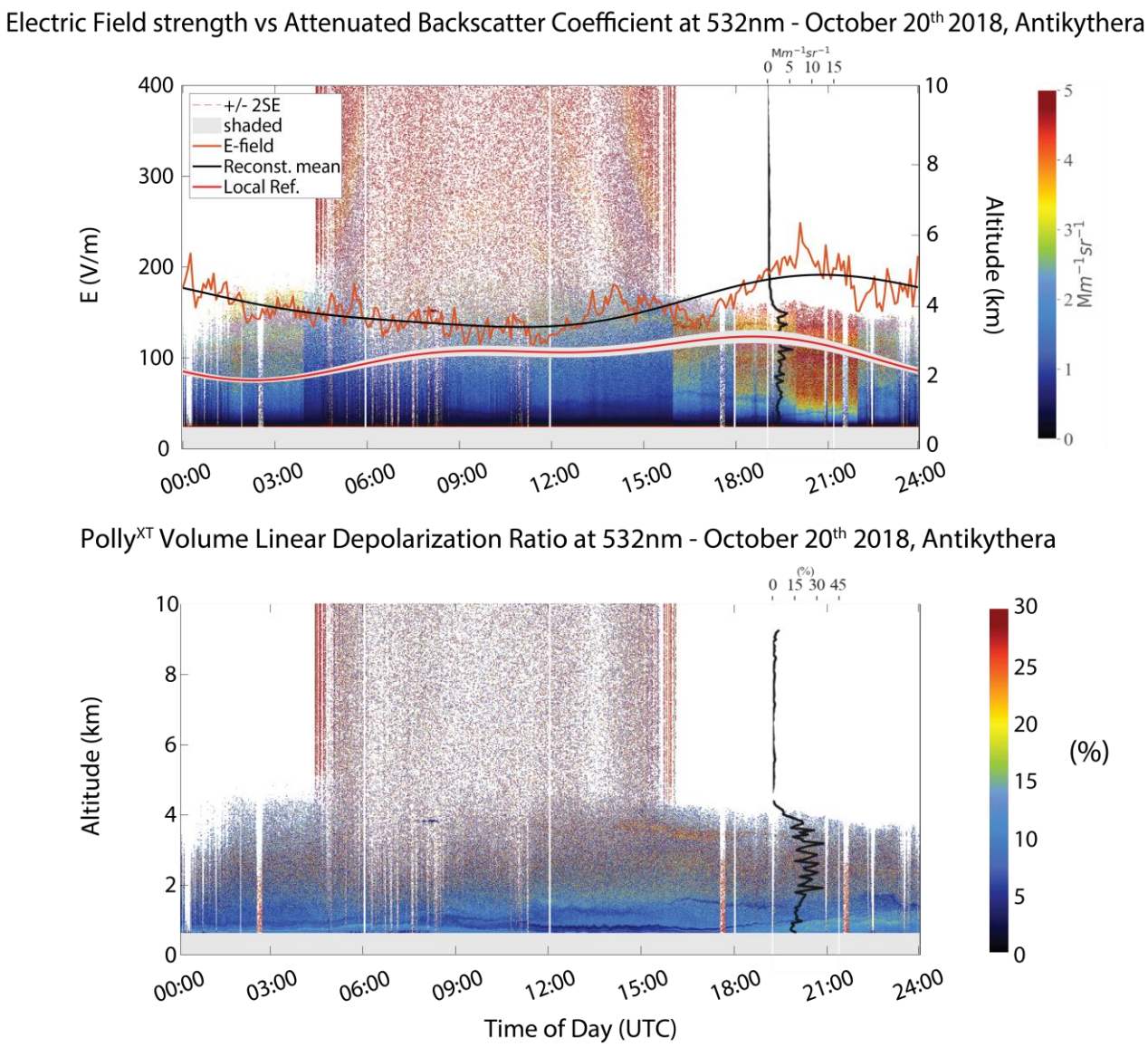

Figure 4.10: **<u>Top panel</u>:** Timeseries of the vertical electric field strength (orange), the extracted Localized Reference (ref.) Electric Field (red) and the reconstructed (reconstr.) mean electric field variation (black) from the field mill dataset, for the recorded 20 October 2018 dust layer at Antikythera. The E-field data are plotted with the time–height evolution of the attenuated backscatter coefficient (Mm^{-1} sr^{-1}) and the particle backscatter coefficient (β) profile (Mm^{-1} sr^{-1}, black vertical line) at 532 nm from the Polly^{XT} lidar, which was co-located with the field mill. Areas of increased particle concentration are denoted with red tones, while β values are derived by averaging between 18:00 and 21:00 UTC. **<u>Bottom panel</u>:** Volume Linear Depolarization Ratio (δ_v, %) at 532 nm for the same dust layer as obtained from the Polly^{XT} lidar and the Particle Linear Depolarization Ratio (δ_p, %) profile (black vertical line) again averaged between 18:00 and 21:00 UTC. Large δ_v values are depicted with red tones.

4.7.2. Cases of Electric Field Reduction

Several dust load cases were detected, both in Finokalia and Antikythera, where the near-ground electric field strength exhibits a decrease when compared to the local reference field and, particularly, when high dust particle concentrations were present. In the specific study, we select the cases of March 2018 and June 2019 in terms of the similar temporal injection of dust particles, large AOD values and similar layer progression throughout the day (Figure 4.11 and Figure 4.12). From the δ_p profiles, we deduce that for both cases, the elevated layer between 2 and 4 km consists primarily of dust particles, while the decrease of δ_p towards the bottom of the layer is indicative of downward mixing inside the MABL, with marine particles of lower δ_p. The mean E-field remains positive and well below the reference field, exhibiting an increase as dust injection initiates at ~ 09:00 UTC and then a decrease along the plume's progression (Figure 4.11).

The dust plume of June 2019 instils a similar electrical behaviour to the ground E-field (Figure 4.12), as the bottom of the layer seems to progressively move towards lower altitudes during late afternoon and the total dust load remains persistent. The mean E-field is positive and consistently below the reference field, exhibiting an increase close to fair weather values when particle injection begins towards noon and dust concentration is rising, but later drops further below the LREF as the layer progresses to lower altitudes. Following the 1D model outputs for such a case (see Section 4.4.2), this observed reduction could be attributed to either electrically neutral dust aloft or to electrically active dust with the charged regions in relatively small separation distances within the layer. Under the electrically active dust case, a charge imbalance of less than 10 %, can be adequate to interpret the observed reduction of the E-field below the LREF for even smaller separation distances. But the detection of such an E-field reduction below the LREF cannot conclusively characterize the electrical activity of the dust layer aloft.

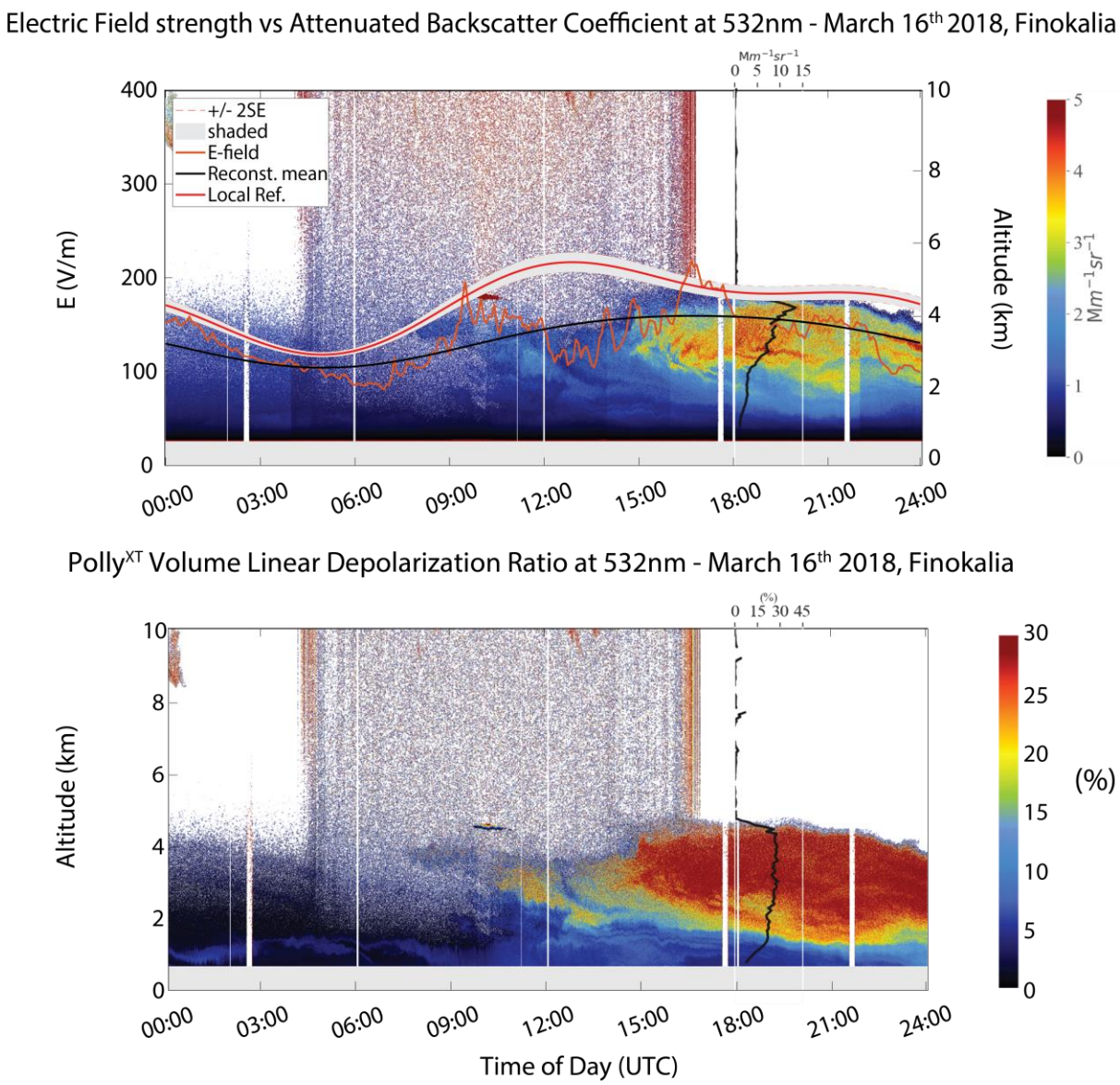

Figure 4.11: **<u>Top panel</u>:** Timeseries of the vertical electric field strength (orange), the extracted Localized Reference (ref.) Electric Field (red) and the reconstructed (reconstr.) mean electric field variation (black) from the field mill dataset, for the recorded 16 March 2018 dust layer at Finokalia. The E-field data are plotted with the time-height evolution of the attenuated backscatter coefficient (Mm^{-1} sr^{-1}) and the particle backscatter coefficient (β) profile (Mm^{-1} sr^{-1}, black vertical line) at 532 nm from the Polly^{XT} lidar, which was co-located with the field mill. Areas of increased particle concentration are denoted with red tones, while β values are derived by averaging between 18:00 and 21:00 UTC. **<u>Bottom panel</u>:** Volume Linear Depolarization Ratio (δ_v, %) at 532 nm for the same dust layer as obtained from the Polly^{XT} lidar and the Particle Linear Depolarization Ratio (δ_p, %) profile (black vertical line) again averaged between 18:00 and 21:00 UTC. Large δ_v values are depicted with red tones.

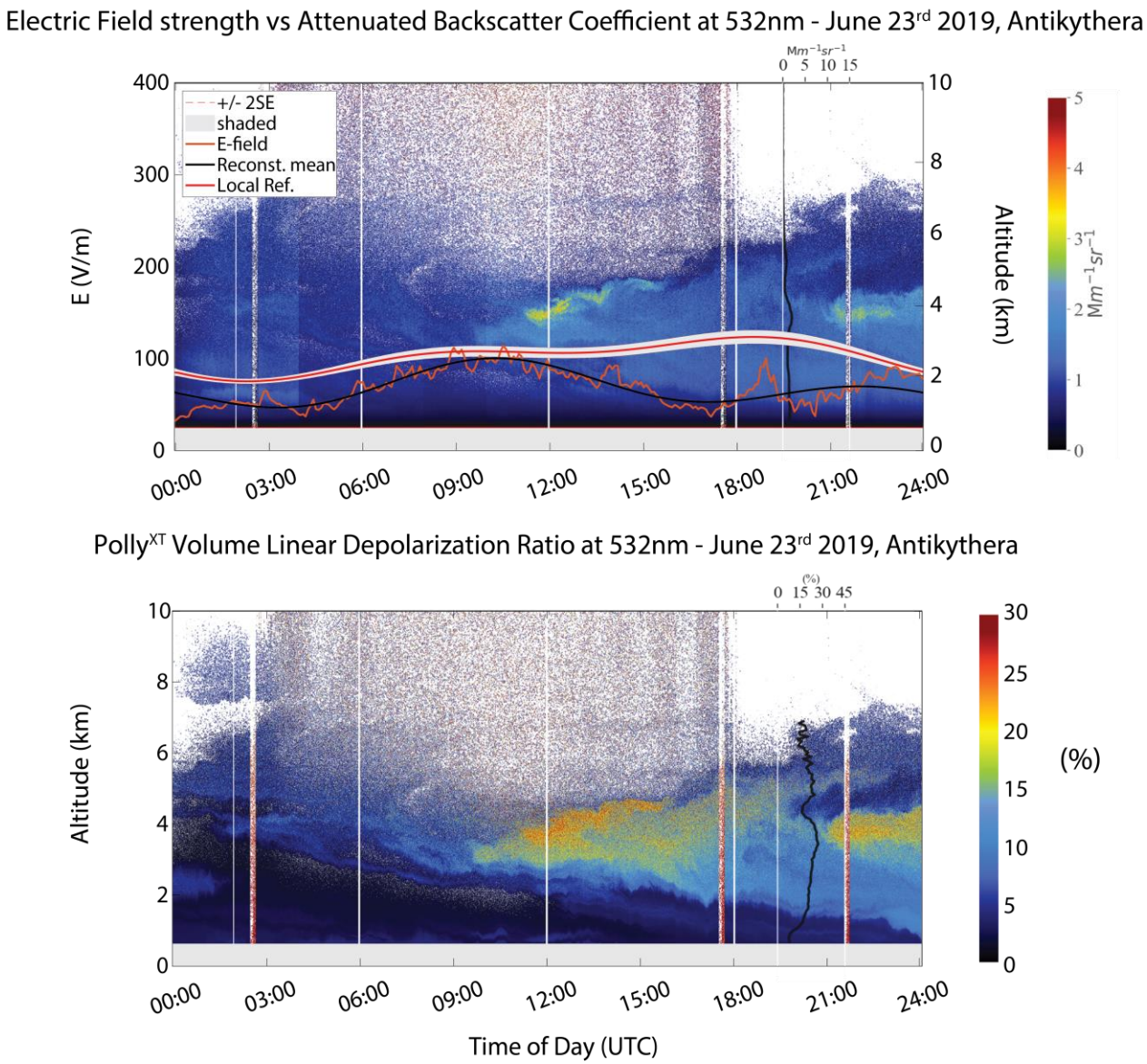

Figure 4.12: **<u>Top panel</u>:** Timeseries of the vertical electric field strength (orange), the extracted Localized Reference (ref.) Electric Field (red) and the reconstructed (reconstr.) mean electric field variation (black) from the field mill dataset, for the recorded 23 June 2019 dust layer at Antikythera. The E-field data are plotted with the time-height evolution of the attenuated backscatter coefficient (Mm^{-1} sr^{-1}) and the particle backscatter coefficient (β) profile (Mm^{-1} sr^{-1}, black vertical line) at 532 nm from the Polly^{XT} lidar, which was co-located with the field mill. Areas of increased particle concentration are denoted with reddish tones, while β values are derived by averaging between 18:00 and 21:00 UTC. **<u>Bottom panel</u>:** Volume Linear Depolarization Ratio (δ_v, %) at 532 nm for the same dust layer as obtained from the Polly^{XT} lidar and the Particle Linear Depolarization Ratio (δ_p, %) profile (black vertical line) again averaged between 18:00 and 21:00 UTC. Large δ_v values are depicted with reddish tones.

4.8. Electric Field Dependence on the Bottom Charged Area Height

From the above results, the question that arises is whether the proximity of the lower cylinder, to the ground itself, is capable to reproduce the electric field enhancement feature above the LREF. It becomes clear that two mechanisms act upon the enhancement of the ground electric field. The first is the decrease of the contribution of the upper layer as it moves upwards, due to the enhancement of the columnar resistance between the layer and the ground. The second is the increase of the contribution of the lower layer as it moves downwards, due to the decrease of the columnar resistance between the layer and the ground. The closer the lower layer is to the ground the smaller the separation with the upper layer is required for the enhancement of the electric field.

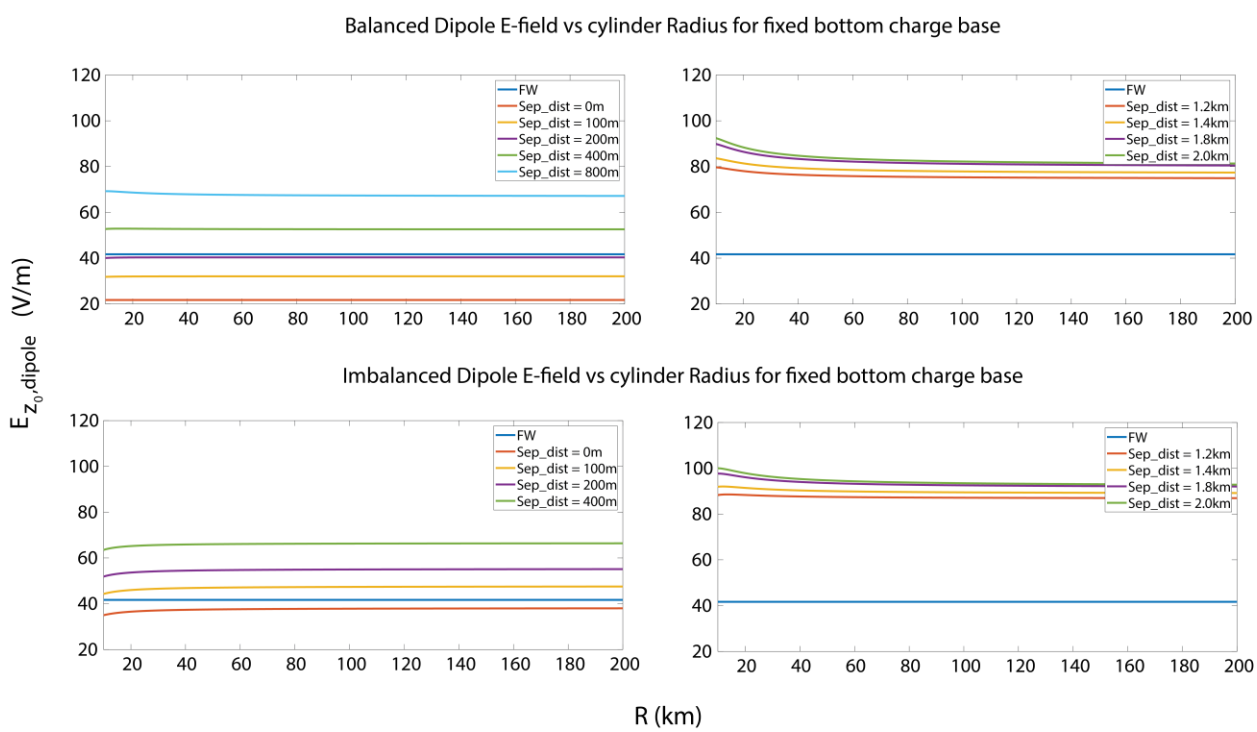

Figure 4.13: Dipole electric field strength at ground level ($E_{z_0,dipole}$) as a function of the cylinder radius *R*, with the bottom cylinder at 2 km fixed central height within the dust layer. The separation distance (Sep_dist) between the upper and bottom charged layer increases as the upper cylinder moves towards the top of the dust layer, for both cases of balanced and imbalanced dipoles.

In order to validate the influence of each parameter, we re-examine the ground E-field behaviour by keeping the lower cylinder at a fixed altitude of 2 km (close to the dust layer base, similarly to thundercloud activity e.g., Mallios and Pasko, 2012) and we, then, increase the separation distance. As observed in Figure 4.13, the increasing separation distance causes the E-field to increase at the ground and when it becomes large enough (top and bottom right panels), the upper cylinder does no longer influence the ground E-field. At this point, for both balanced and imbalanced dipoles with cylinder radius larger than ~ 40 km, the field converges to a constant value. This becomes clearer when comparing Figure 4.13 with Figure 4.6. When the separation distance is 400 m, the electric field at the ground is larger than the reference field in the case of Figure 4.13, while at Figure 4.6, separation distance equal to 400 m happens when the bottom layer is at 2.75 km. In this case, the field is lower than the reference value which indicates that the closer the bottom layer is to the ground, the smaller the separation distance needed for the enhancement of the ground electric field above the reference field. Moreover, the E-field value for zero separation distance is consistently below the calculated fair weather value. As such, observations of enhanced E-field above the fair weather values, for dust driven days, can be reproduced only when an electrically active dust layer is transported above the field mill.

If we assume that the bottom charged area is close to the lofted layer base, we would expect an increase to the ground electric field as the layer progressively moves towards lower altitudes. For the comparison of the E-field timeseries with the descending layer base (Figure 4.14), we use the cross component of the lidar attenuated backscatter coefficient at 532 nm, from which we can derive information on the vertical extent of the aerosol layers. More specifically, we applied a methodology where the first derivative of the attenuated backscatter coefficient is used to determine layer boundaries (Flamant et al., 1997; Mattis et al., 2008). The local maximum and local minimum of the derivative are considered to be the bottom and top of the layer respectively. The agreement between the height-time displays of the attenuated backscatter coefficient and the corresponding gradient (Figure 4.9 to Figure 4.12 and Figure 4.14) can be used to verify the results of the gradient method. As seen in the July 2017, March 2018 and June 2019 dust events, there is an enhancement of the reconstructed mean E-field followed by the layer base progression towards the ground, for specific timeframes within the day. This could signify the presence of positive charges accumulated to the layer base.

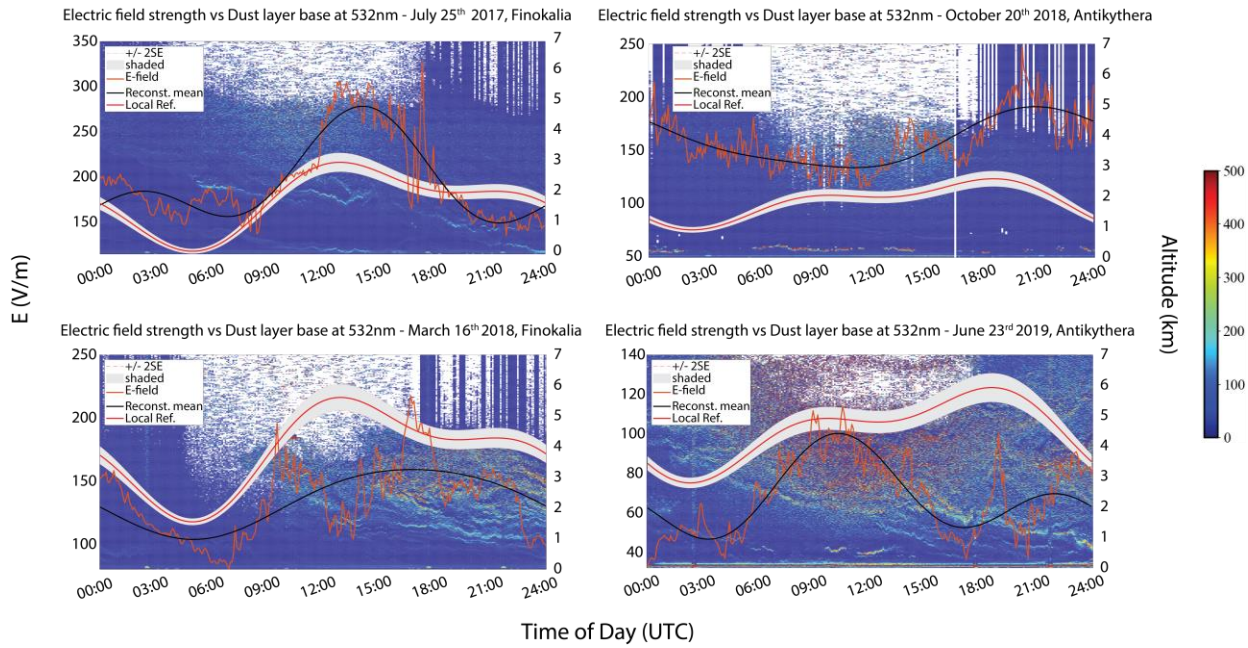

Figure 4.14: Timeseries of the vertical electric field strength (orange), the extracted Localized Reference Electric Field (red) and the reconstructed mean field variation (black), plotted with the first derivative of the cross component of the Polly^{XT} attenuated backscatter coefficient at 532 nm against the altitude, for the dust cases of 25 July 2017, 20 October 2018, 16 April 2018 and 23 June 2019. The dust layer bottom base is signified by the positive maximum values of the derivative within the 0-500 colorbar range.

4.9. Model and LREF Methodology Generalization

The methodology followed for the calculation of the ground electric field can be expanded to the area away from the central axis of the charged cylinders. As the cylinder radius increases and the infinite plate regime is approached, effects due to charged layer edges that induce radial electric field components, do not impact the sensor axis for a larger horizontal extent of the charged layer. This expands the analytical calculation as it becomes valid within a band region further away from the cylinder center. In the small radius regime, the sensor becomes sensitive to edge effects and the edge field can be far stronger than the on-axis field. If we assume that a transient dust layer is transported with a mean wind speed of 10 m s^{-1}, implying a regional scale transport, then in a period of 2 hrs the edge will be 72 km away from the sensor axis (fast transits), a sufficient distance to not affect the vertical component of the electric field. Although these variations are present on the raw timeseries (observed peak activity in Figure 4.9 to Figure 4.12), in the reconstruction of the LREF variations with timescales shorter than 6 hrs are the lower limit to the FFT input and are therefore

excluded. This leaves the LREF unbiased to edge effects. Problems might be caused in our analysis in the case of very slowly moving dust layers, that are transported with wind speeds less than 1 m/s. Dust layer edge effects can provide basic information on the layer properties and could be incorporated in our cylindrical layer formalism, but this consists a subject of further investigation in the near future.

4.10. Conclusions on ground-based methods

Near-ground electric field strength observations during Saharan dust advection over Greece exhibit three distinct responses of enhancement, reduction or sign reversal when compared to local fair weather values. In this paper, we present four cases of transient dust events that influence the ground electric field recorded at two atmospheric remote sensing stations synergistically with a lidar system and a field mill electrometer. Moreover, this work attempts to use only ground-based atmospheric electricity instrumentation as a proxy for electrified dust detection, with characterization in terms of optical properties from lidar observations. To quantify the effect of charged dust particles, we implemented a reference electric field representing the local fair weather field, using long-term measured timeseries, and examine the possible physical mechanisms that could explain the electric field behaviour. Our findings suggest that dust cases with the reconstructed mean E-field magnitude above the reference field indicate charge separation within the layer either as a balanced/imbalanced dipole (or a multipole) of charge layers, while when the mean field is completely below the reference field, dust electrical activity characterization is inconclusive. This reduction below the local fair weather field can be attributed to either the conductivity reduction due to dust acting as a passive neutral element or to charge separation between areas of accumulated charge.

The electrified dust scheme is approximated either via the absence of dust charge separation or with thin cylindrical finite charge geometries that allow explaining the electric field dependence on the layer height and the separation distance between the charge regions. Both concepts have been suggested to explain the observed E-field responses at ground. However, the lack of observational evidence validating the charge strata morphology, which might be far from similar to the elevated layers morphology due to the charged dust particles complex transport dynamics, necessitates consistent dust layer profiling measurements.

Chapter 5

Vertical Profiling of Desert Dust Electrical Properties[5]

To constrain the modelling formalism proposed in Section 2 and complement our methodology on the detection of electrified dust with ground-based methods, as it proved challenging just by ground-based methods we have performed extensive profiling measurements of dust electrical properties, deploying airborne platforms within the Saharan Air Layer. Numerous studies of the electrical properties in dusty environments, related to lofted particle charging, indicate that it is a rather complex mechanism which greatly affects the particle dynamics. The electrification of desert dust particles can differentiate their settling velocities and, therefore, can affect the removal of large particles from the atmospheric circulation. A systematic effort to orderly measure the electrical properties of elevated dust layers, with the subsequent monitoring of the respective parameters on

[5] **This section is based on my contribution in:**

Daskalopoulou, V., Hloupis, G., Mallios, S. A., Makrakis, I., Skoubris, E., Kezoudi, M., Ulanowski, Z. and Amiridis, V.: *Vertical profiling of the electrical properties of charged desert dust during the pre-ASKOS campaign*., in: 15th COMECAP, 26–29 September 2021, Ioannina, Greece, 204–208, ISBN 978-960-233-267-2,, 2021b. **and related sensor implementaions**

Mallios, S., **Daskalopoulou, V.**, Spanakis-Misirlis, V., Hloupis, G. and Amiridis, V.: *Novel Measurements of Desert Dust Electrical Properties: A Multi-Instrument Approach during the ASKOS 2022 Campaign*, , 22, doi:10.3390/environsciproc2023026022, 2023.

Marinou E., Paschou P., Tsikoudi I., Tsekeri A., **Daskalopoulou V.**, Kouklaki D., Siomos N., Spanakis-Misirlis V., Voudouri K.A., Georgiou T., et al. *An Overview of the ASKOS Campaign in Cabo Verde*. Environmental Sciences Proceedings. 2023; 26(1):200. https://doi.org/10.3390/environsciproc2023026200.

a ground reference level, was made in the major AEOLUS Calibration/Validation experiment of ASKOS in Cape Verde, in 2022. The preparatory phase of the campaign was carried out in Cyprus, in November 2019, where the initial prototypes of the novel, low-cost and disposable atmospheric electricity sensors were tested on-field. The profiling information from Cyprus reveals the presence of charged dust particles within the elevated plumes with accumulation of charges on layer boundaries, which result in relatively low E-fields within the layers for the recorded AODs. It also revealed the dependence of the measurement platform from the prevailing meteorological conditions, especially the wind gusts, and lead to the implementation of a new version that would take into account the rotational position of the sensors, so as to quantify the measured field contribution of all the three xyz-components.

In order to target large dust AODs, greater than the ones reaching the Eastern Mediterranean originating directly from a well-studied source, the Sahara Desert, the two major phases of the ASKOS experiment provided the ideal opportunity for extensive dust electrification observations. It also offered the possibility to exploit the particle size distribution sampling from During the next phase of the ASKOS experiment, we re-installed the experimental suite to the premises of the state-of-the-art infrastructure of OSCM. ASKOS gave the opportunity of monitoring massive dust outbreaks, very close to the emitting source, monitor the ground-electric field for reference and exploit the capabilities of various remote sensing instruments for the optical characterization of the dust layer properties. The large number of cases and the subsequent volume of data produced by the campaign, consists an unprecedent dataset for the evaluation of the dust transport models and, solely, as an atmospheric electricity dataset will provide insight in multiple processes, not restrictively constrained to desert dust studies. For the scientific purposes of this thesis, we narrow down to specific case study, a dust affected day with a distinct elevated layer between 2 - 4 km within SAL, discuss the raw output data, compare the electric field profiling measurements obtained by the different instrumentation, while the near ground observations are evaluated with the ground-based fieldmill output. Moreover, the sensors' performance is assessed by utilizing measurements of the co-located Polly^{XT} lidar, for the characterization of the vertical distribution of aerosol optical properties above the launching site. Ultimately, the electric field retrievals from the both the MiniMill and the Space charge sensor coincide with a very good agreement, pointing that although observational variations of the E-field are present within the layer where bipolar charge stratification is present, our indications show that the E-fields are not adequate enough to produce

a total vertical orientation of the particle sizes present. Nonetheless, a thorough study of the electrification processes during ASKOS is conducted by combining the quality assured vertical profiling measurements and will be published in the near future.

5.1. Vertical profiling during the pre-ASKOS campaign

An extensive preparatory measurements period was organized in Cyprus during November 2019, in the framework of the ASKOS 2022 activities, coordinated by the NOA-ReACT team. The campaign focused on the preparation and testing of novel instruments that would continuously monitor desert dust activity, and also, aimed at monitoring the electrical properties of lofted dust layers along with meteorological conditions over an observational site that would provide characteristic conditions of the Eastern Mediterranean environment. for this purpose, two operational sites were selected at the wider residential area of Nicosia (Aglantzia-CyI, 35°08'30.8"N 33°22'51.8"E) and the rural site of Orounda (CyI-UAV Research Laboratory site, 35°05'41.3"N 33°04'53.8"E). Balloon launches were instrumented from both locations during early morning and mid-noon hours (Table 5.1) under varying dust load conditions.

Table 5.1: Launches calendar during the pre-ASKOS phase in Cyprus.

Observational Day	Launch (UTC)	Instruments[6]	Measured quantities
12/11/2019	12:38:28-13:30:56	MiniMill, IC	E-field (Vm^{-1}), ion density (cm^{-3})
14/11/2019	12:51:23-13:54:50	MiniMill, IC	E-field (Vm^{-1}), ion density (cm^{-3})
15/11/2019	11:07:51-12:41:23	MiniMill, IC	E-field (Vm^{-1}), ion density (cm^{-3})
16/11/2019	13:00:33-14:06:30	IC	ion density (cm^{-3})
17/11/2019a	08:05:46-08:49:33	IC	ion density (cm^{-3})
17/11/2019b	10:29:26-11:36:19	MiniMill, IC	E-field (Vm^{-1}), ion density (cm^{-3})
18/11/2019	11:08:44-12:37:42	MiniMill, IC	E-field (Vm^{-1}), ion density (cm^{-3})

[6] MiniMill: Miniature fieldmill v1, IC: ion counter

5.1.1. Data Acquisition and Processing

Measurements of the vertical electric field strength and atmospheric ion density along the altitude were performed with the initial prototypes of tethered low-cost, portable and disposable atmospheric electricity sensors (see Section 3.3). The first instrument, and most widely used for similar applications, was a miniature fieldmill electrometer, similar to the instrumentation discussed by Harrison and Marlton (Harrison and Marlton, 2020). During the soundings, the MiniMill was mounted, with the rotating vane flat-ground, on a DFM-09 GRAW meteorological radiosonde providing pressure, temperature, wind speed/wind direction measurements while the mill data were interfaced to the embedded XDATA radiosonde protocol, in a similar way as discussed in Section 3.3.3. Complementarily to the electric field measurements, atmospheric ion density was measured with the use of the commercially low-cost KT-401 Air Ion Tester Counter, a miniature hand-held ion counter mainly used for measurements of in-lab ion concentrations. The tester measures ion density in single polarity by logging the maximum value of either the positive or negative ion population at each recording and was specifically altered in order to convert the instrument LED reading to a 16-bit transmission package. In order to have co-located measurements with the varying electric fields, the ion counter was also mounted close to the minimill during launch and the data were transmitted through a dedicated Lora long-range telemetry system. Moreover, the AOD was monitored by two co-located Cimel sunphotometers in Agia Marina Xyliatou (when the launching site was in Orounda) and Nicosia, respectively, integrated in the Aerosol Robotic Network (AERONET, https://aeronet.gsfc.nasa.gov/, last access: 3 February 2021).

For the specific study, we exploit the collected dataset from between November 12th to November 18th 2019 and, as a first step, compare the minimill outputs with the fair weather electric field in order to qualitatively distinguish the field perturbations attributed to charged dust. Ideally, under strict fair weather conditions, complete lack of aerosol particles in the atmospheric circulation is expected, since it guarantees that the only mechanism of atmospheric ions loss is the ion-ion recombination. As the concentration of aerosols increases, additional loss can be due to ions attaching to the particles, which leads to a perturbation of the ion density from fair weather values. In the steady state of a fair weather electrified atmosphere, the conduction current equals to zero, hence the vertical electric field strength is given by, the simplistic yet not so confining for this research, Equation (4.7):

$$E_{z,FW} = -\frac{V_{ion}}{l \exp\left(\frac{z}{l}\right)\left(1 - \exp\left(-\frac{H}{l}\right)\right)}$$

5.1.2. Electric Field Strength profiles

We present the profiles of the electric field strength (V m^{-1}) measured with the miniature field mills during days that were affected by dust outbreaks over Cyprus from the two launching locations of Orounda and Aglantzia (Figure 5.1) and the atmospheric ionic content (ions cm^{-3}) as measured by our custom ion counters (Table 5.1). The calculated fair weather electric field is overplotted with the data (Figure 5.1, black line) in order to discern potential divergence from the steady state electrical content. E-fields generally follow the exponential decrease with the altitude, remain in the same order of magnitude as the fair weather electric field which indicates a weak electrification profile (Figure 5.1, top panel-black line).

As seen in most of the cases of Figure 5.1, areas of increased electric field become apparent above the planetary boundary layer, where dust downward mixing occurs. The increases coincide with the presence of elevated dust layers at the specific altitudes, as inferred from the daily average AOD values, but for a better characterization of the optical properties of the particles aloft retrievals of the aerosol properties are needed (e.g., lidar depolarization profiles). Such field perturbations in various heights (same polarity as the fair-weather E-field) denote that atmospheric conductivity decreases in the specific altitudes due to ion attachment to dust particles, and, since the conduction current remains constant the electric field should increase. All data presented here are only from the radiosonde ascending course, as cross-communication over the occupied territories of Cyprus is forbidden and telemetry was manually terminated in most of the cases due to the radiosondes' dominant North-Western orbit. There was an operating co-located pulsating lidar in Nicosia from CIMEL, but the backscatter time-height plots information can be used only to discern the existence of dust particles vertically in the atmosphere, as presented for a typical dust day at 17th November 2019 (Figure 5.1, bottom panel). Generally, all the campaign days were affected with moderate mixed dust-sea salt concentrations up to 1 km in altitude and then there were days that dust reached up to 4 km in a relatively large uniform layer. We tried to avoid launches during times of increased cirrus clouds presence, since the incoming clouds above the station would further disturb the

vertical electric field measured by the minimills but also the local E-field due to conductivity reduction and potential edge effects.

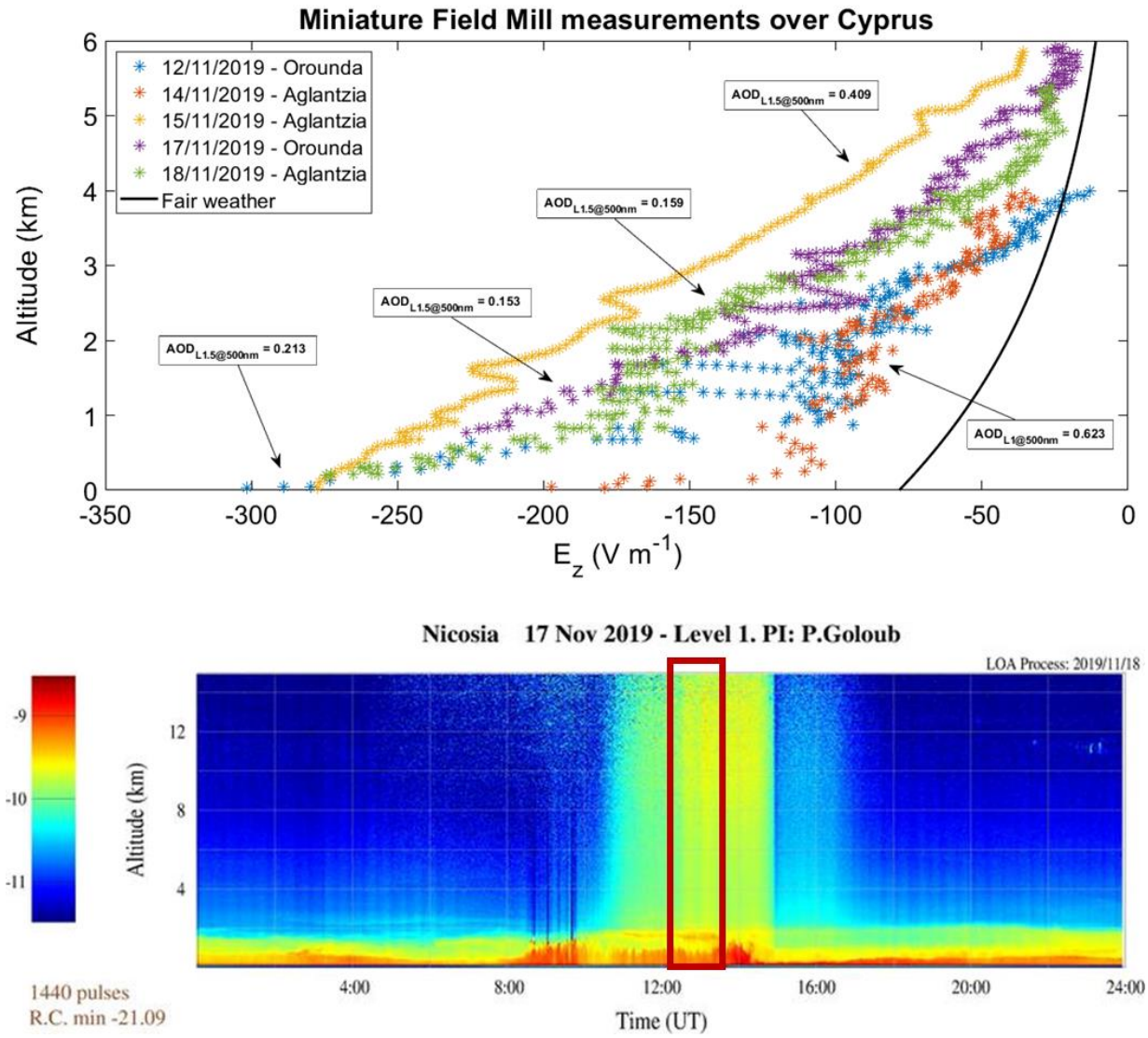

Figure 5.1: **<u>Top panel:</u>** Vertical distribution of the atmospheric electric field strength (various colours), as recorded by five different balloon-borne miniature fieldmill electrometers that were flown on consecutive dust days in Cyprus. The calculated fair-weather (black line) electric field is plotted for comparison. Minus sign indicates that the field points downwards. AOD products are of level 1.5 or level 1 at 500 nm, when the latter was not available for the specific day. **<u>Bottom panel</u>**: Lidar backscatter time-height plot from the co-located lidar in Nicosia, for the dust case in November 17th 2019. Dust is denoted in reddish tones, is

persistent up to ~ 2 Km altitude throughout the day and the red frame is the specific radiosonde launching window.

During the launches, wind perturbations and differential positioning of the radiosonde might result in the overestimation of the recorded electric field, discussed above, due to the mill vanes being exposed to the x-y components of the field or due to the scavenging of charged particles to the sensing electrode by side drifts (Markson et al., 1999). To provide a first estimation of the

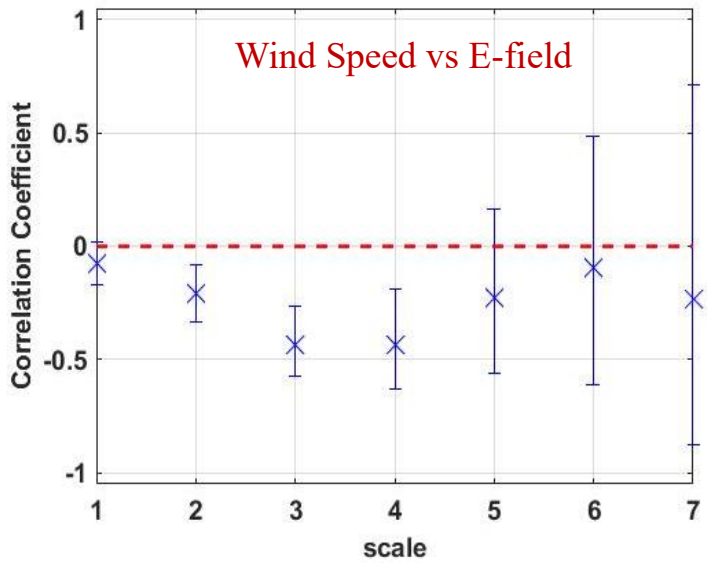

Figure 5.2: Multiscale correlation using the maximal overlap discrete wavelet transform between the measured electric field strength and co-located wind speed values.

similarities between the trends of the electric field and the co-located meteorological parameters, we perform a wavelet correlation analysis on wind speed interpolated DFM-09 data to the measured mill altitudes (Figure 5.2). For the purposes of identification of the possible correlation between the measured E-filed and wind speed, a multiscale correlation using the Maximal Overlap Discrete Wavelet Transform was performed (Benjamini and Yekutieli, 2001; Percival and Walden, 2000; Whitcher et al., 2000). Results indicate the existence of anticorrelation in medium scales which can be explained since the increase of wind speed, which is expected to produce mill's deviation from the vertical position, produces a decreased detection of the vertical component but not rapidly. This is why the anticorrelation is not present in lower scales which correspond to lower periods.

5.1.3. Atmospheric Ion Density profiles

Furthermore, smooth ion density profiles, such as the one over the 12th of November (blue/dark grey markers) exhibit stratifications at altitudes similar to the mills, indicating areas of dust particle accumulation within the layers (Figure 5.3, top and bottom panels). That could potentially explain the loss of ions due to them being attached to the particles, but field values are fairly larger than what is expected through modelling of these attachment rates. This relation between the measured electric field strength and ion attachment rates should be further examined in future research.

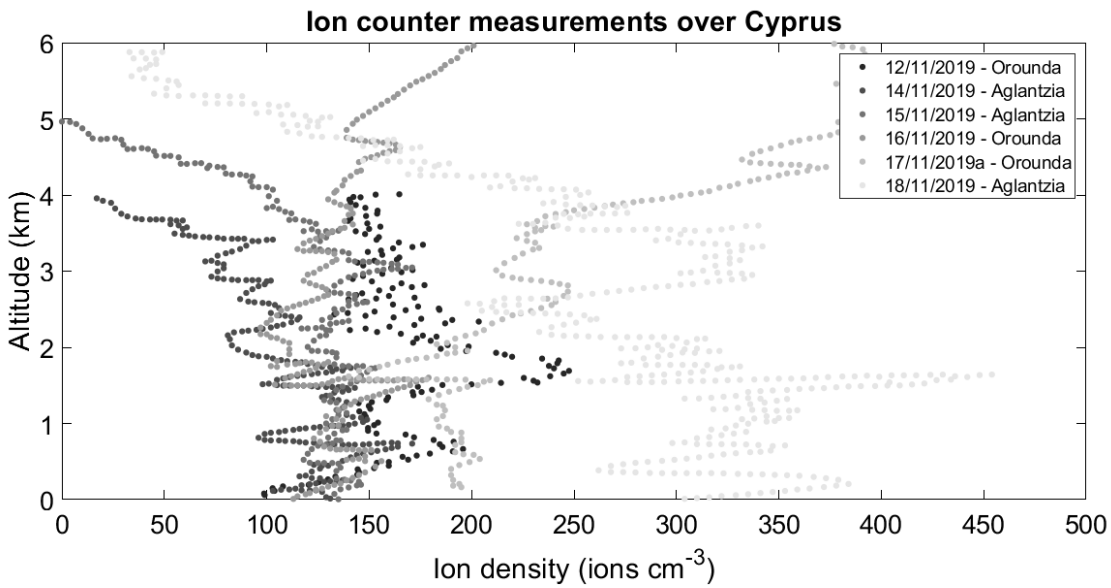

Figure 5.3: Vertical distribution of the ion density (ions cm^{-3}) measured by the custom ion counters for the same launches with the miniature field mills, over the two locations of Orounda and Aglatzia, Cyprus.

5.1.4. Conclusions on the first stage of Profiling

We presented the preliminary profiling results of the electrical properties of Saharan dust layers in the framework of the pre-ASKOS Cal/Val activities and the D-TECT ERC project. A suite of low-cost and disposable atmospheric electricity sensors was tested and tethered to meteorological balloons over dust episodes in Cyprus. The profiling information reveals the presence of charged dust particles within the elevated plumes with accumulation of charges on layer boundaries, as

expected. MiniMill measurements appear to be smooth with perturbations over the transition of the mill within the layer, but significantly deviated due to possible anticorrelation with wind speed. Further analysis with a wavelet correlation technique reveals the potential similarities between these physical parameters.

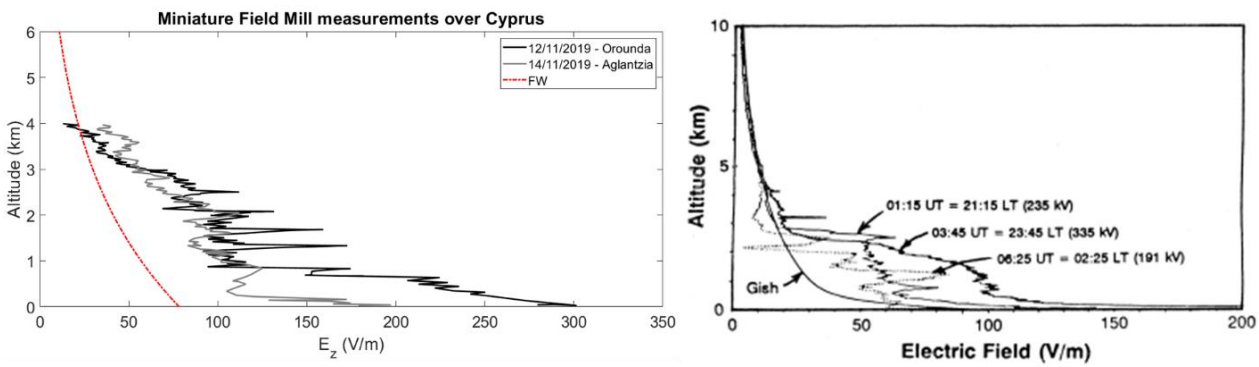

Figure 5.4: Comparison of the E-field behavior between profiling measurements in Australia (right, adapted by Markson et al., 1999) and two cases in Cyprus (left). Spikes in the E-field strength present are attributed to the horizontal drift of the balloon orbit to areas of significantly different columnar resistance than in each the launching site.

By comparing the behavior of two specific E-field profiles (e.g., for the 12/11 and 14/11) up to 4 km with previously reported simultaneous soundings that targeted ionospheric potential measurements by Markson et al. (1999), we observe that the characteristic spike features between 1 to 2 km are present also in our measurements meaning that discrepancies in the measurement may be due to the variable columnar resistance in the areas along the radiosonde paths, that can drift horizontally for more than 30 km at times. Markson et al. (1999) state that in order to compensate for the above and acquire accurate E-field soundings over land: i. air masses with enhanced electric fields in the mixed layer should be avoided, ii. passage through or near clouds should be avoided and iii. preferably, areas with dry air within the PBL that inhibits aerosol growth should be targeted. Considering these guidelines, we have implemented an upgraded version of the Minimill electrometer, incorporate a space charge sensor (see Sections 3.3.1 and 3.3.2) in our launches and choose diverse conditions for their integration in the next phase ASKOS.

5.2. Vertical profiling during the ASKOS campaign

We have highlighted the importance of real-time profiling of the electrical properties in dust layers. These observations are sparse throughout the recent years, mainly due to the very specific requirements in terms of sensor implementations/sensitivity that would be adequately tested so as to provide accurate measurements of crucial parameters. Moreover, the dust layer variability in terms of layer internal structure and particle sedimentation combined with the timescales of particle electrification mechanisms have different timescales, therefore, the data should be spaced tightly apart in order to be assimilated to a time-dynamic model.

5.2.1. Data Acquisition

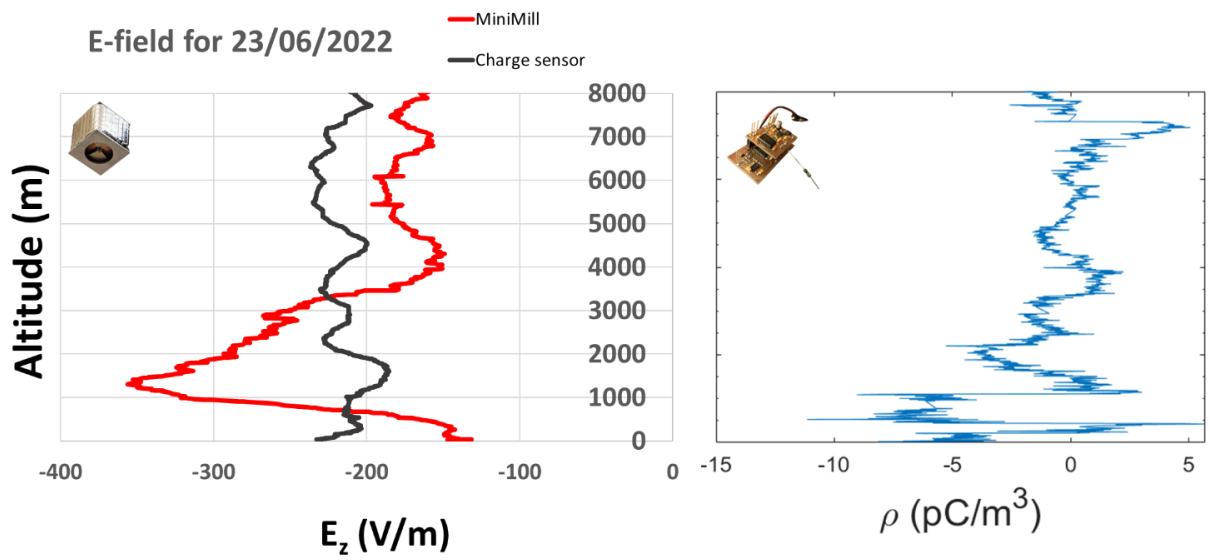

Figure 5.5: Left panel: Raw E-field strength in V m^{-1} from the MiniMill (red) and the calculated E-field from the Space Charge sensor (dark grey). Right panel: Raw space charge density in pC m^{-3} (blue).

The MiniMill provided directly the atmospheric electric field strength, while the charge sensor provided the space charge density (directly) and the electric field strength (indirectly) for an average altitudes of ~ 14 km. The sensors' data were transmitted through an XDATA protocol chaining to the DFM-09 GRAW radiosondes, with co-located P, T, U meteorological parameters. We focus on the electricity launch (electrosonde term coined after ASKOS) of the 23rd June 2022 (Figure 5.5),

released at 17:58:15 UTC. In this following subsections the post-processing procedure of the measurements is described for the derivation of the final values of the electric field vertical profiles.

5.2.2. MiniMill Processing Methodology

Electric field measurements from the MiniMill were found to be sensitive to the instrument's rotation with respect to the vertical axis (the roll and pitch angles). Therefore, a correction is necessary in terms of the following expression:

$$E_z^{cor} = E_z^{meas} \cos\theta_{roll} \cos\theta_{pitch}, \tag{5.1}$$

where E_z^{cor} is the corrected value of the vertical electric field component, E_z^{meas} is the measured value, θ_{roll} is the roll angle and θ_{pitch} is the pitch angle. Moreover, values of the electric field strength that correspond to angular difference larger than π radians between two consecutive measurements of the roll and pitch angles are neglected, because for these values the MiniMill plates will point upwards instead of downwards.

5.2.3. Charge Sensor Processing Methodology

The measurements from the charge sensor are less sensitive to its rotation, due to its symmetric, spherical electrode. Under the assumption that the electric field is mainly vertical everywhere, except on the boundaries of the charge layer (since its horizontal extend it much larger than its vertical depth), the electric field can be calculated from the measured total charge density using the following expressions:

$$\frac{d^2V}{dz^2} = -\frac{\rho_{tot}}{\varepsilon_0}, \tag{5.2}$$

$$E_z = -\frac{dV}{dz}, \tag{5.3}$$

where V is the electrical potential, ρ_{tot} is the total charge density, and ε_0 is the vacuum permittivity. Equation (5.2) is solved using an SOR (Successive-over-relaxation) algorithm, with the value of the electrical potential being set equal to zero at the ground, and equal to 250 kV at 40 km altitude (from the GEC considerations). Another issue that had to be addressed is the self-calibration feature of the space charge sensor. Every 5 minutes the space charge sensor enters a self-calibration mode, which lasts for approx. 20 seconds. Being at this mode, the sensor measurements are discarded, which results in appearance of measurement gaps and therefore discontinuities in the space charge vertical profile, that influence the derived potential and electric field values. The gap problem can be solved by taking advantage of the Poisson's equation linearity. The domain can be divided in sub domains, each one between the calibration states of the sensor. The values of the total charge density outside the range of the sub domain are set equal to zero. The electric field distribution as calculated from the Poisson's equation at each sub domain, at the electro-sonde altitude range of 0-15 km, and the total vertical profile is the summation of the electric field values due to all the sub domains.

As the balloon ascends, the atmospheric conditions (such as the temperature which falls to values below zero) deteriorate the battery life and the reliability of the measurements can become questionable. Therefore, not all the sub domains are taken into account for the calculation of the electric field vertical profile, but only those whose total contribution leads to electric field values at the ground closest to the values measured by the ground fieldmill or by the MiniMill, if for some reason the ground fieldmill measurements are not available during the electro-sonde launch period.

5.2.4. Results and Discussion

Figure 5.6a depicts the vertical profile of the corrected electric field vertical component derived from the MiniMill and the space charge sensor for the selected day. It is clear that both instruments are in principle in a good agreement. Moreover, the electric field strength value is the same order of magnitude with the one that corresponds to the fair weather conditions at about -100 V/m. Figure 5.6b shows the vertical profile of the total charge density. As shown, the charge density exhibits its highest values at altitudes below 500 m due to the presence of low clouds within the MBL, and as the altitude increases the value decreases trending towards its fair weather values, as expected.

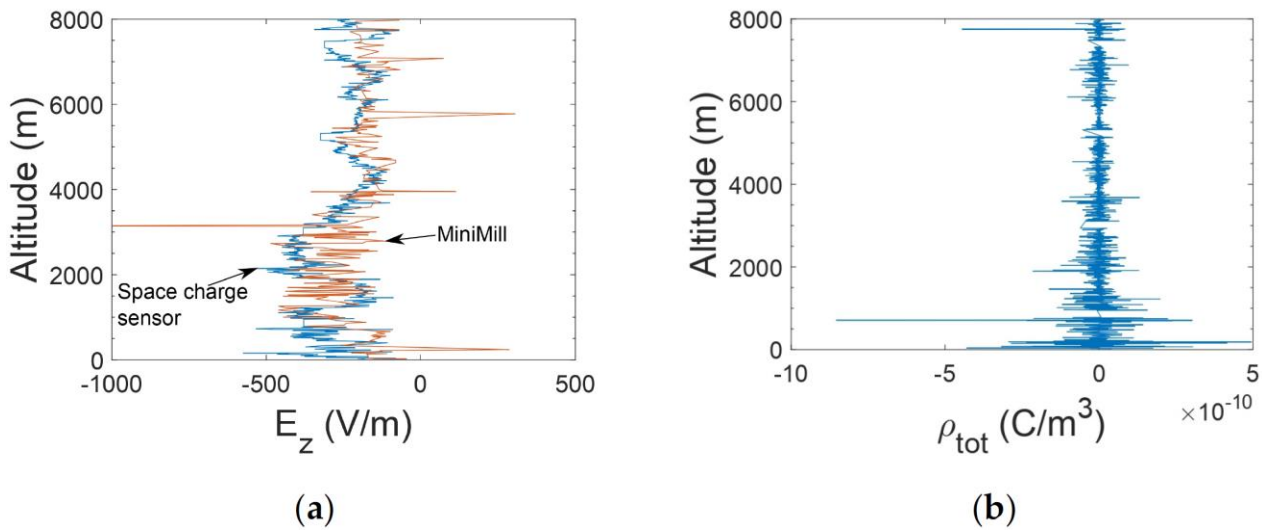

Figure 5.6: Vertical profiles of the electric field vertical component and the total charge density: (a) The corrected vertical profiles of the electric field vertical component measured by the MiniMill and the space charge sensor; (b) Vertical profile of the total charge density measured by the space charge sensor.

Figure 5.6 illustrates an assessment of the performance of the MiniMill and the space charge sensor, while at the same time it provides insights on the behavior of their measured quantities. In Figure 5.6a, we obtain a time-height plot of the attenuation backscatter coefficient (top panel) and the depolarization ratio (bottom panel) from the Polly^{XT} lidar, that are characteristic of dust presence in the area and can delineate the dust layer's structure. It is apparent that up to 1 km there are low altitude clouds resulting to large backscatter values, and then the dust layer that gradually extends to an altitude range between 2 - 4 km. It is expected for the electric field to increase inside the clouds and within the dust layer and to decrease in the intermediate regions (Harrison et al., 2020; Mallios et al., 2021a). On the other hand, an enhancement of the total charge density at the boundaries of both the cloud and the dust layer is anticipated, and a decrease in the intermediate regions. At the top panel of Figure 5.7b, the smoothed vertical profile of the electric field vertical component as derived by the MiniMill and the space charge sensor is depicted. The smoothing has been performed by a running average algorithm with a time window of 3 minutes, for the elimination of fast temporal variations. According to the MiniMill there is a gradual increase of the electric field strength up to 1.5 km altitude, and then a gradual decrease. This does not coincide with the expected behavior. Contrarily, the results of the space charge sensor show a gradual increase of the electric field up to 1 km (which is approximately the top of the cloud) and then a

gradual decrease up to 1.5 km altitude (the intermediate region between the cloud and the dust layer). Then, there is a gradual increase with altitude inside the dust layer up to 3 km altitude, which is approximately the center of the dust layer and then a decrease as the latitude increases to values higher than 4 km the top of the dust layer. The two peaks at 2 km altitude and 2.7 km altitude are most likely due to internal stratification of the layer. Therefore, it can be concluded that the pro-file obtained by the space charge sensor is in better agreement with the expected profile by the theory.

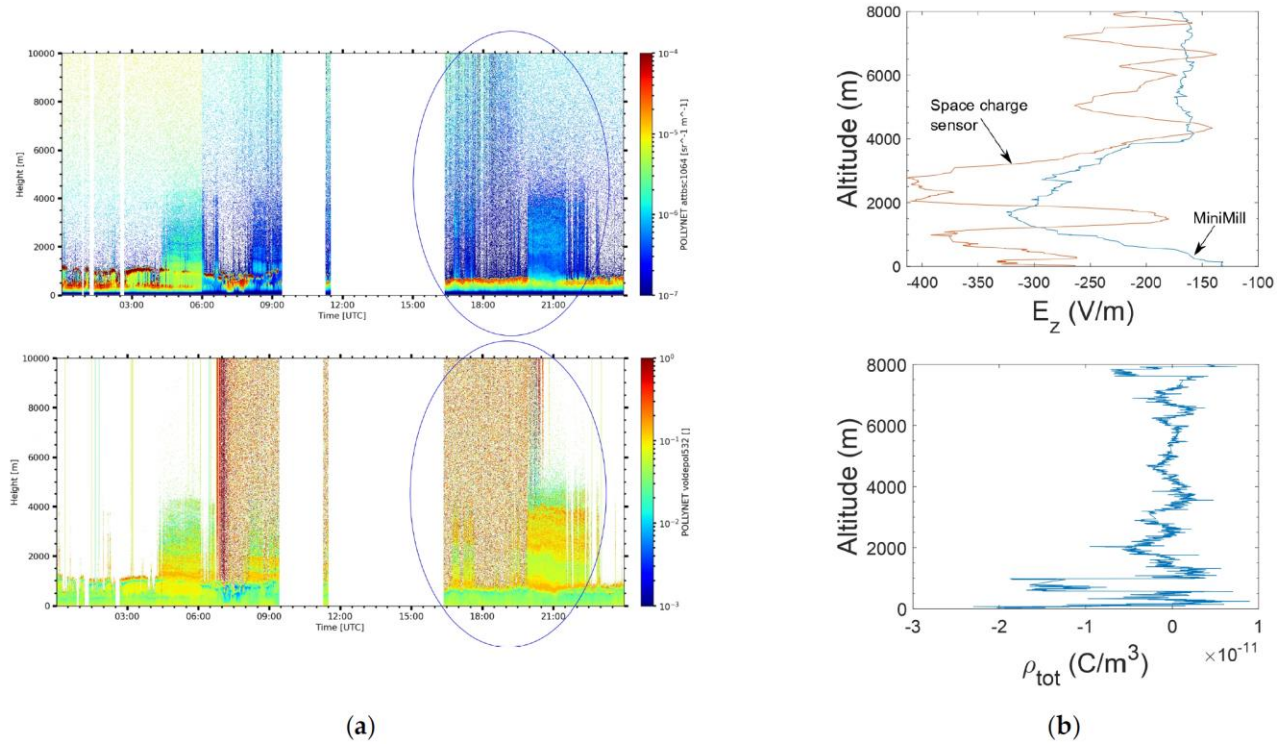

(**a**) (**b**)

Figure 5.7: Assessment of the measurements with the PollyXT lidar products: (a) Attenuated backscatter co-efficient at 1064 nm (top panel) and volume depolarization ratio (bottom panel); (b) Smoothed vertical profiles of the electric field vertical component (top panel) and smoothed vertical profile of the total charge density (bottom panel).

Similar conclusions can be derived by the vertical profile of the total charge density (bottom panel of Figure 5.7b). In this case, the extremum values of the charge density (maximum values of opposite polarity) indicate the boundaries of a particle layer, either a cloud or a dust layer. The presented profile shows a stratification inside the dust layer. One sub layer can be identified in the range 1.5-3 km, and another sub layer in the range 3-4.5 km. This is in agreement with the bottom panel of Figure 2a, where there is a layer between 2 and 3.5 km, and a layer between 3.5-4 km.

5.2.5. Conclusions on the second stage of Profiling

Synergistic measurements of the vertical atmospheric field and the total charge density in the presence of dust events are presented through the launches of balloon-borne instrumentation, including a MiniMill electrometer and a space charge sensor, under dust events during ASKOS experimental campaign, in June/September 2022. There is a calculated agreement in the values of the electric field vertical component strength measured by the two different instruments, which in turn is of the same order of magnitude with the fair weather electric field strength. However, the vertical profile obtained by the space charge sensor is more accurate than the one obtained by the MiniMill, as can been seen in conjunction with the lidar products. This difference can be attributed to the high sensitivity of the MiniMill to the meteorological conditions that cause perturbations to its axis with respect to the vertical direction. Further work that will characterize the sensors' response for various of the measured cases is intended.

Chapter 6

Observations of Dust Orientation with SolPol[7]

Chapter 6 encompasses all the effort behind consistent measurements of linear polarization under clear and dusty sky conditions with a novel instrument such as the SolPol, the characterization of our measurements and the attempt to physically interpret the complex observations in terms of indications for particle orientation. Sections 6.1 and 6.2 comprise the core observations section where we present the total acquired dataset a selected two-year operation in Antikythera and compare between days affected by elevated dust layers and days without. Then, in Sections 6.3 to 6.4 we discuss the dependence of the derived orientation trends to crucial parameters such as the Sun's position and the aerosol optical depth (AOD) so as to verify that the excess in LP is attributed to preferentially oriented dust particles within the examined layers. Detailed calculations for the methodologies and technical descriptions presented in the chapter are provided in Appendix A.1.

6.1. Aerosol Optical Properties

We present the observational dataset of SolPol acquired in 2020 and 2021, when the instrument was installed at the PANGEA observatory in Antikythera, focusing on linear polarization measurements.

[7] **This chapter is based on my contribution in:**

Daskalopoulou, V., Raptis, P. I., Tsekeri, A., Amiridis, V., Kazadzis, S., Ulanowski, Z., Charmandaris, V., Tassis, K., and Martin, W.: *Observations of Dust Particle Orientation with the SolPol direct sun polarimeter*, Atmos. Meas. Tech. Discuss. [preprint], https://doi.org/10.5194/amt-2023-121, accepted, 2023.

SolPol's behaviour during this period is consistent with previous operations when tested in indoors conditions. Generally, observations were initiated just after sunrise and terminated before sunset when the Sun disk started to be shadowed by nearby topography. Before each deployment, the instrument general condition was thoroughly checked in terms of instrument alignment, tracking accuracy, power supply levels consistency and the optimal communication between peripherals and the assembly control units to ensure minimum mishaps or potential disconnections of the assembly rotator. Overall, this is a good report of a novel instrument with an exquisite degree of sensitivity and accuracy. It also provides a unique data set of observations of atmospheric linear polarization and a description of its features, all information very useful to understand the new batch of space borne polarimeters in the upcoming years.

Circular polarization (CP) by scattering at aerosols, cloud droplets, and ice crystals is several orders of magnitude smaller than linear polarization, while scattering by the molecular atmosphere is expected to not cause any circular polarization (e.g. Emde et al., 2017). Kemp et al. (1987) report CP values of the order of $\sim 3 \times 10^{-6}$ in 550 nm, for the case of targeting specific cardinal co-ordinates in the Sun's disk, with half the aperture angular diameter used in SolPol. These measurements could potentially be enhanced by regions of intense magnetic activity and strong area-dependent circular polarization near the solar limb. While, to our understanding, in the whole Sun disk measurements CP values drop to the order of $\sim 10^{-7}$ due to mainly the use of a larger aperture that would increase the observed effective diameter and subsequently, if the increase in circularly polarized flux (V) is not linear to the increase in total solar flux (I), the CP will decrease. This is similar to what is observed by SolPol in the forward scattering direction, where CP is 1-2 orders of magnitude less than LP under dust presence and near-zero for background days. A thorough review by Gassó et al. (2022) on circular polarization by atmospheric constituents, proposes that circular dichroism from aligned atmospheric dust particles could produce CP features but its magnitude has not been defined yet. Since the phenomenon is expected to be borderline detectable with the discussed polarimeter configurations, in interstellar dust degrees of LP and CP by aligned grains become comparable (Kolokolova and Nagdimunov, 2014), we choose to focus on linear dichroism observations and attempt to reproduce the findings of Bailey et al. (2008). For that reason, the Stokes V parameter observations and analysis with SolPol are not discussed here but we aim to further process these data in future studies.

6.1.1. Characterization through the Polly^{XT} lidar

For the comprehensive characterization of the vertical distribution of aerosol optical properties, we exploit the profiling capabilities of the co-located Polly^{XT} Raman polarization lidar (Engelmann et al., 2016) of the National Observatory of Athens (NOA), as part of the European Aerosol Research Lidar Network (EARLINET - https://polly.tropos.de/calendar/location/38?&individual_page=2020, last visited: 16/12/2022). This multi-wavelength system is equipped with three elastic channels at 355, 532 and 1064 nm, two vibrational Raman channels at 387 and 607 nm, two channels for the detection of the cross-polarized backscattered signal at 355 and 532 nm, and one water vapour channel at 407 nm. The basic lidar quantity used is the Volume Linear Depolarization Ratio (VLDR, δ_v) at 532 nm. VLDR (%) is the ratio of the cross-polarized to the co-polarized backscattered signal (Freudenthaler et al., 2009), where cross- and co- are defined with respect to the plane of polarization of the emitted laser pulses. VLDR values are influenced by both atmospheric particles and molecules, with high δ_v values being indicative of irregularly shaped particles (i.e., atmospheric dust). Typical δ_v values for Saharan dust are in the range of 20 % to 30 % at 532 nm (Haarig et al., 2017). The 2020 and 2021 dust events reaching Antikythera, presented herein, are characterized by generally large concentrations of airborne dust particles from the middle of the day onwards with δ_v exceeding 15%, followed by dust settling towards the ground at late afternoon. The dust layers are mostly detached and homogeneous with some vertical mixing with non-depolarizing marine particles occurring within the Marine Boundary Layer (MBL).

6.1.2. Aerosol Optical Depth (AOD) measurements

The Aerosol Optical Depth (AOD) was monitored by the CIMEL sunphotometer, part of the NASA Aerosol Robotic Network (AERONET - https://aeronet.gsfc.nasa.gov/, last visited: 12/12/2022), which was also installed in PANGEA along with Polly^{XT} and SolPol. For all the cases examined, mean AOD values were used and varied from 0.047 to 0.502 at 500 nm. Moreover, near-surface wind speed measurements presented here were obtained from a co-located Davis Vantage Pro2 weather station at an altitude of 198 m asl.

6.2. Polarization Measurements

Figure 6.1 consists of a collection of all the recorded days within this timeframe, where measurement set durations within the day varied between consecutive sixteen-minute sequences to the maximum two-hour retrievals. We subplot the *Q/I* (black dots), *U/I* (purple dots) and DOLP (blue dots) parameters again in ppm with time of the day in UTC, for cases of both lofted dust layers reaching the station and cases with background/clean conditions.

We label the days as dust driven (D) days with various dust loads, clean days (C) that are mostly characterized by concentrations of marine particles within the MBL, but lack dust particle presence, and of half-clean (HC) days where dust presence becomes prominent sometime within the day and potentially mixes within the MBL. This classification is inferred from the Polly^{XT} VLDR values for each day (not presented here for all the cases for brevity reasons, but can be publicly accessed in the Polly-NET website https://polly.tropos.de/) and the AOD values by AERONET. We also include a dedicated test day (TD) with diffuse light testing for various SolPol aperture sizes (see Section 6.5) and two consecutive half-day retrievals with a relatively high dust load for which a larger aperture was used.

6.2.1. Reference Cases

Focusing on DOLP behaviour for clean days, the measured polarization values span from $0.5 \cdot 10^{-6}$ usually at local noon when linear polarization of transmitted sunlight is expected to minimize in near zenith viewing angles, up to 50 x 10^{-6} in large solar zenith angles (i.e., early in the day or in the afternoon). Minimum linear polarization values for these days are consistent with early observations of polarization from the whole Sun at the same spectral region as SolPol, noted in Kemp et al. (1987) work using a similar polarimeter apparatus. Moreover, the maximum values indicate the maximum bias consisting of pure Rayleigh scattering events, by the molecular atmosphere at low altitudes, within the SolPol FOV and the total instrumental errors that can add to the light polarization state. A statistical analysis of all the clean day results is discussed in detail in Section 6.3 and determines the exact reference instrumental bias.

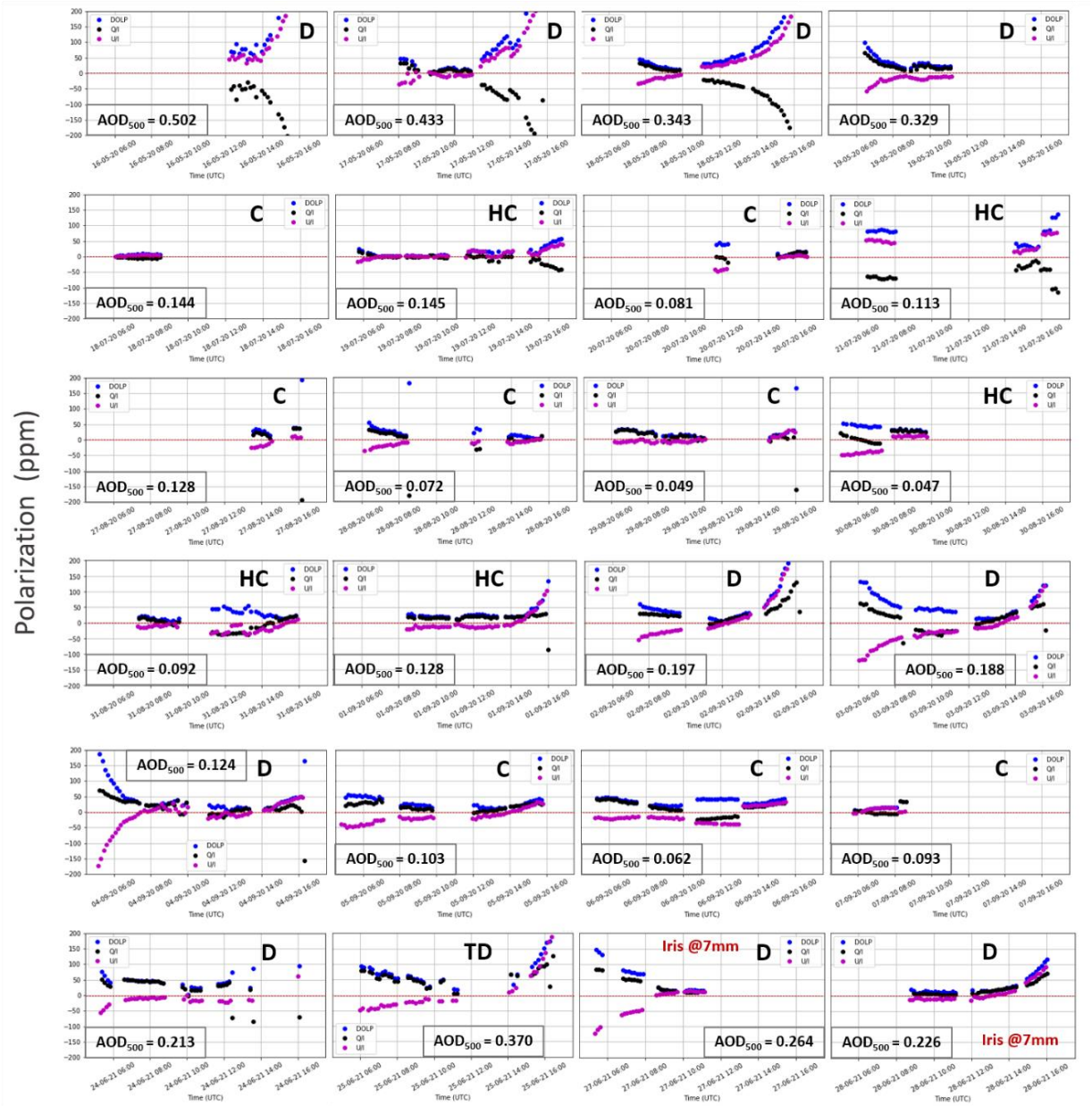

Figure 6.1: Complete SolPol linear polarization measurements acquired between May 2020 to June 2021 at the PANGEA observatory, Antikythera. Each daily observation consists of the normalized *Q*/*I* (black dots), *U*/*I* (purple dots) and DOLP (blue dots) in ppm with time, while labels D: stands for dust driven days with various loads, C: for clean days with low aerosol content, HC: for half-clean days where dust outbreaks occurred at some point within the day, and TD: is a dedicated test day with alternating iris sizes. Mean AOD level 1.5 values are provided for each day by AERONET (https://aeronet.gsfc.nasa.gov/, last visited: 12/12/2022). DOLP values during clean (C) days determine the instrument noise level for the polarization measurements, while during dust events (D) the DOLP values peak early in the morning and in the afternoon, reaching polarization values of more than 200 ppms per case.

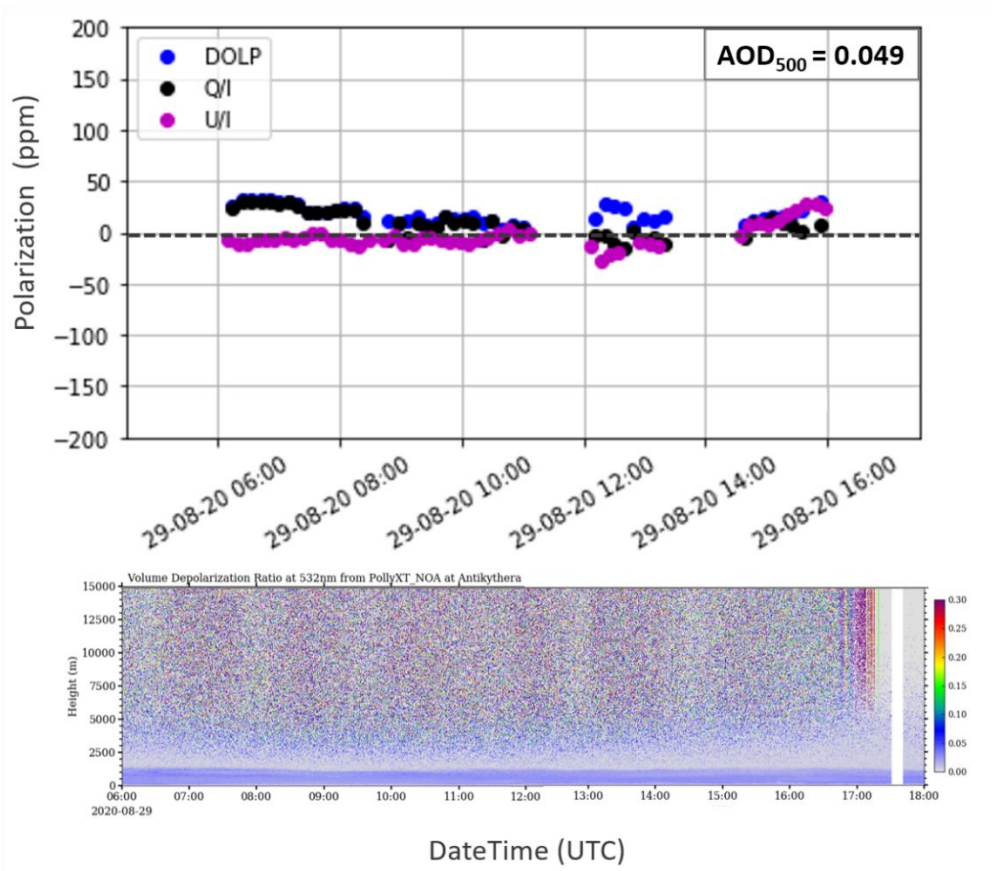

Figure 6.2: **<u>Top panel:</u>** Daily progression of linear polarization (in ppm) for the measurements on 29 August 2020, at the PANGEA observatory in Antikythera, expressed through the normalized *Q*/*I* (black dots), and *U*/*I* (purple dots) Stokes parameters and DOLP (blue dots). All values do not exceed the 50 ppm threshold regardless of the instrument viewing angle. **<u>Bottom panel:</u>** Time-height plot of the Volume Linear Depolarization Ratio (δ_v) at 532 nm with the altitude, as retrieved from the Polly^{XT} lidar at PANGEA for the same day. Low δ_v values denote that there is low concentration of depolarizing particles for the total duration of the SolPol measurement.

A typical measurement for a clean day behaviour is provided for the August 29th 2020 case study which was chosen above for the bias correction comparison and is delineated in Figure 6.2. The top panel presents the daily progression of the linear polarization parameters in ppm expressed through the *Q/I* (black dots), and *U*/*I* (purple dots) Stokes parameters and DOLP (blue dots). Measured linear polarization does not exceed the 50 ppm threshold regardless of the instrument viewing angle from the zenith, the average daily AOD has a low value of 0.049 in 500 nm, while the SolPol retrieval is compared to the time-height plot of the VLDR at 532 nm, as retrieved from the Polly^{XT} lidar. Low δ_v values (< 5 %), shown in blue tones, denote that there is a generally low concentration of non-depolarizing particles within the MBL for the total duration of the SolPol measurement, thus no indication of desert dust presence.

6.2.2. Dust-driven Cases

Under dust driven days, the dissimilarity becomes apparent. The most interesting feature with the presence of dust particles are the large polarization values towards the morning and evening of each measurement day. Linear polarization values reach up to 700 ppm in extreme cases. Such values are exhibited during heavily dust affected days, e. g. from the 16/05/2020 to 18/05/2020 where we have recorded the largest dust optical depth values for the specific period of observation (Figure 6.1). The increasing trend of the DOLP values with time (usually after 14:00 UTC) is mirrored in early morning measurements as the instrument monitors the atmospheric column with a decreasing SZA. This is our first consistent indication that preferentially - vertically or horizontally - aligned dust particles could be present in the observed layers and cause the dichroic extinction of transmitted sunlight through the layer. The specific trend is also in line with the reported observations in La Palma by Ulanowski et al. (2007), which were later demonstrated in detail by Bayley et al. (2008), that showed a fractional linear polarization increase with increasing SZA during dust events. And that polarization exhibited changes for different days roughly in proportion to the change in dust optical depth. Figure 6.1 illustrates the collective and quantitative behavior of the observed days for up to 200 ppm so that the clean day trends are also discernible in comparison, while the exact polarization values are discussed in the following sections where we group all the above observations with respect to the solar zenith angle.

To better describe these high values of the dichroic extinction of sunlight passing through dust layer(s), a dust-affected case study on September 2nd 2020, is also highlighted (Figure 6.3). During the specific day, a transient dust layer originating from the Western Sahara travelled towards the station, and was monitored reaching the Polly^{XT} lidar system already one day before, at altitudes between 2.5 km and 5 km. The dust layer continued progressing through the day with some downward mixing of settling dust particles within the MBL occurring between 04:00 and 06:00 UTC, but then the layer detached and the larger concentrations, denoted with red tones in the VLDR quicklooks (> 20-25 %), accumulated between 2 km and 3 km creating a thin layer that persisted within the day. It is also observed that the near-ground dust concentration is very low, with the very thin layer created below 500 m after about 15:00 UTC, being potentially a mixture of dust particles and particles of marine origin with δ_v values around 15 % (at this height range lidar overlap issues may be present). The day had zero cloud cover and a nominal irradiance curve was recorded by the

SolPol detector (Figure 3.10). As presented in the polarization graph (Figure 6.3, top panel), the degree of linear polarization shows a decreasing trend from early morning as the day progresses towards local noon. Although the measurement sequence started a bit later than the previously presented clean day sequence, the trend is clear. The DOLP values are low, ~ 2 ppm near zenith, and reach up to 400 ppm when the observed increasing trend maximizes at the end of the sequence just before 16:00 UTC. The excess in linear polarization above the 50 ppm threshold (inferred from the reference day) becomes prominent for this case.

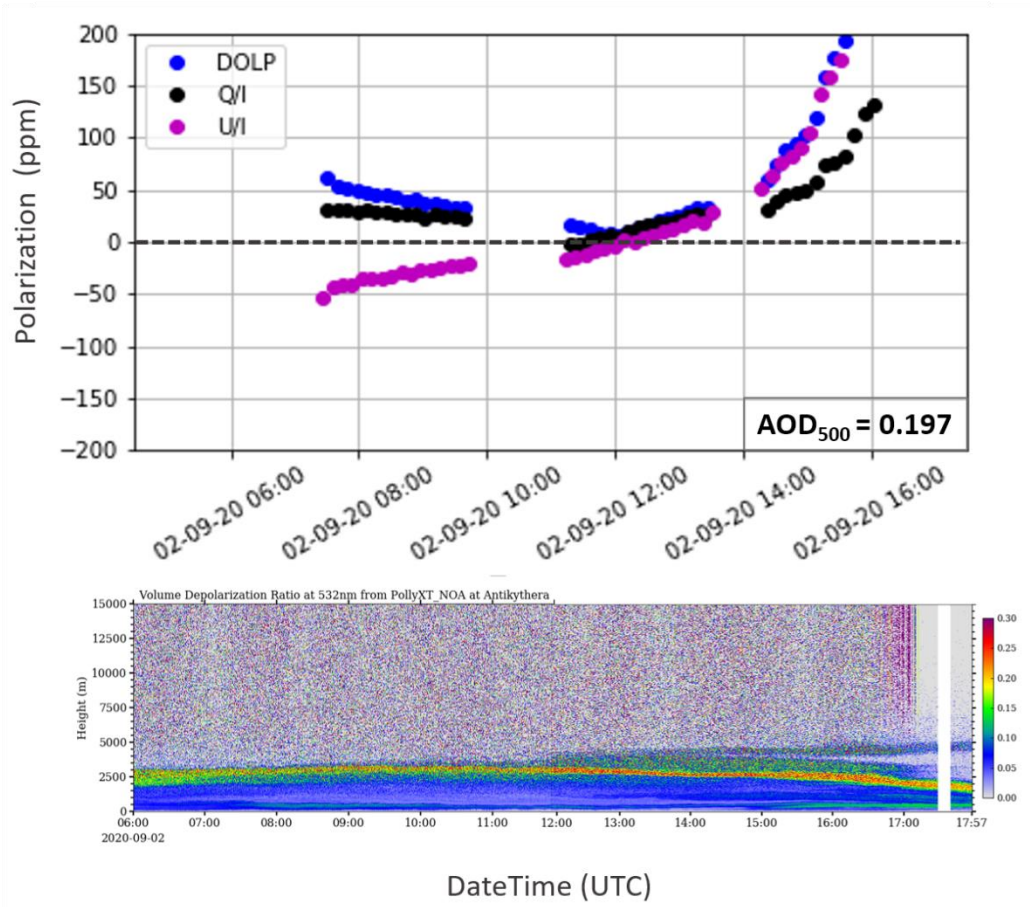

Figure 6.3: **<u>Top panel:</u>** Daily progression of linear polarization (in ppm) for the measurements on 2 September 2020, at the PANGEA observatory in Antikythera, expressed through the normalized *Q*/*I* (black dots), *U*/*I* (purple dots) Stokes parameters and DOLP (blue dots). The increase in linear polarization is exhibited before 08:00 and after 14:00 UTC when the instrument viewing angle increases significantly with respect to the zenith. **<u>Bottom panel:</u>** Time-height plot of the Volume Linear Depolarization Ratio (δ_v) at 532 nm, as retrieved from the Polly^{XT} lidar at PANGEA for the same day. High δ_v values (> 15 %) are indicative of dust particle presence and larger concentrations of dust are denoted with dark orange hues.

6.3. Dependence of the Degree of Linear Polarization (DOLP) on the Solar Zenith Angle (SZA)

Consequently, we discuss the basic factors that can influence the linear polarization behaviour and produce the excess polarization. We, firstly, analyse the dependence of DOLP to the SZA and determine the instrumental noise level based on our reference days. Then, we illustrate the evolution of DOLP with respect to the increasing optical depth and airmass. We further attempt a linear regression between DOLP and high AOD values, while lastly the effect of incident diffuse light, over SolPol's aperture, to the polarization trend is discussed for a dedicated test measurement day.

As the SZA increases, particles that are preferentially aligned can be viewed by different angles and in the aspect that larger number concentrations are present within the instrument line-of-sight. It is, therefore, expected that on near-zenith angles, particles that are aligned with their long axis vertically will not influence the polarization and result in near zero values, similar to what was previously reported on aligned grains (Bailey et al., 2008; Kolokolova and Nagdimunov, 2014). In Figure 6.4, we present an analysis of DOLP measurements in ppm as a function of the solar zenith angle in degrees, for the cases of the selected clean/reference days (Figure 6.4a) and under the observed dust events (Figure 6.4b). A total of eight days per category were used, while days labelled as half-days, the test day and two days with larger irises were excluded. LP in clean days does not exceed the strict 50 ppm limit that was discussed for the single case of Section 4.1.1, regardless of the SZA. This is clearly depicted in the zoomed representation (Figure 6.4c) that modifies the instrument noise threshold (shaded area) accordingly, given that the dataset is statistically significant and that clean days are interspersed between the recorded dust events.

Figure 6.4b illustrates that LP increases with solar zenith angle under dust driven days, a trend that starts at about 30° and is obvious mainly after 50° SZA, with a maximum value of ~ 7×10^{-4} being observed at 74°, which is over one order of magnitude larger than the noise level. Moreover, the polarization curve changes from day to day roughly in proportion to the change in the dust optical depth. This becomes more apparent for large SZAs when dust particle concentrations persist within the day. The segregation between reference days and dust driven days, along with the distinct behaviour of DOLP with increasing SZA is consistent with the findings from stellar polarimetry

(Bailey et al., 2008; Ulanowski et al., 2007) and provides the first indications of particle preferential orientation with a solar polarimeter.

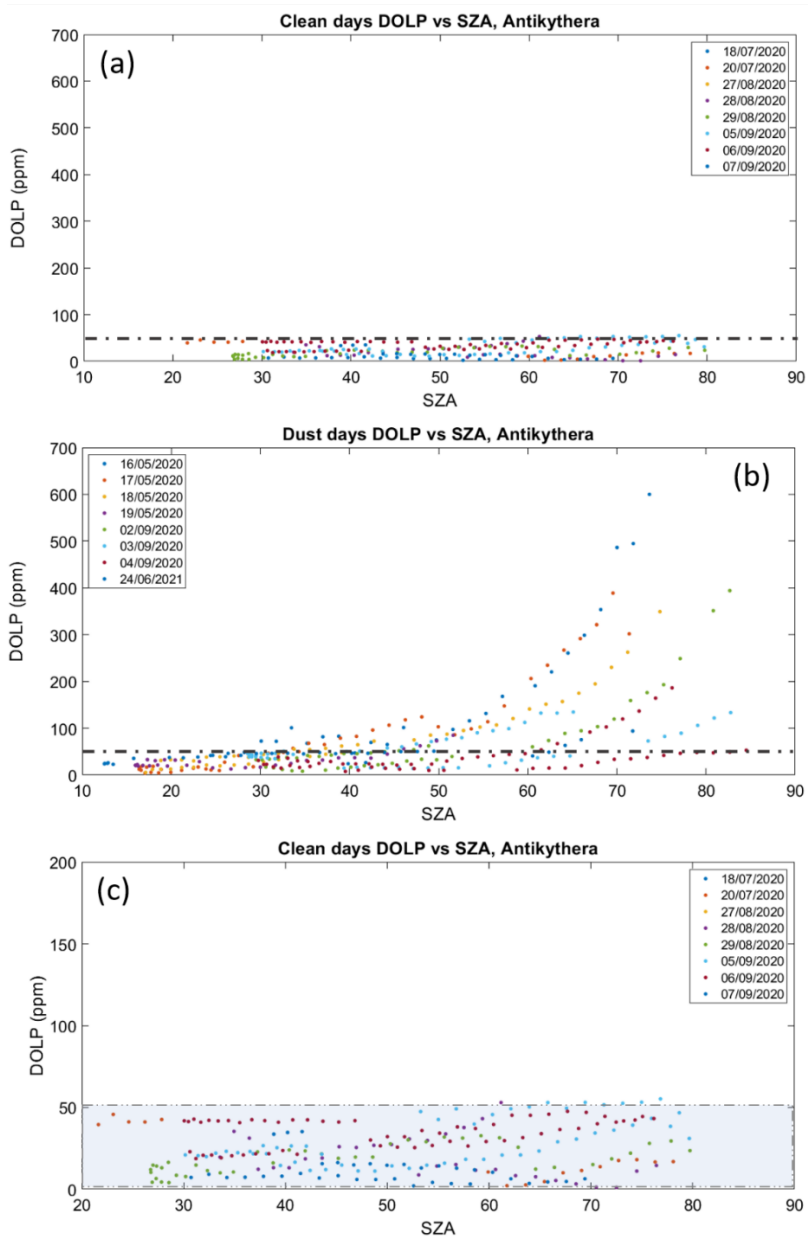

Figure 6.4: Analysis of the DOLP retrievals with the solar zenith angle (SZA, in degrees) for the labelled: (**a**) clean days (C), (**b**) days with dust events (D), and (**c**) a zoomed representation of (a) with the instrument noise threshold (shaded) as deduced by the clean days. The excess in linear polarization (> 50 ppm) becomes apparent for large SZAs (> 50°) when dust particle concentrations persist within the day.

6.3.1. Instrumental Error and Biases

The observed DOLP variation from clean-to-clean day (Figure 6.4c) represents the induced instrumental error under individual measurements, as the differences would be predominantly attributed to the temporal variability of the molecular atmosphere and the dependence of direct solar irradiance to the recorded AOD (e.g. Gueymard, 2012). The threshold value of 50 ppm, is also orders of magnitude larger than other systematic errors in linear polarization caused, for example, by a slight misalignment of the PEM surface with the incoming light axis. According to Kemp et al. 1981 this is of the order of 10^{-7} for misalignment angles of 0.1 degrees which is way beyond any thermal crystal expansion effects or external mechanical stresses to the PEM head in the installation site. Tracking offsets that gradually result to slight angular deviations, cause the targeting of larger off-disk areas and can be a factor that contributes to the characterized instrument bias, as linear polarization increases near the solar limb (e.g. Stenflo, 2005). Although, we performed a test for identifying the effect of diffuse light in the recorded linear polarization signal through incremental alterations of the aperture size (see Section 6.5), sky-scanning tests with a few degrees offset (on steps of 0.5°) on the four cardinal orientations were heavily limited by the PM detection capabilities and were not conclusive.

6.3.2. Comments on the Polarization Angle and Particle Orientation Angle

Information on particle alignment can be extracted from the polarization angle χ (Electric Vector Polarization Angle, EVPA). EVPA indicates the angle between the plane of polarization and the plane of reference and is defined as (e.g., general expression from Hansen and Travis 1974):

$$\chi = \frac{1}{2}\tan^{-1}\left(\frac{U}{Q}\right) \; with \; 0 \leq \chi < \pi \tag{6.1}$$

We are using the normalized U/I and Q/I values as the Stokes input parameters and take into account the constraint that the $\cos 2\chi$ of angles differing by $\pi/2$ should have the same sign as Q/I.

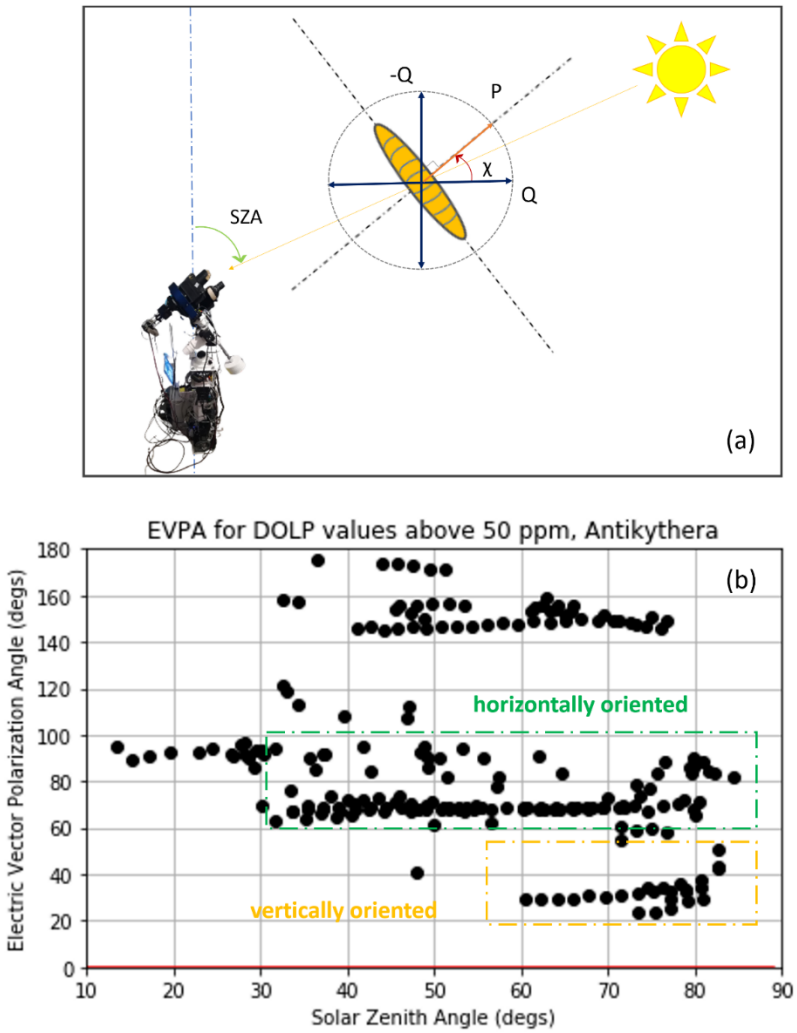

Figure 6.5: (**a**) SolPol viewing geometry for an elongated dust particle with respect to the solar zenith angle (SZA), (**b**) Electric Vector Polarization Angle (EVPA) in degrees with respect the SZA for all SolPol measurement days in 2020 and 2021. EVPA angles correspond to DOLP values > 50 ppm. There is a clear distribution of angles in two distinct clusters around 20° and 70° that correspond to preferentially vertically (yellow tab) and horizontally (green tab).

Figure 6.5 shows the SolPol viewing geometry with respect to the SZA and the calculated EVPAs, as the polarization angles that correspond to measurements of DOLP that are larger than the characterized noise threshold of 50 ppm, which are essentially the observed dust cases. In order to have significant linear polarization and assuming that the particle is elongated, then the particle long axis should be perpendicular to the major axis of the polarization ellipse (Bailey et al., 2008), shown in Figure 6.5a, as the parallel polarization component is predominantly scattered by the

particle while the perpendicular one is transmitted by the particle. The dust cases, here, present a distribution of EVPAs, centred mainly at the values of ~ 20°, 70° and 150° regardless of the increasing SZA (Figure 6.5). The linear feature starts for SZAs between 30° to 60° which is expected as some dust days exhibit dichroic extinction traits relatively close to zenith viewing angles. This points towards the particles being oriented at specific angles such that, preferentially vertically aligned particles correspond to ~ 110° (EVPA 20° ± 90°) mean orientation angle (yellow tab, Figure 6.5) and particles that are preferentially horizontally aligned at mean angles of ~ 160° (EVPA 70° ± 90°) (green tab, Figure 6.5). The observed linear polarization increase at large zenith angles implies that particles adopt both preferential orientations, considering the temporal variation of the dust layers for our observational dataset. Moreover, the increasing trend can be expected to be steeper for vertical particle orientation, because the transition from the zenith (either no dominant orientation or polarization), towards the horizon is stronger for vertical orientation as opposed to horizontal orientation. At horizon level, vertical alignment appears total, while horizontal alignment is only partial due to the fact that particles are still randomly oriented in the horizontal plane.

By the EVPAs considered in this study (Figure 6.5b), particles tend to mostly adopt the horizontal alignment, which is in accordance with previous particle orientation studies stating that the hydrodynamic forces dominate the alignment, as opposed to the electrical forces, and tend to orient the particle horizontally as it falls within the atmosphere (e.g. Mallios et al., 2021, 2022 and reference therin). Nonetheless more synergistic studies on particle dynamics that will take into account the full particle scattering matrix, e.g. through the WALL-E lidar observations (Tsekeri et al., 2021), but also microphysical parameters such as, the particle size distribution, particle charge and asphericity, will be conducted in order to verify our findings and potentially explain the dominant mechanism that could reproduce such an orientation signature.

6.4. Dependence of the Degree of Linear Polarization (DOLP) on the Aerosol Optical Depth (AOD)

In this section, we examine the correlation of the observed excess polarization with the optical thickness of the dust layer. We expect the correlation because dichroic polarization is an extensive property of the particles, hence, its strength increases with the number of particles present in the

incoming light path. As shown in the Figure 6.6 comparison, the DOLP measurements are given for different aerosol optical depth values with respect to the SZA (Figure 6.6a) - or the airmass (i.e. 1/cosSZA) - respectively (Figure 6.6b), for all the acquired cases except the half-clean days and the dedicated test day. We are using the daily average AOD values per full day of SolPol measurements and in the case of days with sparse polarization measurements (either in the morning or afternoon), we derive the mean AOD for the timeperiod that is closer to the measurements. Star markers denote the dust cases (D), circle markers are used to distinguish the clean days (C) and the colour scale referes to various AOD ranges. The maximum recorded AOD for the duration of our measurements in PANGEA observatory was 0.5 at 550 nm, which is large for the characteristic transport conditions of eastern Mediterranean, but relatively small compared to the massive transported loads that are monitored on near dust sources.

We expect that for small AOD values (< 0.1) the linear polarization values will be within the noise threshold as derived from the clean days behavior, as is the case here and since there are no observed dust events with such small loads there are no increasing trends exhibited (dark blue circles). As the optical depth increases, we observe the linear polarization upward feature for a specific SZA, mainly above 40°, intensifying in proportion to the AOD with the highest values of DOLP recorded under heavier dust loads. This indicates that dichroic extinction is potentially enhanced due to the presence of a larger concentration of preferentially oriented dust particles under fixed viewing angles and, consequently, for a stable airmass, as seen in the linear relation of Figure 6.6b. The observed excess in LP is linearly proportional to the increasing airmass, which could be attributed to the particle viewing geometry for fixed AODs or the amount of aligned particles for a fixed viewing geometry as DOLP increases more rapidly for days with larger AODs (Figure 6.6b).

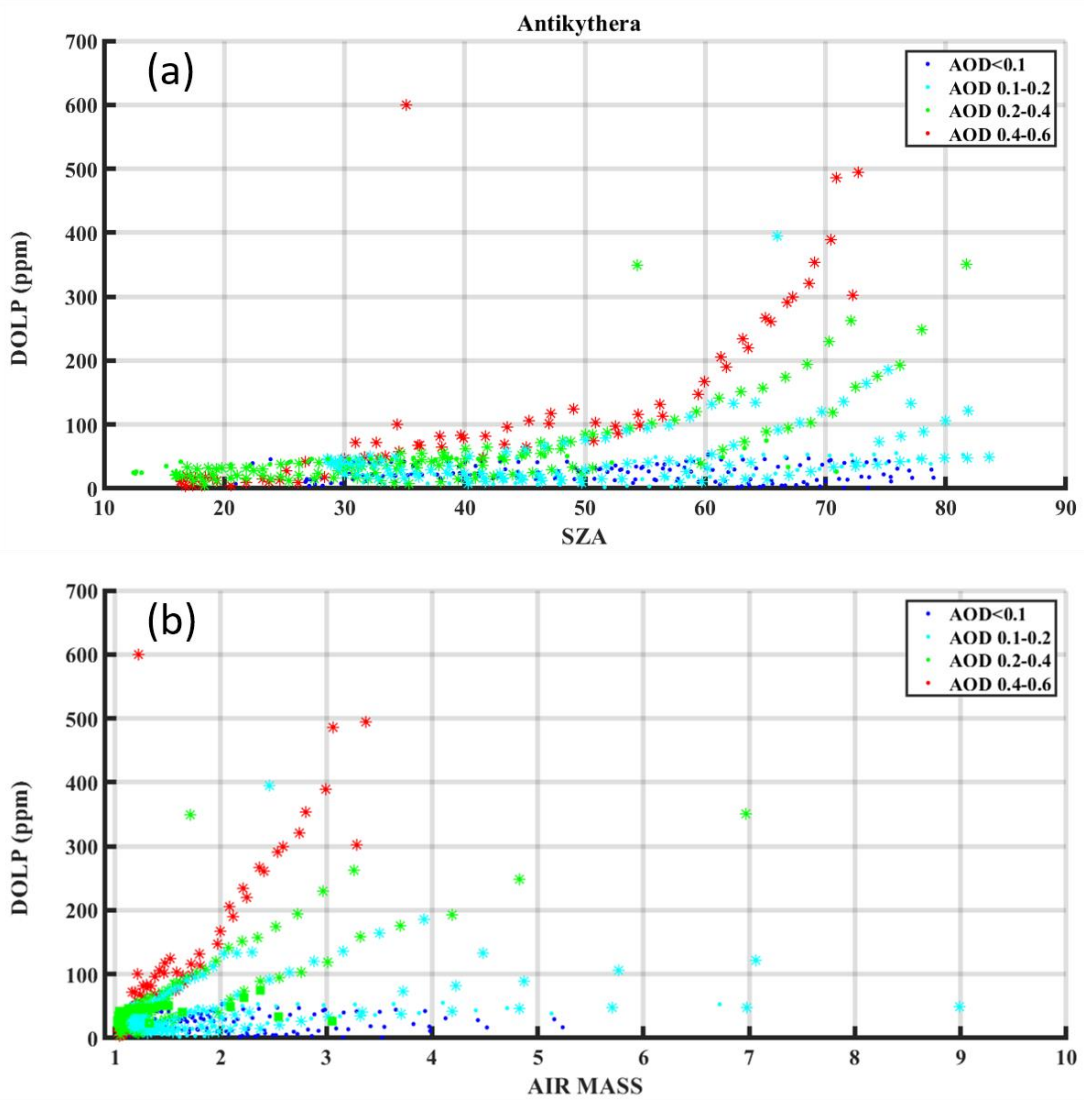

Figure 6.6: (**a**) DOLP as a function of the AOD with respect to the SZA, for the all the SolPol measurements in 2020 and 2021, at the PANGEA observatory. Star markers denote dust days (D), circle markers denote clean days (C) and the colour scale referes to different AOD ranges. For small AOD values (< 0.1), the linear polarization values are within the clean day threshold, while for AODs between 0.1-0.2, the DOLP values begin to exhibit the increasing trend with increasing SZAs, due to the potentially small concentration of preferentially oriented particles along the instrument line of sight. Significant linear polarization values are observed for all the dust days and the trend intensifies further for AODs towards the range between 0.4-0.6. (**b**) DOLP as a function of the airmass for the same AOD ranges. A linear correlation is observed between DOLP and the airmass for AOD values above 0.1, for the dust cases. For larger AODs, the DOLP values surpass the noise threshold for even smaller airmasses.

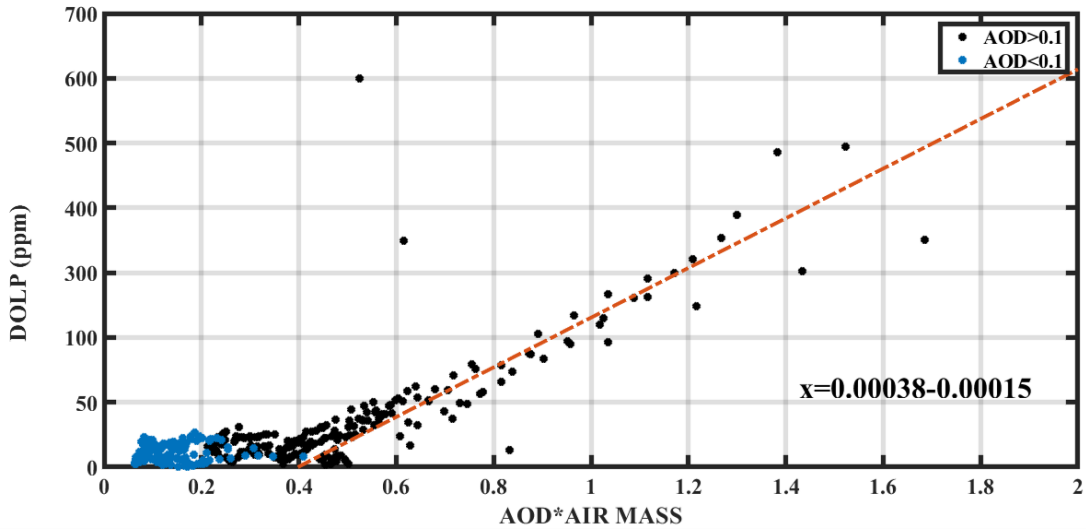

Figure 6.7: Scatterplot of DOLP as a function of the slant AOD, for the SolPol measurements in Antikythera. The linearity observed on AODs over 0.1 corresponds to DOLP signatures from dust days only.

Moreover, this is shown when we inspect the corelation between DOLP and the AOD corrected with airmass (slant optical depth) in Figure 6.7. The distinction has a threshold for AODs above 0.1 that correspond solely to the presence of dust and as we move to larger loads this embeds an increase to the linear polarization values above the noise threshold for even smaller airmasses. The corelation strength could be tested and reproduced in future studies with dust loads close to one, as the potential particle orientation could affect the geometric formalism for the derivation of the AOD.

We should also note though that the increase of DOLP values with AOD may as well indicate contamination of diffuse light (and corresponding polarization properties) in our direct-sun measurements. Thus, it may as well be that we do not measure (only or at all) dichroic extinction, but linear polarization of the diffuse light, with the contamination being stronger for larger AODs. For this purpose we have performed a test for the influence of the diffuse light in our measurements (Section 6.5), and as a future step we plan to perfrom a more complete test, by acquiring observations of high-AOD pollution cases, where we know that the particles are spherical and thus produce no dichroic extinction.

6.5. How does Diffuse Light contribute to Polarization Measurements?

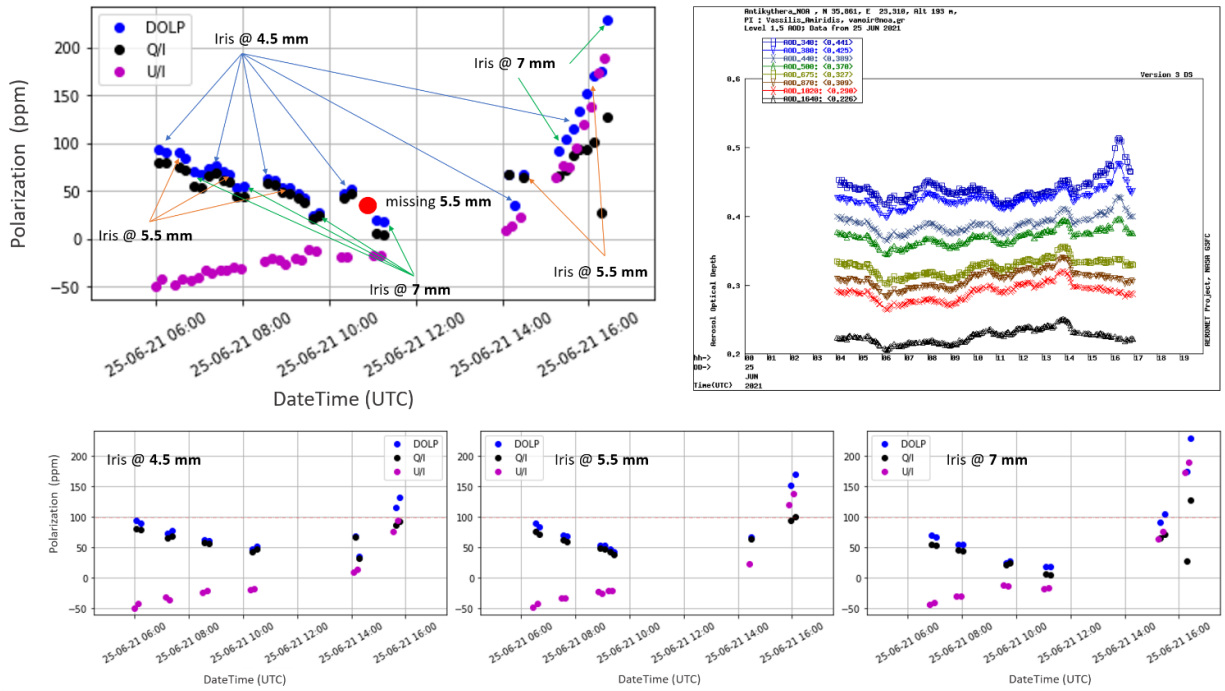

Figure 6.8: Alternating iris size tests for the quantification of diffuse light contribution to the linear polarization observations under the June 25th 2021 dust layer, with an AOD of 0.370 at 500 nm. Top pannels present the normalized *Q* and *U* Stokes parameters, DOLP and the different colour arrows denote the respective iris size for the each measurement set, along with the AOD progression witthin the day from AERONET.

In order to check whether there is a significant contribution to the linear polarization signal attributed to the incoming diffuse light in the polarimeter, we have performed a full day of tests with alternating iris sizes, under a dust event in June 2021 that reached the PANGEA station (Supplementary material, SolPol manual). When increasing the aperture size, we increase the measured diffuse light and subsequently the expected contribution to the observed linear polarization will become prominent on the larger iris sizes. During June 25th 2021 measurements, large dust concentrations were present within the day with a homogeneous layer at altitudes up to 5 km and the optical depth measured by the CIMEL sun-photometer was relatively stable with a mean value of 0.370 at 500 nm. The test procedure comprised alternating iris sizes from small (at

4.5 mm), regular (at 5.5 mm, i.e., the one used for regular SolPol measurements) to large (at 7 mm) through 16-minute measuring intervals so as to ensure that ambient conditions are relatively stable and polarization does not change significantly with the instrument viewing angle (Figure 6.8). The 4.5 mm iris was chosen with respect to a threshold voltage signal to the detector of 1.2 V at large zenith angles. The measuring sequence is consistent with tight observational intervals up until the local noon, but then data become sparse due to SolPol peripheral communication failures. All the dark measurements were performed after each triplet with a closed lid, closed dome and a normally tracking mount. As seen in Figure 6.8, the measured DOLP (black dots) follows a generally decreasing trend from early morning to noon, and a generally increasing trend from noon to afternoon, due to the decreasing and increasing SZA, respectively. This behaviour is disrupted when we change the size of the iris for consecutive measurements until noon. When the iris size changes from 7 mm to 4.5 mm on morning to noon measurements, DOLP increases instead of the expected decrease due to less diffuse light being received by the detector. This proves that by increasing the aperture size, DOLP is less than what was initially expected thus diffused light does not contribute to the polarization trend.

Revisiting Figure 6.4a and the zoomed representation in (c), the measured Rayleigh scattering contribution in the forward direction and under clear conditions (no dust particle presence indicated by the lidar retrievals) to DOLP is less than 50 ppms, when we use the default 5.5 mm aperture size that just contains the Sun's diameter. It also appears to have no dependence on the solar zenith angle for the narrowband filter at 550 nm. If we increase the iris diameter, Rayleigh contributions to the polarization fractions at 550 nm can increase by a factor of two, which is consistent with predicted values for Rayleigh scattering at low altitudes (e.g., Mishchenko et al., 1994 and references therein). Since all measurements are direct sun and we ensure a stable tracking of the sun disk without misalignments, incoming diffuse light within our FOV from scattering angles close to 0° (forward scattered light) will not contribute to DOLP and, in fact, linear polarization will decrease with increasing AOD due to further loss of polarization from multiple scattering (see adapted Figure 6.9 from Hansen and Travis, 1974). Furthermore, these fluctuations due to multiple Rayleigh scattering, are found in diffuse light, and at direct solar irradiance, only the optical depth affects the beam. Since we are confident that the residual contribution of diffuse light to the measured signal, is almost negligible, therefore, the measured linear polarization can be attributed solely to the transmitted sunlight dichroic extinction rather than a diffuse contribution.

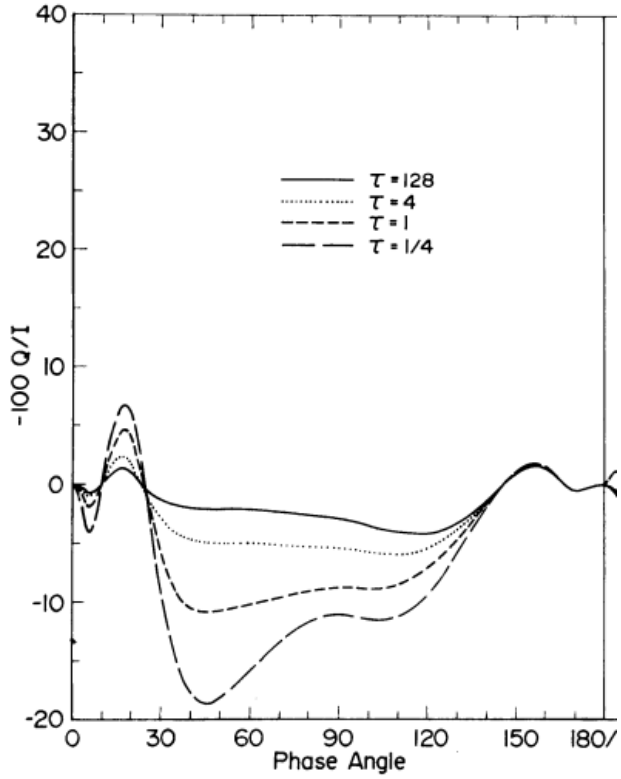

Figure 6.9: Linear polarization, -100 Q/I, as a function of the phase angle for different aerosol optical depths (figure adapted from Hansen and Travis, 1974).

6.6. Could we swift SolPol towards larger wavelengths?

A logical suggestion would be to re-evaluate our SolPol methodology for larger wavelengths in the near infrared (NIR) band region, since we investigate particle size distributions that include coarse mode particles and the NIR DOLP results are expected to be more prominent. Moreover, Rayleigh scattering decreases with increasing wavelength and the molecular contribution to our measurements would be lesser than in the currently operating 550 nm. Nevertheless, mineral dust is often described as "white" or "gray" in terms of its wavelength response. As an example, Bailey et al. (2008) have discussed the only logical question if larger dust particles give polarization signatures in the same manner as small dust particle, which are mostly responsible for interstellar polarization. As seen in Figure 6.10, where the T-matrix calculated ratio of the total extinction coefficient to the dichroism, K_{12} / K_{11}, is presented as a function of the size parameter χ, for larger particles we are in the plateau regime where the mean polarization is essentially the same as that produced by smaller particles. Since larger particles are the

ones that will eventually become preferentially oriented by overcoming randomization due to Brownian motion (e.g., Mallios et al., 2021; Ulanowski et al., 2007), we expect to not observe a significant contribution to the phenomena by switching to longer wavelengths.

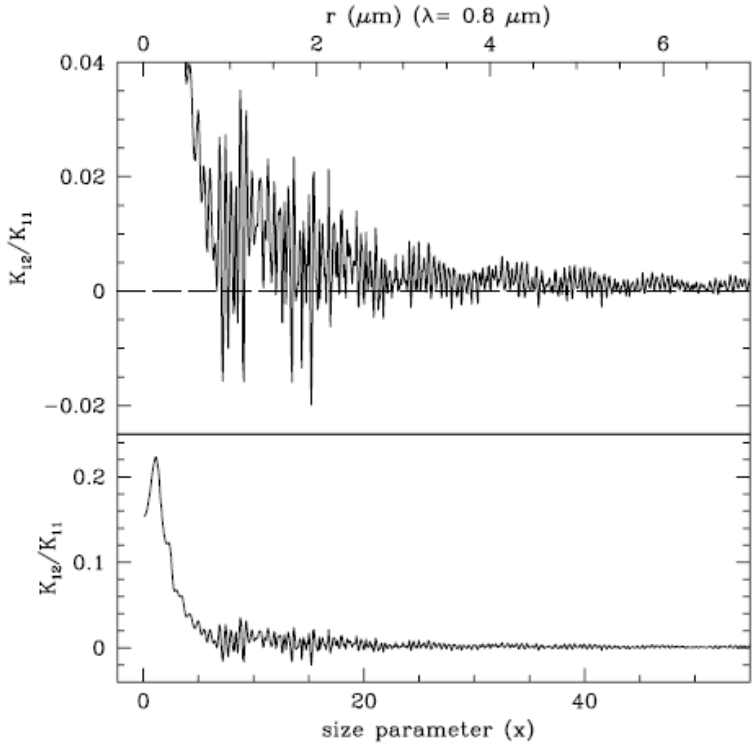

Figure 6.10: Ratio of extinction matrix elements K_{12}/K_{11} for vertically oriented prolate spheroidal particles of axis ratio 1.8 at a zenith distance of 60° as a function of size parameter ($x = 2\pi r/\lambda$). The lower panel shows the full range of variation including the peak corresponding to the small particle regime that causes interstellar polarization. The upper panel is on an expanded scale showing the oscillatory nature of the polarization at larger sizes, but also that the mean level is positive (horizontal polarization). The particle size at a wavelength of 0.8μm is shown on the top scale. Adapted figure from the respective paper of Bailey et al. (2008).

In terms of technical limitations, SolPol is an experimental instrument and its complete characterization was painstakingly long in the framework of the author's PhD research. Therefore, some of the tasks to be tackled would be the need to consider new communication protocols between instrument peripherals in order to operate in a new wavelength and, most importantly, integrate a new photodiode detector operating in the NIR with the capability of detecting such small signals. The responsivity and quantum efficiency of photodiodes decrease with increasing wavelength in the NIR range, meaning that the sensitivity decreases, resulting in lower signal-to-

noise ratios and reduced detection efficiency at longer wavelengths. The limit for reasonable signals from the specific photodiode is about 750-800 nm with a good SNR. When approaching wavelengths beyond 1000 nm it is a very different experiment than what we have setup so far, with encroaching telluric absorption lines beginning to come into play. Going towards the lower wavelengths' direction, i.e., 450 nm might also be interesting in comparison to our previous 550 nm. Instrument filters on the 450 and 750 nm central wavelengths have been set up in the past for lab measurements and Rayleigh contribution field measurements in Hatfield, but definitely the bandwidth of these filters will make a difference in ambient field conditions in Antikythera. Thermal noise is also a significant source of error to be considered in these wavelengths, thus the trade-off led initially to the use of the instrumental configuration as is. Nonetheless, the author strongly encourages revisiting the SolPol assembly configuration in the NIR as an upgrade to be completed in the near future and to provide cross-checked research results on dust orientation from various wavelengths.

6.7. Conclusions

We report on extensive linear polarization measurements with a direct sun polarimeter, the SolPol, and detect signatures of dichroic extinction of sunlight in cases of transient dust layers above the PANGEA observatory, in Antikythera island, Greece. This phenomenon could be attributed to potentially preferentially aligned dust particles within the instrument line of sight towards the sun, a concept that reproduces earlier measurements of excess linear polarization of starlight through observations of astronomical sources with known polarization signatures (Bailey et al., 2008; Ulanowski et al., 2007). The similar behaviour, found here, is expressed as a steep increase to the measured DOLP when the Sun is far from its zenith position and when significant dust particle load is present in the atmosphere. The increasing trend is not found under conditions that are characteristic of the background aerosol concentrations in the area. We describe the characterization of the instrument capabilities and quantify the measurement bias from the background reference and through dedicated testing days. In addition, we monitor the excess polarization over various dust loads where the linear polarization feature is persistent and extract the dependence on the AOD. We find that as the AOD increases, the linear polarization values become larger overall and,

therefore, the increasing trend intensifies for viewing angles closer to the horizon, which is again consistent with the previously highlighted work.

Out of the total 24 days of SolPol observations, pronounced increase of DOLP up to 700 ppms only in the (lidar characterized) dust days have been observed as a function of the AOD (sun photometer measured) and of the air mass. Investigating the polarization angle for most of these days, horizontally and vertically oriented particles can explain both DOLP increase with solar zenith angle and also the EVPA levels. However, it would require more measurements with well characterized aerosol optical properties to try to generalize on the capabilities of ground based polarimeters to accurately estimate dust particle orientation. Further work is intended to test the SolPol response on aerosol layers that are not likely to exhibit particle orientation due to the shape of the particles, such as in pollution or smoke layers, and are expected to not affect the polarization of direct light. The anticipated vertically resolved measurements of the novel WALL-E polarization lidar, jointly with the SolPol orientation signatures, can provide strong proof of the existence of oriented aerosol particles in the atmospheric column and elucidate the nature of the alignment process. Our observations have multiple implications for the parametrization of natural dust in aerosol models and for radiative transfer calculations, as particle orientation affects scattering properties. More complementary studies are encouraged as they can pave the way for new aerosol remote sensing developments.

Chapter 7

General Conclusions

Initiating from the modelling effort presented in the specific thesis, calculations hint that the acquired electrical charge on the dust particles is in the range of 0.5 to 2000 elementary charges, when assuming their electrification by ion attachment and triboelectrification as two distinct and simultaneously acting mechanisms. For realistic atmospheric concentration of dust, it is shown that the ion attachment mechanism is dominant and, therefore, particles become on average negatively charged. But under specific conditions of extremely large concentrations, giant mode particles can be locally and temporarily positively charged by ion attachment and triboelectrification alike, while reported laboratory experiments over the years targeting only the triboelectrification, attribute the positive charges to larger particles and negative charges to smaller particles. This effect was shown to be enhanced for size distributions which had a significant component of larger particles. The model results indicate, however, that the electrical force created is not adequate enough to significantly influence the gravitational settling of the charged particles.

Ground-based electric field measurements can be indicative of the electrical behaviour of elevated dust layers. We have observed that elevated layers from dust outbreaks enhance the near-surface electric field, as these layers reach our instrumentation locations. This enhancement was hypothesized due to the existence of bipolar charge separation within the elevated dust layers in order to explain the field behavior. The observed enhancement of the near-surface vertical electric field is found to be up to ~ 100 V m^{-1}. Although higher dust loads are expected to result in such a field enhancement, episodic cases that reduce the electric field (up to ~ 60 V m^{-1}) are also observed from the ground.

Since ground-based observations of dust electrification are not always conclusive, we consequently focus to synergistic measurements of the vertical atmospheric field and the total charge density in the presence of these dust outbreaks through the launches of balloon-borne

instrumentation in large-scale scientific experiments. Vertical profiling of the layer electrical properties is highlighted throughout the thesis. For this purpose, we have proposed and designed two novel miniaturized sensors, while assessing their data that show good agreement in the values of the electric field vertical component strength. The measured in-layer vertical electric fields are of the same order of magnitude with the fair weather electric field strength. The profiling information reveals the presence of charged dust particles within the elevated plumes with accumulation of charges on layer boundaries, but result in relatively low E-fields within the layers for the recorded dust aerosol optical depths. The large volume of the data produced by the campaigns, allowed for only a few cases to be displayed for the purposes of this research. More data evaluation studies will be performed in the future with the methodologies addressed hereafter and will consist an unprecedent dataset on its own for the evaluation of the dust transport models.

Lastly, understanding and detecting dust particle orientation is crucial for studying aerosol dynamics, atmospheric transport, and the impact of dust on climate, as it affects the optical properties, radiative transfer, and deposition patterns of the particles in the Earth's atmosphere. Following, the investigation of the dynamics of charged dust particles simulated as a spheroidal shape shows that particles of sizes less than 1 μm are always randomly oriented due to the Brownian motion being dominant, while particles in the range of 1-100 μm can become vertically oriented for sufficiently large electric field strengths. Particles larger than 100 μm are mainly horizontally oriented, because the atmospheric electric field can never reach the required electric strength Large electric fields are required in order to achieve size-dependent particle alignment, but under specific considerations these fields can become of the order of a few Volts per meter, i.e. of the order of fair weather electric fields. Combining the model results to the measured electrical quantities we conclude that electric field strength may not be sufficient to overcome the threshold value that would orient particles totally vertically. This hints that other factors, such as strong updrafts, can highly contribute to the phenomenon leaving the exact mechanisms of dust orientation a matter of intense discussion.

In order to provide observational evidence of dust particle alignment, we utilize SolPol, a novel experimental instrument, describe its characterization capabilities and quantify the measurement bias from the background reference through dedicated testing days. The valuable SolPol observations present pronounced increase of the linear polarization of light travelling through the dust layers up to 700 ppms only in the (lidar characterized) dust days a function of the aerosol

optical depth and of the air mass. The increasing trend is not found under conditions that are characteristic of the background aerosol concentrations in the area. We monitor the excess polarization over various dust loads where the linear polarization feature is persistent and extract the dependence on the AOD. We find that as the AOD increases, the linear polarization values become larger overall and, therefore, the increasing trend intensifies for viewing angles closer to the horizon, which is again consistent with the previously highlighted work and an indication of persistent dust orientation in the Earth's atmosphere. Moreover, by investigating the polarization angle for most of these days, horizontally and vertically oriented particles can explain both DOLP increase with solar zenith angle and also the EVPA levels. However, more measurements with well characterized aerosol optical properties are needed so as to generalize on the capabilities of ground based polarimeters to accurately estimate dust particle orientation.

Appendices

A.1 SolPol operation documentation

a. SolPol operation manual

Instrument operation can be at times very demanding in terms of the required installation and assembly process, initialization procedure, data acquisition and even control error mitigation. Therefore a concise, user-friendly and universally accessible manual of operation is of importance both for the experienced technician and the acting Principal Investigator (PI) of the instrument at hand. Moreover, considering the diverse operation conditions and potential mobility of experimental setups, there is a growing need for clear instructions that can be easily reproduced at any level, are homogenized with the Research Infrastructure (RI) / network demands, but can also be updated in near-real time conditions.

Code hosting platforms for version control and extended collaboration between individuals and Institutes, such as the Git suite tools, can provide a freely distributed and open source solution for the creation and maintenance of such operation manuals. Having installed, characterized and extensively operated the novel solar polarimeter - SolPol - in PANGEA, we experienced the need for a decentralized access to the instrument operation. Since SolPol is an experimental instrument with a previous in-lab configuration, its installation on the remote station was not a menial task due to the lack of coherent sources of information. Thus, a detailed installation / operation manual will provide the required insight for its on-demand operation and act as a publicly available source of information regardless of the operator or hosting Institute. By combining the collaborative features of GitLab with the powerful documentation capabilities of document generators such as Sphinx, we can ensure a streamlined and accessible manual for instrument users. Ultimately, the final product can be used as a template for other photometric intruments and their core representation within various consortia. The first level information is documented in the following GitHub repository and the interactive manual can be found in full form under the GitLab handle:

GitHub: @**NOA-ReACT/SolPol** and Gitlab repo: @ **ModusElectrificus/solpol_manual**

a.i Basic SolPol apparatus configuration

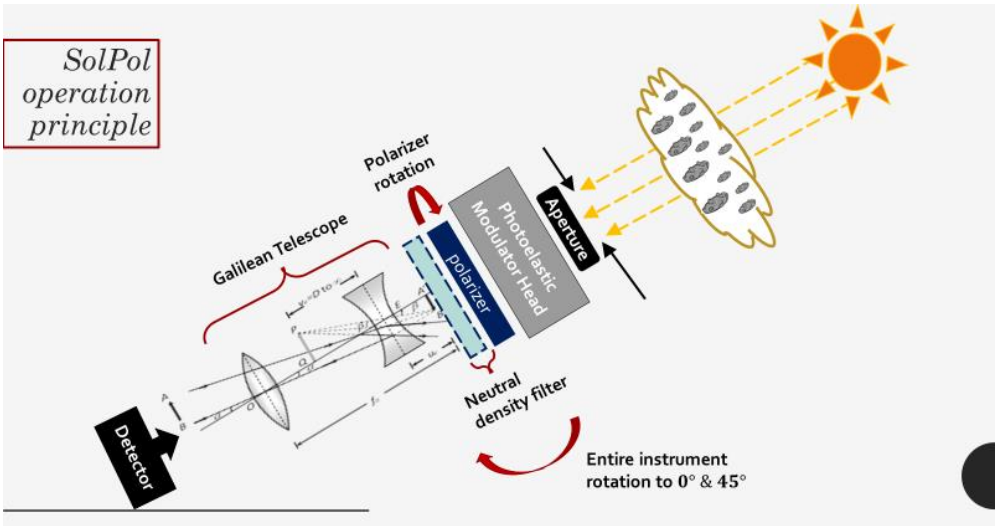

Figure A.1: Sketch of the assembly apparatus with the individual components placed in order through the optical axis, as the light is travelling from top right to bottom left.

HEADER file details:

SOLAR POLARIMETER

1. Polarimeter Position [deg]
2. Rotator Position [deg]
3. PEM Setting [nm]
4. Retardation [waves]
5. Wavelength Filter (Wavelength-Bandwidth)
6. ND-Filter
7. Time (UTC)
8. Bias Voltage on Diode
9. LabJack, mean DC (AIN0)
10. LabJack, other
11. Lock-in, 1w
12. Lock-in, 2w

MEASUREMENT details:

- Measurement starts when **PEM** is @0° and **Polarizer** @41° (must always check on **solpol.exe** status board)
- File naming:
  pol_DDMMYYYY_HHMM_LOC_DURATION.txt
- where HHMM is the PC time, LOC is one of "antik", "ath" or "cy" for Antikythera, Athens and Cyprus data, respectively, and DURATION is the measurement duration as either "onehour", "twohours" or "sixteenmin".
- 5 measurements per polarizer position (~41°, 131°,221° and 311°) per assembly position (0° & 45°)
- Each measurement (4 Polarizer pos. – 1 PEM pos.) last ~4mins
- Ends ALWAYS with assembly at **45°**
- Total **2hrs file length** 8334 lines, where 160 hits should account for each polarizer position, size 91-92 Kb. The ½ goes for 1hr measurements.
- Full day measurement starts @6 UTC ends @16 to 16:15 UTC
- Dark measurements with shutter closed and instrument either in **Tracking** mode ☛ **poldarkT**, or **non-Tracking** mode → **poldarkNT**
- Darks available only during Aug. – Sept. 2020 & 2021 datasets
- PEM aperture 23 mm @ 90 % efficiency
- Instrument FOV ~1° solid angle

MEASUREMENT sequence:

- Open **solpol.exe**, **picoscope.exe** and **opticstarview.exe** CCD camera program
- Hit the **Find** button in **solpol.exe** → wait for **"All peripherals found"** reading in the program screen
- Select in solpol.exe the **550nm** filter option and wait for Filter Wheel to operate (Picoscope indication varies)
- If sun appears on camera, polar alignment and parking positions are OK
- Slightly move the tracker to **N-S** & **E-W** directions through EQtab in order to target directly the Sun → maximization of the intensity signal in Picoscope voltage reading (reach at least 2.5 V & above if morning set-up)
- Hit track rate "Solar" (Sun icon) in EQtab and minimize tab
- Hit Initialize and wait for parameters
- Hit **Start** sequence → choose appropriate duration → save file and start (*wait for PEM to turn after 4'*)

SUN TRACKER Initialization & Tracking sequence:

Type: **EQ3 – SynScan** (max. load of 10Kgs, less accurate in prolonged tracking) + **EQmod** direct PC control

- Open **CartesduCeil.exe** → Choose the appropriate observatory site, then → Telescope → Connect (Telescope EQtab opens)
- in EQmod tab → **Unpark** (co-ordinates scenario should be set to the specific instrument location)
- in **CartesduCeil.exe** search tab → Sun (Enter) → pointer on Sun (left click) → Telescope → Slew, tracker moves

a.ii Instrument Set-up Antikythera

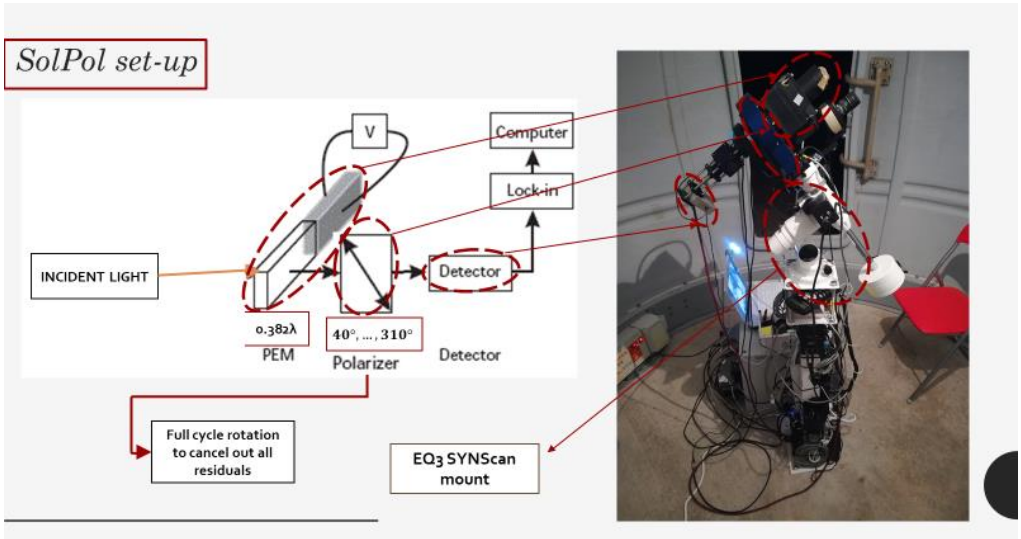

Figure A.2: Schematic of the instrument setup within the astronomical dome in Antikythera.

SolPol polarimeter includes a Photo Elastic Modulator (PEM) that operates at a resonant frequency of 47 kHz, a rotatable linear polarizer, an imaging telescope, neutral density filters, a field of view limiting aperture, and a large area diode detector (Martin et al., 2010). The design is quite a venerable one and follows the design of the PlanetPol instrument (Bailey et al., 2008; Hough et al., 2006). The entire assembly can be rotated about the optical axis so that biases can be removed. The instrument measures the Stokes parameters that provide the linear and circular polarization from the whole solar disk plus a surrounding area of the sky depending on the choice of telescope and limiting aperture. Earlier measurements by Kemp with a nearly identical polarimeter design indicated that the whole solar disk has a linear polarization of ~ 10^{-6} from an observatory at 6300 ft altitude (Kemp et al., 1987; Kemp and Barbour, 1981).

Figure A.3 shows the basic SolPol design. There are no optical elements before the PEM, which is followed by the linear polarizer. Neutral density filters establish the signal levels at the 1cm silicon diode detector which uses a transimpedance amplifier to generate the signal voltage. The filter wheel contains six filters: RGB broad band filters (with measured transmission curves) and three 40nm narrow band filters at 400, 550, and 700 nm centre wavelengths. The polarimeter currently operates at 550 nm. A 12-bit A/D converter records the diode signal and an SR830 Lock-

in amplifier records the first and second harmonic modulation signals (modulated by the PEM). The polarizer position and the instrument rotation are controlled from a LabView virtual instrument program, which also controls the recording of data from the detector.

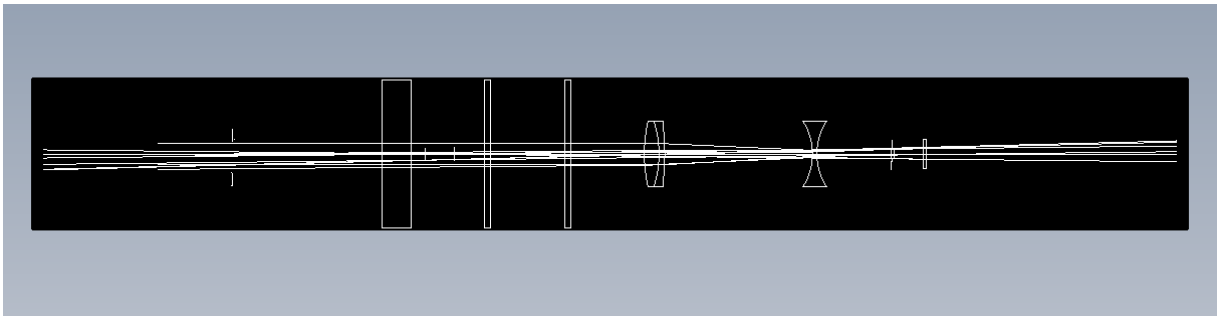

Figure A.3: SolPol configuration. From left to right: 10mm aperture stop (as given for the initial configuration, but we've measured it in 5.5 mm in Antikythera), PEM, linear polarizer, neutral density filters, Lens 1 & 2 Galilean telescope, 3.5 mm field stop, photodiode detector.

a.iii Instrument Parts and Specs

- Hinds Instruments – **Photoelastic Modulator (PEM)** Series II FS47, (Im. 1 in Figure A.5, **Optical head + Electronic head**)
  - Range: **400 nm - 750 nm**
  - Cost: **(~ 12k £)**
- **Rotatable Linear Polarizer**, optical axis initially aligned with PEM axis
  - attached to Thorlabs Heavy Duty rotation stage (Im. 2 in Figure A.5)
  - rotated through a Thorlabs K-cube stepper motor controller
  - rotation controlled by the APT Thorlabs software

The linear polarizer is attached to a Heavy-Duty rotation stage, connected to the Pyxis rotator (front side) and glued to the PEM (Im. 2, Figure A.5). For the polarizer rotation in 41°, 131°, 221°, 311° rotation, the stage is controlled by a Thorlabs Kinesis K-cube stepper motor (not depicted).

- Optec Inc. PYXIS 3-inch camera field rotator (Im. 3, Figure A.5).

The Pyxis is a simple rotator used to attach CCD cameras on large telescopes for rotating the viewing field of the camera on long exposures. In SolPol it is used to rotate the entire instrument assembly from 0° to 45°.

- NAUTILUS Rotating Filter Wheel (Im. 4, Figure A.5),
  - operation at 550 nm
  - 7 available slots
- Galilean **Telescope** (Im. 5, Figure A.5)
- Photodiode **detector** (also Im. 5, Figure A.5)
- **CCD camera** for Sun tracking (Im. 6, Figure A.5)
- Signal amplifier, through a transimpedance, SR830 DSP Lock-In Amplifier (Im. 7, Figure A.5)
- PEM – 100 head controller unit (Im. 8, Figure A.5).

a.iv Photoelastic modulator (PEM) operation principle

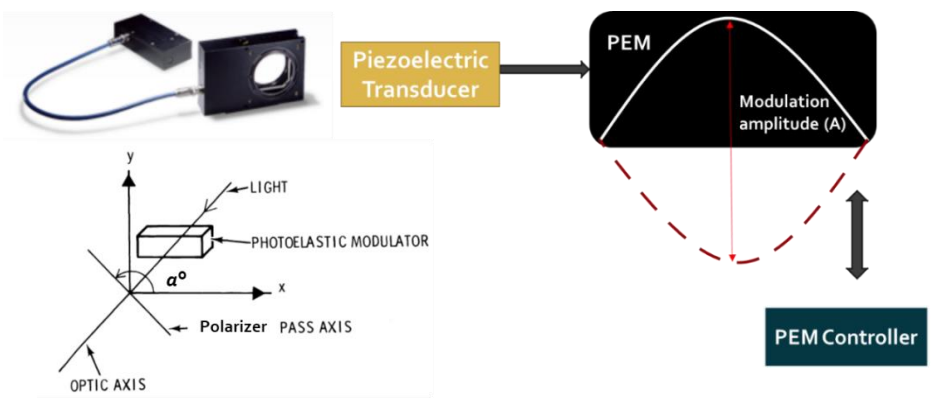

Figure A.4: PEM assembly and principle of operation

The SolPol PEM SII FS47 is comprised of a fused silica crystal bar with photoelastic capabilities and a piezoelectric transducer. If the optical element is compressed or stretched it induces a retardation (i.e., phase difference between the polarization components) of the incoming light (Figure A.4). The strain stress in the PEM crystal is induced by standing mechanical acoustic waves, which are produced by the transducer, attached to the head. The resulting retardation is time-periodic, and is provided by:

$$\delta(t) = \mathrm{A}\sin\omega t \qquad \text{(A 1)}$$

where δ is the retardation of the PEM and A is the peak amplitude. The resonant frequency ω of the PEM is set at 47 kHz. The PEM controller unit performs many functions in the photoelastic modulator system. Its primary function is to control the peak retardation of the photoelastic modulator optical head. It does this by providing a DC voltage signal to the electronic head which determines the transducer vibration amplitude and thus the strain amplitude in the optical element. A current feedback loop from the electronic head enables the controller to maintain stable peak retardation levels. For SolPol, the PEM is calibrated by the Bessel function zero methods (PEM User's manual, pg. 82). For the Bessel function zero method, the direct-current (DC) term is kept invariable, independent of the birefringence. The DC intensity also becomes independent of changes attributed to the optical system, such as angular position of the polarizer. Normalization of the AC signals by the DC signal, renders the ratio independent of fluctuations from the intensity source.

PEM specs

- **Fused siclica resonant bar** – initially non birefringent, stress-induced
- **Standing acoustic waves** imposed by transducer, at resonant freq. of 47 kHz
- Induced birefringence signifies that different polarization states are refracted on different directions
- **Fundamental vibration along the crystal optical axis** (Figure A.**4**; Stokes et al., 1976)
- According to the modulation amplitude, PEM can be used as any retardation plate between λ/4 to λ/2
- for 1ω the modulation efficiency is at 0.7342 and for 2ω at 0.6106, remains unchanged for dark measurements
- **PEM limitations:** mixing of linear & circular polarizations produced by residual strain in the fused silica (Stokes, R. A., 1976)

Figure A.5: Instrument parts and peripherals. **Im. 1:** Photoelastic Modulator head (PEM), **Im. 2:** linear polarizer and Pyxis rotation stage, **Im. 3:** Pyxis camera (assembly) rotator, **Im. 4:** filter wheel, **Im. 5:** Galilean telescope and photodiode detector, **Im. 6:** CCD camera, **Im. 7:** Lock-in amplifier and **Im. 8:** PEM head controller.

a.v Instrument assembly rotation

The measurement sequence of SolPol includes the rotation of the whole instrument assembly by 0° and 45° (see measurements performed at 0° and 45° rotation in Table 1 of the following Section). The relative position of the PEM and linear polarizer for the instrument assembly rotation at 0° and 45° is shown in the following figure.

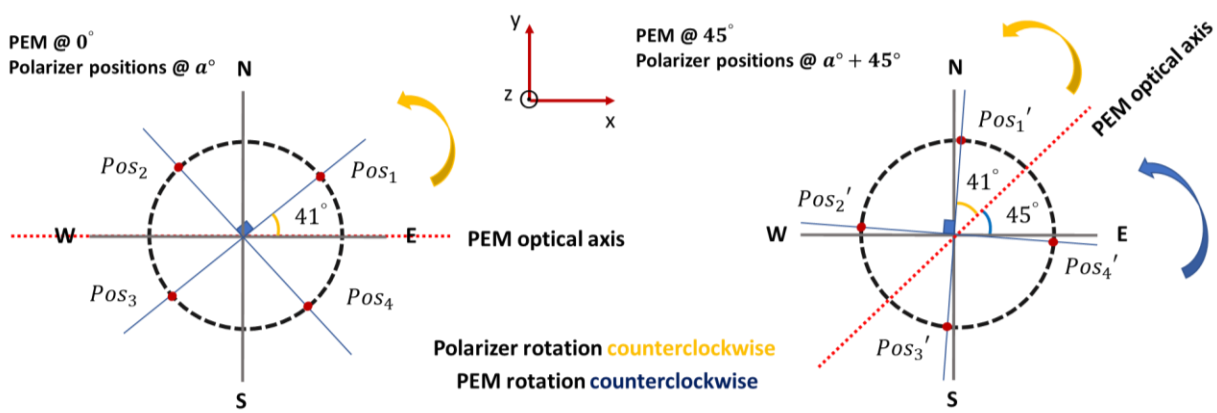

a.v.1. SolPol light modulation and measurements

The Mueller matrix of the PEM is:

$$\boldsymbol{M_{PEM}} = \begin{bmatrix} 1 & 0 & 0 & 0 \\ 0 & \mathrm{G} + \mathrm{H}\cos 4\psi & \mathrm{H}\sin 4\psi & -\sin\delta\sin 2\psi \\ 0 & \mathrm{H}\sin 4\psi & \mathrm{G} - \mathrm{H}\cos 4\psi & \sin\delta\cos 2\psi \\ 0 & \sin\delta\sin 2\psi & -\sin\delta\cos 2\psi & \cos\delta \end{bmatrix} \tag{A 2}$$

with $\mathrm{G} = \frac{1}{2}(1 + \cos\delta)$ and $\mathrm{H} = \frac{1}{2}(1 - \cos\delta)$, $\delta = \mathrm{A}\sin\omega\mathrm{t}$, ψ is the polarization position angle, i.e., the angle between the PEM optical axis and the produced parallel polarization component. For the SolPol measurements $\psi = 0°$, thus Equation (A 2) is written as Equation (A 3).

$$\boldsymbol{M_{PEM,0^\circ}} = \begin{bmatrix} 1 & 0 & 0 & 0 \\ 0 & 1 & 0 & 0 \\ 0 & 0 & cos\delta & sin\delta \\ 0 & 0 & -sin\delta & cos\delta \end{bmatrix} \tag{A 3}$$

The Mueller matrix for a rotating linear polarizer is (as in Freudenthaler 2016; S.10.8.2):

$$\boldsymbol{M_{Pol.,a^\circ}} = \frac{1}{2}\begin{bmatrix} 1 & cos2a & sin2a & 0 \\ cos2a & cos^2 2a & sin2acos2a & 0 \\ sin2a & sin2acos2a & sin^2 2a & 0 \\ 0 & 0 & 0 & 0 \end{bmatrix} \tag{A 4}$$

a.v.2. Assembly without rotation

The Stokes vector of the light that reaches the detector is calculated as following:

$$\boldsymbol{I'_{\alpha^o}} = \boldsymbol{M_{Pol.,a^\circ}}\boldsymbol{M_{PEM}}\boldsymbol{I} = \frac{1}{2}\begin{bmatrix} I + Qcos2a + (Ucos\delta + Vsin\delta)sin2a \\ Icos2a + Qcos^2 2a + (Ucos\delta + Vsin\delta)sin2acos2a \\ Isin2a + Qsin2acos2a + (Ucos\delta + Vsin\delta)sin^2 2a \\ 0 \end{bmatrix} \tag{A 5}$$

Using the Bessel functions (), and omitting the terms higher than J_2, the intensity measured at the detector is provided by Eq. 7.

$$\begin{aligned} \cos\delta = \cos(\mathrm{A}\sin\omega\mathrm{t}) = J_0(A) + 2J_2(A)\cos 2\omega\mathrm{t} \\ \sin\delta = \sin(\mathrm{A}\sin\omega\mathrm{t}) = 2J_1(A)\sin\omega\mathrm{t} \end{aligned} \tag{A 6}$$

$$I'_{\alpha^o} = \frac{1}{2}I + \frac{1}{2}Q\cos2a + \left[U\left[\frac{1}{2}J_0(A) + J_2(A)\cos 2\omega\mathrm{t}\right] + VJ_1(A)\sin\omega\mathrm{t}\right]\sin2a \tag{A 7}$$

a.v.3. Assembly rotated by 45°

The whole assembly is rotated by 45°, thus the reference coordinate system is rotated by 45°. Then, the Stokes vector of the incoming sunlight appears in the new reference coordinate system to be rotated by an angle -45°, and the Stokes vector $\mathbf{I_{rot}}$ is calculated using $\mathbf{R_{-45^\circ}}$ (as in Freudenthaler 2016; S.5.1.7).

$$\boldsymbol{I_{rot}} = \boldsymbol{R_{-45°}}\boldsymbol{I} = \begin{bmatrix} I \\ U \\ -Q \\ V \end{bmatrix} \tag{A 8}$$

where $\boldsymbol{R_{-45°}}$ is provided in (A 9).

$$\boldsymbol{R_{-45°}} = \begin{bmatrix} 1 & 0 & 0 & 0 \\ 0 & cos90° & sin90° & 0 \\ 0 & -sin90° & cos90° & 0 \\ 0 & 0 & 0 & 1 \end{bmatrix} = \begin{bmatrix} 1 & 0 & 0 & 0 \\ 0 & 0 & 1 & 0 \\ 0 & -1 & 0 & 0 \\ 0 & 0 & 0 & 1 \end{bmatrix} \tag{A 9}$$

The light that reaches the detector is calculated as following:

$$\boldsymbol{I'_{rot,a^o}} = \boldsymbol{M_{Pol.,a^o}}\boldsymbol{M_{PEM}}\boldsymbol{I_{rot}} = \frac{1}{2}\begin{bmatrix} I + Ucos2a - (Qcos\delta - Vsin\delta)sin2a \\ Icos2a + Ucos^2 2a - (Qcos\delta - Vsin\delta)sin2acos2a \\ Isin2a + Usin2acos2a - (Qcos\delta - Vsin\delta)sin^2 2a \\ 0 \end{bmatrix} \tag{A 10}$$

Using the Bessel functions (A 6), the intensity measured at the detector is provided in (A 11).

$$I'_{rot,a^o} = \frac{1}{2}I + \left[VJ_1(A)\,sin\,\omega t - Q\left[\frac{1}{2}J_0(A) + J_2(A)\,cos\,2\omega t\right]\right]sin2a + \frac{1}{2}Ucos2a \tag{A 11}$$

a.vi Measurements

Table A1 shows the measurements at the detector, as a function of (a) the Stokes components, (b) the linear polarizer angles and (c) the rotation of the assembly.

Table A1: same as Table 3.1

n	I'	Assembly without rotation	Assembly rotated at 45°
0	DC	$\frac{1}{2}(I + Q\cos 2a + UJ_0(A)\sin 2a)$	$\frac{1}{2}(I - QJ_0(A)\sin 2a + U\cos 2a)$
1	1ωt	$VJ_1(A)\ \sin\omega t\ \sin 2a$	$VJ_1(A)\ \sin\omega t\ \sin 2a$
2	2ωt	$UJ_2(A)\cos 2\omega t\ \sin 2a$	$-QJ_2(A)\cos 2\omega t\sin 2a$

In order to have $J_0(A) = 0 \Leftrightarrow A = 2.4048 = \delta \cdot 2\pi$, thus the retardance phase shift induced by the PEM is δ = 0.382. For this value of A, $J_3(A) = 0.199$, so **there is a significant modulation at 3ωt**[8]**, which we omit.** The intensity of the incoming sunlight, I, is calculated from the DC signal, Q is calculated (after the assembly is rotated by 45°) from the AC signal with frequency of $2\omega t$, and U is calculated (without rotation of the assembly) from the AC signal with frequency of $2\omega t$.

$$I = I_{meas} - I_{mean,dark} \tag{A 12}$$

$I_{mean,dark}$ is the average intensity of the same-day dark measurement

The voltage output recorded at the lock-in amplifier provides Q/I, U/I as shown in the following equations:

$$v(dc) = I/2 \tag{A 13}$$

$$v(1\omega) = VJ_1(A)/\sqrt{2} \tag{A 14}$$

$$v(2\omega) = -QJ_2(A)/\sqrt{2} \tag{A 15}$$

a.vii Multiple iris sizes test

In order to check whether there is a significant contribution to the linear polarization signal attributed to the incoming diffuse light in the instrument, we have performed a full day of tests with alternating iris sizes. The idea is that with larger iris we increase the diffused light measured by the instrument. If there is contribution of the diffused light to the measured linear polarization, then the latter should also increase with larger iris. SolPol has a default aperture size of 5.5 mm that exactly encompasses the solar disk, provided that its tracking sequence and polar alignment are stable throughout the measurement (which we ensure before every observational sequence).

During the 25/06/2021 dust event that reached the PANGEA station, we have conducted the following test procedure (Figure 6.8): 1. alternating iris sizes from small **@4.5 mm** to regular **@5.5 mm** to large **@7 mm** through 16' measuring intervals so as to ensure that ambient conditions are relatively stable and that polarization does not change significantly with the instrument viewing

[8] Equal to $VJ_3(A)\sin(3\omega t)\sin 2a$ when the assembly is not rotated and $VJ_3(A)\sin(3\omega t)\sin 2a$ when rotated by 45°.

angle, 2. the measuring sequence is consistent with **tight observational intervals** up till the local noon, but then the data sequence becomes sparse due to failures with the assembly rotator PC communication, 3. the monitored mean AOD values through the co-located sunphotometer **do not vary significantly within the day** (AOD at 440 nm is approximately 0.4) and 4. dark measurements with a **closed lid**, **closed dome** and **tracking mount** were performed after each triplet.

b. SolPol dark measurements tests

b.i. Dark Tracking & Non-Tracking tests

There were two setups when conducting dark measurements (dark plastic cap adjusted to the front of the PEM every time, so that no light reaches the crystal, there is no internal mechanic shutter in the instrument & the dome is closed when performing dark measurements):

i. the EQ mount tracks the Sun, when the Sun is above the horizon
ii. the EQ mount is parked and does not track the Sun

Dark measurements were performed during August – September – October 2020 periods, either in brief time-windows between regular measurements, in order not to lose much of the daylight, either during nighttime without tracking due to the unfavorable position of the tracker. The 17 - 18/10/2020 are total days with dark measurements. If we exploit only the mean DC voltage (I in Volts) from the dark measurements and later subtract it from the respective DC output of the regular measurement (Kemp and Barbour, 1981), then the tracking mode doesn't seem to significantly and persistently affect the mean DC value. As seen in Figure A.6 to Figure A.8, it not clear which of the two modes DC current is dominant at each measurement day, therefore we are using both setups when feasible. The DC Not Tracking current appears to be larger than the Tracking DC current in most of the cases. We should note here that we avoided moving the hosting dome during any of these sequences, as we have observed some spikes (electronic noise due to dome shutter/rotation motor) in the Picoscope reading.

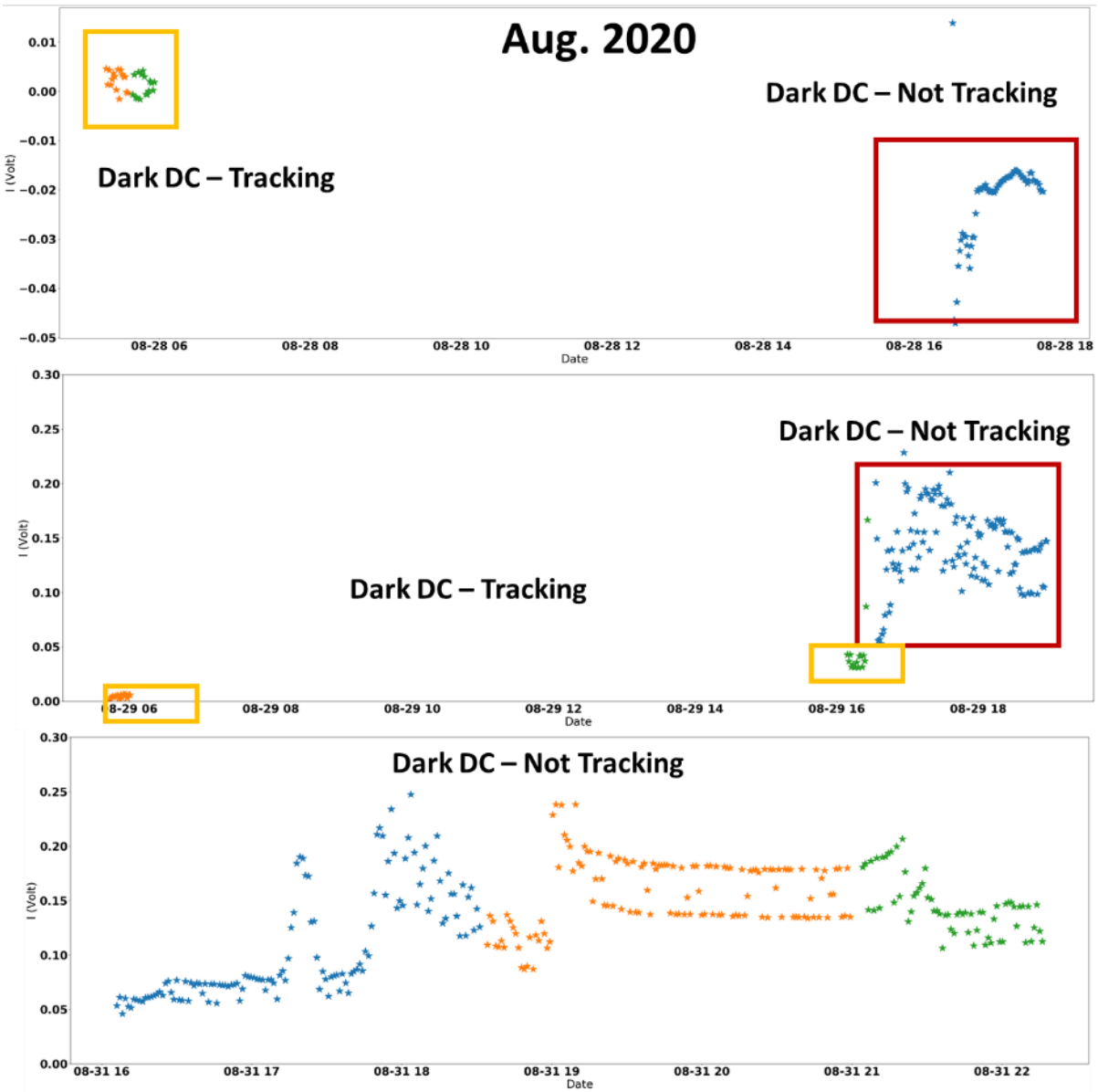

Figure A.6: DC voltage output (*I*) during August 2020 (28, 27 and 31/08) dark measurements. Different colours are used for each measurement set within the same day and may vary with the number of sets. "Tracking" mode dark outputs are highlighted with the yellow frames, while "Not Tracking" sets are highlighted with the red frames, Date is in UTC. Negative *I* values (in the 28th) are likely due to power leakage in the system, fixed the next day Not Tracking voltage is larger than in the tracking case.

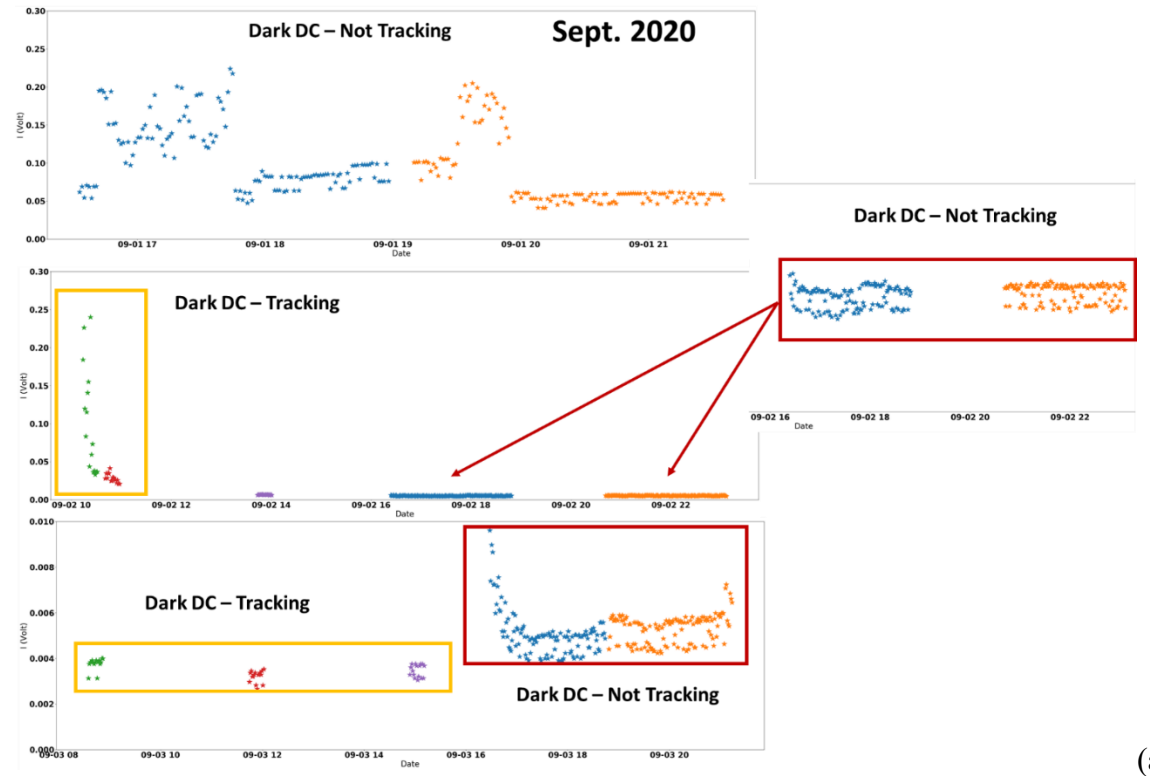

(a)

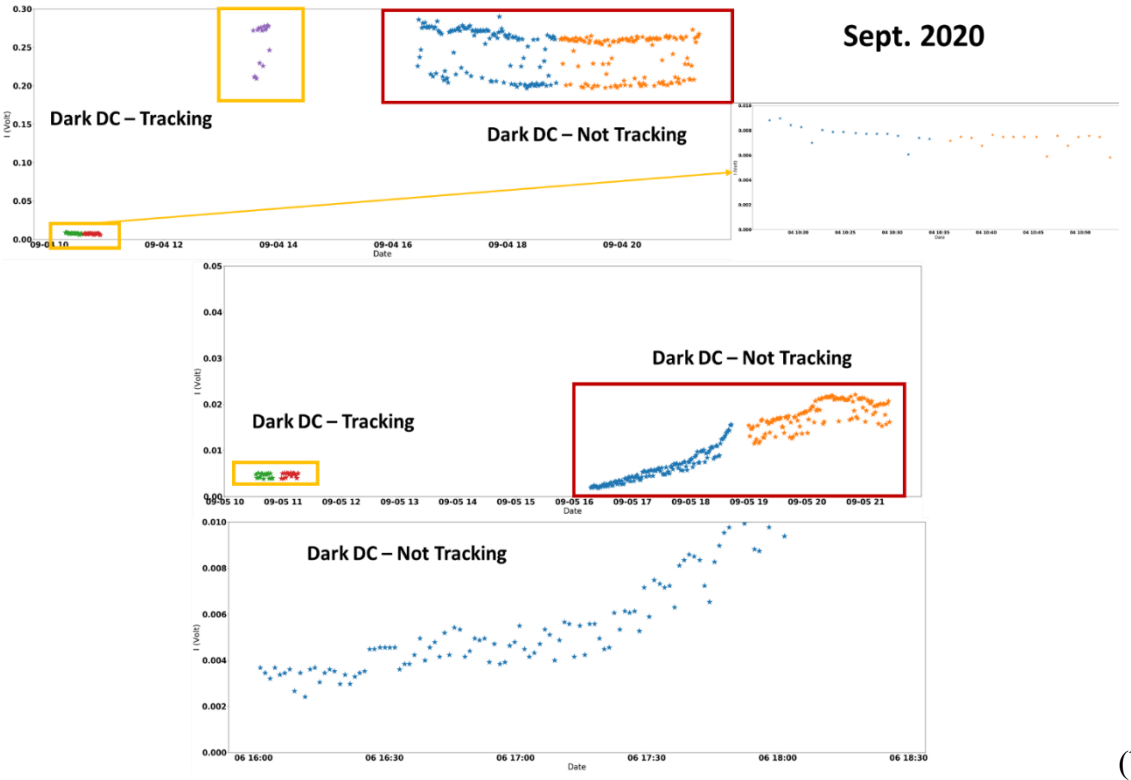

(b)

Figure A.7: (a) & (b) DC voltage output (*I*) during September 2020 (01-06/09) dark measurements. Again, Not Tracking outputs are larger than the Tracking outputs in most cases.

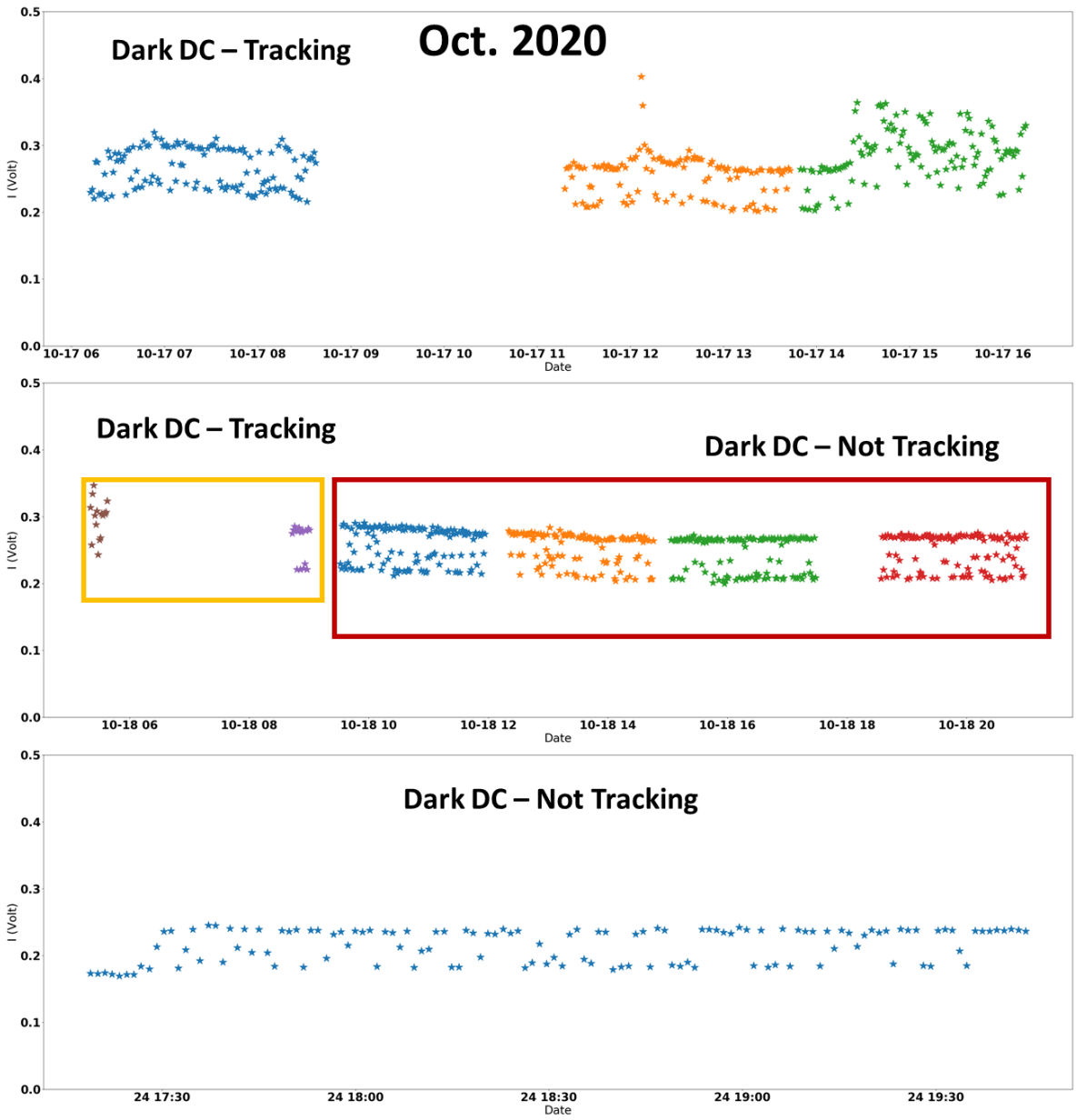

Figure A.8: DC voltage output (*I*) during October 2020 (17, 18 and 24/10) dark measurements. The 17th was a total dark measurements day scheduled with tracking and closed dome due to cloudy conditions and the 18th was a total dark measurements day with Not Tracking/closed dome so as to compare with the previous day. Data from both the 17th and 18th are of the same magnitude, with the Tracking measurements exhibiting a wavelike behavior and becoming randomized during late afternoon (green), while the Not Tracking measurements have an almost constant upper threshold.

b.ii. Dark data fitting

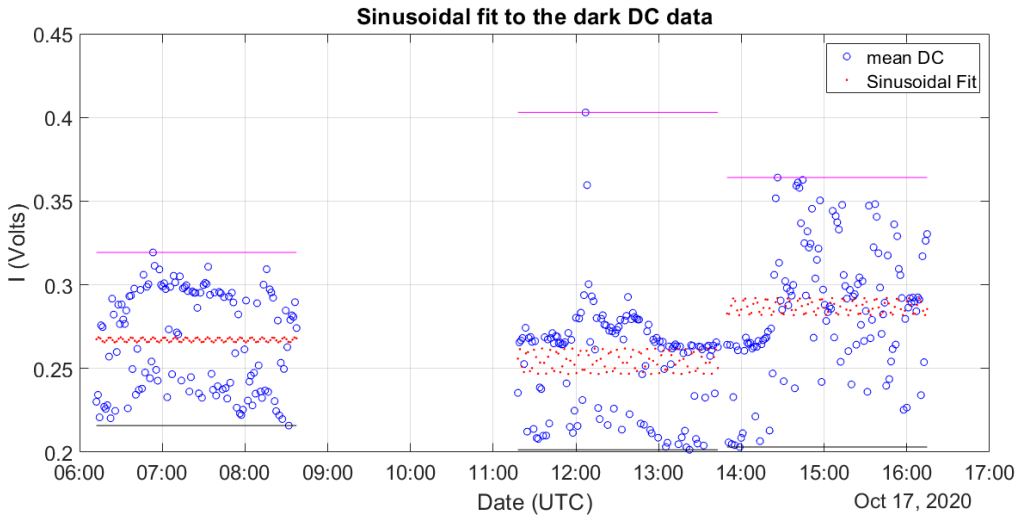

Figure A.9: Attempted fit with a sinusoidal function to the October 17th dark data in order to simulate dark current contribution. I_{dark} values vary within the day, while inner dome temperature would vary at most 1-2° C, since it was kept closed for the entire sequence.

b.iii. Total intensity & raw lock-in outputs

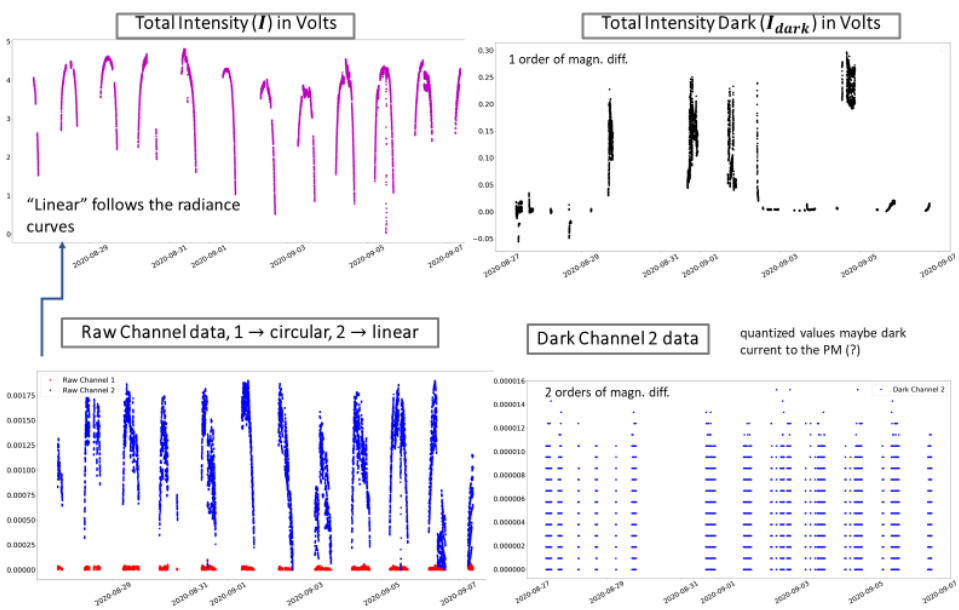

Figure A.10: **<u>Top panel:</u>** variation of I within each measurement day between August 29th and September 7th observations as opposed to I_{dark}. **<u>Bottom panel:</u>** Lock-in amplifier channel 1 (gives circular polarization) and channel 2 (gives linear polarization) raw signals compared to the dark channel 2 data for the same days.

For the extensive measurements period between 29/08/2020 and 07/09/2020 in Antikythera, we depict the variation of the DC current (total intensity I in Volts) as opposed to the total intensity recorded over the dark measurement sequences (I_{dark} in Volts). A difference of 1 order of magnitude is observed.

b.iv. Smaller Iris tests

During the 24/10/2020 measurements (Figure A.11), we experimented with a smaller iris in the front aperture of the instrument, in order to restrict the FOV in a smaller area of the Sun disk. The regular SolPol iris is of 5.5 mm in diameter, whilst the smaller one created from black cardboard paper was of 4 mm in diameter. Crude paper edges could impose non-quantifiable polarization effects, hence the non-zero circular polarization. The test will be repeated with an adjustable metallic diaphragm iris from Thorlabs.

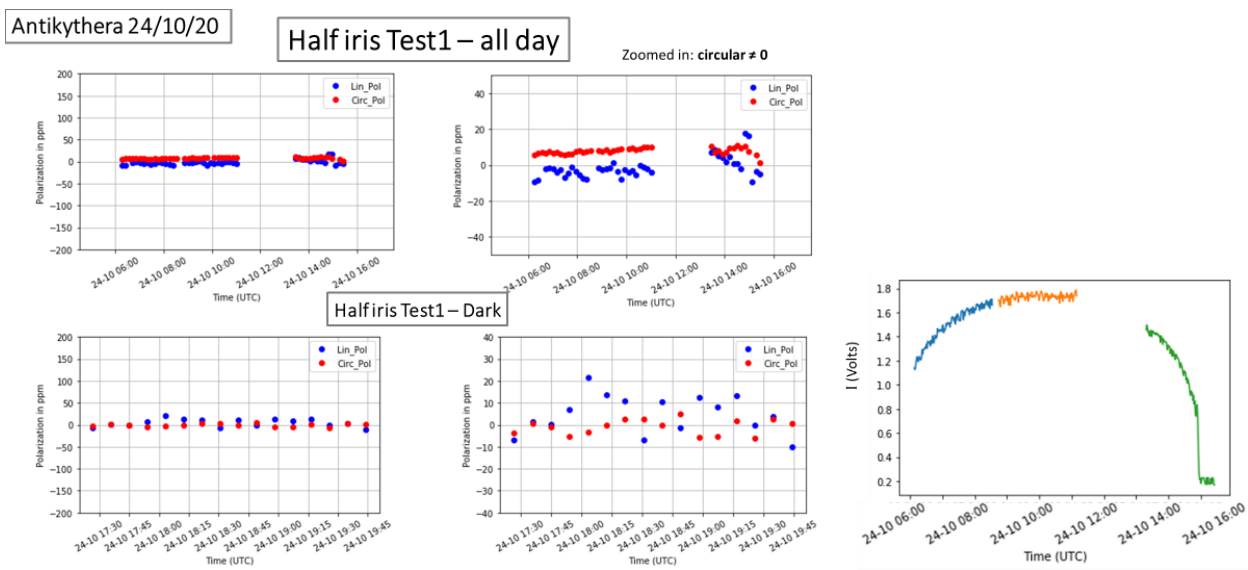

Figure A.11: Full-day measurement with a smaller handcrafted iris mounted below the existing aperture.

b.v. Sky – reading

For the preparation of these tests, we ensured that the initial sun tracking position maximized the recorded voltage in the oscilloscope (recorded each time through the EQmod po-up window) and

then consecutively calculated the right ascension (RA) and declination (DEC) for 0.5, 1 and 2° incremental steps away from the sun disk (Figure A.12). The direction of the polarimeter was constrained only for changes in the local elevation, therefore a complete set of a cross-like sky reading test will be attempted during May 2021.

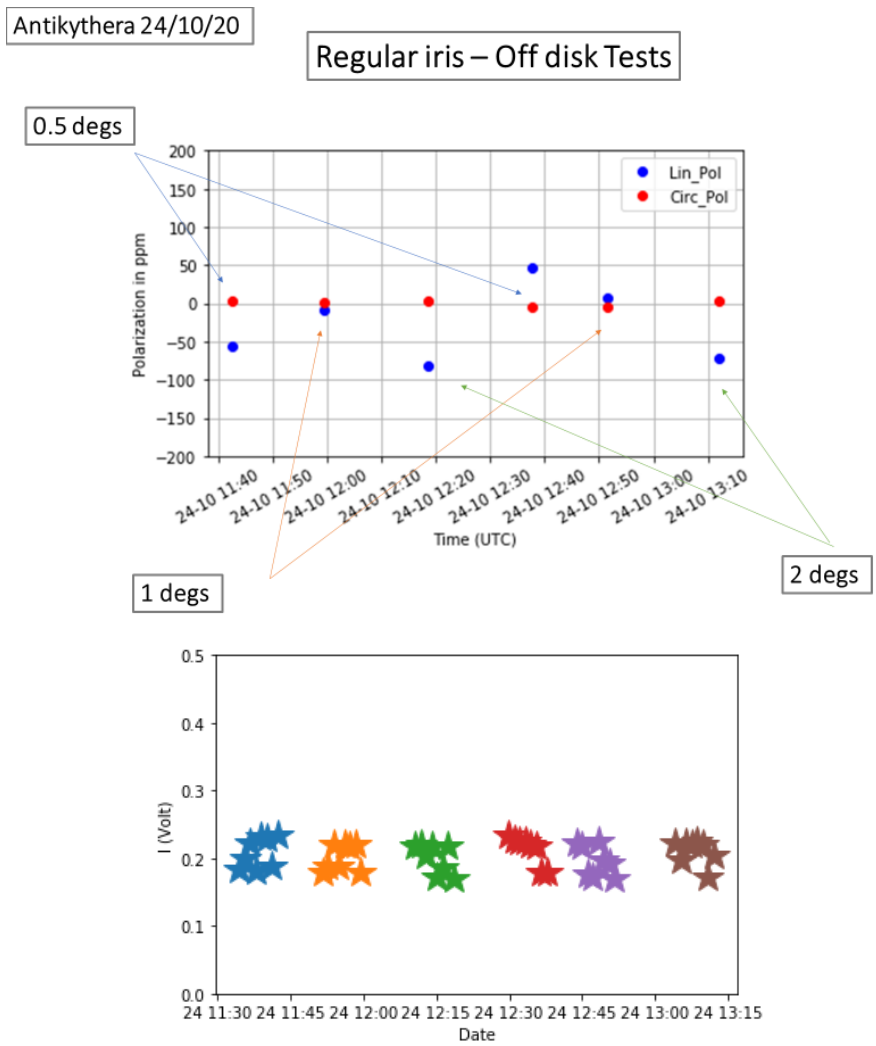

Figure A.12: Top panel: attempted sky-reading at 0.5, 1 and 2 degrees away from the central Sun's disk position that we assume under each measurement initialization with the tracker. Offset angles were calculated for the current day Sun position and manipulated through the Right Ascension and Declination

commands in the EQ ASCOM control software. Bottom panel: light intensity during the off-disk measurements.

b.i. Morning vs Evening distinction

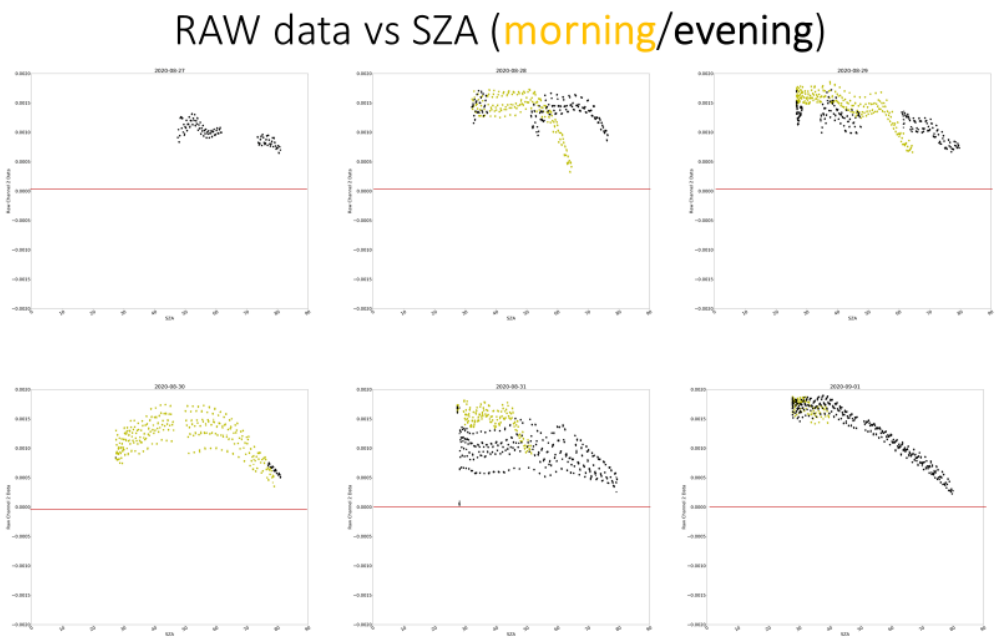

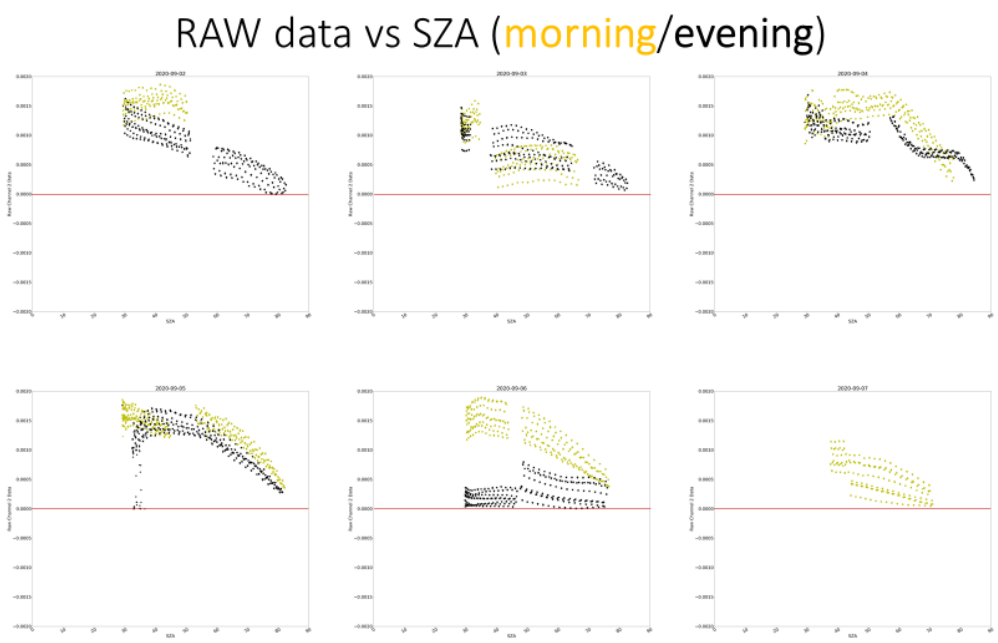

A.2 Atmospheric Electricity Sensor Specs

MiniMill sensor Specs

NOA - MiniMill Fieldmeter Specs

Baud Rate			**Dynamic range**	
Pre Radiosonde	115200		single sensitive channel	
On Radiosonde	9600	8 data bits, no parity, one stop bit (8N1)		
			Noise	
RPMs:			Zero field error	~ 2mV
~ 40 Hz	2400 (average)		Field uncertainty	± 3V/m
Sampling Rate			**Sensitivity**	1 ADC cnt, ± 2.3mV per V/m
Pre Radiosonde	9500 Samples Per Second			
On Radiosonde	1 Sample Per Second		**Resolution**	0 - 1024 ADC cnts, ± 2.4kV
Modes:			**Accuracy**	1 ADC cnt
1) w/ Accelerometer	MPU6050 - Triple Axis Gyroscope & Accelerometer IMU			
2) No rotational information				
			Bandwidth (dB)	through UART
				Radiosonde defined bandwidth
Motor:	FlyCat 2204/260kV Brushless Motor		**Physical**	
			Mass	250 gr
			Power	9V batteries (DC in)
Speed controller:	XXD HW30A 30A Brushless Motor ESC		Cosumption	< 160mA
PCB type:	multilayered		**Electrode Deck**	
PCB1	PTH, 70X70mm, FR4 1mm, 35µm		Radius	45mm
PCB/Electrode	Electrode Deck with copper plating			
Microcontroller type			**Shutter**	
Arduino Nano CH340			Radius	5.83cm
			Thickness	1mm
			Distance from the Electro	4mm
Operating environment	(implemented configuration)			
Temperature	up to - 40°C		**Cube Dimensions:**	
Altitude	msl to ~ 13km		Height	79mm
Humidity	to 100%		Length	76mm
			Width	76mm

Space Charge sensor Specs

NOA - Space Charge Sensor Specs

as in *Nicoll & Harrison 2009* , *Nicoll 2013*

Baud Rate	
Pre Radiosonde	115200
On Radiosonde	9600
	8 data bits, no parity, one stop bit (8N1)

Electrode	
Brass - spherical	
Diameter	15mm
Effective Diameter (deff)	25.4mm

Sampling Rate	
Pre Radiosonde	9500 Samples Per Second
On Radiosonde	1 Sample Per Second

Modes:	
state0	Regular measurement
state1	Calibration period 1
state2	Calibration period 2

Spherical Electrode	
Material	Brass
Diameter	15mm
Thickeness	1.5mm hollow

PCB type:	
PCB1	FR4 1 mm, 35/35µm, double sided (PTH), finish: HAL, 34X26mm
PCB2	FR4 1 mm, 35/35µm, double sided (PTH), finish: HAL, 50X28mm

Microcontroller type
Arduino Nano CH340

Operating environment	
Temperature	up to -60°C (with project box)
Altitude	msl to 16km
Humidity	to 100%

Dynamic range
single sensitive channel

Noise	
Zero field error	1 ADC cnt
Dark voltage	~ 4.6mV

Sensitivity	± 2.3mV
Resolution	± 2.5V
Accuracy	~ 10mV
Bandwidth (dB)	through UART
	Radiosonde defined bandwidth

Physical	
Mass	90 gr (without battery)
Power	9V batteries (DC in)
Consumption	< 100mA

Project Box Dimensions:	
Height	43.8mm
Length	101mm
Width	54mm

GRAW - XDATA - UART

Pin	Use	Comment	Connect To
1	N/C	The red wire	No connection
2	Rx		Microcontroller UART Tx
3	Tx		No connection
4	GND		Ground

For XDATA operation, you only need to connect pin 4 to your board's Ground and pin 2 to your microcontroller's UART Tx pin.

Byte	0-5	6-7	8-9	10-32
Content (example)	xdata=	01	AA	01AAC00158C40A44545FB6C44F7D9C3C
Description	Header	Sensor ID	Daisy Chain counter -or- NOA Sensor ID	What you want to send downstream

At NOA, we use this to identify our sensors:

NOA Sensor ID	Sensor name
0xAA	Field mill sensor
0xAB	Space charge sensor

For the rest of the bytes, you can put any data you want. If sensor ID is not 01, the ground-station software will NOT record XDATA packets.

Ground-station

When dealing with GRAW's ground-station software, you need to deal with the following:

1. Radiosonde initialization - Ozone sensor procedures
2. Mangled data viewer
3. Data storage

Each of these issues will be discussed in the sections below.

Radiosonde Initialization

To make the ground-station store XDATA packages, you must "trick" it to think you have connected a recognized sensor device (e.g. Ozone).

Mangled data viewer

When receiving data from a custom sensor, the perpetually-confused ground-station software does not know to interpret them. Expect to see garbage values at the XDATA view window. This is OK, since the raw XDATA packages are stored separately. You can use the XDATA view window to judge whether you are receiving any packages at all.

Data Storage

The ground-station software stores incoming XDATA packages, alongside with a timestamp, inside the xdata.gsf file (probably inside %USERPROFILE%/Documents/GRAW/Data/, might be different in other machines).

Radiosonde Internals

To figure out the pins, we opened a radiosonde and checked where they hook up. Next to the connector, there is an ADuM3201 dual-channel isolator (dataset attached). The XDATA header is connected to the Isolator as shown in the table below.

XDATA Pin	ADuM3201 Pin	Comment
1	--	Not connected (anywhere?)
2	3	Decode side of ADuM3201, we assume that means Tx of the radiosonde
3	2	Encode side of ADuM3201, we assume that means Rx of the radiosonde
4	4	Ground

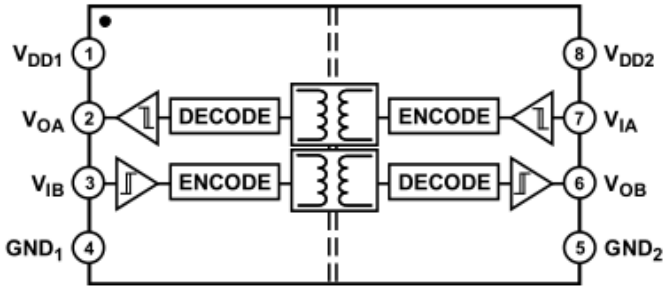

Figure 2. ADuM3201 Functional Block Diagram

Bibliography

Adebiyi, A., Kok, J. F., Murray, B. J., Ryder, C. L., Stuut, J. B. W., Kahn, R. A., Knippertz, P., Formenti, P., Mahowald, N. M., Pérez García-Pando, C., Klose, M., Ansmann, A., Samset, B. H., Ito, A., Balkanski, Y., Di Biagio, C., Romanias, M. N., Huang, Y. and Meng, J.: A review of coarse mineral dust in the Earth system, Aeolian Res., 60(November 2022), doi:10.1016/j.aeolia.2022.100849, 2023.

Adebiyi, A. A. and Kok, J. F.: Climate models miss most of the coarse dust in the atmosphere, Sci. Adv., 6(15), 1–9, doi:10.1126/sciadv.aaz9507, 2020.

Andersson, B.-G., Lazarian, A. and Vaillancourt, J. E.: Interstellar Dust Grain Alignment, Annu. Rev. Astron. Astrophys., 53(1), 501–539, doi:10.1146/annurev-astro-082214-122414, 2015.

Anisimov, S. V., Afinogenov, K. V. and Shikhova, N. M.: Dynamics of undisturbedmidlatitude atmospheric electricity: From observations to scaling, Radiophys. Quantum Electron., 56(11–12), 709–722, doi:10.1007/s11141-014-9475-z, 2014.

Anisimov, S. V., Galichenko, S. V. and Mareev, E. A.: Electrodynamic properties and height of atmospheric convective boundary layer, Atmos. Res., 194, 119–129, doi:10.1016/j.atmosres.2017.04.012, 2017.

Aplin, K. L., Briggs, A. A., Harrison, R. G. and Marlton, G. J.: Measuring ionizing radiation in the atmosphere with a new balloon-borne detector, Sp. Weather, 15(5), 663–672, doi:10.1002/2017SW001610, 2017.

Bagheri, G. and Bonadonna, C.: On the drag of freely falling non-spherical particles, Powder Technol., 301, 526–544, doi:10.1016/j.powtec.2016.06.015, 2016.

Bailey, J., Ulanowski, Z., Lucas, P. W., Hough, J. H., Hirst, E. and Tamura, M.: The effect of airborne dust on astronomical polarization measurements, Mon. Not. R. Astron. Soc., 386(2), 1016–1022, doi:10.1111/j.1365-2966.2008.13088.x, 2008.

Bailey, J., Cotton, D. V., Kedziora-Chudczer, L., De Horta, A. and Maybour, D.: HIPPI-2: A versatile high-precision polarimeter, Publ. Astron. Soc. Aust., doi:10.1017/pasa.2019.45, 2020.

Baran, A. J.: On the scattering and absorption properties of cirrus cloud, J. Quant. Spectrosc.

Radiat. Transf., 89(1–4), 17–36, doi:10.1016/j.jqsrt.2004.05.008, 2004.

Baumgaertner, A. J. G., Lucas, G. M., Thayer, J. P. and Mallios, S. A.: On the role of clouds in the fair weather part of the global electric circuit, Atmos. Chem. Phys., 14(16), 8599–8610, doi:10.5194/acp-14-8599-2014, 2014.

Baumgardner, D., Jonsson, H., Dawson, W., O'Connor, D. and Newton, R.: The cloud, aerosol and precipitation spectrometer: a new instrument for cloud investigations, Atmos. Res., 59–60, 251–264, doi:https://doi.org/10.1016/S0169-8095(01)00119-3, 2001.

Benjamini, Y. and Yekutieli, D.: The control of the false discovery rate in multiple testing under dependency, Ann. Stat., 29(4), 1165–1188, doi:10.1214/aos/1013699998, 2001.

Berg, M. J. and Videen, G.: Digital holographic imaging of aerosol particles in flight, J. Quant. Spectrosc. Radiat. Transf., 112(11), 1776–1783, doi:10.1016/j.jqsrt.2011.01.013, 2011.

Berg, M. J., Heinson, Y. W., Kemppinen, O. and Holler, S.: Solving the inverse problem for coarse-mode aerosol particle morphology with digital holography, Sci. Rep., 7(1), 1–9, doi:10.1038/s41598-017-09957-w, 2017.

Bering, E. A., Few, A. A. and Benbrook, J. R.: The global electric circuit, Phys. Today, 51(10), 24–30, doi:10.1063/1.882422, 1998.

Bohren, C. F.: Absorption and scattering of light by small particles, Absorpt. Scatt. Light by small Part., doi:10.1088/0031-9112/35/3/025, 1983.

Bohren, C. F.: Multiple scattering of light and some of its observable consequences, Am. J. Phys., 55(6), 524–533, doi:10.1119/1.15109, 1987.

Buguet, M., Lalande, P., Laroche, P., Blanchet, P., Bouchard, A. and Chazottes, A.: Thundercloud electrostatic field measurements during the inflight exaedre campaign and during lightning strike to the aircraft, Atmosphere (Basel)., 12(12), doi:10.3390/atmos12121645, 2021.

Cairns, B., Russell, E. E., LaVeigne, J. D. and Tennant, P. M. W.: Research scanning polarimeter and airborne usage for remote sensing of aerosols, Polariz. Sci. Remote Sens., 5158, 33, doi:10.1117/12.518320, 2003.

Cairns, B., Waquet, F., Knobelspiesse, K., Chowdhary, J. and Deuzé, J.-L.: Polarimetric remote sensing of aerosols over land surfaces, in Satellite Aerosol Remote Sensing over Land, edited by A. A. Kokhanovsky and G. de Leeuw, pp. 295–325, Springer Berlin Heidelberg, Berlin, Heidelberg., 2009.

Cakmur, R. V., Miller, R. L., Perlwitz, J., Geogdzhayev, I. V., Ginoux, P., Koch, D., Kohfeld,

K. E., Tegen, I. and Zender, C. S.: Constraining the magnitude of the global dust cycle by minimizing the difference between a model and observations, J. Geophys. Res. Atmos., 111(6), 1–24, doi:10.1029/2005JD005791, 2006.

Chalmers, J.A., 1967. Atmospheric Electricity, second ed. Pergamon press, Oxford, UK.

Chen, S., Jiang, N., Huang, J., Xu, X., Zhang, H., Zang, Z., Huang, K., Xu, X., Wei, Y., Guan, X., Zhang, X., Luo, Y., Hu, Z. and Feng, T.: Quantifying contributions of natural and anthropogenic dust emission from different climatic regions, Atmos. Environ., 191(August), 94–104, doi:10.1016/j.atmosenv.2018.07.043, 2018.

Chiu, C.-S.: Numerical study of cloud electrification in an axisymmetric, time-dependent cloud model, J. Geophys. Res., 83(C10), 5025, doi:10.1029/jc083ic10p05025, 1978.

Chubb, J.: The measurement of atmospheric electric fields using pole mounted electrostatic fieldmeters, J. Electrostat., 72(4), 295–300, doi:10.1016/j.elstat.2014.05.002, 2014.

Chubb, J.: Comparison of atmospheric electric field measurements by a pole mounted fieldmeter and by a horizontal wire antenna, J. Electrostat., 73, 1–5, doi:10.1016/j.elstat.2014.10.003, 2015.

Connolly, B. J., Loth, E. and Smith, C. F.: Shape and drag of irregular angular particles and test dust, Powder Technol., 363, 275–285, doi:10.1016/j.powtec.2019.12.045, 2020.

Corney, R. C., Burns, G. B., Michael, K., Frank-Kamenetsky, A. V., Troshichev, O. A., Bering, E. A., Papitashvili, V. O., Breed, A. M. and Duldig, M. L.: The influence of polar-cap convection on the geoelectric field at Vostok, Antarctica, J. Atmos. Solar-Terrestrial Phys., 65(3), 345–354, doi:10.1016/S1364-6826(02)00225-0, 2003.

Cox, N. L. J., Ehrenfreund, P., Foing, B. H., D'Hendecourt, L., Salama, F. and Sarre, P. J.: Linear and circular spectropolarimetry of diffuse interstellar bands, Astron. Astrophys., 531, doi:10.1051/0004-6361/201016365, 2011.

Creamean, J. M., Suski, K. J., Rosenfeld, D., Cazorla, A., DeMott, P. J., Sullivan, R. C., White, A. B., Ralph, F. M., Minnis, P., Comstock, J. M., Tomlinson, J. M. and Prather, K. A.: Dust and biological aerosols from the Sahara and Asia influence precipitation in the Western U.S, Science (80-.)., 340(6127), 1572–1578, doi:10.1126/science.1227279, 2013.

Cui, Y., Yuan, H., Song, X., Zhao, L., Liu, Y. and Lin, L.: Model, Design, and Testing of Field Mill Sensors for Measuring Electric Fields Under High-Voltage Direct-Current Power Lines, IEEE Trans. Ind. Electron., 65(1), 608–615, doi:10.1109/TIE.2017.2719618, 2018.

Dasgupta Ajou K.: Grain alignment in the intergalactic magnetic field, Astrophys. Space Sci.,

91(2), 395–406, 1983.

Daskalopoulou, V., Raptis, I.-P., Tsekeri, A., Amiridis, V., Kazadzis, S., Ulanowski, Z., Metallinos, S., Tassis, K. and Martin, W.: Monitoring dust particle orientation with measurements of sunlight dichroic extinction, in 15th COMECAP, pp. 508–515, Ioannina, Greece., 2021a.

Daskalopoulou, V., Mallios, S. A., Ulanowski, Z., Hloupis, G., Gialitaki, A., Tsikoudi, I., Tassis, K. and Amiridis, V.: The electrical activity of Saharan dust as perceived from surface electric field observations, Atmos. Chem. Phys., 21(2), 927–949, doi:10.5194/acp-21-927-2021, 2021b.

Daskalopoulou, V., Raptis, P. I., Tsekeri, A., Amiridis, V., Kazadzis, S., Ulanowski, Z., Charmandaris, V., Tassis, K. and Martin, W.: Linear polarization signatures of atmospheric dust with the SolPol direct-sun polarimeter, Atmos. Meas. Tech., 16(19), 4529–4550, doi:10.5194/amt-16-4529-2023, 2023a.

Daskalopoulou, V., Raptis, P. I., Tsekeri, A., Amiridis, V., Kazadzis, S., Ulanowski, Z., Charmandaris, V., Tassis, K. and Martin, W.: Observations of Dust Particle Orientation with the SolPol direct sun polarimeter, Atmos. Meas. Tech. Discuss., 2023, 1–36, doi:10.5194/amt-2023-121, 2023b.

David, G., Esat, K., Thanopulos, I. and Signorell, R.: Digital holography of optically-trapped aerosol particles, Commun. Chem., 1(1), 1–9, doi:10.1038/s42004-018-0047-6, 2018.

DAVIS, M. H.: TWO CHARGED SPHERICAL CONDUCTORS IN A UNIFORM ELECTRIC FIELD: FORCES AND FIELD STRENGTH†, Q. J. Mech. Appl. Math., 17(4), 499–511, doi:10.1093/qjmam/17.4.499, 1964.

DeMott, P. J., Sassen, K., Poellot, M. R., Baumgardner, D., Rogers, D. C., Brooks, S. D., Prenni, A. J. and Kreidenweis, S. M.: African dust aerosols as atmospheric ice nuclei, Geophys. Res. Lett., 30(14), 26–29, doi:10.1029/2003GL017410, 2003.

Denjean, C., Cassola, F., Mazzino, A., Triquet, S., Chevaillier, S., Grand, N., Bourrianne, T., Momboisse, G., Sellegri, K., Schwarzenbock, A., Freney, E., Mallet, M. and Formenti, P.: Size distribution and optical properties of mineral dust aerosols transported in the western Mediterranean, Atmos. Chem. Phys., 16(2), 1081–1104, doi:10.5194/acp-16-1081-2016, 2016.

Dioguardi, F., Mele, D. and Dellino, P.: A New One-Equation Model of Fluid Drag for Irregularly Shaped Particles Valid Over a Wide Range of Reynolds Number, J. Geophys. Res. Solid Earth, 123(1), 144–156, doi:10.1002/2017JB014926, 2018.

van der Does, M., Knippertz, P., Zschenderlein, P., Giles Harrison, R. and Stuut, J. B. W.: The

mysterious long-range transport of giant mineral dust particles, Sci. Adv., 4(12), 1–9, doi:10.1126/sciadv.aau2768, 2018.

Dolginov, A. Z.: Orientation of interstellar and interplanetary grains, Astrophys. Space Sci., 18(1952), 337–349, doi:https://doi.org/10.1007/BF00645399, 1972.

Drakaki, E., Amiridis, V., Tsekeri, A., Gkikas, A., Proestakis, E., Mallios, S., Solomos, S., Spyrou, C., Marinou, E., Ryder, C., Bouris, D. and Katsafados, P.: Modelling coarse and giant desert dust particles, Atmos. Chem. Phys. Discuss., 2022, 1–36, doi:10.5194/acp-2022-94, 2022.

Dubovik, O., Li, Z., Mishchenko, M. I., Tanré, D., Karol, Y., Bojkov, B., Cairns, B., Diner, D. J., Espinosa, W. R., Goloub, P., Gu, X., Hasekamp, O., Hong, J., Hou, W., Knobelspiesse, K. D., Landgraf, J., Li, L., Litvinov, P., Liu, Y., Lopatin, A., Marbach, T., Maring, H., Martins, V., Meijer, Y., Milinevsky, G., Mukai, S., Parol, F., Qiao, Y., Remer, L., Rietjens, J., Sano, I., Stammes, P., Stamnes, S., Sun, X., Tabary, P., Travis, L. D., Waquet, F., Xu, F., Yan, C. and Yin, D.: Polarimetric remote sensing of atmospheric aerosols: Instruments, methodologies, results, and perspectives, J. Quant. Spectrosc. Radiat. Transf., 224, 474–511, doi:10.1016/j.jqsrt.2018.11.024, 2019.

Duff, N. and Lacks, D. J.: Particle dynamics simulations of triboelectric charging in granular insulator systems, J. Electrostat., 66(1–2), 51–57, doi:10.1016/j.elstat.2007.08.005, 2008.

Eden, H. F. and Vonnegut, B.: Electrical Breakdown Caused by Dust Motion in Low-Pressure Atmospheres: Considerations for Mars, Science (80-.)., 180(4089), 962–963, doi:10.1126/science.180.4089.962, 1973.

Emde, C., Buehler, S. A., Davis, C., Eriksson, P., Sreerekha, T. R. and Teichmann, C.: A polarized discrete ordinate scattering model for simulations of limb and nadir long-wave measurements in 1-D/3-D spherical atmospheres, J. Geophys. Res. D Atmos., 109(24), 1–20, doi:10.1029/2004JD005140, 2004.

Emde, C., Buras-Schnell, R., Sterzik, M. and Bagnulo, S.: Influence of aerosols, clouds, and sunglint on polarization spectra of Earthshine, Astron. Astrophys., 605, 1–15, doi:10.1051/0004-6361/201629948, 2017.

Engelmann, R., Kanitz, T., Baars, H., Heese, B., Althausen, D., Skupin, A., Wandinger, U., Komppula, M., Stachlewska, I. S., Amiridis, V., Marinou, E., Mattis, I., Linné, H. and Ansmann, A.: The automated multiwavelength Raman polarization and water-vapor lidar PollyXT: The neXT generation, Atmos. Meas. Tech., 9(4), 1767–1784, doi:10.5194/amt-9-1767-2016, 2016.

Esposito, F., Molinaro, R., Popa, C. I., Molfese, C., Cozzolino, F., Marty, L., Taj-Eddine, K., Di

Achille, G., Franzese, G., Silvestro, S. and Ori, G. G.: The role of the atmospheric electric field in the dust-lifting process, Geophys. Res. Lett., 43(10), 5501–5508, doi:10.1002/2016GL068463, 2016.

Ette, A. I. I.: The effect of the Harmattan dust on atmospheric electric parameters, J. Atmos. Terr. Phys., 33(2), 295–300, doi:10.1016/0021-9169(71)90208-X, 1971.

Farrell, W. M.: Electric and magnetic signatures of dust devils from the 2000–2001 MATADOR desert tests, J. Geophys. Res., 109(E3), E03004, doi:10.1029/2003JE002088, 2004.

Fjeld, R. A. and McFarland, A. R.: Evaluation of select approximations for calculating particle charging rates in the continuum regime, Aerosol Sci. Technol., 10(3), 535–549, doi:10.1080/02786828908959293, 1989.

Fjeld, R. A., Gauntt, R. O. and McFarland, A. R.: Continuum field-diffusion theory for bipolar charging of aerosols, J. Aerosol Sci., 14(4), 541–556, doi:10.1016/0021-8502(83)90010-1, 1983.

Flamant, C., Pelon, J., Flamant, P. H. and Durand, P.: Lidar determination of the entrainment zone thickness at the top of the unstable marine atmospheric boundary layer, Boundary-Layer Meteorol., 83(2), 247–284, doi:10.1023/A:1000258318944, 1997.

Formenti, P., Schütz, L., Balkanski, Y., Desboeufs, K., Ebert, M., Kandler, K., Petzold, A., Scheuvens, D., Weinbruch, S. and Zhang, D.: Recent progress in understanding physical and chemical properties of African and Asian mineral dust, Atmos. Chem. Phys., 11(16), 8231–8256, doi:10.5194/acp-11-8231-2011, 2011.

Forward, K. M., Lacks, D. J. and Sankaran, R. M.: Charge segregation depends on particle size in triboelectrically charged granular materials, Phys. Rev. Lett., 102(2), 1–4, doi:10.1103/PhysRevLett.102.028001, 2009a.

Forward, K. M., Lacks, D. J. and Mohan Sankaran, R.: Particle-size dependent bipolar charging of Martian regolith simulant, Geophys. Res. Lett., 36(13), 1–5, doi:10.1029/2009GL038589, 2009b.

Freier G. D.: The Electric Field of a Large Dust Devil, J. Geophys. Res., 65(10), 1896–1977, 1960.

Freudenthaler, V.: About the effects of polarising optics on lidar signals and the Δ90 calibration, Atmos. Meas. Tech., 9(9), 4181–4255, doi:10.5194/amt-9-4181-2016, 2016.

Freudenthaler, V., Esselborn, M., Wiegner, M., Heese, B., Tesche, M., Ansmann, A., Müller, D., Althausen, D., Wirth, M., Fix, A., Ehret, G., Knippertz, P., Toledano, C., Gasteiger, J.,

Garhammer, M. and Seefeldner, M.: Depolarization ratio profiling at several wavelengths in pure Saharan dust during SAMUM 2006, Tellus, Ser. B Chem. Phys. Meteorol., 61(1), 165–179, doi:10.1111/j.1600-0889.2008.00396.x, 2009.

Fuchs, N. A.: On the stationary charge distribution on aerosol particles in a bipolar ionic atmosphere, Geofis. Pura e Appl., 56(1), 185–193, doi:10.1007/BF01993343, 1963.

Fuchs, N. A., Fuks, N. A. and Davies, C. N.: The Mechanics of Aerosols, Dover Publications. [online] Available from: https://books.google.gr/books?id=5XbZAAAAMAAJ, 1964.

Garcia-Carreras, L., Parker, D. J., Marsham, J. H., Rosenberg, P. D., Brooks, I. M., Lock, A. P., Marenco, F., Mcquaid, J. B. and Hobby, M.: The turbulent structure and diurnal growth of the Saharan atmospheric boundary layer, J. Atmos. Sci., 72(2), 693–713, doi:10.1175/JAS-D-13-0384.1, 2015.

Gassó, S., Knobelspiesse, K. D., Adebiyi, A. A., Huang, Y., Samset, B. H., Kok, J. F., Sparks, W. B., Hough, J., Germer, T. A., Chen, F., DasSarma, S., DasSarmad, P., Robbd, F. T., Mansete, N., Kolokolovaf, L., Reida, N., Macchetto, F. D., Martin, W., Chen, L., Peng, C. C., Gu, W., Fu, H., Jian, X., Zhang, H. H., Zhang, G., Zhu, J., Wang, X., Tang, M., Yang, P., Wen, X., Lv, Y., Chu, Z., Peng, C. C., Liu, Y., Wu, S., Rubin, N. A., D'Aversa, G., Chevalier, P., Shi, Z., Chen, W. T., Capasso, F., Mishchenko, M. I., Hovenier, J. W., Stam, D. M., De Haan, J. F., Hovenier, J. W., Stammes, P., Fort, A., Mugnaini, M., Vignoli, V., Rocchi, S., Perini, F., Monari, J., Schiaffino, M., Fiocchi, F., Zhao, W., Li, Z., Zhang, H. H., Yuan, Y., Zhao, Z., Hess, M., Koepke, P. and Schult, I.: Circular Polarization in Atmospheric Aerosols, IEEE Trans. Instrum. Meas., 20(8), 16843–16858, doi:10.1109/TIM.2021.3135341, 2022.

Gasteiger, J., Wiegner, M., Groß, S., Freudenthaler, V., Toledano, C., Tesche, M. and Kandler, K.: Modelling lidar-relevant optical properties of complex mineral dust aerosols, Tellus, Ser. B Chem. Phys. Meteorol., 63(4), 725–741, doi:10.1111/j.1600-0889.2011.00559.x, 2011.

Geier, M. and Arienti, M.: Detection of preferential particle orientation in the atmosphere: Development of an alternative polarization lidar system, J. Quant. Spectrosc. Radiat. Transf., 149, 16–32, doi:10.1016/j.jqsrt.2014.07.011, 2014.

Ginoux, P.: Effects of nonsphericity on mineral dust modeling, J. Geophys. Res. Atmos., 108(2), doi:10.1029/2002jd002516, 2003.

Ginoux, P., Chin, M., Tegen, I., Prospero, J. M., Holben, B. N., Dubovik, O. and Lin, S. J.: Sources and distributions of dust aerosols simulated with the GOCART model, , 106(273), 20555–

20273, 2001.

Guan, L., Li, S., Zhai, L., Liu, S., Liu, H., Lin, W., Cui, Y., Chu, J. and Xie, H.: Study on skylight polarization patterns over the ocean for polarized light navigation application, Appl. Opt., 57(21), 6243, doi:10.1364/ao.57.006243, 2018.

Gueymard, C. A.: Temporal variability in direct and global irradiance at various time scales as affected by aerosols, Sol. Energy, 86(12), 3544–3553, doi:10.1016/j.solener.2012.01.013, 2012.

Gunn, R.: Diffusion Charging of Atmospheric Droplets By Ions, and the Resulting Combination Coefficients, J. Meteorol., 11(5), 339–347, doi:10.1175/1520-0469(1954)011<0339:dcoadb>2.0.co;2, 1954.

Haarig, M., Ansmann, A., Althausen, D., Klepel, A., Groß, S., Freudenthaler, V., Toledano, C., Mamouri, R. E., Farrell, D. A., Prescod, D. A., Marinou, E., Burton, S. P., Gasteiger, J., Engelmann, R. and Baars, H.: Triple-wavelength depolarization-ratio profiling of Saharan dust over Barbados during SALTRACE in 2013 and 2014, Atmos. Chem. Phys., 17(17), 10767–10794, doi:10.5194/acp-17-10767-2017, 2017.

Haldoupis, C., Rycroft, M., Williams, E. and Price, C.: Is the "Earth-ionosphere capacitor" a valid component in the atmospheric global electric circuit?, J. Atmos. Solar-Terrestrial Phys., 164(August), 127–131, doi:10.1016/j.jastp.2017.08.012, 2017.

Hansen, J. E. and Travis, L. D.: Light scattering in planetary atmospheres, Space Sci. Rev., 16(4), 527–610, doi:10.1007/BF00168069, 1974.

Harper, J. M., Harvey, D., Huang, T., McGrath, J., Meer, D. and Burton, J. C.: The lifetime of charged dust in the atmosphere, , 1–8 [online] Available from: http://arxiv.org/abs/2206.06848, 2022.

Harrison, R. G.: Ion-aerosol-cloud processes in the lower atmosphere, Rev. Geophys., 41(3), 1012, doi:10.1029/2002RG000114, 2003.

Harrison, R. G.: The Carnegie Curve, Surv. Geophys., 34(2), 209–232, doi:10.1007/s10712-012-9210-2, 2013.

Harrison, R. G. and Ingram, W. J.: Air-earth current measurements at Kew, London, 1909-1979, Atmos. Res., 76(1–4), 49–64, doi:10.1016/j.atmosres.2004.11.022, 2005.

Harrison, R. G. and Marlton, G. J.: Fair weather electric field meter for atmospheric science platforms, J. Electrostat., 107(August), 103489, doi:10.1016/j.elstat.2020.103489, 2020.

Harrison, R. G. and Nicoll, K. A.: Fair weather criteria for atmospheric electricity measurements,

J. Atmos. Solar-Terrestrial Phys., 179(February), 239–250, doi:10.1016/j.jastp.2018.07.008, 2018.

Harrison, R. G., Nicoll, K. A., Ulanowski, Z. and Mather, T. A.: Self-charging of the Eyjafjallajökull volcanic ash plume, Environ. Res. Lett., 5(2), 3–7, doi:10.1088/1748-9326/5/2/024004, 2010.

Harrison, R. G., Barth, E., Esposito, F., Merrison, J., Montmessin, F., Aplin, K. L., Borlina, C., Berthelier, J. J., Déprez, G., Farrell, W. M., Houghton, I. M. P., Renno, N. O., Nicoll, K. A., Tripathi, S. N. and Zimmerman, M.: Applications of Electrified Dust and Dust Devil Electrodynamics to Martian Atmospheric Electricity, Space Sci. Rev., 203(1–4), 299–345, doi:10.1007/s11214-016-0241-8, 2016.

Harrison, R. G., Nicoll, K. A., Marlton, G. J., Ryder, C. L. and Bennett, A. J.: Saharan dust plume charging observed over the UK, Environ. Res. Lett., 13(5), doi:10.1088/1748-9326/aabcd9, 2018.

Harrison, R. G., Nicoll, K. A., Mareev, E., Slyunyaev, N. and Rycroft, M. J.: Extensive layer clouds in the global electric circuit: their effects on vertical charge distribution and storage, Proc. R. Soc. A Math. Phys. Eng. Sci., 476(2238), 20190758, doi:10.1098/rspa.2019.0758, 2020.

Hayman, M., Spuler, S., Morley, B. and VanAndel, J.: Polarization lidar operation for measuring backscatter phase matrices of oriented scatterers., Opt. Express, 20(28), 29553–29567, doi:10.1364/OE.20.029553, 2012.

Hayman, M., Spuler, S. and Morley, B.: Polarization lidar observations of backscatter phase matrices from oriented ice crystals and rain, Opt. Express, 22(14), 16976, doi:10.1364/oe.22.016976, 2014.

Hendry, A. and Antar, Y. M. M.: Radar observations of polarization characteristics and lightning-induced realignment of atmospheric ice crystals, Radio Sci., 17(5), 1243–1250, doi:10.1029/RS017i005p01243, 1982.

Hough, J. H., Lucas, P. W., Bailey, J. A., Tamura, M., Hirst, E., Harrison, D. and Bartholomew-Biggs, M.: PlanetPol: A Very High Sensitivity Polarimeter, Publ. Astron. Soc. Pacific, 118(847), 1302–1318, doi:10.1086/507955, 2006.

Houghton, I. M. P., Aplin, K. L. and Nicoll, K. A.: Triboelectric charging of volcanic ash from the 2011 Grímsvötn eruption, Phys. Rev. Lett., 111(11), doi:10.1103/PhysRevLett.111.118501, 2013.

Huang, Y., Kok, J. F., Kandler, K., Lindqvist, H., Nousiainen, T., Sakai, T., Adebiyi, A. and

Jokinen, O.: Climate Models and Remote Sensing Retrievals Neglect Substantial Desert Dust Asphericity, Geophys. Res. Lett., 47(6), 1–11, doi:10.1029/2019GL086592, 2020.

Huang, Y., Adebiyi, A. A., Formenti, P. and Kok, J. F.: Linking the Different Diameter Types of Aspherical Desert Dust Indicates That Models Underestimate Coarse Dust Emission, Geophys. Res. Lett., 48(6), 1–12, doi:10.1029/2020GL092054, 2021.

Van de Hulst, H. C.: Light scattering by small particles, Q. J. R. Meteorol. Soc., 84(360), 198–199, doi:https://doi.org/10.1002/qj.49708436025, 1958.

Huneeus, N., Schulz, M., Balkanski, Y., Griesfeller, J., Prospero, J., Kinne, S., Bauer, S., Boucher, O., Chin, M., Dentener, F., Diehl, T., Easter, R., Fillmore, D., Ghan, S., Ginoux, P., Grini, A., Horowitz, L., Koch, D., Krol, M. C., Landing, W., Liu, X., Mahowald, N., Miller, R., Morcrette, J.-J., Myhre, G., Penner, J., Perlwitz, J., Stier, P., Takemura, T. and Zender, C. S.: Global dust model intercomparison in AeroCom phase I, Atmos. Chem. Phys., 11(15), 7781–7816, doi:10.5194/acp-11-7781-2011, 2011.

Ilin, N. V., Slyunyaev, N. N. and Mareev, E. A.: Toward a Realistic Representation of Global Electric Circuit Generators in Models of Atmospheric Dynamics, J. Geophys. Res. Atmos., 125(6), 1–24, doi:10.1029/2019JD032130, 2020.

Inculet, I. I., Castle, G. S. P. and Aartsen, G.: Generation of bipolar electric fields during industrial handling of powders, Chem. Eng. Sci., 61(7), 2249–2253, doi:10.1016/j.ces.2005.05.005, 2006.

Ito, A., Adebiyi, A. A., Huang, Y. and Kok, J. F.: Less atmospheric radiative heating by dust due to the synergy of coarser size and aspherical shape, Atmos. Chem. Phys., 21(22), 16869–16891, doi:10.5194/acp-21-16869-2021, 2021.

Jickells, T. D., An, Z. S., Andersen, K. K., Baker, A. R., Bergametti, C., Brooks, N., Cao, J. J., Boyd, P. W., Duce, R. A., Hunter, K. A., Kawahata, H., Kubilay, N., LaRoche, J., Liss, P. S., Mahowald, N., Prospero, J. M., Ridgwell, A. J., Tegen, I. and Torres, R.: Global iron connections between desert dust, ocean biogeochemistry, and climate, Science (80-.)., 308(5718), 67–71, doi:10.1126/science.1105959, 2005.

Jokinen, O., Lindqvist, H., Kandler, K., Kemppinen, O. and Nousiainen, T.: Stereogrammetric Shapes of Mineral Dust Particles, , 331–358, 2018.

Kalinin, A. V., Slyunyaev, N. N., Mareev, E. A. and Zhidkov, A. A.: Stationary and nonstationary models of the global electric circuit: Well-posedness, analytical relations, and

numerical implementation, Izv. - Atmos. Ocean Phys., 50(3), 314–322, doi:10.1134/S0001433814030074, 2014.

Kamra, a. K.: Measurements of the electrical properties of dust storms, J. Geophys. Res., 77(30), 5856, doi:10.1029/JC077i030p05856, 1972.

Kamra, A. K. and Vonnegut, B.: A Laboratory Investigation of the Effect of Particle Collisions on the Generation of Electric Fields in Thunderstorms, J. Atmos. Sci., 28(4), 640–644, doi:https://doi.org/10.1175/1520-0469(1971)028<0640:ALIOTE>2.0.CO;2, 1971.

Kanagy, S. P. and Mann, C. J.: Electrical properties of eolian sand and silt, Earth Sci. Rev., 36(3–4), 181–204, doi:10.1016/0012-8252(94)90057-4, 1994.

Kandler, K., Lieke, K., Benker, N., Emmel, C., KÜPPER, M., MÜLLER-EBERT, D., EBERT, M., SCHEUVENS, D., SCHLADITZ, A., SCHÜTZ, L. and WEINBRUCH, S.: Electron microscopy of particles collected at Praia, Cape Verde, during the Saharan Mineral Dust Experiment: particle chemistry, shape, mixing state and complex refractive index, Tellus B, 63(4), 475–496, doi:https://doi.org/10.1111/j.1600-0889.2011.00550.x, 2011.

Katz, S., Yair, Y., Price, C., Yaniv, R., Silber, I., Lynn, B. and Ziv, B.: Electrical properties of the 8–12th September, 2015 massive dust outbreak over the Levant, Atmos. Res., 201(November 2017), 218–225, doi:10.1016/j.atmosres.2017.11.004, 2018.

Kemp, J. C. and Barbour, M.: A PHOTOELASTIC-MODULATOR POLARIMETER AT PINE MOUNTAIN OBSERVATORY, Publ. Astron. Soc. Pacific, 93, 521–525, 1981.

Kemp, J. C., Henson, G. D., Steiner, C. T. and Powell, E. R.: The optical polarization of the Sun measured at a sensitivity of parts in ten million, Nature, 326(6110), 270–273, doi:10.1038/326270a0, 1987.

Kemppinen, O., Nousiainen, T. and Jeong, G. Y.: Effects of dust particle internal structure on light scattering, Atmos. Chem. Phys., 15(20), 12011–12027, doi:10.5194/acp-15-12011-2015, 2015.

Kemppinen, O., Laning, J. C., Mersmann, R. D., Videen, G. and Berg, M. J.: Imaging atmospheric aerosol particles from a UAV with digital holography, Sci. Rep., 10(1), 1–12, doi:10.1038/s41598-020-72411-x, 2020.

Kezoudi, M., Tesche, M., Smith, H., Tsekeri, A., Baars, H., Dollner, M., Estelle´s, V., Bu¨hl, J., Weinzierl, B., Ulanowski, Z., Mu¨ller, D. and Amiridis, V.: Measurement report: Balloon-borne in situ profiling of Saharan dust over Cyprus with the UCASS optical particle

counter, Atmos. Chem. Phys., 21(9), 6781–6797, doi:10.5194/acp-21-6781-2021, 2021.

Klett, J. D.: Ion Transport to Cloud Droplets by Diffusion and Conduction, and the Resulting Droplet Charge Distribution, J. Atmos. Sci., 28(1), 78–85, doi:https://doi.org/10.1175/1520-0469(1971)028<0078:ITTCDB>2.0.CO;2, 1971.

Klett, J. D.: Orientation Model for Particles in Turbulence, J. Atmos. Sci., 52(12), 2276–2285, 1995.

Knippertz, P. and Stuut, J. B. W.: Mineral dust: A key player in the earth system, Springer Netherlands, Netherlands., 2014.

Knobelspiesse, K., Barbosa, H. M. J., Bradley, C., Bruegge, C., Cairns, B., Chen, G., Chowdhary, J., Cook, A., Di Noia, A., Van Diedenhoven, B., Diner, D. J., Ferrare, R., Fu, G., Gao, M., Garay, M., Hair, J., Harper, D., Van Harten, G., Hasekamp, O., Helmlinger, M., Hostetler, C., Kalashnikova, O., Kupchock, A., Longo De Freitas, K., Maring, H., Vanderlei Martins, J., McBride, B., McGill, M., Norlin, K., Puthukkudy, A., Rheingans, B., Rietjens, J., Seidel, F. C., Da Silva, A., Smit, M., Stamnes, S., Tan, Q., Val, S., Wasilewski, A., Xu, F., Xu, X. and Yorks, J.: The Aerosol Characterization from Polarimeter and Lidar (ACEPOL) airborne field campaign, Earth Syst. Sci. Data, 12(3), 2183–2208, doi:10.5194/essd-12-2183-2020, 2020.

Kok, J. F. and Renno, N. O.: Enhancement of the emission of mineral dust aerosols by electric forces, Geophys. Res. Lett., 33(19), 2–6, doi:10.1029/2006gl026284, 2006.

Kok, J. F. and Renno, N. O.: The effects of electric forces on dust lifting: Preliminary studies with a numerical model, J. Phys. Conf. Ser., 142, 1–6, doi:10.1088/1742-6596/142/1/012047, 2008.

Kok, J. F. and Renno, N. O.: Electrification of wind-blown sand on Mars and its implications for atmospheric chemistry, Geophys. Res. Lett., 36(5), 2–6, doi:10.1029/2008GL036691, 2009.

Kok, J. F., Parteli, E. J. R., Michaels, T. I. and Karam, D. B.: The physics of wind-blown sand and dust, Reports Prog. Phys., 75(10), 1–119, doi:10.1088/0034-4885/75/10/106901, 2012.

Kok, J. F., Ridley, D. A., Zhou, Q., Miller, R. L., Zhao, C., Heald, C. L., Ward, D. S., Albani, S. and Haustein, K.: Smaller desert dust cooling effect estimated from analysis of dust size and abundance, Nat. Geosci., 10(4), 274–278, doi:10.1038/ngeo2912, 2017.

Kok, J. F., Adebiyi, A. A., Albani, S., Balkanski, Y., Checa-Garcia, R., Chin, M., Colarco, P. R., Hamilton, D. S., Huang, Y., Ito, A., Klose, M., Li, L., Mahowald, N. M., Miller, R. L., Obiso, V., Pérez García-Pando, C., Rocha-Lima, A. and Wan, J. S.: Contribution of the world's main dust source regions to the global cycle of desert dust, Atmos. Chem. Phys., 21(10), 8169–8193,

doi:10.5194/acp-21-8169-2021, 2021.

Kok, J. F., Storelvmo, T., Karydis, V. A., Adebiyi, A. A., Mahowald, N. M., Evan, A. T., He, C. and Leung, D. M.: Mineral dust aerosol impacts on global climate and climate change, Nat. Rev. Earth Environ., 4(2), 71–86, doi:10.1038/s43017-022-00379-5, 2023.

Kokhanenko, G. P., Balin, Y. S., Klemasheva, M. G., Nasonov, S. V., Novoselov, M. M., Penner, I. E. and Samoilova, S. V.: Scanning polarization lidar LOSA-M3: Opportunity for research of crystalline particle orientation in the ice clouds, Atmos. Meas. Tech., 13(3), 1113–1127, doi:10.5194/amt-13-1113-2020, 2020.

Kolokolova, L. and Nagdimunov, L.: Comparative analysis of polarimetric signatures of aligned and optically active ("homochiral") dust particles, Planet. Space Sci., 100, 57–63, doi:10.1016/j.pss.2014.01.002, 2014.

Kourtidis, K., Szabóné André, K., Karagioras, A., Nita, I. A., Sátori, G., Bór, J. and Kastelis, N.: The influence of circulation weather types on the exposure of the biosphere to atmospheric electric fields, Int. J. Biometeorol., doi:10.1007/s00484-020-01923-y, 2020.

Lacks, D. J. and Levandovsky, A.: Effect of particle size distribution on the polarity of triboelectric charging in granular insulator systems, J. Electrostat., 65(2), 107–112, doi:10.1016/j.elstat.2006.07.010, 2007.

Lacks, D. J. and Shinbrot, T.: Long-standing and unresolved issues in triboelectric charging, Nat. Rev. Chem., 3(8), 465–476, doi:10.1038/s41570-019-0115-1, 2019.

Lawless, P. a: PARTICLE CHARGING BOUNDS, SYMMETRY RELATIONS, AND AN ANALYTIC CHARGING RATE MODEL FOR THE CONTINUUM REGIME, Aerosol Sci. Technol., 27(2), 191–215, 1996.

Lazarian, A.: Tracing magnetic fields with aligned grains, J. Quant. Spectrosc. Radiat. Transf., 106(1–3), 225–256, doi:10.1016/j.jqsrt.2007.01.038, 2007.

Leinardi, R., Pavan, C., Yedavally, H., Tomatis, M., Salvati, A. and Turci, F.: Cytotoxicity of fractured quartz on THP-1 human macrophages: role of the membranolytic activity of quartz and phagolysosome destabilization, Arch. Toxicol., 94(9), 2981–2995, doi:10.1007/s00204-020-02819-x, 2020.

Lelieveld, J., Berresheim, H., Borrmann, S., Crutzen, P. J., Dentener, F. J., Fischer, H., Feichter, J., Flatau, P. J., Heland, J., Holzinger, R., Korrmann, R., Lawrence, M. G., Levin, Z., Markowicz, K. M., Mihalopoulos, N., Minikin, A., Ramanathan, V., De Reus, M., Roelofs, G. J., Scheeren, H.

A., Sciare, J., Schlager, H., Schultz, M., Siegmund, P., Steil, B., Stephanou, E. G., Stier, P., Traub, M., Warneke, C., Williams, J. and Ziereis, H.: Global air pollution crossroads over the Mediterranean, Science (80-.)., 298(5594), 794–799, doi:10.1126/science.1075457, 2002.

Li, F., Vogelmann, A. M. and Ramanathan, V.: Saharan dust aerosol radiative forcing measured from space, J. Clim., 17(13), 2558–2571, doi:10.1175/1520-0442(2004)017<2558:SDARFM>2.0.CO;2, 2004.

Li, S., Wang, R., Dai, C., Xu, W. and Zhan, J.: The impact of aerosols on the polarization patterns of full-sky background radiation, Opt. Express, 31(12), 19918–19930, doi:10.1364/oe.492041, 2023.

Li, X., Maring, H., Savoie, D., Voss, K. and Prospero, J. M.: Dominance of mineral dust in aerosol light-scattering in the North Atlantic trade winds, Nature, 380(6573), 416–419, doi:10.1038/380416a0, 1996.

Lindqvist, H., Jokinen, O., Kandler, K., Scheuvens, D. and Nousiainen, T.: Single scattering by realistic, inhomogeneous mineral dust particles with stereogrammetric shapes, Atmos. Chem. Phys., 14(1), 143–157, doi:10.5194/acp-14-143-2014, 2014.

Long, Z. and Yao, Q.: Evaluation of various particle charging models for simulating particle dynamics in electrostatic precipitators, J. Aerosol Sci., 41(7), 702–718, doi:10.1016/j.jaerosci.2010.04.005, 2010.

Mach, D. M., Koshak, W. J.: General Matrix Inversion Technique for the Calibration of Electric Field Sensor Arrays, J. Atmos. Ocean. Technol., 24(9), 1576–1587, doi:10.1175/JTECH2080.1, 2007.

Mach, D. M., Blakeslee, R. J., Bateman, M. G. and Bailey, J. C.: Electric fields , conductivity , and estimated currents from aircraft overflights of electrified clouds, , 114(May), 1–15, doi:10.1029/2008JD011495, 2009.

Mahowald, N., Albani, S., Kok, J. F., Engelstaeder, S., Scanza, R., Ward, D. S. and Flanner, M. G.: The size distribution of desert dust aerosols and its impact on the Earth system, Aeolian Res., 15, 53–71, doi:10.1016/j.aeolia.2013.09.002, 2014.

Mallios, S. A. and Pasko, V. P.: Charge transfer to the ionosphere and to the ground during thunderstorms, J. Geophys. Res. Sp. Phys., 117(8), 1–16, doi:10.1029/2011JA017061, 2012.

Mallios, S. A., Drakaki, E. and Amiridis, V.: Effects of dust particle sphericity and orientation on their gravitational settling in the earth's atmosphere, J. Aerosol Sci., 150(August), 105634,

doi:10.1016/j.jaerosci.2020.105634, 2020.

Mallios, S. A., Papangelis, G., Hloupis, G., Papaioannou, A., Daskalopoulou, V. and Amiridis, V.: Modeling of Spherical Dust Particle Charging due to Ion Attachment, Front. Earth Sci., 9(August), 1–22, doi:10.3389/feart.2021.709890, 2021a.

Mallios, S. A., Daskalopoulou, V. and Amiridis, V.: Orientation of non spherical prolate dust particles moving vertically in the Earth's atmosphere, J. Aerosol Sci., 151(January), 105657, doi:https://doi.org/10.1016/j.jaerosci.2020.105657, 2021b.

Mallios, S. A., Daskalopoulou, V. and Amiridis, V.: Modeling of the electrical interaction between desert dust particles and the Earth's atmosphere, J. Aerosol Sci., 165(June), 106044, doi:10.1016/j.jaerosci.2022.106044, 2022.

Marinou, E., Amiridis, V., Binietoglou, I., Tsikerdekis, A., Solomos, S., Proestakis, E., Konsta, D., Papagiannopoulos, N., Tsekeri, A., Vlastou, G., Zanis, P., Balis, D., Wandinger, U. and Ansmann, A.: Three-dimensional evolution of Saharan dust transport towards Europe based on a 9-year EARLINET-optimized CALIPSO dataset, Atmos. Chem. Phys., 17(9), 5893–5919, doi:10.5194/acp-17-5893-2017, 2017.

Marinou, E., Tesche, M., Nenes, A., Ansmann, A., Schrod, J., Mamali, D., Tsekeri, A., Pikridas, M., Baars, H., Engelmann, R., Voudouri, K. A., Solomos, S., Sciare, J., Groß, S., Ewald, F. and Amiridis, V.: Retrieval of ice-nucleating particle concentrations from lidar observations and comparison with UAV in situ measurements, Atmos. Chem. Phys., 19(17), 11315–11342, doi:10.5194/acp-19-11315-2019, 2019.

Marinou, E., Paschou, P., Tsikoudi, I., Tsekeri, A., Daskalopoulou, V., Kouklaki, D., Siomos, N., Spanakis-Misirlis, V., Voudouri, K. A., Georgiou, T., Drakaki, E., Kampouri, A., Papachristopoulou, K., Mavropoulou, I., Mallios, S., Proestakis, E., Gkikas, A., Koutsoupi, I., Raptis, I. P., Kazadzis, S., Baars, H., Floutsi, A., Pirloaga, R., Nemuc, A., Marenco, F., Kezoudi, M., Papetta, A., Močnik, G., Díez, J. Y., Ryder, C. L., Ratcliffe, N., Kandler, K., Sudharaj, A. and Amiridis, V.: An Overview of the ASKOS Campaign in Cabo Verde, Environ. Sci. Proc., 26(1), doi:10.3390/environsciproc2023026200, 2023.

Markson, R.: the Global Circuit Intensity: Its Measurements and Variation over the Last 50 Years, Bull. Am. Meteorol. Soc., 88(2), 223–241 [online] Available from: http://10.0.4.151/BAMS-88-2-223%5Cnhttps://manowar.tamucc.edu/login?url=http://search.ebscohost.com/login.aspx?direct=tr

ue&db=syh&AN=24454612&site=ehost-live&scope=site, 2007.

Markson, R., Ruhnke, L. H. and Williams, E. R.: Global scale comparison of simultaneous ionospheric potential measurements, Atmos. Res., 51(3), 315–321, doi:10.1016/S0169-8095(99)00016-2, 1999.

Martin, W. E., Hesse, E., Hough, J. H., Sparks, W. B., Cockell, C. S., Ulanowski, Z., Germer, T. A. and Kaye, P. H.: Polarized optical scattering signatures from biological materials, J. Quant. Spectrosc. Radiat. Transf., 111(16), 2444–2459, doi:10.1016/j.jqsrt.2010.07.001, 2010.

Martin, W. E., Hesse, E., Hough, J. H. and Gledhill, T. M.: High-sensitivity Stokes spectropolarimetry on cyanobacteria, J. Quant. Spectrosc. Radiat. Transf., 170, 131–141, doi:10.1016/j.jqsrt.2015.10.014, 2016.

Mattis, I., Müller, D., Ansmann, A., Wandinger, U., Preißler, J., Seifert, P. and Tesche, M.: Ten years of multiwavelength Raman lidar observations of free-tropospheric aerosol layers over central Europe: Geometrical properties and annual cycle, J. Geophys. Res. Atmos., 113(20), 1–19, doi:10.1029/2007JD009636, 2008.

Mehri, T., Kemppinen, O., David, G., Lindqvist, H., Tyynelä, J., Nousiainen, T., Rairoux, P. and Miffre, A.: Investigating the size, shape and surface roughness dependence of polarization lidars with light-scattering computations on real mineral dust particles: Application to dust particles' external mixtures and dust mass concentration retrievals, Atmos. Res., 203, 44–61, doi:10.1016/j.atmosres.2017.11.027, 2018.

Miller, R. L. and Tegen, I.: Climate response to soil dust aerosols, J. Clim., 11(12), 3247–3267, doi:10.1175/1520-0442(1998)011<3247:CRTSDA>2.0.CO;2, 1998.

Mischenko, M., Travis, L. and Lacis, A.: Part I: Basic Theory of Electromagnetic Scattering, Absorption, and Emission, Scatt. absorption, Emiss. Light by small Part., 1–128, 2002a.

Mischenko, M., Travis, L. D. L., Lacis, A. A., Mishchenko, M. I., Travis, L. D. L. and Lacis, A. A.: Scattering, absorption, and emission of light by small particles, NASA Goddard Inst. Sp. Stud., 1–128, 2002b.

Mishchenko, M. I., Lacis, A. A. and Travis, L. D.: Errors induced by the neglect of polarization in radiance calculations for rayleigh-scattering atmospheres, J. Quant. Spectrosc. Radiat. Transf., 51(3), 491–510, doi:10.1016/0022-4073(94)90149-X, 1994.

Mishchenko, M. I., Travis, L. D., Kahn, R. A. and West, R. A.: Modeling phase functions for dustlike tropospheric aerosols using a shape mixture of randomly oriented polydisperse spheroids,

J. Geophys. Res. Atmos., 102(14), 16831–16847, doi:10.1029/96jd02110, 1997.

Mishev, A.: Short- and Medium-Term Induced Ionization in the Earth Atmosphere by Galactic and Solar Cosmic Rays, edited by P. Zanis, Int. J. Atmos. Sci., 2013, 184508, doi:10.1155/2013/184508, 2013.

Moilanen, J. and Gritsevich, M.: Light scattering by airborne ice crystals – An inventory of atmospheric halos, J. Quant. Spectrosc. Radiat. Transf., 290, doi:10.1016/j.jqsrt.2022.108313, 2022.

Muir, M. S.: The potential gradient sunrise effect in atmospheric electricity, J. Atmos. Terr. Phys., 39(2), 229–233, doi:10.1016/0021-9169(77)90116-7, 1977.

Neely, R. R., Stillwell, R. A., Cole, S., Thayer, J. P., Shupe, M., Goerke, M., Dorsi, S. and Ulanowski, J.: PROPERTIES OF HORIZONTALLY ORIENTED ICE CRYSTALS OBSERVED BY POLARIZATION LIDAR OVER SUMMIT, GREENLAND, in EPJ Web of Conferences, vol. 05007, pp. 10–13., 2018.

Nicoll, K., Airey, M., Cimarelli, C., Bennett, A., Harrison, G., Gaudin, D., Aplin, K., Koh, K. L., Knuever, M. and Marlton, G.: First In Situ Observations of Gaseous Volcanic Plume Electrification, Geophys. Res. Lett., 46(6), 3532–3539, doi:10.1029/2019GL082211, 2019.

Nicoll, K., Harrison, G., Marlton, G. and Airey, M.: Consistent dust electrification from Arabian Gulf sea breezes, Environ. Res. Lett., 15(8), doi:10.1088/1748-9326/ab9e20, 2020.

Nicoll, K. A.: Measurements of Atmospheric Electricity Aloft, Surv. Geophys., 33(5), 991–1057, doi:10.1007/s10712-012-9188-9, 2012.

Nicoll, K. A.: Note: A self-calibrating electrometer for atmospheric charge measurements from a balloon platform, Rev. Sci. Instrum., 84(9), 1–4, doi:10.1063/1.4821500, 2013.

Nicoll, K. A. and Harrison, R. G.: A lightweight balloon-carried cloud charge sensor, Rev. Sci. Instrum., 80(1), 0–4, doi:10.1063/1.3065090, 2009.

Nicoll, K. A., Harrison, R. G. and Ulanowski, Z.: Observations of Saharan dust layer electrification, Environ. Res. Lett., 6(1), 1–8, doi:10.1088/1748-9326/6/1/014001, 2011a.

Nicoll, K. A., Harrison, R. G. and Ulanowski, Z.: Observations of Saharan dust layer electrification, Environ. Res. Lett., 6(1), doi:10.1088/1748-9326/6/1/014001, 2011b.

Nicoll, K. A., Harrison, R. G., Silva, H. G., Salgado, R., Melgâo, M. and Bortoli, D.: Electrical sensing of the dynamical structure of the planetary boundary layer, Atmos. Res., 202, 81–95, doi:10.1016/j.atmosres.2017.11.009, 2018.

Nousiainen, T. and Kandler, K.: Light scattering by atmospheric mineral dust particles, in Light Scattering Reviews 9: Light Scattering and Radiative Transfer, edited by A. A. Kokhanovsky, pp. 3–52, Springer Berlin Heidelberg, Berlin, Heidelberg., 2015.

Pan, P., Wang, X., Yang, T., Pu, X., Wang, W., Bao, C. and Gao, J.: High-similarity analytical model of skylight polarization pattern based on position variations of neutral points, Opt. Express, 31(9), 15189, doi:10.1364/oe.489534, 2023.

Percival, D. B. and Walden, A. T.: Wavelet Methods for Time Series Analysis, Cambridge University Press., 2000.

Povel, H.-P.: Imaging Stokes polarimetry with piezoelastic modulators and charge-coupled-device image sensors, Opt. Eng., 34(7), 1870, doi:10.1117/12.200596, 1995.

R. Siebenmorgen, N. V. V. and S. B.: Dust in the diffuse interstellar medium Extinction, emission, linear and circular polarisation, Astron. Astrophys., A82(56), 18, doi:10.1098/rsta.2006.1875, 2014.

Raina, B. N. and Makhdomi, B. A.: On the sunrise effect in atmospheric electricity, J. Atmos. Terr. Phys., 42(2), 155–160, doi:10.1016/0021-9169(80)90075-6, 1980.

Ramaprakash, A. N., Rajarshi, C. V., Das, H. K., Khodade, P., Modi, D., Panopoulou, G., Maharana, S., Blinov, D., Angelakis, E., Casadio, C., Fuhrmann, L., Hovatta, T., Kiehlmann, S., King, O. G., Kylafis, N., Kougentakis, A., Kus, A., Mahabal, A., Marecki, A., Myserlis, I., Paterakis, G., Paleologou, E., Liodakis, I., Papadakis, I., Papamastorakis, I., Pavlidou, V., Pazderski, E., Pearson, T. J., Readhead, A. C. S., Reig, P., Słowikowska, A., Tassis, K. and Zensus, J. A.: RoboPol: A four-channel optical imaging polarimeter, Mon. Not. R. Astron. Soc., 485(2), 2355–2366, doi:10.1093/mnras/stz557, 2019.

Reddell, B. D., Benbrook, J. R., Bering, E. A., Cleary, E. N. and Few, A. A.: Seasonal variations of atmospheric electricity measured at Amundsen-Scott South Pole Station, J. Geophys. Res. Sp. Phys., 109(A9), 1–17, doi:10.1029/2004JA010536, 2004.

Renard, J.-B., Dulac, F., Berthet, G., Lurton, T., Vignelles, D., Jégou, F., Tonnelier, T., Jeannot, M., Couté, B., Akiki, R., Verdier, N., Mallet, M., Gensdarmes, F., Charpentier, P., Mesmin, S., Duverger, V., Dupont, J.-C., Elias, T., Crenn, V., Sciare, J., Zieger, P., Salter, M., Roberts, T., Giacomoni, J., Gobbi, M., Hamonou, E., Olafsson, H., Dagsson-Waldhauserova, P., Camy-Peyret, C., Mazel, C., Décamps, T., Piringer, M., Surcin, J. and Daugeron, D.: LOAC: a small aerosol optical counter/sizer for ground-based and balloon measurements of the size distribution and nature

of atmospheric particles -- Part 1: Principle of measurements \hack{\newline}and instrument evaluation, Atmos. Meas. Tech., 9(4), 1721–1742, doi:10.5194/amt-9-1721-2016, 2016.

Renard, J. B., Dulac, F., Durand, P., Bourgeois, Q., Denjean, C., Vignelles, D., Couté, B., Jeannot, M., Verdier, N. and Mallet, M.: In situ measurements of desert dust particles above the western Mediterranean Sea with the balloon-borne Light Optical Aerosol Counter/sizer (LOAC) during the ChArMEx campaign of summer 2013, Atmos. Chem. Phys., 18(5), 3677–3699, doi:10.5194/acp-18-3677-2018, 2018.

Renno, N. O. and Kok, J. F.: Electrical activity and dust lifting on earth, Mars, and beyond, Space Sci. Rev., 137(1–4), 419–434, doi:10.1007/s11214-008-9377-5, 2008.

Riousset, J. A., Pasko, V. P., Krehbiel, P. R., Thomas, R. J. and Rison, W.: Three-dimensional fractal modeling of intracloud lightning discharge in a New Mexico thunderstorm and comparison with lightning mapping observations, J. Geophys. Res. Atmos., 112(15), 1–17, doi:10.1029/2006JD007621, 2007.

Rycroft, M. J., Harrison, R. G., Nicoll, K. A. and Mareev, E. A.: An overview of earth's global electric circuit and atmospheric conductivity, Space Sci. Rev., 137(1–4), 83–105, doi:10.1007/s11214-008-9368-6, 2008.

Ryder, C. L., Highwood, E. J., Rosenberg, P. D., Trembath, J., Brooke, J. K., Bart, M., Dean, A., Crosier, J., Dorsey, J., Brindley, H., Banks, J., Marsham, J. H., McQuaid, J. B., Sodemann, H. and Washington, R.: Optical properties of Saharan dust aerosol and contribution from the coarse mode as measured during the Fennec 2011 aircraft campaign, Atmos. Chem. Phys., 13(1), 303–325, doi:10.5194/acp-13-303-2013, 2013.

Ryder, C. L., McQuaid, J. B., Flamant, C., Rosenberg, P. D., Washington, R., Brindley, H. E., Highwood, E. J., Marsham, J. H., Parker, D. J., Todd, M. C., Banks, J. R., Brooke, J. K., Engelstaedter, S., Estelles, V., Formenti, P., Garcia-Carreras, L., Kocha, C., Marenco, F., Sodemann, H., Allen, C. J. T., Bourdon, A., Bart, M., Cavazos-Guerra, C., Chevaillier, S., Crosier, J., Darbyshire, E., Dean, A. R., Dorsey, J. R., Kent, J., O'Sullivan, D., Schepanski, K., Szpek, K., Trembath, J. and Woolley, A.: Advances in understanding mineral dust and boundary layer processes over the Sahara from Fennec aircraft observations, Atmos. Chem. Phys., 15(14), 8479–8520, doi:10.5194/acp-15-8479-2015, 2015.

Ryder, C. L., Marenco, F., Brooke, J. K., Estelles, V., Cotton, R., Formenti, P., McQuaid, J. B., Price, H. C., Liu, D., Ausset, P., Rosenberg, P. D., Taylor, J. W., Choularton, T., Bower, K., Coe,

H., Gallagher, M., Crosier, J., Lloyd, G., Highwood, E. J. and Murray, B. J.: Coarse-mode mineral dust size distributions, composition and optical properties from AER-D aircraft measurements over the tropical eastern Atlantic, Atmos. Chem. Phys., 18(23), 17225–17257, doi:10.5194/acp-18-17225-2018, 2018a.

Ryder, C. L., Marenco, F., Brooke, J. K., Estelles, V., Cotton, R., Formenti, P., McQuaid, J. B., Price, H. C., Liu, D., Ausset, P., Rosenberg, P., Taylor, J. W., Choularton, T., Bower, K., Coe, H., Gallagher, M., Crosier, J., Lloyd, G., Highwood, E. J. and Murray, B. J.: Coarse mode mineral dust size distributions, composition and optical properties from AER-D aircraft measurements over the Tropical Eastern Atlantic, Atmos. Chem. Phys. Discuss., 98, 1–49, doi:10.5194/acp-2018-739, 2018b.

Saidou Chaibou, A. A., Ma, X. and Sha, T.: Dust radiative forcing and its impact on surface energy budget over West Africa, Sci. Rep., 10(1), 1–18, doi:10.1038/s41598-020-69223-4, 2020.

Saito, M. and Yang, P.: Advanced Bulk Optical Models Linking the Backscattering and Microphysical Properties of Mineral Dust Aerosol, Geophys. Res. Lett., 48(17), 1–12, doi:10.1029/2021GL095121, 2021.

Saito, M., Yang, P., Ding, J. and Liu, X.: A Comprehensive Database of the Optical Properties of Irregular Aerosol Particles for Radiative Transfer Simulations, J. Atmos. Sci., 78(7), 2089–2111, doi:https://doi.org/10.1175/JAS-D-20-0338.1, 2021.

Sartor, J. D.: The Role of Particle Interactions in the Distribution of Electricity in Thunderstorms, J. Atmos. Sci., 24(6), 601–615, doi:https://doi.org/10.1175/1520-0469(1967)024<0601:TROPII>2.0.CO;2, 1967.

Shao, Y., Wyrwoll, K. H., Chappell, A., Huang, J., Lin, Z., McTainsh, G. H., Mikami, M., Tanaka, T. Y., Wang, X. and Yoon, S.: Dust cycle: An emerging core theme in Earth system science, Aeolian Res., 2(4), 181–204, doi:10.1016/j.aeolia.2011.02.001, 2011a.

Shao, Y., Ishizuka, M., Mikami, M. and Leys, J. F.: Parameterization of size-resolved dust emission and validation with measurements, J. Geophys. Res. Atmos., 116(8), doi:10.1029/2010JD014527, 2011b.

Siingh, D., Gopalakrishnan, V., Singh, R. P., Kamra, A. K., Singh, S., Pant, V., Singh, R. and Singh, A. K.: The atmospheric global electric circuit: An overview, Atmos. Res., 84(2), 91–110, doi:10.1016/j.atmosres.2006.05.005, 2007.

Silva, H. G., Lopes, F. M., Pereira, S., Nicoll, K., Barbosa, S. M., Conceição, R., Neves, S.,

Harrison, R. G. and Collares Pereira, M.: Saharan dust electrification perceived by a triangle of atmospheric electricity stations in Southern Portugal, J. Electrostat., 84, 106–120, doi:10.1016/j.elstat.2016.10.002, 2016.

Skalidis, R. and Tassis, K.: High-accuracy estimation of magnetic field strength in the interstellar medium from dust polarization, , (2009) [online] Available from: http://arxiv.org/abs/2010.15141, 2020.

Solomos, S., Kallos, G., Kushta, J., Astitha, M., Tremback, C., Nenes, A. and Levin, Z.: An integrated modeling study on the effects of mineral dust and sea salt particles on clouds and precipitation, Atmos. Chem. Phys., 11(2), 873–892, doi:10.5194/acp-11-873-2011, 2011.

Solomos, S., Kalivitis, N., Mihalopoulos, N., Amiridis, V., Kouvarakis, G., Gkikas, A., Binietoglou, I., Tsekeri, A., Kazadzis, S., Kottas, M., Pradhan, Y., Proestakis, E., Nastos, P. T. and Marenco, F.: From tropospheric folding to Khamsin and Foehn winds: How atmospheric dynamics advanced a record-breaking dust episode in Crete, Atmosphere (Basel)., 9(7), doi:10.3390/atmos9070240, 2018.

Stenflo, J. O.: Polarization of the Sun's continuous spectrum, Astron. Astrophys., 429(2), 713–730, doi:10.1051/0004-6361:20041667, 2005.

Stokes, R. A., E. P. A. and S. J. B.: A New Astronomical Polarimeter, Opt. Eng., 15(1), doi:https://doi.org/10.1117/12.7971898, 1976.

Stolzenburg, M. and Marshall, T. C.: Charge structure and dynamics in thunderstorms, Space Sci. Rev., 137(1–4), 355–372, doi:10.1007/s11214-008-9338-z, 2008.

Tegen, I., Hollrig, P., Chin, M., Fung, I., Jacob, D. and Penner, J.: Contribution of different aerosol species to the global aerosol extinction optical thickness: Estimates from model results, J. Geophys. Res. Atmos., 102(20), 23895–23915, doi:10.1029/97jd01864, 1997.

Tinsley, B. A. and Zhou, L.: Initial results of a global circuit model with variable stratospheric and tropospheric aerosols, J. Geophys. Res., 111(August), 1–23, doi:10.1029/2005JD006988, 2006.

Toth III, J., Rajupet, S., Squire, H., Volbers, B., Zhou, J., Xie, L., Sankaran, R. M. and Lacks, D.: Electrostatic forces alter particle size distributions in atmospheric dust, Atmos. Chem. Phys. Discuss., 1–14, doi:10.5194/acp-2019-650, 2019.

Tsekeri, A., Amiridis, V., Louridas, A., Georgoussis, G., Freudenthaler, V., Metallinos, S., Doxastakis, G., Gasteiger, J., Siomos, N., Paschou, P., Georgiou, T., Tsaknakis, G., Evangelatos, C. and Binietoglou, I.: Polarization lidar for detecting dust orientation: system design and

calibration, Atmos. Meas. Tech., 14(12), 7453–7474, doi:10.5194/amt-14-7453-2021, 2021.

Ulanowski, Z., Hesse, E., Kaye, P. H. and Baran, A. J.: Light scattering by complex ice-analogue crystals, J. Quant. Spectrosc. Radiat. Transf., 100(1–3), 382–392, doi:10.1016/j.jqsrt.2005.11.052, 2006.

Ulanowski, Z., Bailey, J., Lucas, P. W., Hough, J. H. and Hirst, E.: Alignment of atmospheric mineral dust due to electric field, Atmos. Chem. Phys., 7(24), 6161–6173, doi:10.5194/acp-7-6161-2007, 2007.

Veselovskii, I., Goloub, P., Podvin, T., Bovchaliuk, V., Derimian, Y., Augustin, P., Fourmentin, M., Tanre, D., Korenskiy, M., Whiteman, D. N., Diallo, A., Ndiaye, T., Kolgotin, A. and Dubovik, O.: Retrieval of optical and physical properties of African dust from multiwavelength Raman lidar measurements during the SHADOW campaign in Senegal, Atmos. Chem. Phys., 16(11), 7013–7028, doi:10.5194/acp-16-7013-2016, 2016.

Veselovskii, I., Hu, Q., Goloub, P., Podvin, T., Korenskiy, M., Derimian, Y., Legrand, M. and Castellanos, P.: Variability in lidar-derived particle properties over West Africa due to changes in absorption: Towards an understanding, Atmos. Chem. Phys., 20(11), 6563–6581, doi:10.5194/acp-20-6563-2020, 2020.

Waitukaitis, S. R., Lee, V., Pierson, J. M., Forman, S. L. and Jaeger, H. M.: Size-dependent same-material tribocharging in insulating grains, Phys. Rev. Lett., 112(21), 1–5, doi:10.1103/PhysRevLett.112.218001, 2014.

Weinzierl, B., Ansmann, A., Prospero, J. M., Althausen, D., Benker, N., Chouza, F., Dollner, M., Farrell, D., Fomba, W. K., Freudenthaler, V., Gasteiger, J., Groß, S., Haarig, M., Heinold, B., Kandler, K., Kristensen, T. B., Mayol-Bracero, O. L., Müller, T., Reitebuch, O., Sauer, D., Schäfler, A., Schepanski, K., Spanu, A., Tegen, I., Toledano, C. and Walser, A.: The Saharan aerosol long-range transport and aerosol-cloud-interaction experiment: Overview and selected highlights, Bull. Am. Meteorol. Soc., 98(7), 1427–1451, doi:10.1175/BAMS-D-15-00142.1, 2017.

Whitcher, B., Guttorp, P. and Percival, D. B.: Wavelet analysis of covariance with application to atmospheric time series, J. Geophys. Res. Atmos., 105(D11), 14941–14962, doi:https://doi.org/10.1029/2000JD900110, 2000.

Wieland, S., Balmes, A., Bender, J., Kitzinger, J., Meyer, F., Ramsperger, A. F. R. M., Roeder, F., Tengelmann, C., Wimmer, B. H., Laforsch, C. and Kress, H.: From properties to toxicity: Comparing microplastics to other airborne microparticles, J. Hazard. Mater., 428, 128151,

doi:https://doi.org/10.1016/j.jhazmat.2021.128151, 2022.

Williams, E., Nathou, N., Hicks, E., Pontikis, C., Russell, B., Miller, M. and Bartholomew, M. J.: The electrification of dust-lofting gust fronts ('haboobs') in the Sahel, Atmos. Res., 91(2–4), 292–298, doi:10.1016/j.atmosres.2008.05.017, 2009.

Williams, E. R.: The global electrical circuit: A review, Atmos. Res., 91(2–4), 140–152, doi:10.1016/j.atmosres.2008.05.018, 2009.

Wright, H. L.: The influence of atmospheric suspensoids upon the earth's electric field as indicated by observations at kew observatory, Proc. Phys. Soc., 45(2), 152–171, doi:10.1088/0959-5309/45/2/303, 1933.

Yair, Y. and Levin, Z.: Charging of polydisperse aerosol particles by atmospheric ions, J. Geophys. Res., 94(D11), 13.085-13.901, 1989.

Yair, Y., Katz, S., Yaniv, R., Ziv, B. and Price, C.: An electrified dust storm over the Negev desert, Israel, Atmos. Res., 181, 63–71, doi:10.1016/j.atmosres.2016.06.011, 2016.

Yang, H. and Li, Z.-Y.: The Effects of Dust Optical Properties on the Scattering-induced Disk Polarization by Millimeter-sized Grains, Astrophys. J., 889(1), 15, doi:10.3847/1538-4357/ab5f08, 2020.

Yaniv, R., Yair, Y., Price, C. and Katz, S.: Local and global impacts on the fair-weather electric field in Israel, Atmos. Res., 172–173, 119–125, doi:10.1016/j.atmosres.2015.12.025, 2016.

Yaniv, R., Yair, Y., Price, C., Mkrtchyan, H., Lynn, B. and Reymers, A.: Ground-based measurements of the vertical E-field in mountainous regions and the "Austausch" effect, Atmos. Res., 189, 127–133, doi:10.1016/j.atmosres.2017.01.018, 2017.

Yurkin, M. A. and Hoekstra, A. G.: The discrete dipole approximation: An overview and recent developments, J. Quant. Spectrosc. Radiat. Transf., 106(1–3), 558–589, doi:10.1016/j.jqsrt.2007.01.034, 2007.

Yurkin, M. A. and Hoekstra, A. G.: The discrete-dipole-approximation code ADDA: Capabilities and known limitations, J. Quant. Spectrosc. Radiat. Transf., 112(13), 2234–2247, doi:10.1016/j.jqsrt.2011.01.031, 2011.

Zhang, H. and Zheng, X.: Quantifying the large-scale electrification equilibrium effects in dust storms using field observations at Qingtu Lake Observatory, , (June), 2018.

Zhang, H. and Zhou, Y. H.: Reconstructing the electrical structure of dust storms from locally observed electric field data, Nat. Commun., 11(1), doi:10.1038/s41467-020-18759-0, 2020.

Zhang, H., Zheng, X. J. and Bo, T.: Electrification of saltating particles in wind-blown sand: Experiment and theory, J. Geophys. Res. Atmos., 118(21), 12086–12093, doi:10.1002/2013JD020239, 2013.

Zhao, H., Castle, G. S. P., Inculet, I. I. and Bailey, A. G.: Bipolar charging of poly-disperse polymer powders in fluidized beds, IEEE Trans. Ind. Appl., 39(3), 612–618, doi:10.1109/TIA.2003.810663, 2003.

Zheng, X.-J.: Electrification of wind-blown sand: Recent advances and key issues, Eur. Phys. J. E, 36(12), 138, doi:10.1140/epje/i2013-13138-4, 2013.

Zheng, X. J., Huang, N. and Zhou, Y.-H.: Laboratory measurement of electrification of wind-blown sands and simulation of its effect on sand saltation movement, J. Geophys. Res. Atmos., 108(D10), doi:https://doi.org/10.1029/2002JD002572, 2003.

Zhou, L. and Tinsley, B. A.: Production of space charge at the boundaries of layer clouds, J. Geophys. Res. Atmos., 112(11), 1–17, doi:10.1029/2006JD007998, 2007.